

Seyfert Galaxies : Nuclear Radio Structure and Unification

A thesis
submitted for the degree of
Doctor of Philosophy
in the Faculty of Science

by

Dharam Vir Lal




DEPARTMENT OF PHYSICS
INDIAN INSTITUTE OF SCIENCE
BANGALORE - 560 012, INDIA
April 2001

To my parents

Declaration

I hereby declare that the work reported in this thesis titled "Seyfert Galaxies : Nuclear Radio Structure and Unification" is entirely original and has been carried out by me independently in the Department of Physics, Indian Institute of Science, and Indian Institute of Astrophysics, under the Joint Astronomy Programme, under the supervision of Dr. Prajval Shastri, Indian Institute of Astrophysics, Bangalore 560 034. I further declare that this work has not formed the basis for the award of any degree, diploma, fellowship, associateship or similar title of any University or Institution.

In keeping with the general practice of reporting scientific observations, due acknowledgement has been made whenever the work described is based on the findings of other investigators. Any omission which might have occurred by oversight or error in judgement is regretted.



(Dharam Vir Lal)

Department of Physics
Indian Institute of Science
Bangalore 560 012, India.

Acknowledgements

"To live is the rarest thing in the world. Most people exist, that is all."

Oscar Wilde (1854 -1900)

I would like to express my gratitude towards Late Prof. V. K. Kapahi, for guiding me towards the path I must take. I am grateful to Prof. K. R. Anantharamaiah and Prof. A. Pramesh Rao, who introduced me to radio astronomy and created an interest in this field.

I wish to express my thanks to my supervisor Dr. Prajval Shastri for her constant guidance and support during the last six years and especially during the last few months when she was hard pressed for time. Without her persistence and vision this thesis would have been impossible.

I thank our collaborator Dr. Denise C. Gabuzda, who made time for me in her busy schedule, came to Bangalore for discussions and guided me during my stay at JIVE, The Netherlands. My special thanks to her for helping me with the thesis writing. I thank the JIVE-institute for their support.

I thank Dr. H. C. Bhatt, Dr. A. K. Pati, Prof. T. P. Prabhu and Prof. C. Sivaram, who helped me with useful discussions whenever I sought their assistance. I also thank Prof. D. C. V. Mallik, Prof. R. Nityananda and Dr. Pijush Bhattacharjee for their guidance during the course-work.

I thank the Director, IIA, Dr. Ramanath Cowsik and the IISc-JAP-convenors, Dr. Arnab Rai Choudhuri and Dr. Chanda Jog for providing the necessary facilities for my work. I thank the Chairman, Board of Graduate Studies, IIA, Prof. S. S. Hasan, and other members of the board as well.

I thank the librarian Dr. A. Vagiswari, Ms. Christina Louis and all the library staff for their services. I thank Mr. J. S. Nathan and Mr. A. V. Ananth of the computer division.

This thesis work involves observations made on NRAO and EVN instruments. "The National Radio Astronomy Observatory (NRAO) is a facility of the National Science Foundation operated under cooperative agreement by Associated Universities, Inc". "I thank the staff of the EVN observatories who made these observations possible". Partial support for this research work came from the "Indo-Russian Integrated Long Term Programme". This research also has made use of:

- the NASA/IPAC Extragalactic Database (NED) which is operated by the Jet Propulsion Laboratory, California Institute of Technology, under contract with the National Aeronautics and Space Administration
- NASA's Astrophysics Data System Abstract Service
- the SIMBAD database, operated at CDS, Strasbourg, France

I take this opportunity to remember Charu, my beloved senior, for showing me (by example) how to face challenges in life with a smile. My thanks to Alex for all that he has taught me and for being there for me through all those difficult times.

Special thanks to my friends at IIA for the good times we had, especially my batch mates- Geetha, Sridhar and Suresh and the rest of the gang Bhatti, Preeti, Mahesh, Manoj, Raji, Ravi & seniors- Arun, Dilip, Holger, Krishna, Nayak, Sankar and Sivarani. I also thank Amit, Kunj and Renu, for those early cheerful days in IISc.

My thanks to my colleagues at IIA, AtishJana, Bhargavi, DilipJana, Geetanjali, Kathir, Latha, Mangala, Manas, Pandey, Pavan, Peyman, Rabbi, Ramachandra, Ramesh, Reji, Sahoo, Saidur, Shalima, Sonjoy, Swara and Vaishali; JAP-mates, Ambika, Ashish, Chaitra, Divya, Ishwar, Moja, Niruj, Rajaguru, Shanmugam, Sudip and Srik

I thank George, Anusha and Susan for making me feel at home. Mrs. Jain and her family for homely dinners. Special thanks to Gopans and Raja for keeping me cheerful. Thanks to my good friend Maithili, for the many wonderful times.

I thank my brother, Prakash and bhabhiji, Gayatri, for their constant support through all the years I have been away from home. I also thank my brother, Raj, and his family. I thank my younger brother, Jai, and also Kamal & Shalu. Special thanks to the little ones, Vishu, Anoo, Manoo, Rishu and Rikkoo for their love and affection. And finally my thanks to all those who have been waiting patiently for this to happen!

Contents

1	Introduction	1
1.1	Overview	1
1.2	Active galactic nucleus	1
1.3	AGN taxonomy	2
1.3.1	Radio-loud and radio-quiet AGNs	2
1.3.1.1	Radio-loud objects	2
1.3.1.2	Radio-quiet objects	4
1.4	Seyfert galaxies	4
1.4.1	Discovery, classification and detection	7
1.4.2	Observed properties of Seyfert galaxies	9
1.4.3	Overall structure and geometry	10
1.4.4	Unified scheme model	12
1.5	Motivation	14
1.6	Thesis outline	15
2	Motivation and methodology	17
2.1	Introduction	17
2.2	A challenge to the unification scheme	17
2.3	The goal	18
2.4	Aperture synthesis and Very Long Baseline Interferometry	19
2.4.1	Aperture synthesis	19

2.4.1.1	The aim of aperture synthesis	20
2.4.1.2	The principle of aperture synthesis	21
2.4.1.3	Interferometry techniques	22
2.4.1.4	Very Large Array	27
2.4.2	Very Long Baseline Interferometry	28
2.4.2.1	VLBI techniques	29
2.4.2.2	The Very Long Baseline Array	32
2.4.2.3	The European VLBI Network	32
2.4.2.4	The phased arrays as VLBI elements	32
2.5	Construction of our sample	33
2.5.1	<i>Bona fide</i> Seyfert galaxies	33
2.5.2	Criterion to minimise obscuration of optical properties	34
2.5.3	Criteria for the feasibility of our experiment	35
2.5.4	Criteria based on orientation independent parameters	38
2.5.4.1	Heliocentric redshift	38
2.5.4.2	Luminosity of the [O III] λ 5007 emission line: Measure of intrinsic AGN power	38
2.5.4.3	Stellar luminosity of the host galaxy	39
2.5.4.4	Absolute bulge luminosity of the host galaxy	42
2.5.4.5	Hubble type of the host galaxy	43
2.5.5	Our Seyfert sample	44
2.6	Summary	46
3	Observations and results	49
3.1	Introduction	49
3.2	Observations	49
3.2.1	VLBI observations	49

3.2.2	VLA observations	52
3.3	Data reductions	52
3.3.1	VLBI data	52
3.3.2	VLA data	53
3.4	Results and analysis	54
3.4.1	The radio images	54
3.4.2	Description of the sources	55
3.5	Summary	84
4	Radio emission on kpc and pc-scales: Interpretation	91
4.1	Introduction	91
4.2	Seyfert nuclei: Starburst or accretion-powered central engine ?	92
4.3	Tests of the unified scheme for Seyfert galaxies	95
4.3.1	The contradiction with the unification scheme and its resolution	95
4.3.2	The pc-scale radio luminosities	97
4.3.3	kpc-scale radio luminosities	98
4.3.4	Projected linear sizes	99
4.3.5	Source spectral indices	102
4.3.6	Relativistic beaming in Seyfert galaxies?	104
4.4	CfA Seyfert galaxy sample: kpc-scale radio morphology	107
4.4.1	Radio luminosity comparisons	108
4.4.2	Projected linear sizes	109
4.4.3	Relativistic beaming	112
4.5	Summary	114
5	Further tests of unification: Infrared and X-ray data	119
5.1	Introduction	119
5.2	The infrared luminosity distribution	119

5.2.1	The mid-infrared luminosity	120
5.2.2	The far-infrared luminosity	120
5.3	The radio–infrared correlation	124
5.4	X-ray data	132
5.4.1	Hard X-ray luminosity	132
5.4.2	X-ray photon indices	133
5.5	Summary	135
6	Conclusions and future work	137
6.1	Summary of results	137
6.2	Future work	139
	Bibliography	141

List of Tables

2.1	Table showing 6σ correlated flux densities on various baselines.	37
2.2	Table showing the list of Seyfert 1 and Seyfert 2 galaxies that constitute our sample, with the parameters that were used to constraint it.	47
3.1	Observing log.	50
3.2	Target sources of our observations, VLA phase calibrators, flux density calibrator and VLBI fringe finders.	51
3.3	Radio variability of Mrk 348.	58
3.4	Radio variability of Mrk 231.	70
3.5	Parameters for VLBI maps.	87
3.6	Parameters for VLA maps.	88
3.7	VLBI observational results.	89
3.8	VLA observational results.	90
4.1	Table showing the detected components, their positions (with respect to the phase centre), corresponding flux density, size, brightness temperature of bright component, radio power and supernova rates (ν_{SN}) necessary to reproduce radio emission.	93
4.2	Table giving total, core flux densities, and the corresponding radio power on arcmin (NVSS, Condon et al. 1998), arcsec, and mas-scales, and logarithm of the linear size of source in pc; arcsec and mas-scale data are from our observations unless otherwise indicated.	116

4.3	Source flux densities and spectral indices.	117
5.1	Table showing infrared and radio properties.	123
5.2	NVSS, VLA <i>A</i> array, and VLBI radio flux densities and luminosities correlated with infrared flux densities and luminosities for all IRAS wavebands. Table gives the Spearman's rank correlation coefficients (γ_{ff} and γ_{uu}) and their corresponding significances (α_{ff} and α_{uu}).	125
5.3	Table showing X-ray properties.	135

List of Figures

1.1	The main classes of AGNs.	3
1.2	Cartoon illustrating the nested structures thought to be present within Seyfert galaxies.	11
1.3	Zeroth order model of Seyfert galaxies.	14
2.1	Two element interferometer.	23
2.2	VLA array antenna positions (inset shows inner 500×500 m ²) during our observations.	28
2.3	Histograms showing distribution of ratio of minor to major isophotal diameter axes (b/a) for the two Seyfert sub-classes (final sample).	35
2.4	Geographical positions of the VLBI stations used in our observations.	37
2.5	Histograms showing distribution of redshift (z) for the two Seyfert sub-classes.	39
2.6	Histograms showing distribution of [O III] $\lambda 5007$ luminosity for the two Seyfert sub-classes.	40
2.7	Histograms showing distribution of total stellar absolute magnitude of the host galaxy for the two Seyfert sub-classes; values in the bins indicate M_B^{total} for the sources.	42
2.8	Histograms showing distribution of absolute magnitude of the bulge (B band) for the two Seyfert sub-classes; values in the bins indicate absolute bulge magnitude for the sources.	43

2.9	Histograms showing distribution of the Hubble type (T) for the two Seyfert sub-classes (mainly from RC3 catalog and Whittle (1992A)).	45
2.10	Histograms showing distribution of the Hubble type (T) for the two Seyfert sub-classes, (mainly from Malkan et al (1998), RC3 catalog, and Whittle (1992A)).	45
3.1	6 cm MERLIN image of Mrk 348.	57
3.2	VLA and VLBA image of Mrk 348.	57
3.3	Plot showing radio variability of Mrk 348.	59
3.4	5 GHz VLA (left) and VLBI (right) image of Mrk 1.	60
3.5	5 GHz VLA (left) and VLBI (right) image of MCG 8-11-11.	61
3.6	5 GHz VLA (left) and VLBI (right) image of NGC 2273.	62
3.7	5 GHz VLA (left) and VLBI (right) image of Mrk 78.	63
3.8	6 cm VLA (left) and VLBI (right) images of Mrk 78.	63
3.9	6 cm VLA (left) and VLBI (right) image of Mrk 1218.	64
3.10	6 cm VLA (left) and VLBI (right) image of NGC 2639.	65
3.11	6 cm VLA image of NGC 2639.	65
3.12	5 GHz VLA (upper), 18 cm VLBA image (middle) and 6 cm VLBA (lower) image of NGC 4151.	67
3.13	6 cm VLA (left) and VLBI (right) image of Mrk 766.	68
3.14	6 cm VLA image of Mrk 766.	68
3.15	Plot showing radio variability of Mrk 231.	71
3.16	8.4 GHz VLA (left) and 5 GHz VLBA (right) image of Mrk 231.	72
3.17	CLEANed VLA image of Mrk 231 at 1.4 GHz (left) and VLBA 15 GHz images of Mrk 231 (right).	72
3.18	5.0 GHz small VLA image of NGC 5135.	73
3.19	5 GHz VLA (left) and VLBI (right) image of Mrk 477.	74

3.20	6 cm VLA image of Mrk 477.	74
3.21	6 cm VLA (left) and VLBI (right) image of NGC 5929.	76
3.22	8.4 GHz VLA image of NGC 5929 (left) and Our 6 cm VLA image of NGC 5929 and NGC 5930 (right).	76
3.23	5 GHz VLA (left) and VLBI (right) image of NGC 7212.	78
3.24	3.5 cm VLA image of NGC 7212 (left) and 5 GHz VLA map of NGC 7212 (right).	78
3.25	5 GHz VLA (left) and VLBI (right) image of Ark 564.	79
3.26	5 GHz VLA (left) and VLBI (right) image of NGC 7469.	80
3.27	VLA image of NGC 7469.	80
3.28	5 GHz VLA (upper) and 8.4 GHz VLA and VLBA (lower) image of Mrk 926.	82
3.29	5 GHz VLA (left) and VLBI (right) image of Mrk 530.	83
3.30	VLBI image of Mrk 530 - II.	83
3.31	5 GHz VLA (left) and VLBI (right) image of Mrk 533.	85
3.32	3.6 cm VLA image of Mrk 533.	85
3.33	5 GHz VLA (left) and VLBI (right) image of NGC 7682.	86
4.1	Histograms showing distribution of brightness temperature (K) of the bright- est component detected on mas-scales.	96
4.2	Histograms showing the ratio of flux density detected on mas-scales to the emission detected on arcsec-scales.	97
4.3	Histograms showing distribution of total radio luminosity ($\text{ergs s}^{-1}\text{Hz}^{-1}$) on mas-scales.	98
4.4	Histograms showing total radio power ($\text{ergs s}^{-1}\text{Hz}^{-1}$) on arcsec-scales.	99
4.5	Histograms showing core radio power ($\text{ergs s}^{-1}\text{Hz}^{-1}$) on arcsec-scales.	100
4.6	Histograms showing total (NVSS at 1.4 GHz) radio power ($\text{ergs s}^{-1}\text{Hz}^{-1}$) on arcsec-scales.	101

-
- 4.7 Histograms showing projected radio linear size (pc) on arcsec-scales; arrows denote objects that are unresolved. 102
- 4.8 Scatter plot of projected linear size (pc) *versus* radio luminosity on kpc-scales (ergs s⁻¹Hz⁻¹); symbols +, ×, *, and ◊ denotes resolved Seyfert 1, resolved Seyfert 2, unresolved Seyfert 1, and unresolved Seyfert 2 galaxies respectively. 103
- 4.9 Spectral indices (between 1.5 and 5 GHz) of the sample sources; the spectral index between 1.5 and 8.4 GHz is used for Mrk 348 (denoted by asterisk '*'). 104
- 4.10 Histograms of the fraction of the total radio flux density detected on mas-scales as against the extended radio emission. 107
- 4.11 Histograms showing the total detected radio power (ergs s⁻¹Hz⁻¹) for the CfA Seyfert sample using VLA *A* array at 8.4 GHz. 109
- 4.12 Histograms showing the radio luminosity (ergs s⁻¹Hz⁻¹) for the CfA Seyfert sample using VLA *C* array at 8.4 GHz; '*' and '#' denote an error of ~ 20% in flux density calibration for Seyfert 1 and 2 galaxies respectively, and arrows denote undetected objects. 110
- 4.13 Histograms showing the total extended radio power (ergs s⁻¹Hz⁻¹) for the CfA Seyfert sample at 8.4 GHz; single-headed arrow indicates non-detection on VLA *A* configuration and double-headed arrow indicates non-detection on both the configurations. 111
- 4.14 Histograms showing projected linear size (pc) of the source as measured by VLA *A* array (CfA Seyfert galaxy sample); arrows indicate unresolved objects. 112
- 4.15 Histograms showing projected linear size (pc) of the source as measured by VLA *C* array (CfA Seyfert galaxy sample); '#' for an object in a bin denotes the VLA *A* array linear size for it, and arrows indicate unresolved objects. 113
- 4.16 Histograms showing fraction of the radio core flux density detected by VLA *A* array as against the extended flux density at 8.4 GHz for CfA Seyfert sample. 114

5.1	Histograms showing distribution of total 12 μm luminosity ($\text{ergs s}^{-1}\text{Hz}^{-1}$).	121
5.2	Histograms showing distribution of total 25 μm luminosity ($\text{ergs s}^{-1}\text{Hz}^{-1}$).	121
5.3	Histograms showing distribution of total 60 μm luminosity ($\text{ergs s}^{-1}\text{Hz}^{-1}$); values in the bins indicate $\log(\text{infrared luminosity})$ for the sources.	122
5.4	Histograms showing distribution of total 100 μm luminosity ($\text{ergs s}^{-1}\text{Hz}^{-1}$).	122
5.5	The radio (NVSS, D array) <i>versus</i> mid-infrared (12 μm) scatter diagram showing Seyfert galaxies from our sample; '+' indicates Seyfert 1 galaxies and 'x' Seyfert 2 galaxies.	126
5.6	The radio (NVSS, D array) <i>versus</i> far-infrared (25 μm) scatter diagram show- ing Seyfert galaxies from our sample; '+' indicates Seyfert 1 galaxies and 'x' Seyfert 2 galaxies.	126
5.7	The radio (NVSS, D array) <i>versus</i> far-infrared (60 μm) scatter diagram show- ing Seyfert galaxies from our sample; '+' indicates Seyfert 1 galaxies and 'x' Seyfert 2 galaxies.	127
5.8	The radio (NVSS, D array) <i>versus</i> far-infrared (100 μm) scatter diagram showing Seyfert galaxies from our sample; '+' indicates Seyfert 1 galaxies and 'x' Seyfert 2 galaxies.	127
5.9	The kpc-scale radio (5 GHz) <i>versus</i> mid-infrared (12 μm) scatter diagram showing Seyfert galaxies from our sample; '+' indicates Seyfert 1 galaxies and 'x' Seyfert 2 galaxies.	128
5.10	The kpc-scale radio (5 GHz) <i>versus</i> far-infrared (25 μm) scatter diagram showing Seyfert galaxies from our sample; '+' indicates Seyfert 1 galaxies and 'x' Seyfert 2 galaxies.	128
5.11	The kpc-scale radio (5 GHz) <i>versus</i> far-infrared (60 μm) scatter diagram showing Seyfert galaxies from our sample; '+' indicates Seyfert 1 galaxies and 'x' Seyfert 2 galaxies.	129

5.12	The kpc-scale radio (5 GHz) <i>versus</i> far-infrared (100 μm) scatter diagram showing Seyfert galaxies from our sample; '+' indicates Seyfert 1 galaxies and 'x' Seyfert 2 galaxies.	129
5.13	The pc-scale radio (5 GHz) <i>versus</i> mid-infrared (12 μm) scatter diagram showing Seyfert galaxies from our sample; '+' indicates Seyfert 1 galaxies and 'x' Seyfert 2 galaxies.	130
5.14	The pc-scale radio (5 GHz) <i>versus</i> far-infrared (25 μm) scatter diagram showing Seyfert galaxies from our sample; '+' indicates Seyfert 1 galaxies and 'x' Seyfert 2 galaxies.	130
5.15	The pc-scale radio (5 GHz) <i>versus</i> far-infrared (60 μm) scatter diagram showing Seyfert galaxies from our sample; '+' indicates Seyfert 1 galaxies and 'x' Seyfert 2 galaxies.	131
5.16	The pc-scale radio (5 GHz) <i>versus</i> far-infrared (100 μm) scatter diagram showing Seyfert galaxies from our sample; '+' indicates Seyfert 1 galaxies and 'x' Seyfert 2 galaxies.	131
5.17	Histograms showing distribution of 2-10 keV X-ray luminosity (ergs s^{-1}); the objects with '*' have measurement not from ASCA instrument.	133
5.18	Histograms showing distribution of photon index; the objects with '*' have measurement not from ASCA instrument.	134

List of Symbols

- α : spectral index defines as $S_\nu \propto \nu^{-\alpha}$, p. 55
- α_{ff} : significance of Spearman's rank correlation,
for 'flux density–flux density' scatter diagram, p. 124
- α_{ll} : significance of Spearman's rank correlation
for 'luminosity–luminosity' scatter diagram, p. 124
- β : v/c , v is the velocity, p. 105
- Γ : X-ray power law photon index, p. 133
- γ : Lorentz factor, $\frac{1}{\sqrt{1-\beta^2}}$, p. 105
- γ_{ff} : Spearman's rank correlation coefficient
for 'flux density–flux density' scatter diagram, p. 124
- γ_{ll} : Spearman's rank correlation coefficient
for 'luminosity–luminosity' scatter diagram, p. 124
- η_s : VLBI system efficiency, p. 36
- θ : angle between point source and line joining two antennas, p. 22
- λ : emission wavelength, p. 22
- ν : emission frequency, p. 105
- ν_{SN} : supernova rate, p. 92
- τ : geometric delay, p. 22
- ϕ_{ij} : phase angle on the baseline formed by stations i and j , p. 30
- ϕ_{123} : closure phases, p. 30
- Ω : solid angle, p. 31
- ω : angular frequency of radiation, p. 22

A_{1234}	: closure amplitudes, p. 31
$B(x, y)$: synthesised beam, p. 25
B_T^c	: total observed optical luminosity in the B band (corrected), p. 39
D	: Doppler factor, p. 105
E	: electric field, p. 22
F_{5007}	: [O III] $\lambda 5007$ emission line flux, p. 41
$F_{H\beta}$: $H\beta$ emission line flux, p. 41
g_i	: complex antenna gain, p. 31
H_0	: Hubble constant, p. 15
M_B^{total}	: absolute magnitude of the host galaxy corrected for nuclear non-stellar emission, p. 40
$(M_B)_{bulge}$: absolute bulge magnitude, p. 42
$M_\odot \text{ yr}^{-1}$: star-formation rate in solar mass year ⁻¹ , p. 92
P	: probability, p. 132
q_0	: the cosmological deceleration parameter; assumed to be 0 unless stated otherwise, p. 15
\Re	: real part of a complex quantity, p. 24
R	: ratio of observed radio emission from the compact feature to that from the outer components, p. 106
$S(u, v)$: sampling function, p. 25
S_ν	: flux density, p. 55
T	: Hubble type of the galaxy, p. 13
T_A	: antenna temperature, p. 31
T_s	: system temperature, p. 31
t_{int}	: integration time, p. 36
V	: voltage, p. 22
$V(b)$: complex visibility of the source, p. 24
z	: redshift, p. 4

List of Constants

c	Speed of light in vacuum	$2.99792458 \times 10^{10} \text{ cm sec}^{-1}$
au	Astronomical unit	$1.49597892(1) \times 10^{13} \text{ cm}$
pc	Parsec	$3.0856(1) \times 10^{18} \text{ cm}$
ly	Light year	$9.4605 \times 10^{17} \text{ cm} = 6.324 \times 10^4 \text{ au}$
M_{\odot}	Solar mass	$1.989(2) \times 10^{33} \text{ g}$
R_{\odot}	Solar radius	$6.9598(7) \times 10^{10} \text{ cm}$
L_{\odot}	Solar luminosity	$3.826(8) \times 10^{33} \text{ erg sec}^{-1}$

Chapter 1

Introduction

1.1 Overview

‘Active galaxy’ is a general term which refers to any galaxy that produces significant emission in addition to that from its constituent stars. In this Chapter we introduce the various types of active galactic nuclei that are generally recognised (Section 1.3), and try to make clear as we proceed how these may or may not be related. We then focus on Seyfert galaxies, develop a unification model for them and present evidence in support and against it (Section 1.4). In the final two Sections (Sections 1.5 and 1.6) we discuss our goal and the organisation of the thesis.

1.2 Active galactic nucleus

A galaxy that has an exceptionally high luminosity from its nucleus and which radiates large amounts of non-stellar radiation is known as an active galactic nucleus (AGN). A typical active galaxy will exhibit some (or all) of the following properties: a bolometric luminosity in excess of 10^{37} watts; a much (several orders of magnitude) higher output of radiation than a normal galaxy; a highly luminous and compact central core, known as an AGN which varies in brightness, narrow jets of radiating matter emerging from the central core; large-scale clouds (\sim kpc) of radio-emitting material; and broad emission lines ($\Delta v \geq 1000$ km s $^{-1}$) in its spectrum (*e.g.* Krolik 1999, pp. 5-13).

A complete picture of an AGN can be obtained only by observing it at many wavelengths, preferably simultaneously over the entire electromagnetic spectrum. Active galaxies are classified according to their appearance, luminosity and spectra into the following principal types: Seyfert galaxies, radio galaxies, quasars, BL Lacertae ob-

jects (BL Lacs). There are only surprisingly subtle spectroscopic differences between a quasar with a luminosity of 10^{48} erg s^{-1} and what had previously been identified as a ‘Seyfert galaxy nucleus’ of luminosity 10^{42} erg s^{-1} (Peterson 1997). The evidence is overwhelming that these two astronomical categories must have a single common physical explanation. Thus, today, hardly any distinction is made between a ‘quasar’ and a ‘Seyfert nucleus’, as their main difference is in their luminosity (Urry & Padovani 1995).

1.3 AGN taxonomy

In the following Section we briefly describe the different classes of AGNs.

1.3.1 Radio-loud and radio-quiet AGNs

The commonly adopted criterion (Kellermann et al. 1989) to distinguish between radio-loud and radio-quiet AGNs is the ratio of radio to optical, $R_{R/O}$, of flux densities (in, say, mJy) at 6 cm (5 GHz) and 4400 Å; for radio-loud objects $R_{R/O}$ is generally greater than 10, and most radio-quiet objects fall in the range $R_{R/O} < 10$. The distribution of $R_{R/O}$ divide AGNs into two classes: radio-loud and radio-quiet objects. Radio-quiet AGNs primarily reside in spiral host galaxies, while radio-loud AGNs are found in elliptical hosts (Antonucci 1993).

1.3.1.1 Radio-loud objects

1. Quasars:

Quasars comprise the most luminous class of AGNs, with nuclear magnitudes $M_B < -23$ (Schmidt & Green 1983). Historically, quasars were distinguished from other AGNs since they were spatially unresolved on the Palomar Sky Survey photographs. Many of these sources are now known to be surrounded by a low surface brightness halo or ‘fuzz’, which does indeed appear to be starlight from the host galaxy (Peterson 1997).

2. Radio galaxies:

Strong radio sources are typically identified with giant elliptical galaxies. Two types of radio galaxies have optical spectra of the sort that one identifies with the AGN activity; broad-line radio galaxies (BLR galaxies; widths are typically

$\Delta v \approx 5000 \text{ km s}^{-1}$) and narrow-line radio galaxies (NLR galaxies; $\Delta v < 1000 \text{ km s}^{-1}$) (Peterson 1997).

3. BL Lac objects and optically violent variables:

In general, AGNs show continuum variability at all wavelengths at which they have been observed, from X-rays to radio wavelengths. A small subset of quasars show short time-scale variations that are abnormally large, *e.g.* $\Delta m \geq 0.1$ mag in the visible wavelengths on time-scales as short as a day. In addition to their large variations in flux density, they also tend to have high polarisation which also varies, in both magnitude and position angle. These sources are always radio-loud and are known as ‘optically violent variables’ (OVVs) quasars (Peterson 1997).

Some of the properties of OVVs are shared by ‘BL Lac objects’, named after the prototype of the class, BL Lacertae, which was originally identified as a highly variable star. BL Lac objects are distinguished by the absence of strong emission or absorption lines in their spectra.

It is believed that both OVVs and BL Lacs are those AGNs which have a strong relativistically beamed component close to the line of sight. Collectively, OVVs and BL Lacs are sometimes referred to as ‘blazars’.

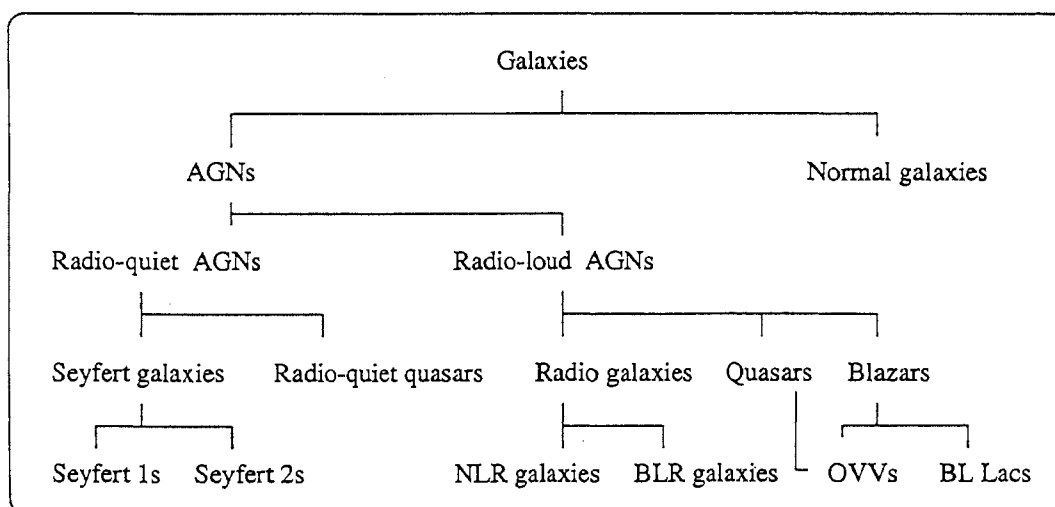


Figure 1.1: The main classes of AGNs.

1.3.1.2 Radio-quiet objects

1. Radio-quiet quasar:

Objects where the ratio of radio emission to the optical emission is < 10 , are referred to as radio-quiet quasars (Peterson 1997, p. 18).

2. Seyfert galaxies:

An AGN sitting in a spiral host galaxy, having a bright active nucleus, and a spectrum covering a wide range of ionisations is known as a Seyfert galaxy (Peterson 1997, p. 21). They are low-luminosity AGNs, with $M_B > -23$ for the active nucleus (Schmidt & Green 1983)

1.4 Seyfert galaxies

As said above, there are a number of different classes of AGN; Seyfert galaxies constitute the low luminosity end of the AGN phenomenon, *i.e.* their nuclear luminosities are roughly comparable with the total luminosity. Carl Seyfert (1943) was the first to recognise “a very small proportion of extragalactic nebulae” which consistently had a dominant nucleus with high-excitation emission lines that were wider than the absorption lines of normal galaxies.

Over the past two decades much effort has gone into finding Seyfert galaxies amongst the more normal galaxy population (Krolik 1999, pp. 22-37). Efficient ways to detect Seyfert galaxies include looking specifically for galaxies with excess of ultraviolet emission, bright X-ray emission, or unusual far-infrared colours, since these are common characteristics of Seyfert galaxies (Krolik 1999, pp. 22-37). Currently, about 800* Seyfert galaxies are known, though the number continues to rise.

A few attempts to explain activity in Seyfert galaxies have been made in the past using starburst alone or a combination of AGN and starburst. The following paragraph discusses the starburst model.

Can AGN activity be powered by a starburst alone?

A significant fraction of galaxies show the signatures of recent large-scale star formation activity (Smith et al. 1998B). Such galaxies are known widely as “starburst galaxies”. These are generally characterised by an excess of blue colours

*A catalog of all known Seyfert galaxies has been maintained by Veron-Cetty and Veron, and in its last edition (1998) about 790 Seyfert galaxies were listed with redshifts, $z < 0.1$ and brighter than 17^m in V band

and strong H II region–type emission-line spectra (due to a large number of O and B–type stars) compared with normal galaxies. They also show relatively strong radio emission (due to recent supernova remnants) (Peterson 1997, p. 28). In some cases, the starburst is apparently confined to an unresolved region at the galactic center, which looks very much like an active nucleus (Peterson 1997, p. 28). These “nuclear starbursts” are typically 10 times brighter than the giant H II region complexes seen in normal spirals and are thus distinct from the otherwise inactive late-type spirals.

It is the majority view that although the AGNs may harbour starburst activity in their nuclei, they are powered by a ‘monster’ (supermassive black hole) (Krolik & Begelman 1998). But there is also the alternate view that AGNs are powered by starbursts alone.

Starburst model: AGNs without black holes Terlevich and his colleagues have argued that a great majority of the AGNs are powered by massive stars and supernovae, albeit somewhat unusual stars in a highly unusual environment. Below we briefly summarise: (1) how this model attempts to explain properties of Seyfert galaxies. The arguments are given in more detail in Terlevich & Melnick (1985), Terlevich & Melnick (1987, 1988), Terlevich, Melnick & Moles (1987), and Terlevich (1989, 1990A, 1990B); and (2) the problem faced by this model in explaining the activity in Seyfert galaxies.

The starting point for this model is a starburst occurring in the nucleus of an early-type galaxy. The duration of the episode of star formation is a few million years. The observational manifestations of this nuclear starburst are hypothesised to differ from those of ordinary regions of high-mass star-formation. The nuclear starburst rate is usually a factor of hundred more than normal star-formation rate. For the first several million years (during the main sequence phase of the massive stars) the nuclear starburst will look like an ordinary giant H II region. After several million years, the starburst enters the ‘Warmer’ phase. ‘Warmers’ is the name given by Terlevich & Melnick (1985) to post-main-sequence ‘bare-core’ stars with $T_{eff} > 10^4$ K. They take an input spectra predicted for ‘Warmers’ and show that the spectra naturally account for the narrow emission lines ($\Delta v < 1000$ kms⁻¹) seen in Seyfert galaxies. After about 10 million years the starburst enters the phase in which it is dominated by emission from supernovae and supernova remnants (SNRs). Depending on the strengths of the

starburst, the phase is supposed to produce Seyfert nuclei or radio-quiet quasars. The X-ray, ultraviolet, and radio continua are produced by a combination of supernovae and SNRs which interact with the inter-stellar medium. The optical continuum is produced by supernovae while the infrared continuum is reprocessed thermal emission. The strong broad ($\Delta v > 1000 \text{ kms}^{-1}$) emission lines seen are hypothesised to be produced by individual supernovae. The variability of the lines and continuum arises due to ‘flares’ of total energy 10^{49-50} ergs lasting a few weeks and associated with individual supernovae (short-term); and longer term variations with energies of 10^{51-52} ergs and time-scales of \sim year that are driven by individual SNRs interacting with the dense inter-stellar medium. Terlevich (1989, 1990B) argues that these variability time-scales and energies are consistent with individual optical events in Seyfert nuclei.

Problems with the starburst model: The starburst model of Terlevich and his colleagues tries to explain activity seen in a Seyfert nucleus. This model does not attempt to explain radio-loud AGNs, it also fails to explain the kpc-scale jets seen in the Seyfert galaxies. For explaining kpc-scale jets seen in Seyfert galaxies, the host galaxy has to be seen edge-on, so that the emission from starburst and SNRs in the disk of the galaxy would be able to show kpc-scale elongated structures. This then is highly geometry dependent. However when the galaxy is mapped at higher resolutions (sub-arcsec to mas-scales) the individual emission from SNRs is resolved out and the kpc-scale emission is no longer jet-like (*e.g.* M 82: Muxlow et al. 1994; ARP 220: Smith et al. 1998A). Also, elongated radio structures are seen in face-on host galaxies as well, therefore the star-burst model is insufficient to explain activity in Seyfert galaxies.

Seyfert-starburst connection It is therefore reasonable to assume that Seyfert galaxies are primarily powered by a supermassive black hole (‘monster’). However, galaxy interactions (tidal etc.) are expected to trigger star-formation and also provide material to fuel the central supermassive black hole (Heckman 1990A). Further, there may still be a strong physical link between the ‘monster’ and the starburst phenomenon (Heckman 1990B). The [O III] emission line maps in several Seyfert galaxies have been used to decompose the ionised gas into a ‘monster’ and a ‘starburst’ component (*e.g.* Wilson et al. 1986, Baldwin et al. 1987, Keel 1987, and Pogge 1989). A possible way to discriminate between the ‘monster’ and the starburst components is the morphology of the radio-emission: attribute those

sources with ‘linear’ (jet-like, double, or triple) morphologies to the ‘monster’ and those with diffuse morphologies to regions of star-formation (Heckman 1990B).

Heckman and his group (Heckman et al 1997) believe that compact starburst activity may coexist with AGNs in some Seyfert galaxies, the radio emission from starburst region consists of synchrotron radiation from SNRs plus thermal free-free emission from H II regions, whereas radio emission from the ‘monster’ (or AGN) is purely non-thermal emission.

From a wide range of studies, a picture of the structure of the central regions of Seyfert galaxies has emerged. Briefly, the gravitational field of a supermassive (10^6 - $10^8 M_{\odot}$) black hole provides the ultimate energy source, as gas falls inwards *via* a luminous accretion disk. A small region of fast moving clouds surrounds this central engine, spanning a few light days or weeks, while a larger region of slower moving clouds extends out to a few kiloparsecs. In some cases, oppositely directed collimated jets of low density gas plow into the surrounding galaxy, accelerating the interstellar medium and creating jet-like or linear radio structures. In at least some Seyfert galaxies, dense gas and dust cloud shroud the innermost regions, hiding them from our direct view, though the radiation escapes from the nucleus in other directions to light up the gas and dust residing much further out in the galaxy (Krolik 1999).

The conditions that give rise to Seyfert activity are still under debate. Though Seyfert galaxies are found in a wide range of galaxy types, they are more commonly found in reasonably early-type spirals (Dahari 1985; *e.g.* types S0/a, Sa, Sb in the Hubble classification scheme (Sandage 1975)). It seems, therefore that prerequisites favouring Seyfert activity include a massive galaxy bulge and the presence of an interstellar medium (Heckman 1990B).

1.4.1 Discovery, classification and detection

The early identification of nearby Seyfert galaxies rested on two observational properties, *viz.* their unusual nuclear spectra and their unusual nuclear surface brightness. Fath in 1908 noted strong emission lines in the spectrum of the nucleus of NGC 1068 while studying galaxy spectra (Fath 1909). These observations were later confirmed by Hubble (1926). It was not until 1943 that Carl Seyfert recognised a distinct class of galaxies with unusually bright and concentrated nuclei, and studied a few more of similar kinds (Seyfert 1943).

Khachikian & Weedman (1974) identified two types of Seyfert galaxies on the basis of the widths of the nuclear emission lines. While spectra of type 2 Seyfert galaxies

have a single set of relatively narrow emission lines (whose width can be characterised in terms of full width at half maximum, $\text{FWHM} \approx 300\text{-}1,000 \text{ km s}^{-1}$), in the spectra of type 1 Seyfert galaxies the hydrogen and helium lines have an additional much broader component ($\text{FWHM} \geq 1,000 \text{ km s}^{-1}$). In the simplest cases, the broad component is either absent (Seyfert 2) or strong and dominant (Seyfert 1). With better data it became clear that there is a wide range in the relative strength of the broad and narrow emission lines, and this led Osterbrock in 1981 to refine the Seyfert classification by introducing intermediate types (Osterbrock 1981, Osterbrock & Pogge 1985). They chose the hydrogen $\text{H}\beta$ line at rest wavelength 4861 \AA . As the broad component of $\text{H}\beta$ becomes weaker relative to the narrower component, the Seyfert type changes from 1 to 1.2 to 1.5 to 1.8. For Seyfert 1.8 galaxies, weak broad wings are just visible at the base of $\text{H}\beta$ while in Seyfert 1.9 galaxies they are only visible on the $\text{H}\alpha$ emission line at 6563 \AA . In practice, these Seyfert sub-types have not been formally defined but instead give an overall indication of the degree to which the broad component is present.

The first survey which identified many Seyfert galaxies was that of Markarian and his collaborators at the Byurakan observatory, Armenia, during the period 1962 to 1981 (Markarian 1967, Markarian et al. 1986). This survey used a technique known as ‘objective prism spectroscopy’ to find galaxies with unusually blue continuum emission. The combination gives relatively wide field photographs in which each star and galaxy that appeared unusual was listed. The survey covered $\sim 10,000$ square degrees and yielded 1500 galaxies with blue continua, of which $\sim 10\%$ were Seyfert galaxies.

X-ray emission also provides an effective means to find Seyfert galaxies (Veron 1986). Starting in the late 1970s, surveys have included observations of the Ariel V, HEAO-1, Einstein and ROSAT satellites. Some of these were all-sky surveys, some included deeper pointed observations, some were sensitive to hard X-rays (2-10 keV) and others to soft X-rays ($\sim 0.2\text{-}4 \text{ keV}$).

In 1982, the IRAS satellite provided a large list of galaxies which were relatively bright in the far infrared (25-100 μm). Although bright, infrared flux density by itself is no guarantee of Seyfert activity, the ‘colour’ of the infrared emission can help distinguish between Seyfert and normal galaxies. Normal galaxies have colder dust ($\sim 30 \text{ K}$) than Seyfert galaxies ($\sim 100\text{-}300 \text{ K}$) in which nuclear activity provides an additional heating source. Thus, IRAS-selected galaxies with ‘warm’ spectra have yielded many Seyfert galaxies (Miley et al. 1985, de Grijp et al. 1987).

Perhaps the most reliable method of detecting Seyfert galaxies, though also the least efficient, is optical spectroscopy of the galactic nuclei. In the early 1990s the

CfA redshift survey of about 2,000 galaxies brighter than absolute magnitude 14-15, found about 2.5% to be Seyfert galaxies with an even mix of Seyfert 1 and Seyfert 2 galaxies (Huchra & Burg 1992). Using smaller apertures and higher quality data, the deep Palomar survey of the nuclei of nearly 500 bright galaxies from the RSA catalogue (Sandage & Tammann 1981) yielded about 10% Seyfert galaxies, including many of lower luminosity.

The following Section gives the observed properties of Seyfert galaxies.

1.4.2 Observed properties of Seyfert galaxies

Seyfert 1 galaxies show spectrophotometrically observed broad (FWHM of the lines $\geq 1000 \text{ km}^{-1}$) emission lines and Seyfert 2 galaxies show narrow (FWHM $< 1000 \text{ km}^{-1}$) lines. The technique of spectropolarimetry yielded spectra that showed broad lines in polarised light in Seyfert 2 galaxies. This polarised light was interpreted to be the light that was initially moving out of the nucleus in one direction which was then reflected into our line of sight. This provides a sort of periscope, allowing one to look around a corner and into the nucleus from a different direction. The mirrors of the periscope are dust particles or electrons in the surrounding gas which scatter light in all directions, some of which comes towards us. Since the scattered light is so faint compared to the normal light we need a way to isolate them. Fortunately, the scattering process also induces polarisation, and so the polarised light spectra shows a Seyfert 1 form, strong non-stellar continuum and broad hydrogen and helium lines. Such a technique could detect BLRs in a Seyfert 2 galaxy, *e.g.* NGC 1068 (Miller & Goodrich 1990). Subsequently Tran et al. (1992) and Tran (1995), added a few more Seyfert 2 galaxies to the list.

The nucleus of face-on Seyfert 2 galaxies is clearly seen in $\text{H}\alpha$ as the brightest knot in the central region, but is barely detected in the ultraviolet images (*e.g.* Colina et al. 1997). Kinney et al. (1991) showed similar ultraviolet slopes for Seyfert 2 and Seyfert 1 galaxies, they also show that there is a paucity of ionising photons in Seyfert 2 galaxies (lack of ultraviolet emission in Seyfert 2 galaxies is also supported by Mas-Hesse et al.'s (1994) observations). The featureless continuum is stronger in Seyfert 1 than in Seyfert 2 galaxies. Seyfert 1 galaxies have bright nuclei, whereas in Seyfert 2 galaxies the featureless continuum and broad lines are either weak or absent (*e.g.* Lawrence 1987).

Both types of Seyfert galaxies possess narrow line regions which can be imaged in [O III] $\lambda 5007$ emission lines in the well-resolved cases (*e.g.* Whittle et al 1988) and are

sometimes cone-shaped (Pogge 1989, Evans et al. 1991A, Evans et al. 1991B, Evans et al. 1993, and Evans et al. 1994). It seems that the ionizing radiation is roughly collimated before emerging into the narrow line region, perhaps due to an obscuring torus (Kriss et al. 1994). The narrow line regions appear smaller in Seyfert 1 than Seyfert 2 galaxies.

For a given far-infrared luminosity Mas-Hesse et al. (1994), (and also Lawrence & Elvis 1982), found a significant lack of soft X-ray emission in Seyfert 2 galaxies compared to Seyfert 1 galaxies. The infrared emission of Seyfert 1 and Seyfert 2 galaxies are quite similar, whereas the ratio of soft X-ray to infrared emission is higher for Seyfert 1 than for Seyfert 2 galaxies (Mas-Hesse et al. 1994). Similarly, the hard X-ray emission show similar distribution for both kinds of Seyfert galaxies (Mas-Hesse et al. 1994).

Observations of Seyfert galaxies in radio waveband show that: (1) both kinds of Seyfert galaxies have similar amount of molecular gas. Maiolino et al. (1997) and Curran (2000) found no difference in the mean ratio of CO and far-infrared luminosity between the two Seyfert classes. Thus, both Seyfert types, type 1 and type 2 Seyfert galaxies, have the same amount of molecular gas. (2) Greenhill et al. (1995) detected a subparsec diameter disk in the nucleus of NGC 4258; they made a VLBI synthesis map of the luminous H₂O maser in the nucleus of NGC 4258. They explained their data using a model where they established a 0.2 pc diameter Keplerian disk for the nucleus of NGC 4258. Later Gallimore et al. (1997) found pc-scale H₂O maser emission which is perpendicular to the large scale (kpc-scale) jet which they attribute to the emission due to an ionised disk surrounding an AGN, and (3) lastly, in recent observations, Morganti et al. (1999) found that Seyfert 2 galaxies tend to have a larger projected radio linear size than Seyfert 1 galaxies, whereas there is no statistically significant difference in radio power between Seyfert 1 and Seyfert 2 galaxies (Morganti et al. 1999).

We now present a brief outline of the basic structure of Seyfert galaxies.

1.4.3 Overall structure and geometry

Figure 1.2 gives a cartoon of the structures nested from innermost to outermost. The region sizes probably scale with luminosity, larger for quasars and smaller for low luminosity Seyfert galaxies. The values given are rough guides for the case of a typical Seyfert galaxy.

The ultimate origin of the energy which drives nuclear activity is believed to lie in the gravitational field of a central supermassive black hole of mass $\sim 10^7$ - $10^8 M_{\odot}$

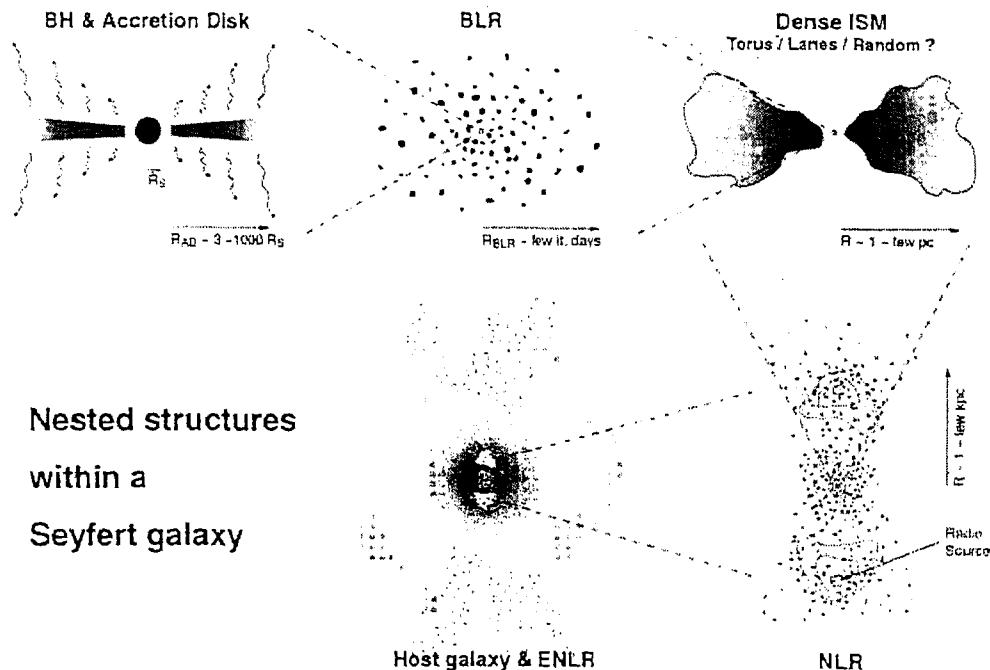


Figure 1.2: Cartoon illustrating the nested structures thought to be present within Seyfert galaxies.

(Peterson 1997, p. 32, also see Section 1.4 for a contrary view). Gas falls into the black hole *via* an accretion disk, which radiates powerfully across much of the electromagnetic spectrum. The disk may span from a few Schwarzschild radii (Krolik 1999, p. 97) to a few thousand Schwarzschild radii, probably with X-ray emission coming from the inner parts, ultraviolet and optical from farther out (Peterson 1997, pp. 118-122). It is this radiation which floods out into the galaxy and ionises any surrounding gas, causing it to radiate emission lines. The innermost center contains gas with density $\sim 10^9$ - 10^{12} atom cm^{-3} moving with speeds of a few thousand km s^{-1} . Doppler shifts therefore lead to broad emission lines, hence the name: Broad Line Region (BLR) (Peterson 1997, p. 67). Outside the BLR, on scales from one to a few parsec (pc) lies thick dense gas, possibly in the form of a torus. This gas blocks radiation coming from the innermost regions, which can only escape out of the equatorial plane along the torus axis (Peterson 1997, pp. 112-113). This partially collimated radiation field emerges further into the galaxy to ionise gas residing in a region out to a few kiloparsec (kpc). In this region, the gas has a lower density $\sim 10^2$ - 10^6 atoms cm^{-3} and moves with

speeds of a few hundred km s^{-1} , leading to narrower emission lines, hence the name: Narrow Line Region (NLR) (Peterson 1997, p. 93). Because of the partially collimated radiation field, the NLR often appears elongated or even biconical, with axis matching that of the central radiation field (Pogge 1989). When a radio source emerges from the inner regions as a bipolar flow, it accelerates and possibly shocks the NLR (Bicknell et al. 1998). The entire NLR and associated radio structure usually fills a region, a few kpc across, within the bulge of the host galaxy, but randomly aligned with respect to obvious galactic structures and orientation (Kinney 2000). If there is a more extended gaseous component, it can be illuminated by the central ionising radiation field, leading to faint extended emission, sometimes showing conical or biconical form. This is the so called Extended Narrow Line Region (ENLR) (Peterson 1997, p.120).

Inherent in this picture is a lack of symmetry, rooted in the non-spherical accretion that powers the Seyfert galaxy. Both the radiation and radio emitting flows are anisotropically emitted and the origin of the anisotropy might arise in either of the two ways: (a) an intrinsic nuclear axis, perhaps defined by a black hole spin and/or the accretion disk, and (b) partial obscuration by dense gas which blocks radiation in some directions but not in others. For Seyfert galaxies, partial obscuration is thought to be important. The simplest geometry envisioned is a thick disk or torus a few parsecs to 100s of parsecs in size and aligned with the central axis. More recently, images from the Hubble Space Telescope (HST) have shown that dust lanes and filaments are common in the central few hundred parsecs (Malkan et al. 1998). Either way, the fact that the nuclear radiation can only emerge along particular lines of sight raises an interesting possibility which was first noted by Lawrence & Elvis (1982): namely, that Seyfert 2 galaxies might actually be Seyfert 1 galaxies but oriented in such a way that our view to the central region is blocked. On the basis of the ratio of hard to soft X-ray flux densities in Seyfert galaxies, they concluded that Seyfert 2 galaxies were in fact obscured Seyfert 1 galaxies. Stated slightly differently, the same Seyfert galaxy might appear as Seyfert 1 from some directions and a Seyfert 2 from others. This constitutes a ‘unification scheme’, since apparently different classes of objects are ‘unified’ into a single class.

1.4.4 Unified scheme model

This is the key idea which is being used to organise and make sense of our large and growing observational information about Seyfert galaxies.

The unified scheme is consistent with the observations that the narrow-line spectra

of types 1 and 2 are statistically indistinguishable from one another, so Seyfert 2 galaxies seem to be Seyfert 1 galaxies without the broad lines. This, along with several observations listed above (Section 1.4.3) led to the unification hypothesis, in which Seyfert 2 galaxies are intrinsically Seyfert 1 galaxies whose continuum and broad-line emission is attenuated in the direction of the observer.

A breakthrough occurred when Antonucci & Miller (1985) found that the polarisation spectra of some Seyfert 2 galaxies such as NGC 1068 contained broad emission lines like those seen in Seyfert 1 spectra.

Obscuration forms the essence of the orientation based unification scheme. A torus of dense obscuring gas and dust is believed to girdle the continuum source and BLR. Looking down the axis of the torus one can directly see the BLR and accretion disk. However, when viewed edge-on, the torus blocks our view of the BLR (and absorbs soft X-ray), making the AGN look a type 2 (Figure 1.3). The same torus blocks ionising photons from reaching the NLR in certain directions, hence explaining the cone-shaped NLRs that are seen in some Seyfert 2 galaxies (Pogge 1989). Thus, different orientations of axis-symmetric active nucleus to our line of sight show different kinds of Seyfert galaxies, ‘pole-on’ viewing angles produce Seyfert 1 galaxies and ‘edge-on’ viewing produce Seyfert 2 galaxies (Figure 1.3).

Evidence against the unified scheme While the unified scheme is simple and attractive, there are some observational results that are inconsistent with it. They are listed below.

- Hubble type (T) of Seyfert galaxies.
Recently Malkan et al. (1998), found that Seyfert 2 galaxies, on average, tend to have later morphological types than the Seyfert 1 galaxies.
- The close environments of Seyfert galaxies:
Dultzin-Hacyan et al. (1999) confirmed an important but disturbing result that Seyfert 2 galaxies have an excess of nearby companions over Seyfert 1 galaxies.
- The scattered BLR is not detected in many Seyfert 2 galaxies.
- Lower detection rates of compact features at radio wavelength in Seyfert 1 than Seyfert 2 galaxies.
Roy et al. (1994) using 275 km long single baseline, Parkes-Tidbinbilla Interferometer (PTI) at 1.7 or 2.3 GHz (PTI: Norris et al. 1988B and Norris et al.

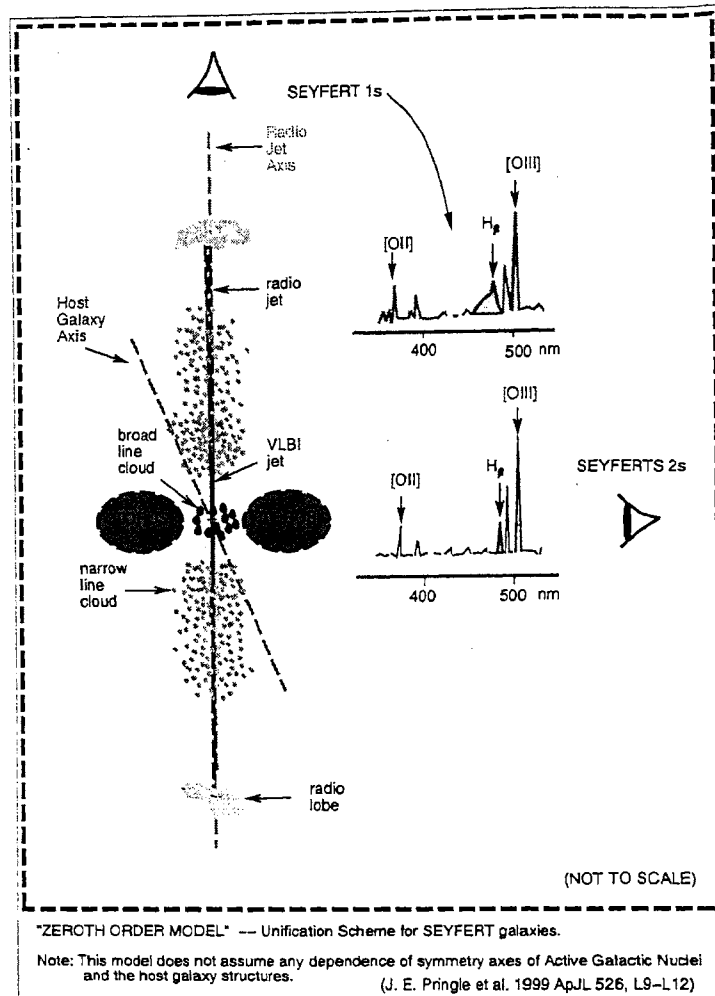


Figure 1.3: Zeroth order model of Seyfert galaxies.

1992) found a surprising result that compact radio cores are much more common in Seyfert 2 than in Seyfert 1 galaxies. This was in their far-infrared selected samples and possibly in the combined mid-infrared and optically selected sample as well, which is inconsistent with the unification scheme.

1.5 Motivation

It was Roy et al.'s (1994) observational result which prompted us to take up this study. In the unified scheme, since the torus is expected to be transparent to emission at radio wavelengths, the compact features should be similarly visible in Seyfert 1 and

Seyfert 2 galaxies. Further, the inconsistency with the unification scheme cannot be eased by invoking relativistic beaming, because then, the face-on AGNs, *viz.*, Seyfert 1 galaxies, would be more likely to show compact structures. We aimed to rigorously test the predictions of the unified scheme by investigating the compact radio morphology of Seyfert galaxies. To achieve this goal, we constructed a sample of Seyfert 1 and Seyfert 2 galaxies that are matched in orientation independent parameters.

Our goal was to study the pc-scale radio structures of Seyfert galaxies so as to test if indeed Seyfert 1 galaxies have a lower tendency to show compact radio structures as compared to Seyfert 2 galaxies. We used global 6 cm Very Long Baseline Interferometry to probe the pc-scale structures.

1.6 Thesis outline

In Chapter 2, the result that poses a challenge to the unified scheme, which we aim to address, is discussed. We introduce aperture synthesis and Very Long Baseline Interferometry (VLBI) which is the key to achieve pc-scale resolution. We then outline our rationale for the selection of our sample and describe its construction.

In Chapter 3, we first give the description of the observing procedure, data reductions and analysis. We give the description of the images for our sample sources supplemented by data from the literature wheresoever necessary.

Chapter 4 uses results from Chapter 3 within the formalism in which our sample was constructed to test the unified scheme. We present our interpretations in the framework of the starburst *versus* accretion powered central engine debate as well as the unified scheme hypothesis and relativistic beaming.

Chapter 5 compares the radio data with data at other wavebands that are published in the literature. We primarily focus on the infrared and the X-ray emission.

The final chapter (Chapter 6) summarizes the main results obtained in the thesis and brings together the conclusions from this work, highlighting our contribution to the understanding of Seyfert galaxy phenomenology. We also critically assess the strengths and weaknesses of our work and highlight opportunities for further study.

A Hubble constant of $H_0 = 75 \text{ km s}^{-1} \text{ Mpc}^{-1}$ and $q_0 = 0$ is used throughout the thesis unless mentioned otherwise.

Chapter 2

Motivation and methodology

2.1 Introduction

In this Chapter the challenge to the unified scheme that we propose to address is first discussed. Subsequently the construction of our sample is described.

The Sections 2.2 and 2.3 discuss the challenge to the unification scheme and our goal. The techniques of aperture synthesis and Very Long Baseline Interferometry (VLBI) (Section 2.4) are introduced, where the emphasis is on the steps involved while working with the Very Long Baseline Interferometry data. Section 2.5 discusses the construction of the sample and Section 2.5.3 discusses the criteria for the feasibility of our experiment where, the choice of our interferometric array is described. The phased-VLA (see Section 2.4.2.4) was chosen as one of our VLBI stations in the array. We therefore have simultaneous arcsec-scale data for our objects, and can derive ratios of the emission on mas-scales and arcsec-scales which are unaffected by possible variability.

2.2 A challenge to the unification scheme

As described in detail in Chapter 1, the challenge to the unified scheme has been the low detection rates of compact structures in Seyfert 1 galaxies as compared to Seyfert 2 galaxies. Roy et al. (1994), using 275 km-long single baseline Parkes-Tidbinbilla Interferometer (PTI) at 1.7 and 2.3 GHz (PTI: Norris et al. 1988B and Norris et al. 1992) found no significant difference between disk radio luminosities of Seyfert 1 and Seyfert 2 galaxies in their eclectic sample (the far-infrared selected samples of de Grijp et al. (1987) and Norris et al. (1990), the optically selected samples of Norris et al. (1990) and Edelson (1987; the CfA Seyfert sample), and the mid-infrared selected

sample of Spinoglio & Malkan (1989)). But they did obtain a surprising result that compact radio cores are much more common in Seyfert 2 than in Seyfert 1 galaxies in their far-infrared selected samples and in the combined mid-infrared and optically selected sample as well. This is inconsistent with the unification scheme. The unified scheme would predict an equal fraction of detections for Seyfert 1 and Seyfert 2 galaxies.

It was this observational result which prompted us to take up the VLBI study of Seyfert galaxies that we describe in the following Section. We note that the inconsistency with the unification scheme cannot be eased by invoking relativistic beaming. In that case it is the face-on AGNs, *viz.*, Seyfert 1 galaxies, whose cores would be more Doppler boosted than Seyfert 2 galaxies, and therefore are more likely to show compact structures. We aimed to rigorously test the predictions of the unified scheme by investigating the compact radio morphology of Seyfert galaxies. To achieve this goal, we constructed a sample of Seyfert 1 and Seyfert 2 galaxies that are matched in orientation independent parameters.

2.3 The goal

Our goal was not only to test whether Seyfert 1 galaxies have a lower tendency to show compact radio structures than Seyfert 2 galaxies, but more generally to see if there were any systematic differences between the compact radio structures in the two sub-classes or not, in order to test the unified scheme. We used global 6 cm Very Long Baseline Interferometry to investigate the compact radio morphology of Seyfert galaxies.

Often in any sample of Seyfert galaxies the differences observed can be explained by the selection techniques used for assembling the sample. For example, in the Markarian Survey, Markarian (1967) and Markarian et al. (1986) discovered 1500 galaxies with a strong ultraviolet continuum. They found all galaxies with $U - B < 0.3$ and a decreasing fraction of the redder galaxies. Spectroscopic investigations have shown that $\sim 10\%$ are Seyfert galaxies. This sample suffers from deficiency of Seyfert 2 galaxies, which is most probably a result of the survey selection effect. This is due to the fact that Seyfert 2 galaxies do not have excessive ultraviolet continua and thus could easily elude the ultraviolet search method. Hence, Meurs & Wilson (1984) find a higher fraction of Seyfert 1 galaxies. The CfA Seyfert galaxy sample is the first of the optically selected complete samples with spectroscopic identifications and is due to Huchra & Burg (1992). This is treated to be complete by them and the sample is within the spatial bounds and magnitude limit of the CfA survey. The sample has an equal number of Seyfert 1 and Seyfert 2 galaxies (25 & 23 respectively). The

unresolved optical nucleus of a Seyfert grows fainter with the square of distance, whilst the surface brightness of its host galaxy remains constant over a constant aperture. Therefore, in this sample the ratio of the two components (the host galaxy to the active nucleus surface brightness) is highly variable. Similarly, the IRAS survey would most probably detect reddened Seyfert 1 galaxies, but it may not be easy to isolate them from the much more luminous starburst galaxies (Heckman 1990A and 1990B). In other words, the Seyfert samples based on the IRAS survey would be contaminated due to the presence of luminous starburst galaxies. Soft X-ray surveys may contain a population of soft X-ray Seyfert 1 galaxies (Seyfert 2 galaxies are weak soft X-ray sources and cannot be efficiently discovered by X-ray soft surveys: Veron 1986).

Thus, most of the Seyfert galaxy samples (optical, infrared, and/or X-ray) have their biases and hence do not provide a good platform to test the unification scheme hypothesis. A Seyfert sample selected based on the orientation independent parameters which are measures of AGN power and host galaxy properties would provide a good platform to test the predictions of the unification scheme hypothesis.

Before describing our sample selection criteria (Section 2.5), we present some information about radio interferometry and VLBI in particular in the following Section (2.4).

2.4 Aperture synthesis and Very Long Baseline Interferometry

2.4.1 Aperture synthesis

Aperture synthesis is a method where two or more antennas are arranged so that their relative positions may be altered to occupy successively the whole area of a much larger equivalent antenna. By combining mathematically the information derived from these different positions, it is possible to obtain high resolution maps equivalent to that of a single large antenna.

Interferometry is the pre-eminent method of achieving high angular resolution. Virtually all radio-wavelength systems use the principle of the Michelson interferometer and determine the amplitude and relative phase of the signal reaching each of the antennas in the interferometer. In a conventional radio interferometer the radio telescopes are linked to a common clock to maintain the coherence* of the interferom-

*Coherence is a statistical description of the radiation field due to a signal from the source in terms of the correlation between the vibrations at different points in the field. With a perfectly

eter and the signal from each telescope is brought together, through appropriate phase delays,[†] to be correlated in real time to produce the interferometer fringes.

Long baseline interferometry achieves high angular resolution by using two or more widely ($> 1,000$ km) separated radio telescopes and recording data on magnetic tapes, which are later brought together and cross-correlated off line.

The operation of a radio telescope is limited by two dominating factors. One is the sensitivity, which specifies the smallest radio flux density which may be detected, and the other is the angular resolving power. The relative importance of these factors is strongly dependent upon the type of investigation and specialised instruments are often developed for particular applications.

2.4.1.1 The aim of aperture synthesis

The angular resolution of a telescope is proportional to the ratio of observing wavelength and diameter of the antenna. Thus in the radio domain of the electromagnetic spectrum, the angular resolution is much worse than in the optical for a given telescope size, *e.g.* the diffraction limit of a large optical telescope of 6 m diameter is 0.025 arcseconds whereas a filled aperture radio telescope of similar size would give a diffraction limit of $\sim 1/2$ degree. The radio astronomical antennas have to be of large size to achieve comparable angular resolution. But even at the highest radio frequencies such as 43 GHz, a 100 m diameter antenna has an angular resolution of ~ 15 arcsec. To further enhance the angular resolution, a possibility is to use two or more telescopes at large separations. This idea of linking together signals from two physically distinct telescopes, has advanced from two element interferometers (Michelson interferometer) up to the concept of aperture synthesis using many telescopes spaced at distances limited only by the size of the Earth.

A two-element interferometer measures the cross correlation of the electric field measured at two different places on the image plane *i.e.* the earth's surface. This correlation coefficient is equal to a component of the Fourier transform of the radiation intensity distribution in the sky (or sky brightness distribution). Thus, a given baseline of an interferometer measures one Fourier component of the source. To construct the source we need to measure all (as many as possible) the Fourier components of the monochromatic point source, the variations of the electric field at any two point in space are completely correlated.

[†]One of the reason for the phase difference between wavefronts reaching the earth at two different points is: as the earth rotates the 'hour angle' increases and so the 'phase difference' between the two signals in a two element interferometer changes. The rate at which this happens is called the 'fringe frequency'. This needs to be compensated in a long baseline interferometer.

source. The two-element interferometer (*e.g.* PTI, (Norris et al. 1988B and Norris et al. 1992)) achieves resolution in the direction parallel to the projected baseline. In this way one is limited to a few kinds of scientific investigations. Earlier attempts (Mills 1952) using a two-element interferometer allowed observers to measure angular sizes of discrete radio sources. One can extend this idea to multi-element interferometry by using many combinations of two-element interferometers. Then the angular resolution equivalent of a “single dish” with the dimension of the largest baseline can be achieved, while at the same time increasing the total number of Fourier components measured. Thus, aperture synthesis is aimed at obtaining high angular resolution maps of radio sources using a large number of Fourier components measured simultaneously.

2.4.1.2 The principle of aperture synthesis

The two-element interferometer is an important building block in the synthesis of larger apertures (Ryle & Hewish 1960). A filled aperture antenna has all element spacings, from zero to some upper limit fixed by its maximum dimension, with their relative weighting determined by the geometry of the antenna surface and the feed system; whereas as discussed above, a two-element interferometer of a given baseline measures one Fourier component of the source, corresponding to that baseline. To obtain a large number of Fourier components and thereby high angular resolution in all directions, Ryle and his co-workers in Australia (Ryle & Hewish 1960, Christiansen 1953, and Mills & Little 1953) extended the two-element interferometer to multi-element interferometry.

If the phase as well as the fringe amplitude can be found for a number of baselines then we may be able to do inverse Fourier transform and find the two-dimensional sky brightness distribution.[‡] To measure a large number of Fourier components of the source, we can either deliberately vary the relative positions of the antennas in time and/or have several elements. Another method of measuring large number of Fourier components of the source is to use the rotation of earth to change the aspect of baseline(s). This type of antenna system with multi-elements is called an array. The term array, now applied to a collection of antennas whose outputs are correlated pairwise,

[‡]van-Cittert Zernicke Theorem

A radio-astronomical interferometer measures the cross-correlation of the signals measured at two different places on the image plane. Thus

$$R_{12} = \langle E_1 \cdot E_2 \rangle,$$

where R_{12} is the correlation coefficient and it is equal to the Fourier transform of the sky brightness distribution. This statement is called the van-Cittert Zernicke theorem.

is essentially a large number of two-element interferometers operating simultaneously. An array which contains all of the relative positions of a filled aperture is called a 'skeleton array'. One can obtain a particular "system response pattern" (response of the instrument to a point source, see Section 2.4.1.3) by combining the outputs from many antennas with a given set of baselines. Arrays of antenna elements are essentially probes of the spatial coherence (also termed as the visibility) of the radiation field. With a large number of elements suitably connected, a sufficient number of spatial coherence components can be measured in a reasonably short period of time in order to obtain a satisfactory reconstruction of the angular brightness distribution. The baseline coverage is augmented both by the earth's rotation, and by changing the relative positions of the antennas themselves.

If the number of spacings cover all baselines up to some maximum (up to the diameter of an equivalent aperture) then we have synthesized a fully filled aperture. However, typically we have a limited number of baselines and so the aperture is only partially filled.

2.4.1.3 Interferometry techniques

The two-element interferometer provides high resolution by correlating the signals of the two antennas. The correlation is normally achieved by multiplication of the signals, which produces a spatial modulation of the primary beam of the antennas with interference fringes. In this way fine structure is introduced into the primary beam to increase the resolution.

A schematic diagram illustrating the geometry for two antennas receiving a signal from a point source of monochromatic radiation of frequency ω is shown in Figure 2.1. A voltage V proportional to the electric field E caused by the source is generated at the feed of each telescope, at slightly different times. This time difference is called the geometric delay and is denoted by τ . The voltages at the multiplier input are

$$\begin{aligned} V_1 &\propto E \cos (\omega t), \\ V_2 &\propto E \cos [\omega(t - \tau)] \\ &= E \cos [\omega t - (2\pi B/\lambda) \cos \theta], \end{aligned}$$

where B is the separation of the two antennas, λ is the wavelength of the radiation and θ is the angle between the point source and line joining the two antennas. The expression $(B/\lambda)\cos \theta$, the interference term, gives the phase path length difference of the radiation travelled along the two possible paths. The diurnal motion of the Earth

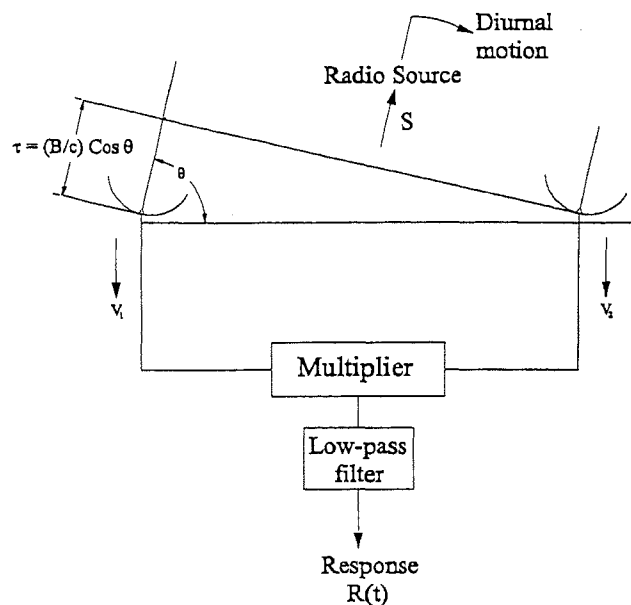


Figure 2.1: Two element interferometer.

causes θ to vary with time. The output $R(t)$ of the correlator after a high frequency term is rejected by a low pass filter is

$$R(t) \propto S \cos [(2\pi B/\lambda) \cos \theta(t)].$$

This is the basic equation of interferometry. Here, E^2 has been replaced by S . Or

$$R(t) \propto S \cos [2\pi \mathbf{B} \cdot \mathbf{s}(t)],$$

where \mathbf{B} is the physical spacing of the interferometer in units of wavelength and its direction is that of the line joining the elements. \mathbf{s} gives the direction to the source.

In a connected element interferometer, the signals from individual telescopes are correlated in real time. The present day connected element interferometry uses several elements to occupy some of the positions that are present in a large aperture. The relative positions get changed due to the rotation of the earth. If a radio source is followed in its diurnal motion by all the elements, the relative positions between the antennas as viewed by the radio source, change both in length and orientation. Thus, by utilizing both the rotation of the earth and many elements suitably placed, very large apertures can be synthesized.

The response of a two-element interferometer to an extended source can be obtained by considering the source to be a collection of point images and summing their

individual responses. Therefore, the response to the extended source is

$$R(t) \propto \int d\sigma I(\sigma) \cos [2\pi \mathbf{B} \cdot (\mathbf{s}(t) + \boldsymbol{\sigma})],$$

which is the response to a point source (previous Equation) integrated over the source. In this Equation, σ denotes the spatial variable in the plane of the sky and $I(\sigma)$ is the true brightness distribution of the source on the sky. If \mathbf{s} is the phase center, any other point is denoted by $\mathbf{s}(t) + \boldsymbol{\sigma}$, $I(\sigma)$ describes the brightness distribution (angular distribution of the power), and the flux density of the source is equal to $\int d\sigma I(\sigma)$.

Since the angular size of the region observed is limited by the extent of the antenna response (typically less than one degree), the phase term in the above equation can be expanded to first order for sufficient accuracy.

$$\begin{aligned} \mathbf{B} \cdot (\mathbf{s} + \boldsymbol{\sigma}) &\approx \mathbf{B} \cdot \mathbf{s}(t) + \mathbf{B} \cdot \boldsymbol{\sigma} \\ &= \mathbf{B} \cdot \mathbf{s}(t) + \mathbf{b} \cdot \boldsymbol{\sigma}. \end{aligned}$$

Since $\boldsymbol{\sigma}$ is nearly perpendicular to \mathbf{s} , only the projected spacing \mathbf{b} is used in the second term of the cosine. The response becomes

$$R(t) = \int_{-\infty}^{\infty} d\sigma I(\sigma) \cos [2\pi \mathbf{B} \cdot \mathbf{s}(t) + 2\pi \mathbf{b} \cdot \boldsymbol{\sigma}].$$

This may be expanded into

$$\begin{aligned} R(t) &= \cos (2\pi \mathbf{B} \cdot \mathbf{s}(t)) \int_{-\infty}^{\infty} d\sigma I(\sigma) \cos (2\pi \mathbf{b} \cdot \boldsymbol{\sigma}) \\ &\quad - \sin (2\pi \mathbf{B} \cdot \mathbf{s}(t)) \int_{-\infty}^{\infty} d\sigma I(\sigma) \sin (2\pi \mathbf{b} \cdot \boldsymbol{\sigma}) \end{aligned}$$

or

$$\begin{aligned} R(t) &= \Re \left[\exp \{i2\pi \mathbf{B} \cdot \mathbf{s}(t)\} \int_{-\infty}^{\infty} d\sigma I(\sigma) \exp \{i2\pi \mathbf{b} \cdot \boldsymbol{\sigma}\} \right] \\ &= \Re [V(\mathbf{b}) \exp \{i2\pi \mathbf{B} \cdot \mathbf{s}(t)\}] \end{aligned}$$

where

$$V(\mathbf{b}) = \int_{-\infty}^{\infty} d\sigma I(\sigma) \exp \{i2\pi \mathbf{b} \cdot \boldsymbol{\sigma}\},$$

is the complex visibility of the source. The components of \mathbf{b} (in units of wavelengths) along east and north directions are denoted as u and v respectively. The integral, denoted as the visibility function V , is a complex number. The amplitude of V is proportional to the amplitude of the fringe pattern while the argument of V equals the phase shift in the fringe pattern from that of the response to a point source at the

phase center. From the above equation the visibility function is obviously the Fourier transform of the brightness distribution.

In practice, a Cartesian coordinate system, moving at the diurnal rate in the neighborhood of the source, is used. Let $\mathbf{s} = (\alpha, \delta)$ and $\sigma = (x, y)$, where, x is an eastward displacement from α , and y is a northward displacement from δ . With such a coordinate system, and the convention that the phase increases for a source displacement towards the north and the east, we get

$$V(u, v) = \int dx \int dy I(x, y) \exp \{+i2\pi (ux + vy)\}.$$

Thus for an extended source the emission may be recovered from the observed response by performing the inverse Fourier transform

$$I(x, y) = \int du \int dv V(u, v) \exp \{-i2\pi (ux + vy)\}.$$

Since $I(x, y)$ is real, $V(-u, -v) = V^*(u, v)$. Thus at any instant the correlator output provides a measure of the visibility at two points in the (u, v) plane. In practice, the spatial coherence function V is not known everywhere, but is sampled at particular places on the (u, v) plane.

As an interferometer observes a point on the celestial sphere, the rotation of the earth causes the u and v components of the baseline to trace out an elliptical locus. This ellipse is the projection onto the (u, v) plane of the circular locus traced out by the tip of the baseline vector. For an array of antennas, the ensemble of elliptical loci is known as the sampling function. The sampling can be described by a sampling function $S(u, v)$, which is zero where no data have been recorded. Then instead of the previous equation, one actually calculates

$$I^D(x, y) = \int du \int dv V(u, v) S(u, v) \exp \{-i2\pi (ux + vy)\}. \quad (2.1)$$

Radio astronomers often refer to $I^D(x, y)$ calculated this way as the 'dirty image'; its relation to the desired intensity distribution $I(x, y)$ is seen by using the Fourier theorem

$$I^D(x, y) = I(x, y) * B(x, y), \quad (2.2)$$

where the '*' denotes convolution, and

$$B(x, y) = \int du \int dv S(u, v) \exp \{-i2\pi (ux + vy)\},$$

is called the synthesized beam or 'point spread function' or 'dirty beam' corresponding to the sampling function $S(u, v)$. Equation 2.2 says that I^D is the true intensity distribution I convolved with the synthesized beam B .

We can measure only I^D , the Fourier transform of the sampled visibility function, and not I . The dirty beam can be thought of as composed of two parts: a compact central lobe surrounded by a series of *sidelobes* that can initially be strong and fall off with distance from the central peak. A deconvolution (Cornwell & Wilkinson 1984) algorithm solves the convolution equation for an estimate of the true sky brightness I . The following is a discussion on the simplest and also the most widespread deconvolution algorithm called CLEAN (Högbom 1974).

The ‘CLEAN’ Algorithm:

CLEANing corrects a map for the presence of sidelobes described above. It is a band-limited deconvolution in which the brightness distribution is decomposed into a sum of beam patterns.

The ‘CLEAN’ algorithm provides one solution to the convolution equation by representing a radio source by number of point sources in an otherwise empty field of view. A simple iterative approach is employed to find the positions and strengths of these point sources. The final deconvolved image, usually known as the ‘CLEAN’ image, is the sum of these point components convolved with a ‘CLEAN’ (usually elliptical Gaussian) beam.

The basic steps are:

1. Find the peak brightness in the “dirty” (observed) map and log its position and amplitude.
2. Position the centre of the synthesised beam pattern, or “dirty” beam, there.
3. Multiply the “dirty” beam with the amplitude of the peak times a number called the loop gain, which is typically 0.1 and is always less than 1.
4. Subtract the multiplied “dirty” beam from the “dirty” map.
5. The result will be a residual map which in the next step will be considered as the new “dirty” map.
6. Steps 1 to 5 are iterated until some cutoff level has been reached. The usual criterion for stopping the iterations is when the noise level has been reached, *i.e.*, when we believe that all the real emission has been identified and removed from the dirty map.

7. The clean components found by the iterative procedure are convolved with a restoring, or “clean”, beam corresponding to the appropriate resolution of the interferometer. These elliptical Gaussian components are then added on to the last residual map. The resulting image is called the “clean” map.

2.4.1.4 Very Large Array

The Very Large Array (VLA) is a 27 element interferometric array (each element is of 25 m diameter) laid out in “Y” shape, stationed in New Mexico, US. It produces images of the radio sky at a wide range of frequencies and resolutions. The basic data produced by the array are the visibilities, or measures of the spatial coherence function, formed by correlation of signals from the elements of the array. The most common mode of operation uses these data, suitably calibrated, to form images of the radio sky as a function of sky position and frequency. Another mode of observing (commonly called phased array) allows operation of the array as a single element through coherent summation of the individual antenna signals. This mode is commonly used for VLBI observing and for observations of rapidly varying objects, such as pulsars.

The VLA can vary its resolution over a range exceeding a factor of ~ 50 through movement of its component antennas. There are four basic arrangements, called configurations, whose scales vary by the ratios 1 : 3.2 : 10 : 32 from smallest to largest. These configurations are denoted D , C , B , and A respectively. In addition, there are 3 ‘hybrid’ configurations labeled BnA , CnB and DnC , in which the North arm antennas are deployed in the next larger configuration relative to the SE and SW arm antennas. These hybrid configurations are especially well suited for observations of sources south of $\delta = -15$ degree or north of $\delta = +75$ degree. Figure 2.2 shows VLA array antenna positions during our observations.

Observing time intervals on the VLA vary in duration from as short as 1/2 an hour to as long as several weeks. Most observing runs have durations of a few hours, with only one, or perhaps a few, target sources. However, since the VLA is a two-dimensional array, images can be made with data durations of less than one minute. This mode, commonly called ‘snapshot’ mode, is well suited to surveys of relatively strong, isolated objects.

The VLA correlator has two basic modes, Continuum and Spectral Line. In Continuum mode, the correlator provides the four correlations (RR, RL, LR, LL; where R and L refer to right and left circular polarisations) needed for full polarimetric imaging at both sidebands. This mode is particularly well suited to high sensitivity, narrow field-

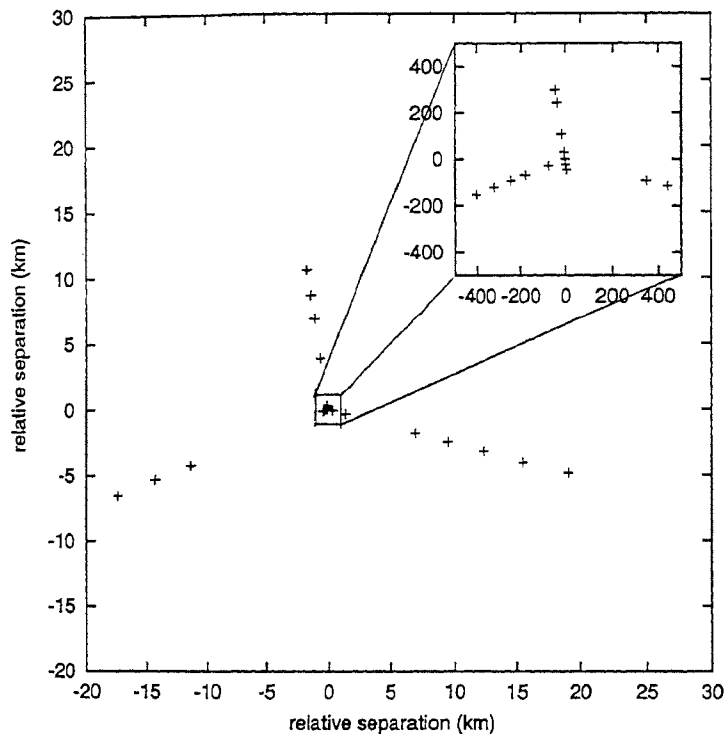


Figure 2.2: VLA array antenna positions (inset shows inner $500 \times 500 \text{ m}^2$) during our observations.

of-view studies. The Spectral Line mode is a spectrum-measuring mode principally intended for observing spectral lines.

2.4.2 Very Long Baseline Interferometry

Very Long Baseline Interferometry (VLBI) was born in the mid 1960's out of the wish of astronomers to achieve better angular resolution than a regular radio interferometer. It is a special case of the aperture synthesis and is an extension of interferometric techniques to the largest obtainable baselines. With telescopes separated by intercontinental distances and operating at cm wavelengths, a resolution of about 1 mas can be achieved. This is the highest angular resolution achieved in any branch of astronomy. VLBI observations are now conducted regularly at many radio observatories around the world at cm wavelengths.

2.4.2.1 VLBI techniques

While the basic principle of VLBI is similar to connected element interferometry, it differs from the normal connected-element radio interferometry in several aspects. In a conventional radio interferometer the radio telescopes are linked to a common clock to maintain coherence of the signals from each telescope which are brought together, through appropriate delays, to be correlated in real time to produce the interferometric fringes. This type of operation is not usually possible in VLBI, because of very long distances between two elements. Mainly the cost considerations have prevented direct communication links to be established.

There are two main technical differences between VLBI and conventional radio interferometry. First, in VLBI each observatory relies on its own highly stable clock to maintain coherence. For mas-resolution a hydrogen maser is usually employed. This has a precision of one part in 10^{14} which is adequate; indeed coherence times are then limited by atmospheric effects. Coherence times range from 100 s at 7 mm wavelength up to tens of minutes at cm wavelengths. Second, the data from each VLBI station are separately digitized and recorded onto magnetic tape for subsequent processing. Later the tapes are brought together and the data correlated to produce the interferometer fringes. The recording system used has high sensitivity and large bandwidths.

Another difference with connected-element radio interferometry has evolved in the way VLBI data are processed to make radio maps. Compared with most conventional radio interferometers, a VLBI array is very sparse and irregularly filled. Also the absolute phase of the interferometer is virtually impossible to determine. Special mapping techniques, *viz.*, self-calibration (or hybrid mapping), have been developed to deal with this situation. The Self-calibration technique (see below for a discussion on it) makes use of the redundancy in the data to determine corrections for telescope dependent errors.

Further differences compared to connected element interferometry result from the varied sizes, construction and locations of each array element which are normally used as multipurpose radio astronomical instruments not optimized for VLBI. The locations of the participating VLBI-antenna elements on the earth's surface are in some sense a random distribution with baseline lengths ranging from several 100 kms to nearly 10,000 kms (Figure 2.4 shows a global map with positions of individual antennas used for our experiment). Therefore the coverage of the so called (u, v) (or projected baseline) plane changes with the experiment and is often quite sparse. The process of recovering the source brightness distribution from the measured interference pattern

(the visibility function) uses deconvolution procedures (*e.g.* the “CLEAN” algorithm or Maximum Entropy Mapping (Narayan & Nityananda 1986)); they have come to play a major role in enhancing the quality of the images obtained with VLBI and/or connected arrays.

The quality of the VLBI images is determined by several factors - the number of telescopes, their collecting area, their relative geographical location, and the celestial coordinates of the source being observed - all of which govern the efficiency with which earth rotation synthesises the large aperture of the array.

Self-calibration: Self-calibration is the correction of the effect of telescope dependent calibration errors on the deconvolved image. If there are three or more telescopes in the array we can construct quantities of the form

$$\Phi_{123} = \phi_{12} + \phi_{23} + \phi_{31},$$

where ϕ_{ij} is the phase angle on the baseline formed by stations i and j . These quantities are known as closure phases, and depend only on the structure of the radio source. Instrumental and/or atmospheric/ionospheric phase errors introduced at any one station will appear twice in the closure phase equation with opposite sign, and so will cancel. For an array of $n > 4$ telescopes the number of independent closure phases exceeds the number of telescopes, and so it is possible to solve for the telescope-dependent phase errors. There is a penalty; the absolute phase information is lost.

A generic mapping algorithm incorporating self-calibration proceeds as follows:

- (a) Choose an initial model I^{model} , *e.g.* point source.
- (b) Predict visibilities for the model $V^{model} = FT(I^{model})$.
- (c) Keep the observed visibility amplitudes.
- (d) Select new visibility phases by modifying model visibility phases to be consistent with the observed closure phases.
- (e) Solve for the antenna phase errors using the least-squares criterion.
- (f) Correct the observed visibilities for the antenna phase errors.
- (g) Form a new dirty image from new visibilities.
- (h) Form a new model I^{model} by CLEANing the new dirty image.

(i) Go back to step (b) and repeat until the process converges.

In a similar way closure amplitudes of the form

$$A_{1234} = \frac{a_{12} \times a_{34}}{a_{13} \times a_{24}}$$

may be constructed from the fringe amplitudes a_{ij} on individual baselines, and used to determine telescope dependent gain errors.

Amplitude calibration: The power received by a radio telescope is given by (*e.g.*, Rolf's 1986)

$$P = \frac{1}{2} \Delta\nu \int I_\nu(\Omega) A(\Omega) d\Omega,$$

where I_ν is the specific intensity of the source as a function of solid angle Ω , A is the effective collecting area of the antenna and $\Delta\nu$ is the receiver bandwidth. By the Nyquist theorem, the received power can be related to an equivalent antenna temperature T_A by the relation

$$P = kT_A \Delta\nu,$$

where k is the Boltzmann's constant. If the source is small with respect to the antenna beam, the usual case in VLBI, then A can be taken out of the integral as a constant. The integral of the intensity is the flux density S , so that

$$T_A = \frac{SA}{2k}.$$

For a VLBI system, based on a quantised signal representation, the computed correlation function ρ , is converted to temperature units by multiplication by the geometric mean of the system temperatures, T_{s1} and T_{s2} . As suggested by the above equation, the conversion to units of flux density is accomplished by multiplying by $2k/\sqrt{A_1 A_2}$. Hence the relation between visibility and normalised correlation is

$$V_{12} = \rho \cdot 10^{26} \cdot S \left[\frac{T_{s1} T_{s2}}{T_{A1} T_{A2}} \right]^{1/2} \quad (\text{Jy}),$$

where the areas are in m^2 . In terms of the complex antenna gain g_i

$$V_{12} = \rho \cdot 2k \cdot 10^{26} \left[\frac{4\pi}{\lambda^2} \right] \left[\frac{T_{s1} T_{s2}}{g_1 g_2} \right]^{1/2} \quad (\text{Jy}),$$

where k is in watts K^{-1} .

The RMS sensitivity is proportional to the term in brackets. Thus the quantity used to describe performance of a station is the system temperature T_s in units of Jy.

Thus, the amplitude calibration requires measurement of the receiver temperature and the antenna gain curve. The former is obtained from tipping scans and the latter is obtained by measuring the antenna temperature of a source as a function of the zenith angle. The ratio of the two provides the necessary calibration for the visibility amplitude.

2.4.2.2 The Very Long Baseline Array

The Very Long Baseline Array (VLBA) is an array of ten, 25 m diameter antennas distributed over the territory of the United States (Napier 1995). It is the first astronomical array dedicated for observing by the method of VLBI. The VLBA offers (1) in absentia, year-round antenna and correlator operation; (2) antenna locations selected to optimize (u, v) plane coverage; (3) 9 receivers in the range 90 cm to 7 mm at each antenna; (4) quick computer control of receiver selection and of frequency selection for a given receiver; and (5) smooth integration of data flow from the acquisition to the processing stages.

2.4.2.3 The European VLBI Network

The European VLBI Network (EVN) is an interferometric array of radio telescopes spread throughout Europe and beyond. It conducts unique, high resolution, radio astronomical observations of cosmic radio sources. It is the most sensitive VLBI array in the world, thanks to the collection of extremely large telescopes that contribute to the network.

In addition to “EVN-only” observations, the EVN array often links-up with the Multi-Element Radio Linked INterferometer (MERLIN), an interferometer network of telescopes distributed around the southern half of the UK. In this extended mode, the baselines of the EVN-MERLIN array ranges from a few tens to many thousands of kilometers. The EVN-MERLIN array is thus sensitive to a wide range of radio structures from the arcsecond scale to the milli-arcsecond scale. The EVN also observes simultaneously with the US VLBA, so-called “global VLBI”, obtaining submilli-arcsecond resolution at frequencies higher than 5 GHz.

2.4.2.4 The phased arrays as VLBI elements

When sensitivity is important to a VLBI experiment, it is advantageous to use all the available antennas at a single geographical location as a phased array (Wrobel et al. 2000B) element in a VLBI network. The signals from the antennas are summed after

correcting for geometric delay and phase. For a phased array of N identical antennas, a beam with an angular width of λ/d_a is formed, where d_a is $N^{-1/2}$ times the diameter of each antenna, thereby increasing the sensitivity of the station as a VLBI unit, by a similar factor.

The normal procedure is to phase the array on a calibrator source which is nearby in the sky to the programme source. If the programme source is strong enough, it can be used for this purpose. Instrumental phases are derived and the results applied to the received signals before summation. Since the array will slowly dephase with time, the phasing sources must be observed periodically and the phases readjusted.

The VLA often participates in VLBI observations along with the VLBA (Section 2.4.2.2), and in Global Network sessions. The VLA has a data acquisition system for writing on instrumentation tapes in VLBA formats, a hydrogen-maser frequency and a time standard. Rather than recording a system temperature, the VLA system records the ratio of antenna temperature to the system temperature, which varies as the array phases up. The flux density of each of the program sources must be used to calibrate the amplitudes on VLBI baselines involving the VLA for that source. Together with the ratio of the antenna and system temperatures for the VLA, the total flux densities of each VLBI source at the epoch of observation are required to form the correct coefficient to calibrate the amplitudes for the VLBI baselines that include the VLA. These total flux densities are obtained from the reduction of the interferometric VLA data that are obtained in parallel with VLBI data from the phased-VLA.

2.5 Construction of our sample

2.5.1 *Bona fide* Seyfert galaxies

Often the similarities between the nuclei of Seyfert galaxies and QSOs have been pointed out (Seyfert and starburst galaxies: Dahari & De Robertis 1988, LINERs and radio-quiet quasars: Falcke 2000, Low-Luminosity AGN: Nagar et al. 2000, etc.) and numerous efforts have been made to demonstrate a continuity between these objects. Any Seyfert sample is rarely ever free from starburst galaxies, LINERs (low-ionisation nuclear emission line regions), radio-quiet quasars or radio-loud objects. In order to specifically limit our study to Seyfert galaxies, we confine our sample to (a) radio-quiet AGNs sitting in spiral hosts, thus avoiding any confusion due to the dichotomy of host-galaxy type which may be linked with the radio-loud/radio-quiet dichotomy, and (b) objects with low optical luminosity, in order to eliminate radio-quiet quasars. We

further define Seyfert 1 galaxies to be those objects which have spectrophotometrically detected BLRs either with permitted line widths $\text{FWHM} > 1000 \text{ km s}^{-1}$ or significantly greater than their forbidden line widths.

Thus, we require that the Seyfert galaxies that we select satisfy the following definition:

- Its host is a spiral galaxy (Weedman 1977) of Hubble type S0 or later (*i.e.* S0, Sa, Sab, Sb, Sbc, and Sc), Sandage (1975).

We restrict our study to spiral hosts and avoid objects of other classes. Radio-loud AGNs tend to reside in elliptical host galaxies (Urry & Padovani 1995) and radio-quiet AGNs inhabit mostly spiral galaxies.

- Objects that have low optical luminosity, $M_B \geq -23$ (Schmidt & Green 1983).
- It is a radio-quiet object, *i.e.* the ratio of 5 GHz to *B*-Band flux density is less than 10 (Kellermann et al. 1989). The distribution of radio flux density for the BQS sample appeared bimodal. The radio-quiet objects were the ones which had radio flux density comparable to the optical flux density.
- nuclear line width of Seyfert 1, $\text{H}\beta_{\text{FWHM}}$ (or $\text{H}\alpha_{\text{FWHM}}$) is more than $1,000 \text{ km s}^{-1}$ (Khachikian & Weedman 1974), and line intensity ratio of $[\text{O III}] \lambda 5007$ to $\text{H}\beta$ is greater than 3 for Seyfert 2 (Dahari & De Robertis 1988).

LINERs or H II region galaxies never have nuclear $\text{H}\beta_{\text{FWHM}}$ (or $\text{H}\alpha_{\text{FWHM}}$) line width more than $1,000 \text{ km s}^{-1}$ (Peterson 1997, p. 24), they also never show line intensity ratio of $[\text{O III}] \lambda 5007$ to $\text{H}\beta$ greater than 3 (Krolik 1999, p. 318). Thus, we avoid any likely contamination due to the presence of LINERs and H II region galaxies in our Seyfert sample.

2.5.2 Criterion to minimise obscuration of optical properties

Next, we restrict our list of objects to those which have ratio of minor to major isophotal diameter axes of the host galaxies to be greater than half. We thereby exclude edge-on spiral hosts, and hence try to minimise obscuration of optical properties due to transmission through an edge-on galactic disk. Figure 2.3 shows the distribution of the ratio of minor to major isophotal diameter axes for the final list of objects for the two Seyfert sub-classes. The isophotal diameter ratios are gleaned from de Vaucouleurs et al. (1991) and Lipovetsky et al. (1988) catalogues. We note that Pringle et al.

(1999) and Nagar & Wilson (1999A) have shown that there is no correlation between the host galaxy rotation axis and the direction of the radio jet.

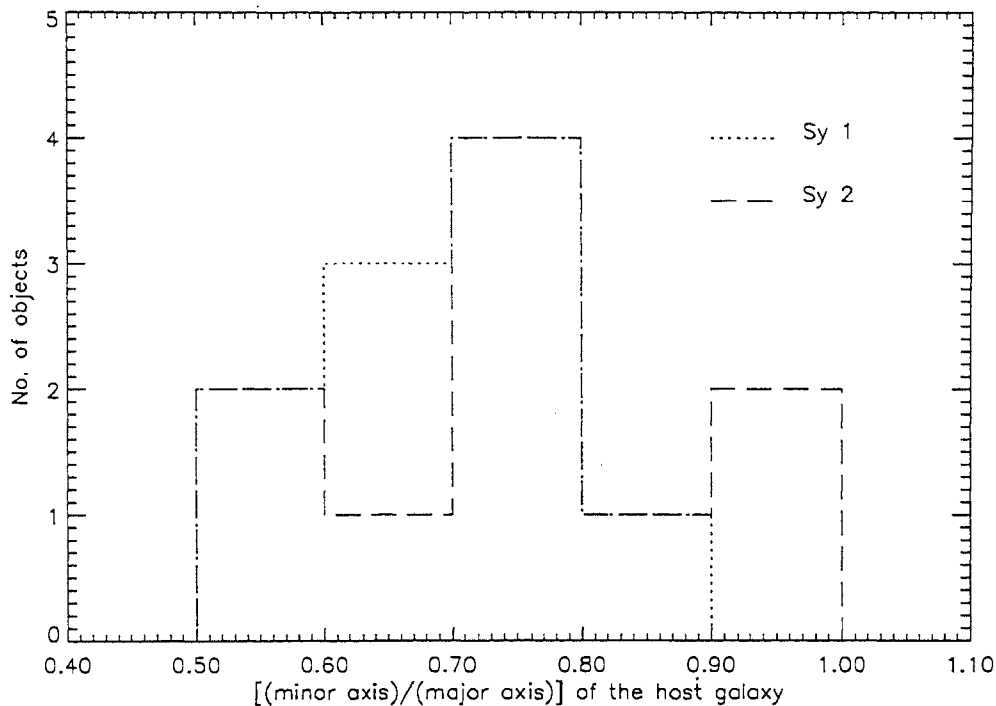


Figure 2.3: Histograms showing distribution of ratio of minor to major isophotal diameter axes (b/a) for the two Seyfert sub-classes (final sample).

2.5.3 Criteria for the feasibility of our experiment

We needed to achieve pc-scale resolution with high sensitivity. The sensitivity of an array is defined by the System Equivalent Flux Density (SEFD; Wrobel 1995, 2000A). The typical zenith SEFDs can be used to estimate root-mean-square (RMS) noise levels on a baseline between 2 VLBI stations.

Determination of the System Equivalent Flux Density

The RMS thermal noise ΔS in the visibility amplitude of a single polarization baseline between antennas i and j is (Wrobel 1995, 2000A)

$$\Delta S = \frac{1}{\eta_S} \times \frac{\sqrt{SEFD_i \times SEFD_j}}{\sqrt{2 \times \Delta\nu \times \tau}} \text{ Jy},$$

and between two identical antennas i and j is

$$\Delta S = \frac{1}{\eta_S} \times \frac{SEFD}{\sqrt{2} \times \Delta\nu \times \tau} \text{ Jy},$$

where $\eta_S \leq 1$ accounts for the VLBI system inefficiency, τ is the integration time (sec) for an individual scan, which should be less than or equal to the coherence time, and $\Delta\nu$ is the bandwidth (Hz).

The RMS thermal noise ΔI_m , expected in a single polarization image, assuming natural weighting (Wrobel 1995) is

$$\Delta I_m = \frac{1}{\eta_S} \times \frac{SEFD}{\sqrt{N \times (N - 1) \times \Delta\nu \times t_{int}}} \text{ Jy beam}^{-1},$$

where N is the number of antennas used and t_{int} is the total integration time on source. For example, the image sensitivity for a total on-source integration time of 8 hours with the full VLBA recording at the maximum data rate (128 Mbits sec⁻¹) is $\Delta I_m \sim 45 \mu\text{Jy beam}^{-1}$.

The RMS noise level σ on a baseline between 2 VLBA antennas for a data rate of 128 Mbits s⁻¹, 2 minute scan integration time, and 6 cm observing wavelength is 4.7 mJy (Wrobel 2000A). A signal of 6σ is required to ensure reliable detection of the correlated signal; *i.e.*, the minimum detectable correlated flux density on each baseline is $6 \times 4.7 = 28.2$ mJy. Increasing the scan integration time will decrease the detectable flux density on all baselines; adding the sensitive Effelsberg (Germany) and phased-VLA to the array will provide additionally reduced detectable flux densities on baselines involving these antennas. We adopted a scan integration time of 8.8 min, since this is convenient from the point of view of tape consumption, and does not exceed the expected coherence time at 6 cm. A single tape pass lasts 44 minutes, and it is most efficient to have the pass duration be an integral multiple of the duration of a scan; with a scan duration of 8.8 minutes, exactly five scans will fit in each tape pass.

Table 2.1 gives 6σ correlated flux densities on various baselines, for the parameters adopted for our experiment.

Thus, if we wish to have at least ~ 4 mJy of correlated flux density, corresponding to the 6σ detection limits for baselines between one of the smaller antennas in the array and either the phased-VLA or Effelsberg, the flux density in compact arcsec-scale structure must be ~ 8 mJy, assuming that 50% of the flux density seen with arcsec-scale resolution would be detected with the above baselines. Therefore, the following constraint was enforced.

Baseline	Correlated flux density
Phased-VLA and Effelsberg	~ 0.7 mJy
Phased-VLA and VLBA	~ 2.6 mJy
Effelsberg and VLBA	~ 3.4 mJy
VLBA and VLBA	~ 13.5 mJy

Table 2.1: Table showing 6σ correlated flux densities on various baselines.

The source must have been observed with at least arcsec-scale resolution, at wavelengths of 6 or 3.6 cms (*i.e.*, VLA *A* or *B* array observations at these wavelengths) and it must have a detected compact component, at these resolutions and wavelengths, with flux density greater than 8 mJy.

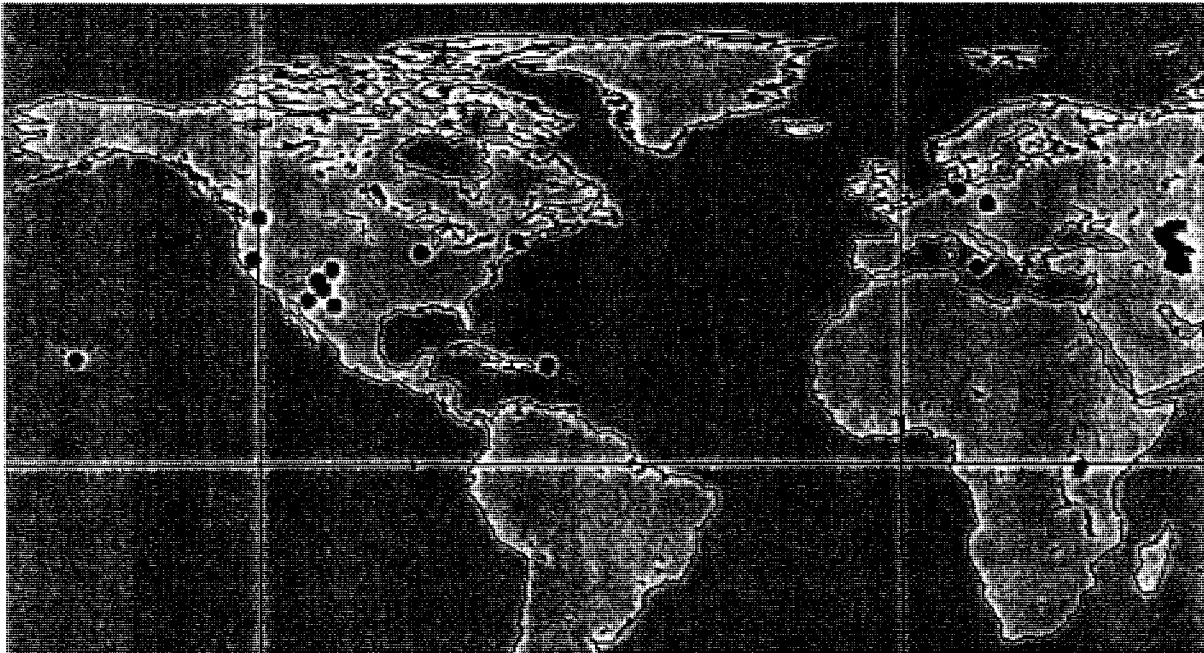


Figure 2.4: Geographical positions of the VLBI stations used in our observations.

We decided to use 11 US stations (10 VLBA antennas and the phased-VLA) and 3 EVN stations. Figure 2.4 shows a global map with positions of individual antennas used for our experiment.

For 6 out of 20 of the objects in our list $\lambda_{6\text{ cm}}$ measurements were not available. We used $\lambda_{3.6\text{ cm}}$ VLA *A* array flux densities and assumed a flat spectral index between

these two wavelengths for these objects. For the flux density of one of the objects (NGC 7212), we used single baseline correlated flux density from Roy et al.'s (1994) work.

This constraint provides us with a reasonable sample size with minimum correlated flux density that is detectable on baselines involving Effelsberg antenna or phased-VLA. Torun and Noto stations provided us with a closure triangle in Europe and gave a range of baseline lengths for the sensitive baselines involving Effelsberg antenna. Similarly for phased-VLA, VLBA stations spread all over the United States provided us with a range of baseline lengths for it.

2.5.4 Criteria based on orientation independent parameters

We discussed in Section 2.2 that Roy et al.'s (1994) result is inconsistent with the unified scheme hypothesis and the inconsistency is only made worse by invoking relativistic beaming. To rigorously test the predictions of the unified scheme, the purportedly face-on and edge-on Seyfert galaxies being compared should be *intrinsically similar* within the framework of the scheme. They should therefore be selected so that they are matched in parameters that are orientation independent. We attempt to do this with orientation independent parameters that are measures of intrinsic AGN power and host galaxy properties. Such a selection would enable us to test the predictions of the unified scheme hypothesis rigorously.

From the short list of objects that met the criteria given in Sections 2.5.1, 2.5.2 and 2.5.3 of our Seyfert definition, minimisation of host galaxy inclination, and the minimum flux density of the compact source, we chose 10 Seyfert 1 and 10 Seyfert 2 galaxies such that the two sub-samples had similar distributions of the following orientation independent observables.

2.5.4.1 Heliocentric redshift

In order to compare the Seyfert 1 and Seyfert 2 galaxies from the same volume of space, we chose them to have similar distribution of redshift (Figure 2.5).

2.5.4.2 Luminosity of the [O III] $\lambda 5007$ emission line: Measure of intrinsic AGN power

It is well known that narrow-line luminosities correlate strongly with nuclear ionising luminosity (Yee 1980, Shuder 1981). The luminosity of the [O III] $\lambda 5007$ emission line is clearly associated with the AGN (Whittle 1992B, 1992C, and Nelson & Whittle

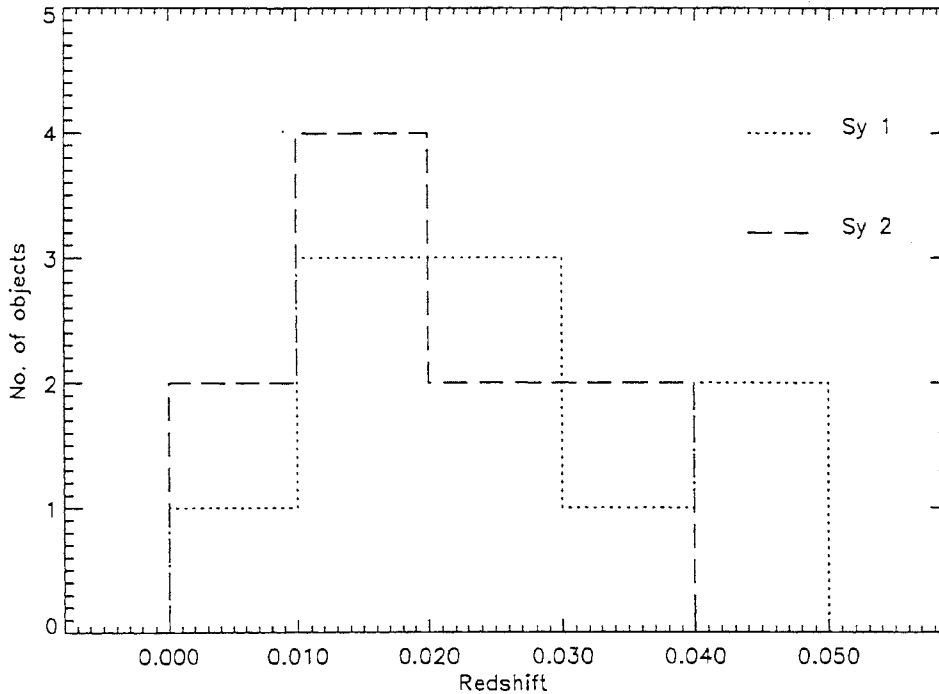


Figure 2.5: Histograms showing distribution of redshift (z) for the two Seyfert sub-classes.

1995) and further, although spatially it could be distributed anisotropically (Pogge 1989, Evans et al. 1991A and 1991B) its luminosity is clearly orientation independent. We therefore use the [O III] $\lambda 5007$ luminosity (see Figure 2.6 for distribution of the [O III] $\lambda 5007$ luminosity) as a measure of the intrinsic AGN power (Nelson & Whittle 1995) and we chose only those Seyfert 1 and Seyfert 2 galaxies which had similar range of [O III] $\lambda 5007$ luminosity.

2.5.4.3 Stellar luminosity of the host galaxy

The host galaxy properties of Seyfert galaxies ought to be orientation independent. Hence, we chose stellar luminosity of the host galaxy (total luminosity of the host corrected for the nuclear non-stellar and emission line flux, redshift (K) correction, the internal absorption, and the Galactic absorption) as one of the parameters.

Determination of “corrected” magnitude of the host, B_T^c :

Most of our sample objects have stellar absolute magnitude of the host galaxy

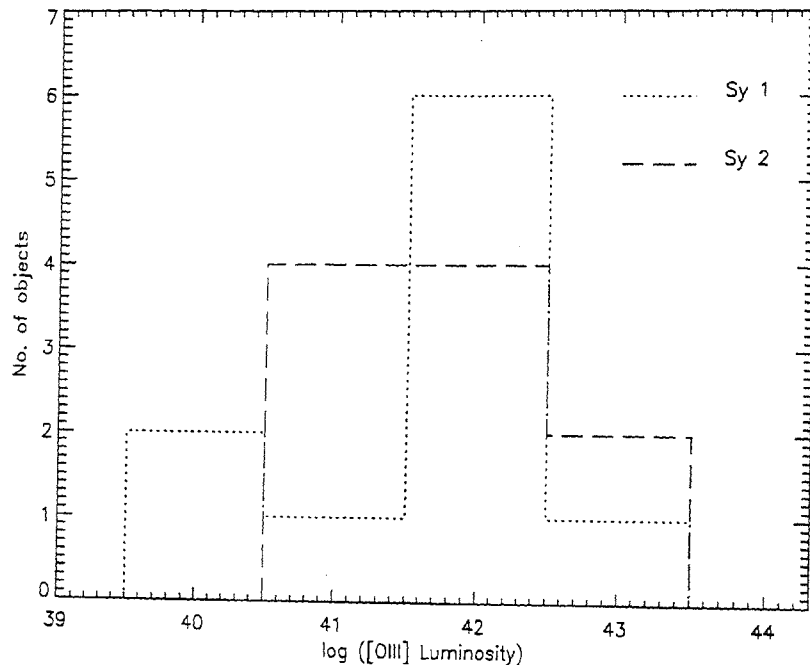


Figure 2.6: Histograms showing distribution of [O III] $\lambda 5007$ luminosity for the two Seyfert sub-classes.

i.e., M_B^{total} tabulated in Whittle (1992A). To determine corrections to total apparent magnitude, B_T (for Mrk 1218, NGC 2639, and Mrk 231), for which M_B^{total} is not available in Whittle (1992A), we stick to the methodology of Whittle (1992A). Four factors, together called $(\Delta m)^{correction}$, contribute to B_T , the first is the nuclear non-stellar and emission line flux, Δm_A , the second is the redshift (K) correction, Δm_K , the third is the correction for internal absorption, Δm_i , and the final correction is the correction due to galactic absorption, Δm_G .

Thus

$$B_T^c = B_T + (\Delta m)^{correction},$$

where

$$(\Delta m)^{correction} = \Delta m_A + \Delta m_K + \Delta m_i + \Delta m_G.$$

The RC3 catalog gives B_T^0 , *i.e.* the B_T corrected for redshift (K) correction, the correction for internal absorption, and the correction due to galactic absorption, *i.e.*

$$B_T^0 = B_T + \Delta m_K + \Delta m_i + \Delta m_G.$$

We then determine B_T^c , using

$$B_T^c = B_T^0 + \Delta m_A.$$

Δm_A , correction due to the non-stellar line and continuum emission is derived from the two line fluxes F_{5007} and $F_{H\beta}$, following the procedure described in Whittle (1992A). If only one of F_{5007} or $F_{H\beta}$ is available, as is the case for NGC 2639, the other is estimated using $F_{5007}/F_{H\beta} = 0.25$ for a Seyfert 1.0. As a function of redshift, z , the effective continuum flux density, F_c , in $\text{ergs s}^{-1} \text{cm}^{-2} \text{\AA}^{-1}$ in the B band due to forbidden and Balmer emission lines is approximated by

$$F_{cF} \simeq (0.62 - 3.5z) F_{5007}/980 \quad (z \leq 0.02),$$

$$F_{cF} \simeq 0.55 F_{5007}/980 \quad (0.02 < z \leq 0.07),$$

$$F_{cH} \simeq 1.42 F_{H\beta}/980 \quad (z \leq 0.03),$$

$$F_{cH} \simeq (1.51 - 3.14z) F_{H\beta}/980 \quad (0.03 < z \leq 0.07).$$

The non-stellar continuum luminosity is derived from $H\beta$, assuming a power law with spectral index α ($F_\nu \propto \nu^\alpha$). The effective continuum flux density in the B Band is given by

$$F_{cC} \simeq 1.10^{(\alpha+2)} (1+z)^{(\alpha+2)} F_{H\beta}/100.$$

We adopt $\alpha = -1.0$ for the non-stellar continuum since this corresponds to the canonical nuclear colors of Seyfert 1 galaxies ($\alpha = -1.0$ is equivalent to $U - B = -0.75$, $B - V = +0.41$). The total non-stellar contribution

$$F_c = F_{cF} + F_{cH} + F_{cC},$$

gives

$$\Delta m_A = 2.5 \log\left(\frac{7.2 \times 10^{-9}}{F_c}\right),$$

which is subtracted from B_T^0 to give B_T^c for Mrk 1218, NGC 2639, and Mrk 231.

M_B^{total} of the host galaxy is then determined using

$$M_B^{total} = B_T^c - 5 \log_{10} \left(\frac{r}{10 \text{ (pc)}} \right),$$

where r is the distance to the object in parsec. Figure 2.7 shows the distribution of the total stellar absolute magnitude for the two Seyfert sub-classes.

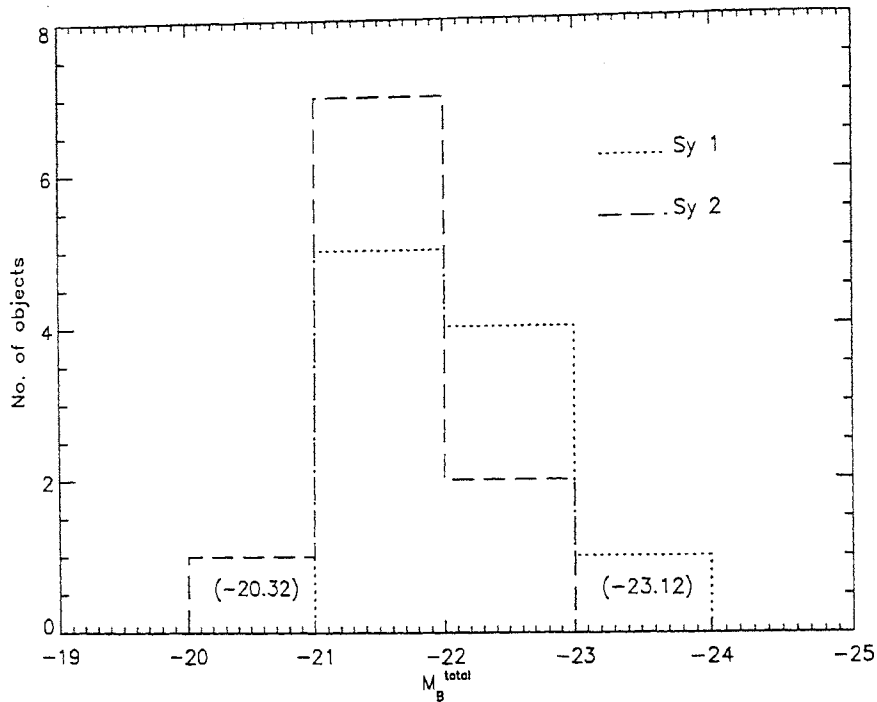


Figure 2.7: Histograms showing distribution of total stellar absolute magnitude of the host galaxy for the two Seyfert sub-classes; values in the bins indicate M_B^{total} for the sources.

2.5.4.4 Absolute bulge luminosity of the host galaxy

Whittle (1992A) has argued that the nuclear stellar velocity dispersion is a measure of the depth of the gravitational potential within a scale of ~ 3 kpc. Further, dispersion velocity of stars correlates with the absolute bulge magnitude (Whittle 1992A, Nelson & Whittle 1995). We took this depth of gravitational potential, and therefore the absolute magnitude of the bulge $(M_B)_{bulge}$, to be an indicator of intrinsic AGN power. We therefore tried to ensure that our two sub-samples did not differ significantly in the distribution of this parameter.

Determination of $(M_B)_{bulge}$

$(M_B)_{bulge}$ is available for most of the objects in Whittle (1992A). For Mrk 1218, NGC 2639, Mrk 231, and Mrk 477, we use the formulation adopted by Whittle (1992A).

Thus

$$(M_B)_{bulge} = (M_B)_{total} - (\Delta m)_{disk},$$

where

$$(\Delta m)_{bulge} = 0.324\tau - 0.054\tau^2 + 0.0047\tau^3,$$

where $\tau = T + 5$, and T is the Hubble type (Sandage 1975).

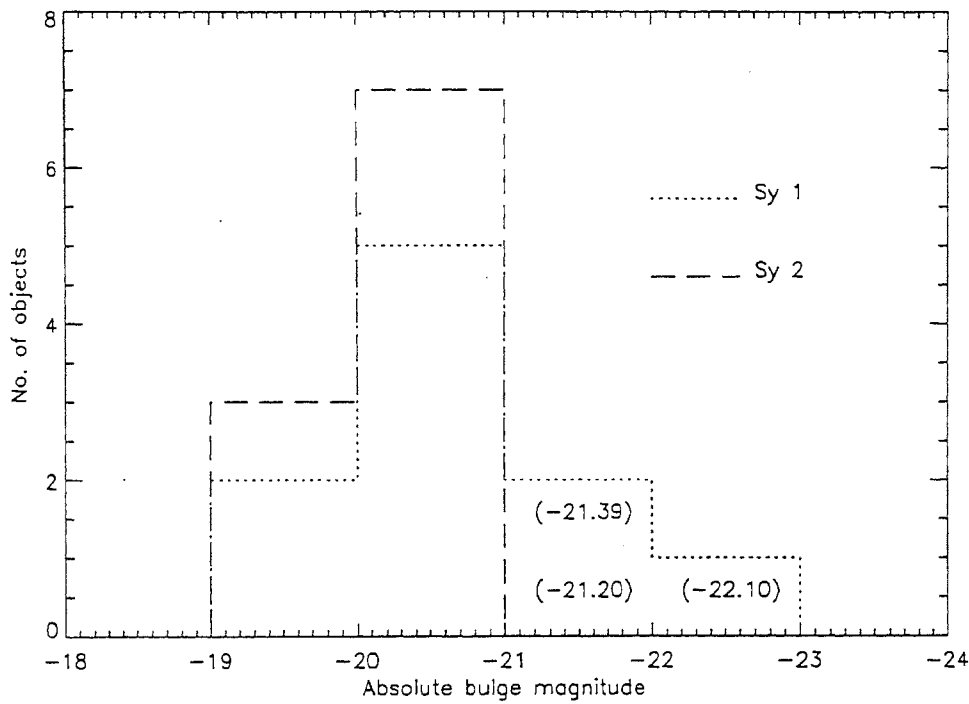


Figure 2.8: Histograms showing distribution of absolute magnitude of the bulge (B band) for the two Seyfert sub-classes; values in the bins indicate absolute bulge magnitude for the sources.

We find that the distribution of $(M_B)_{bulge}$ for the Seyfert sub-samples are statistically not significantly different.

2.5.4.5 Hubble type of the host galaxy

The Hubble type mainly depends on the size of the nuclear bulge relative to the flattened disk (Sandage 1975). Malkan et al. (1998) have argued that the Seyfert 1 galaxies are of earlier Hubble type than Seyfert 2 galaxies. We therefore have considered the distribution of Hubble type of the host galaxy for our sample of Seyfert 1 and Seyfert 2 galaxies.

We use the Hubble type given in the RC3 catalog (de Vaucouleurs et al. 1991) for our sample sources and when not available, we use values from Whittle (1992A) or

Lipovetsky et al. (1988). The Hubble type of one of the objects, Mrk 1218, which was unavailable in de Voucouleurs et al. (1991) and Lipovetsky et al. (1988), is taken from Malkan et al. (1998). We show below, the distribution for Hubble type for the two classes of Seyfert galaxies.

The distributions are shown in Figure 2.9 and are statistically not significantly different for the two sub-classes. We have thus controlled for the Hubble type in our sample. The morphological class given by Malkan et al. (1998) are based on WFPC2, HST images. We also (Figure 2.10) show below, the distribution of Hubble type for the two sub-samples of Seyfert galaxies where the Hubble types are preferentially gleaned from Malkan et al. (1998), 6 out of 10 Seyfert 1 and 7 out of 10 Seyfert 2 galaxies, and then from RC3 or Whittle (1992A) or Lipovetsky (1988).

Thus, of the 126 Seyfert galaxies that had VLA data in the literature, 52 met our detectability criterion. 29 of these 54 had all the required parameters listed in Sections 2.5.1 and 2.5.4 available in the literature. From these 29 we could pick 20 that met our section criteria and were matched in the orientation independent parameters.

2.5.5 Our Seyfert sample

Our aim was to study the pc-scale radio morphology of Seyfert galaxies so as to test the predictions of the unified scheme hypothesis. By matching Seyfert 1 and Seyfert 2 galaxies in the above parameters, particularly [O III] $\lambda 5007$ luminosity (an indicator of intrinsic AGN power) and stellar luminosity of the host galaxy, we ensured that the samples of Seyfert 1 and Seyfert 2 galaxies were intrinsically similar within the framework of unified scheme. Table 2.2 lists our sample of Seyfert galaxies giving all the parameters that were used to construct the sample, *viz.*, ratio of minor to major axis of the host galaxy, the radio flux density of the compact component, redshift, [O III] $\lambda 5007$ line width, [O III] $\lambda 5007$ luminosity, the ratio of emission line intensities of fluxes in [O III] $\lambda 5007$ to H β , stellar luminosity of the host galaxy, bulge absolute luminosity and Hubble type for the two Seyfert sub-classes.

The fact that we avoided edge-on host galaxies results in a selection of sample of Seyfert 1 and Seyfert 2 galaxies differing in one intrinsic respect. Current studies indicate that the orientation of the AGN axis (and therefore the radio-jet) relative to the host galaxy axis is random (*e.g.* Pringle et al. 1999). Thus it follows that our sample has a paucity of Seyfert 1 galaxies with their radio-jets in the host galaxy plane and similarly there is a paucity of Seyfert 2 galaxies with their jet-axis perpendicular to the host galaxy plane. If the gaseous inter-stellar medium of the host galaxy has an

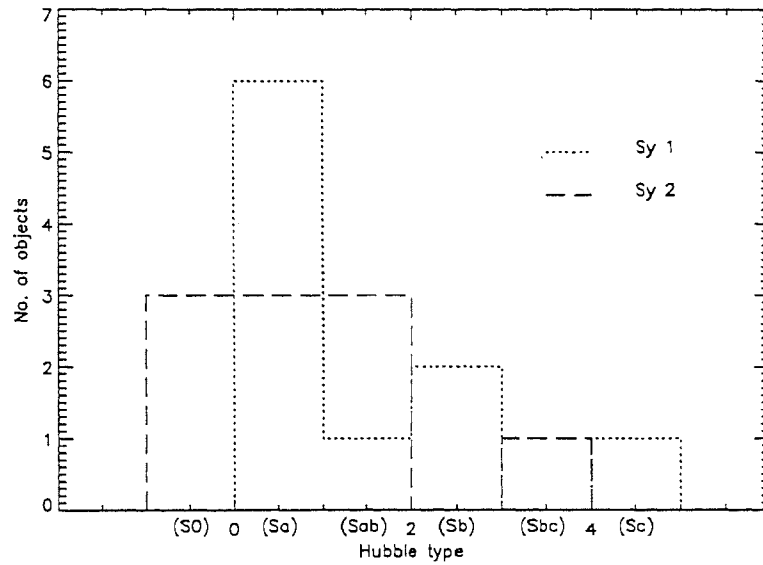


Figure 2.9: Histograms showing distribution of the Hubble type (T) for the two Seyfert sub-classes (mainly from RC3 catalog and Whittle (1992A)).

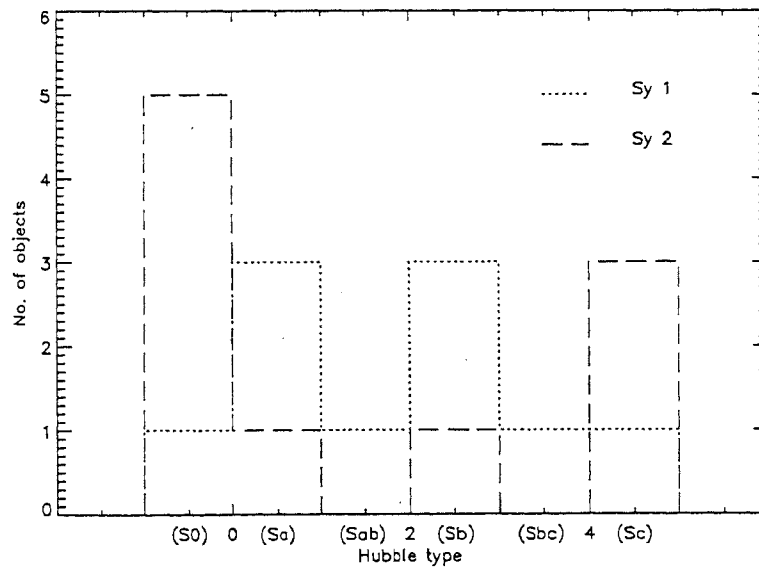


Figure 2.10: Histograms showing distribution of the Hubble type (T) for the two Seyfert sub-classes, (mainly from Malkan et al (1998), RC3 catalog, and Whittle (1992A)).

effect on the propagation of the jet through it, then it implies that there is a physical difference in this respect between our Seyfert 1 and Seyfert 2 galaxies.

2.6 Summary

One of the challenges to the unification scheme is the low detection rates of compact radio structures in Seyfert 1 galaxies as compared to Seyfert 2 galaxies. We address this by probing the mas-scale radio structures for a sample of Seyfert 1 and Seyfert 2 galaxies selected to be intrinsically similar. We do this by constructing a sample of orientation independent parameters, *viz.*, measures of intrinsic AGN power and host galaxy luminosity. The sub-classes (Seyfert 1 and Seyfert 2 galaxies) are also matched in the distributions of redshift and Hubble type. Edge-on host galaxies have been avoided to minimise the effect of the galactic disk on the optical properties. However, there is one respect in which the two sub-classes of Seyfert galaxies differ, *viz.*, the paucity of Seyfert 1 galaxies with their radio-jets in the host galaxy plane and Seyfert 2 galaxies with their jet-axis perpendicular to the host galaxy plane.

Name	(b/a) ⁰	VLA A array compact component S _c (mJy)	Redshift	[O III] line width (km s ⁻¹)	$\frac{F_{\lambda 03}^{\text{O III}}}{F_{\text{H}\beta}^{\text{O III}}}$	[O III] luminosity (ergs s ⁻¹)	M_B^{total}	Bulge ^d luminosity ($M_{B_{\text{bulge}}}$)	T ^h Ref ^h	T ^h from MGT
Seyfert 1s										
0551+464	0.71	32.5	0.025	605.0 ^c	3.5 ^e	42.14 ^c	-23.1 ^c	-22.10	1 Wh92	0
0825+250	0.58	23.0	0.029	1078.0 ^f	3.8 ^c	41.82 ^a	-21.1 ^g	-20.04	1 MGT	1
0840+503	0.60	23.4	0.011	400.0 ^b	0.3 ^g	39.88 ^b	-21.4 ^g	-20.33	1 RC3	3
1208+396	0.71	34.0	0.003	425.0 ^c	3.3 ^e	42.19 ^c	-21.2 ^c	-19.99	2 RC3	3
1215+300	0.87	14.5	0.013	180.0 ^c	3.7 ^c	41.77 ^c	-21.0 ^c	-20.01	1 RC3	3
1254+571	0.74	155.0	0.042	> 600.0 ^e	0.4 ^e	40.27 ^a	-22.3 ^g	-19.75	5 RC3	
2240+294	0.65	8.0	0.024	240.0 ^c	1.0 ^c	41.72 ^c	-21.7 ^c	-20.11	3 Wh92	
2300+086	0.72	21.0	0.016	360.0 ^c	0.6 ^c	41.84 ^c	-22.0 ^c	-20.99	1 RC3	4
2302-089	0.67	9.0	0.047	365.0 ^c	0.6 ^e	42.53 ^c	-22.4 ^c	-21.39	1 Wh92	
2316-000	0.66	10.0	0.030	490.0 ^c	0.3 ^a	41.26 ^c	-22.7 ^c	-21.20	3 RC3	1
Seyfert 2s										
0046+316	1.00	480.0	0.015	365.0 ^c	10.5 ^c	41.69 ^c	-21.1 ^c	-20.27	0 RC3	0
0113+328	0.62	26.0	0.016	520.0 ^c	11.1 ^c	41.85 ^c	-20.3 ^c	-19.46	0 Wh92	5
0645+609	0.76	8.9	0.006	110.0 ^c	10.0 ^c	40.92 ^c	-21.0 ^c	-19.97	1 RC3	3
0737+652	0.55	8.0	0.037	1075.0 ^c	13.2 ^c	42.62 ^c	-22.0 ^c	-20.78	1 Wh92	
1322-295	0.71	15.8	0.014	165.0 ^c	5.1 ^c	41.28 ^c	-22.1 ^c	-20.91	2 RC3	5
1439+537	0.78	18.3	0.038	370.0 ^c	8.8 ^c	43.02 ^c	-21.0 ^c	-20.13	0 Lip	
1524+418	0.93	13.5	0.009	415.0 ^c	4.0 ^c	40.63 ^c	-21.4 ^c	-20.13	2 RC3	0
2204+095	0.50	30.0 ¹	0.027	435.0 ^c	10.8 ^c	42.34 ^c	-21.2 ^c	-20.22	1 Wh92	
2325+085	0.78	27.0 ²	0.029	350.0 ^c	12.9 ^c	42.26 ^c	-22.7 ^c	-20.68	4 RC3	5
2325+032	0.89	13.5 ²	0.017	255.0 ^c	> 4.0 ^c	41.46 ^c	-21.1 ^c	-19.88	2 RC3	0

Abbreviations used; Lip: Lipovetsky et al. 1988, MGT: Malkan et al. 1998, RC3: de Vaucouleurs et al. 1991, Wh92: Whittle 1992A.

⁰All entries are from RC3 catalog (de Vaucouleurs et al. 1991) except Mrk 926 which is from Lipovetsky et al. (1988).

¹Correlated flux density detected at 13 cm by Roy et al. (1994), using the PTY interferometer.

²Calculated from the measurement at $\lambda_{3.6}$ cm.

^aDahari & De Robertis 1988.

^bKeel 1983.

^cWhittle 1992A.

^dsee Section 2.5.4.4

^eKim et al. 1998.

^fGoodrich 1989.

^gsee Section 2.5.4.3

^hsee Section 2.5.4.5

Table 2.2: Table showing the list of Seyfert 1 and Seyfert 2 galaxies that constitute our sample, with the parameters that were used to constraint it.

Chapter 3

Observations and results

3.1 Introduction

We have obtained images of our sample of Seyfert 1 and Seyfert 2 galaxies with mas-scale resolution at 6 cm using Very Long Baseline Interferometry (VLBI). Here we describe the observations and data reduction procedures, and present the radio images. We discuss their radio properties at arcsec and mas-scales in the light of past observations in Sections 3.2 and 3.3 respectively. Section 3.4 describes the results and analysis.

3.2 Observations

We were awarded 24 hours of observing time of the requested 36 hours to observe our sample of Seyfert galaxies (Chapter 2) with the global VLBI array. We could thus observe only 15 of the sources from a total of 20 sample sources. We chose only those objects that had not been observed previously at mas-scales at 5 GHz. This allowed us to exclude Mrk 231 (Ulvestad et al. 1999A), NGC 4151 (Ulvestad et al. 1998B), Mrk 348 (Barvainis & Lonsdale 1998), and Mrk 926 (Mundell et al. 2000). By excluding NGC 5135 (Seyfert 2.0) which is a low-declination object we could fit in 15 of our sample objects into the 24 hours of award time and obtain sufficiently good coverage on each object.

3.2.1 VLBI observations

As described in Chapter 2, VLBI observations were performed using the US and European VLBI networks (EVN). We used 10 VLBA, phased-VLA, and 3 of the EVN stations

viz. Effelsberg (Germany), Torun (Poland) and Noto (Italy). Torun (Poland) and Noto (Italy) telescopes were added to provide short baselines for Effelsberg antenna and to give a closure triangle in Europe. Figure 2.4 shows a global map with positions of individual antennas used for our experiment. Table 3.1 summarizes the log of VLBI observations.

A single VLA antenna has the same system-equivalent-flux-density as a VLBA antenna. When all the 27 VLA (Figure 2.2) antennas are phased, then the baselines between the phased-VLA array and any VLBA antenna is about 4–5 times more sensitive than baselines between any two VLBA antennas; which is similar to the sensitivity on Effelsberg and any VLBA antenna baseline.

Observing date	: February 18, 1998
Stations	: 10-element VLBA, Phased VLA, Effelsberg, Noto and Torun
Wavelength	: 6 cm
Bandwidth	: 50 MHz
Aggregate bit rate	: 128 Mbits s ⁻¹
	(8 baseband channels at 16 MSamples s ⁻¹ of 1 bit samples)
Processor	: Socorro, New Mexico, USA

Table 3.1: Observing log.

Short observations of four compact bright sources, *viz.*, 3C84, 3C345, DA193, and 4C39.25 (Table 3.2) were included in the VLBI schedule as ‘fringe finders’. Detection of these sources provides a general test of the success of the VLBI experiment in terms of the setup at each VLBI station, the station coordinates, source coordinates etc. Seyfert galaxy targets are too weak to be used to phase the VLA array, hence we observed VLA phase calibrators for the phasing (see also Section 3.2.2). The VLA phase-calibrators were observed during the slewing of the VLBI stations, taking advantage of the very high slewing speeds of the VLA antennas.

We used HAZI (Pearson 1994) to generate the (u, v) tracks, and UPTIME (Pearson 1995) to generate source rise and set times at each station and prepared the sequence of sources observed in snapshot mode in order to maximise (i) number of scans, (ii) the (u, v) coverage and (iii) inclusion of as many stations as possible in each scan for each source. For scheduling we used SCHED developed by NRAO (Walker 2001), which generates a VLBA tape control file for each of the stations involved in the experiment. It also prepares an “observe” file for the VLA.

Object	RA (J2000)	Dec (J2000)	Phase Calibrator	RA (J2000)	Dec
Target sources					
Mrk 1	01 ^h 16 ^m 07 ^s .2174	+33°05'21".557	0119+321	01 ^h 19 ^m 35 ^s .0001	+32°10'50".059
MCG 8-11-11	05 ^h 54 ^m 53 ^s .6107	+46°26'21".708	0604+442	06 ^h 04 ^m 35 ^s .6303	+44°13'58".561
NGC 2273	06 ^h 50 ^m 08 ^s .6403	+60°50'44".947	0650+600	06 ^h 50 ^m 31 ^s .2494	+60°01'44".602
Mrk 78	07 ^h 42 ^m 41 ^s .7384	+65°10'37".780	0737+596	07 ^h 37 ^m 30 ^s .0871	+59°41'03".195
Mrk 1218	08 ^h 38 ^m 10 ^s .9453	+24°53'42".924	0837+249	08 ^h 37 ^m 40 ^s .2472	+24°54'23".093
NGC 2639	08 ^h 43 ^m 38 ^s .0723	+50°12'20".073	0832+492	08 ^h 32 ^m 23 ^s .2167	+49°13'21".039
Mrk 766	12 ^h 18 ^m 26 ^s .5170	+29°48'46".500	1217+301	12 ^h 17 ^m 52 ^s .0820	+30°07'00".636
Mrk 477	14 ^h 40 ^m 38 ^s .0973	+53°30'16".062	1419+543	14 ^h 19 ^m 46 ^s .5974	+54°23'14".787
NGC 5929	15 ^h 26 ^m 06 ^s .1670	+41°40'14".420	1458+373	14 ^h 58 ^m 44 ^s .7949	+37°20'21".627
NGC 7212	22 ^h 07 ^m 02 ^s .0590	+10°14'02".590	2151+071	21 ^h 51 ^m 31 ^s .9971	+07°09'26".465
Ark 564	22 ^h 42 ^m 39 ^s .3555	+29°43'30".871	2236+284	22 ^h 36 ^m 22 ^s .4709	+28°28'57".413
NGC 7469	23 ^h 03 ^m 15 ^s .6160	+08°52'26".120	2257+077	22 ^h 57 ^m 17 ^s .3031	+07°43'12".303
Mrk 530	23 ^h 18 ^m 56 ^s .6530	+00°14'37".960	2323-032	23 ^h 23 ^m 31 ^s .9537	-03°17'05".023
Mrk 533	23 ^h 27 ^m 56 ^s .7120	+08°46'44".130	2330+110	23 ^h 30 ^m 40 ^s .8522	+11°00'18".710
NGC 7682	23 ^h 29 ^m 03 ^s .9180	+03°31'59".920	2330+110	23 ^h 30 ^m 40 ^s .8522	+11°00'18".710
Flux density calibrator					
1331+305	13 ^h 31 ^m 08 ^s .2882	+30°30'32".960			
Fringe finders					
3C84	03 ^h 19 ^m 48 ^s .1601	+41°30'42".106			
3C345	16 ^h 42 ^m 58 ^s .8099	+39°48'36".993			
DA193	05 ^h 55 ^m 30 ^s .8056	+39°48'49".166			
4C39.25	09 ^h 27 ^m 03 ^s .0139	+39°02'20".853			

Table 3.2: Target sources of our observations, VLA phase calibrators, flux density calibrator and VLBI fringe finders.

3.2.2 VLA observations

The simultaneous VLA data for the sample due to the phased-VLA being one of the stations in the VLBI array, was an advantageous addition to our database. As discussed earlier (Section 2.4.2.4), when the VLA participates as a phased-array VLBI element, the “VLA-only” correlated data are also written onto a disk. We were awarded 24.5 hours of VLA time for the VLBI observations and we observed the flux density calibrator 1331+305 (3C286) (Table 3.2), in the additional 1/2 hour of time. “VLA-only” aperture synthesis data for Seyfert galaxy targets were obtained whenever the VLBI array was observing these targets. Phase calibrators were selected from the A-category NRAO list (‘S’ class unresolved calibrators, chosen such that the separation between the target source and the phase calibrator is smallest). These phase calibrators served the dual purpose of acting as bright enough sources to phase the VLA for the VLBI observations (Section 3.2.1) and interleaved phase calibrators for the “VLA-only” aperture synthesis data. Since these calibrators were observed during the slew times of the other VLBI stations, they got interleaved between the targets in the “VLA-only” observations conforming to the standard procedure. The target sources thus had data in snapshot mode with 8.8 min on each source and ~ 2 min on the corresponding phase calibrator.

The centre wavelength and bandwidth of the observations are the same as that of the VLBI observations.

Table 3.2 gives the list of Seyfert galaxies and the corresponding VLA phase calibrator used for each of them.

3.3 Data reductions

3.3.1 VLBI data

The data recorded at each station were correlated at the VLBA correlator in Socorro. The amplitude calibration was carried out using the gain curves supplied by each station and the system temperature measured before and after each 8.8 min scan in each baseband channel. The flux densities of the programme sources were used together with the ratios of the VLA antenna and system temperatures to calibrate the amplitudes of baselines involving the VLA. The phases in each baseband channel were aligned, and then used to solve for the (small) residual phase and delay offsets. Before imaging, the data were averaged over frequency, and then over time (with an averaging time of 30 seconds). All the calibration and imaging were carried out using the NRAO

Astronomical Image Processing System (AIPS, AIPS Cookbook 1999) package.

The resulting errors in the visibility amplitudes are about 5% or less, as indicated by the compact fringe finder DA193 ($S = 5.38$ Jy). Finally, as part of the iterative imaging procedure, the assumed antenna gains were calibrated along with the source structure (hybrid mapping) to obtain the best fit. We did the phase-only calibration while doing self-calibration in the iterative imaging procedure. The process of iterative self-calibration procedure to correct for the complex gains of individual antennas was halted when the image quality and the RMS noise stabilized. Since the phased-VLA is more sensitive than the other antennas, we used the phased-VLA as the reference antenna. For the final maps the uniform-weighting scheme was used for the Fourier transform in order to maximise angular resolution. In this scheme, each visibility sample is weighted in inverse proportion to the local density of the (u, v) coverage. The RMS noise levels were typically ~ 0.09 – 0.19 mJy in the final maps.

The model-fitting was done using the Brandeis package (Gabuzda 1988). This package does model-fitting in the Fourier domain and thus gives us an advantage over other algorithms, because it avoids the effect of convolution of the synthesized beam with the source in the final map. The model-fitting provided in the AIPS package operates in the image plane and the observed image is a convolution of the true image and the synthesised beam. Therefore the model-fit result for an unresolved source is given to be of the same angular size as the synthesised beam.

3.3.2 VLA data

The positional information in our final images is limited by the atmospheric phase stability, the closeness of a suitable (astrometric) calibrator, and the calibrator-source cycle time. The accuracies are between 10–50 mas. Here again, all the data processing, including calibration, deconvolution and mapping, was performed using AIPS. 1331+305 (3C286) was used as the flux density calibrator (see VLA calibrator manual 2000), using Perley's revised coefficients as described in the AIPS cookbook. The data were Fourier transformed using the uniform weighting scheme. The sources were subjected to several cycles of self-calibration until the sensitivity approached thermal noise levels. The typical 1σ noise level in the map ranges between ~ 30 – $90 \mu\text{Jy}$. We use maps from the first intermediate frequency (IF) channel as it suffers from lower noise levels as compared to IF2 channel.

The positions, sizes and flux densities of the compact components were found by fitting a two-dimensional Gaussian function using AIPS task JMFIT (which fits an

image with up to four Gaussian components with error estimates), except in the case of extremely irregular objects where the flux density was measured directly with the task TVSTAT (which finds the mean and RMS in a blotched region on the AIPS TV screen). Uncertainties in the flux densities are attributed to confusion, receiver noise, residual atmospheric noise and uncertainties in the flux density as quoted by Rick Perley (VLA calibrator manual 2000). The combined effect of the first three contributions can be measured via the RMS noise (σ) in the maps, which was calculated in areas carefully selected to be clear of emission. The net error in the flux density is thus typically 5% arising from the calibration and the RMS noise. The core flux densities are either found using the MAXFIT (fits a two-dimensional parabola to the maximum within a few pixels of an image position, and gives the peak of surface brightness and its position), or JMFIT in AIPS in those cases where a component coincident with the optical nucleus was clearly delineated.

3.4 Results and analysis

3.4.1 The radio images

Contour maps for all the sources on mas-scales (*i.e.* VLBI images) and the arcsec-scale (*i.e.* VLA) images are shown along with the optical position in the figures below. Spatial scales for VLA maps are usually given in absolute units, whereas relative units with respect to the phase centre are used for VLBI maps. A cross in the arcsec-scale images marks the position of the optical nucleus. The optical positions are from Gaullouët et al. (1975), Clements (1981, 1983), and Argyle & Eldridge (1990) with the size of the cross representing the uncertainty in their observations. Gaullouët et al. (1975) quote typical position errors of 6 arcsecs and an error of 0.09–0.2 arcsecs is shown by others. The ellipse in the lower left-hand corner of the maps shows the shape of the synthesized beam at half power. The beam size along with the position angle (P.A.), peak surface brightness, RMS noise and contour levels for each map are shown in Table 3.5 (mas-scale maps) and Table 3.6 (arcsec-scale maps). All positions are given in J2000 coordinates (except arcsec-scale maps of Mrk 348, NGC 4151, NGC 5135, and Mrk 926, where B1950 coordinates are shown).

Table 3.7 lists the VLBI observational results. It gives object name, a priori coordinates for the VLBI observations, relative position of the individual components detected with respect to the phase centre, the corresponding flux density, the component size as determined by the model fit, the peak surface brightness in the map, and the total

flux density of the source on mas-scales obtained using a model fit.

Data pertaining to the VLA imaging are given in Table 3.8. Individual columns give name of the object, optical position, radio position of the component, the total flux density of the corresponding component, radio type (as per the definition of Ulvestad & Wilson (1984A)) and the largest angular size of the source.

Figures 3.4 to 3.33: VLA and VLBI images, with the spatial scales in absolute units for VLA maps and in relative units with respect to the phase-centre for the VLBI maps. The sequence of images is ordered in R.A. along with the source descriptions. A cross in the arcsec-scale images marks the position of the optical nucleus with the size of the cross representing the uncertainty in the position. The small ellipse at the corner of the image gives the size (FWHM) of the VLA/VLBI beam. The beam size (FWHM) along with the P.A., peak surface brightness, RMS noise and contour levels for all maps due to our measurements are shown in Table 3.5 (mas-scale maps) and Table 3.6 (arcsec-scale maps). All the maps are ours from the February 1998 data unless otherwise specified. For the maps reproduced from the literature, the figure caption gives its reference, contour levels for each map, beam size (FWHM) along with the position angle (P.A.). All positions in our maps are given in J2000 coordinates.

3.4.2 Description of the sources

Detailed descriptions of the radio structures of the Seyfert galaxies from our sample are as follows. The object's name is followed by its IAU name in each case. The sequence is ordered in R.A. For each source, the first paragraph describes the VLA radio morphology and the second gives VLBI-scale radio morphology. The descriptions of Mrk 231, Mrk 348, Mrk 926, NGC 4151, and NGC 5135, the 5 objects from our sample that were not observed by us, are all gleaned from the literature. We also give the two-frequency spectral index, where measurements are available at similar resolution ($\simeq 1$ arcsec) in the literature (the spectral index α , defined as $S_\nu \propto \nu^{-\alpha}$). We also give the projected linear size of the source (and its reference when not from our measurements) corresponding to the contour size which is 5% of the peak surface brightness. We have ensured that in all cases the 5% contour is well above the noise level in the map. Radio variability of the sources and differing angular resolution of the images used can cause large uncertainties in the calculated spectral indices; we have attempted to use data that were obtained as near in time as possible to ours, and with angular resolution as close as possible to ours when calculating spectral indices using our own data and/or data from the literature.

Mrk 348 (0046+316)

This object was not observed by us.

VLA: The map at 8.4 GHz using VLA *A* array (Figure 3.2) is from Nagar et al. (1999B) and it shows an unresolved object. Unger et al.'s (1984) map at 6 cm using MERLIN shows a triple structure, an unresolved core with low-level emission extending ~ 0.1 arcsec in P.A. $\sim -30^\circ$ and 0.2 arcsec in P.A. 170° (Figure 3.1), which is consistent with the results reported by Neff & de Bruyn (1983) obtained using VLBI. The map of Ulvestad & Wilson (1984B) shows an unresolved object, but their 2 cm map shows the object to be slightly resolved on the 0.2 arcsec scale. The largest angular extent of the source is ~ 0.2 arcsec (Unger et al. 1984).

This source is highly variable and we discuss the radio variability at various resolution scales and epochs. Variability in the flux density was first reported by Sramek & Tovmassian (1974, using NRAO 91 m telescope at 5 GHz) shortly after it was discovered to be a radio source. Such variability provides indirect evidence for the existence of an inverted-spectrum, compact radio core. All available 6 and 21 cms flux densities until 1983 (starting from Aug 1972) were discussed by Neff & de Bruyn (1983). They plotted 6 and 21 cms flux densities and concluded that this object is non-constant. Between 1992 - 1995 the flux density varied by $\sim 60\%$, the flux density at 5 GHz varied by 60% between 1980 and 1983. The object does not show such high flux density variability at 1.5 GHz between 1974 - 1992. We present Table 3.3 giving frequency, peak surface brightness, total flux density, corresponding size of the synthesized beam and epoch of observation along with the reference. We show a plot (Figure 3.3) of the flux density as a function of epoch of observation at these frequencies. The object is unresolved at these scales, thus we use either total (when available) or the peak of surface brightness in the plot.

VLBI: Ulvestad et al. (1999B) used VLBA at 15 GHz to image mas-scale structure of this source at two epochs (Figure 3.2). The VLBA image shows a small-scale double source that is aligned with the larger scale radio emission. The total flux density of 122 mJy at 1997.10 was slightly lower than the flux density of 169 mJy measured at 1995.26 (Barvainis & Lonsdale 1998). Mrk 348 has since undergone a major radio flare, with the flux density of the southern component increasing by a factor of 5.5 between 1997.10 and 1998.75, strongly suggesting

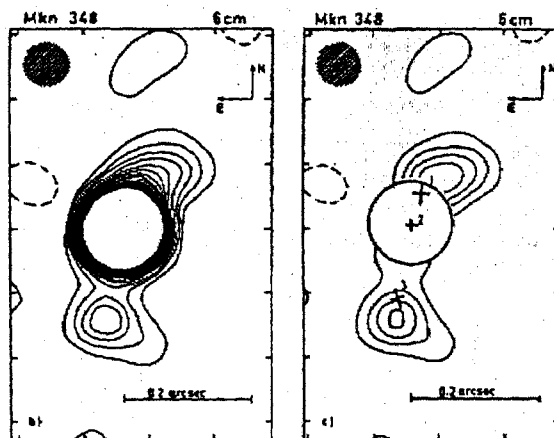


Figure 3.1: 6 cm MERLIN image of Mrk 348 (Unger et al. 1984). “(b)” The angular resolution is 0.07 arcsec, and the contour levels are at -1 and 1% and then at intervals of 1% up to 16% of the peak surface brightness which is 378 mJy per beam. “(c)” 6 cm map of the nucleus of Mrk 348, with a core component subtracted from the map centre. The angular resolution is 0.07 arcsec, and the contour levels are at -20, 20, 40, 60 and 80 per cent of the peak surface brightness which is 21.6 mJy per beam. The crosses labelled 1, 2 and 3 show the positions and half-power sizes of the VLBI components measured by Neff & de Bruyn (1983).

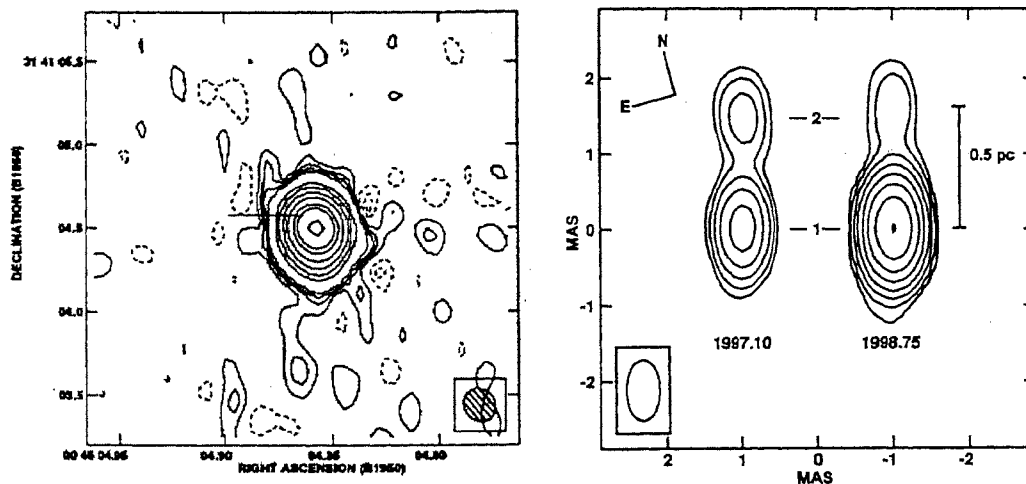


Figure 3.2: 3.6 cm VLA A array (left, Nagar et al. 1999B) image of Mrk 348. the contour levels are at -6, -4, -2, 2, 4, 6, 10, 50, 100, 200 400, 800, 1200 and 2400 times the RMS which is $76 \mu\text{Jy}$; and

15 GHz VLBA (right, Ulvestad et al. 1999B) images of Mrk 348, The images have been rotated by 15° from the cardinal orientation, aligned at the southern radio component, then offset from each other horizontally by 2 mas. Logarithmic contours start at 4 mJy per beam and increase to 512 mJy per beam by factors of 2. The common restoring beam is $0.80 \times 0.45 \text{ mas}^2$ at a P.A. of -15° .

Freq (GHz)	Peak flux density (mJy)	Total flux density (mJy)	Synthesised beam (arcsec)	Epoch of observation	Reference
14.9		565	0.14	Sept 8, 1983	Ulvestad & Wilson 1984A
8.4	310	346	0.28 x 0.20	1995 - 1996	Thean et al. 2000
8.4		238	0.70	Dec 1992 - Feb 1993	Nagar et al. 1999B
5.0		281	3.5 x 6.8	May 1990	Baum et al. 1993
4.9		480	0.40	Sep 8, 1983	Ulvestad & Wilson 1984A
5.0		494	0.07	Sept 1983	Unger et al. 1984
5.0		337	0.07	July 1982	Unger et al. 1984
1.5		302	1.40	Dec 1992 - Feb 1993	Nagar et al. 1999
1.6		260	0.25	July 1982	Unger et al. 1984
1.6		300	0.25	Sept 1980	Unger et al. 1984
1.4		340	25 x 47	Dec 1973 - Jan 1974	Neff & de Bruyn 1983

Table 3.3: Radio variability of Mrk 348.

that it is the galaxy nucleus. The nuclear components are identified by strong variability between epochs, indicating that the double sources represent apparently one-sided jets. The two epoch maps show that the jet has sub-relativistic velocity of $\simeq 0.37c$. The P.A.'s of Unger et al. (1984), and that of the elongated structure seen in the VLBI map are nearly the same, indicating that the kpc-scale and pc-scale elongations have the same axis.

Mrk 1 (0113+328)

VLA: Mrk 1 is a slightly resolved source (Figure 3.4). The total flux density is 27 mJy which is similar to the one presented by Ulvestad et al. (1981) and is less than the value of 38 mJy as found by Sramek & Tovmassian (1975). Ulvestad et al. (1981) suggest that along with an unresolved component there is a faint (~ 2 mJy) extension ~ 0.4 arcsec to the south. The peak of radio surface brightness in our map is displaced from the optical (Clements 1981) nucleus by ~ 1 arcsec and is to the south-west of the optical-core.

VLBI: Unresolved source (Figure 3.4). Kukula et al. (1999) detect a compact radio core surrounded by a halo of emission approximately 100 mas across at 18 cm using the EVN (angular resolution ~ 20 mas). They suggest likely evidence for weak

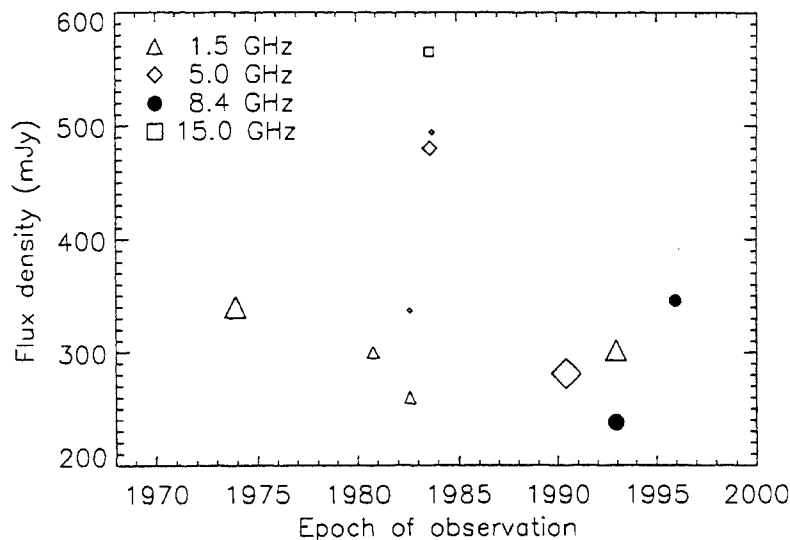


Figure 3.3: Plot showing radio variability of Mrk 348; size of the symbol (scaled as $\{0.5 \times \ln [\text{beam}/0.07] + 0.5\}$) gives the relative resolution of the instrument (larger size of the symbol indicates coarser resolution).

emission extending to the south, perhaps leading into the larger structure (Ulvestad et al. 1981). But, they do not find any evidence for linear structure in this source on scales larger than a few parsec. The maximum extent of the source detected is ~ 30 pc across.

MCG 8-11-11 (0551+464)

VLA: Our map (Figure 3.5) of the source shows a strong nuclear source with the dominant direction for the structure close to it in the north-west (P.A. -45°). It also has extended emission towards the north. The bright core in our map is coincident with the optical (Clements 1981) nucleus, and the total extent of the north-south extension is ~ 3.0 arcsec. The radio image of Schmitt et al. (2000) at 3.6 cm (VLA A array) is similar to ours. The 15 GHz map of Ulvestad & Wilson (1986) resolves the nuclear core into a triple. The largest angular size of the source is ~ 3.5 arcsec.

VLBI: Unresolved source, presumably corresponding to the central compact component in the VLA image (see Figure 3.5). The second weak component shown in the map (if real) has a flux density of ~ 0.6 mJy.

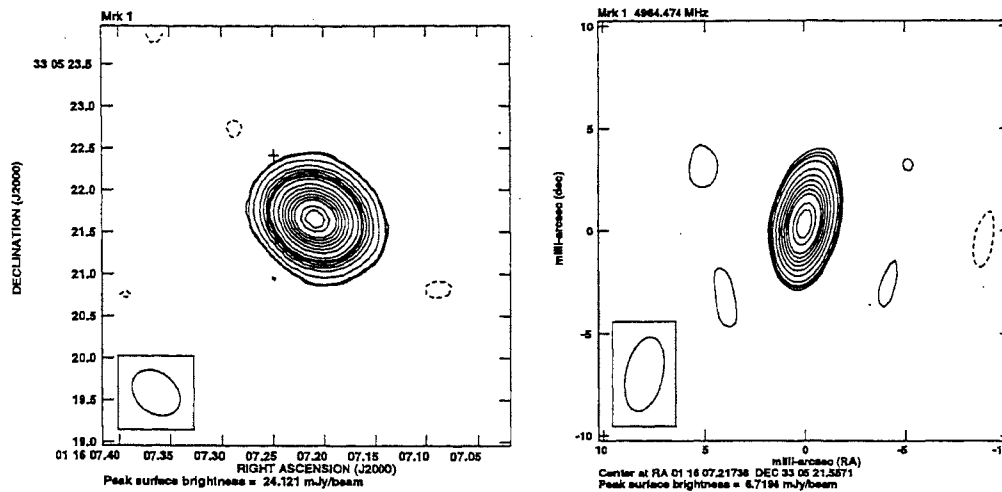


Figure 3.4: 5 GHz VLA (left) and VLBI (right) image of Mrk 1.

NGC 2273 (0645+609)

VLA: Our map (Figure 3.6) has similar features as seen previously by Nagar et al. (1999B) at 8.4 GHz and Ulvestad & Wilson (1984A) at 5 GHz. The source reveals an unequal double with a separation of nearly 1 arcsec at P.A. $\sim -80^\circ$. The 6 cm WSRT image of this source reported by Baum et al. (1993) shows amorphous structure on a larger scale (> 2.5 arcsec). Our core and total flux density for this object are slightly more than that seen in the 6 cm map of Ulvestad & Wilson (1984B) at similar wavelength and resolution. The optical (Argyle & Eldridge 1990) core is ~ 0.6 arcsec east of the peak of radio surface brightness. The largest angular size of the source is ~ 2.3 arcsec.

VLBI: The map (Figure 3.6) is essentially unresolved. There is some evidence from the distribution of CLEAN components for possible weak emission out to ~ 1 mas from the phase center.

Mrk 78 (0737+652)

VLA: Mrk 78 is an extended source and is nearly 4 arcsec on our 5 GHz map (Figure 3.7). The bright core is resolved and is coincident with the optical (Clements 1981) nucleus. The second peak of the surface brightness is nearly 2 arcsec away to the west (P.A. $\sim -90^\circ$). The brighter component seems to show an extension

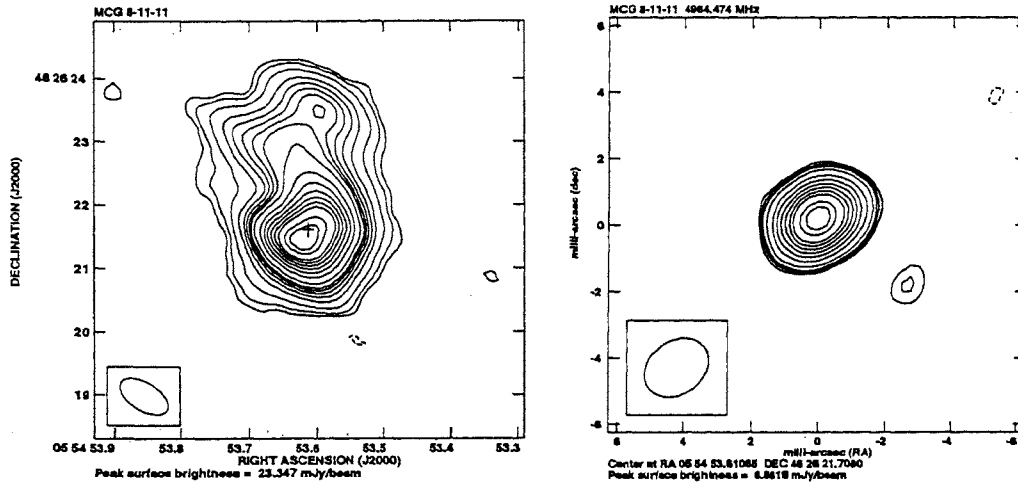


Figure 3.5: 5 GHz VLA (left) and VLBI (right) image of MCG 8-11-11.

towards east (P.A. $\sim 80^\circ$). This extension towards east is displayed more clearly in Figure 3.8 which is a map made with a restoring beam that is half the size of the synthesized beam size and same P.A. The largest angular size of the source is ~ 3.9 arcsec.

VLBI: Our map (Figure 3.7) shows faint extension towards the south-west direction (P.A. $\sim -130^\circ$). The extension is more prominent in the map made with a restoring beam that is half the synthesized beam size and of same P.A. (Figure 3.8). The distribution of the CLEANed components shows a triple component source which is also shown by the model-fit. Model-fit shows that the two components other than the detected bright component are point-like (component size $< 0.5 \times 0.5$ mas²).

Mrk 1218 (0835+250)

VLA: Although this object has been observed in the past by Ulvestad (1986) at 6 cm (VLA *A* array) and 20 cm (VLA *B* array), the map was never published. Our map (Figure 3.9) of this source shows diffuse extensions on fainter levels ($\sim 2\sigma$) along the north-west direction at a P.A. of $\sim -45^\circ$. The total flux density of the source is dominated by the bright core, which is coincident with the optical nucleus (Clements 1983) within the errors. The total flux density of 25.5 mJy measured by us is consistent with the value of 23.0 mJy published previously (Ulvestad

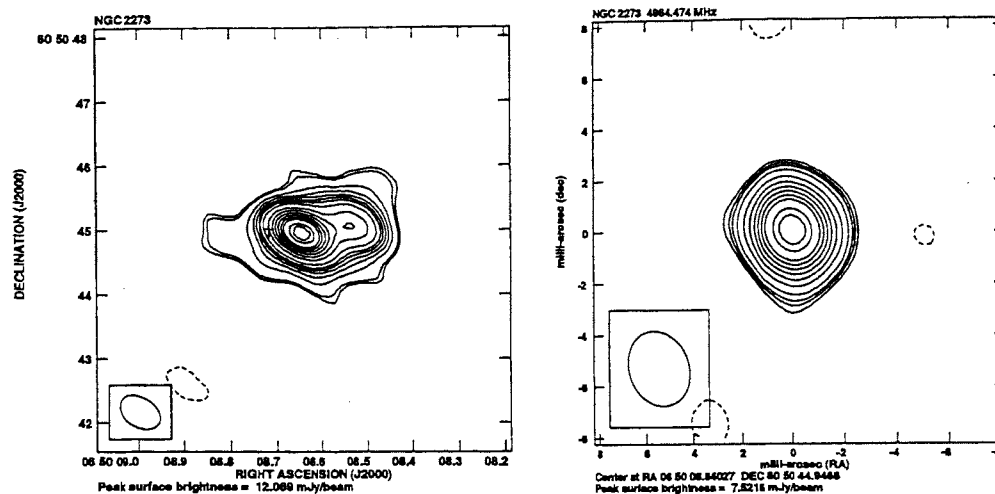


Figure 3.6: 5 GHz VLA (left) and VLBI (right) image of NGC 2273.

1986). The radio spectral index for the source using observations made by us and Ulvestad (1986) at 20 cm, $\alpha_{20 \text{ cm}}^6$ is 0.8. The largest angular size of the source is ~ 1.3 arcsec.

VLBI: The map (Figure 3.9) of this object shows a bright component and faint extensions ~ 4 mas from the peak surface brightness position possibly aligned with the arcsec-scale structure.

NGC 2639 (0840+503)

VLA: This, much studied object is a triple with a bright central core (Ulvestad & Wilson 1989, Figure 3.11). Our map (Figure 3.10) does not resolve the triple structure and as in Ulvestad & Wilson (1989) the peak of radio surface brightness lies to the south-east of the optical core (Argyle & Eldridge 1990). The flux density of this object is presently rising (Wilson 1999, private communication). The spectral index for the source using observations made by Thean et al. (2000) and Ulvestad & Wilson (1989) is $\alpha_{20 \text{ cm}}^6 = 0.5$. The largest angular extent of the source is ~ 1.7 arcsec (Ulvestad & Wilson 1989).

VLBI: The map of the object is shown in Figure 3.10. The two-component model fit suggests that there is a jet towards the east (P.A. $\sim 90^\circ$). The main component consists of almost $\sim 80\%$ of the total detected flux density. Our model fitting

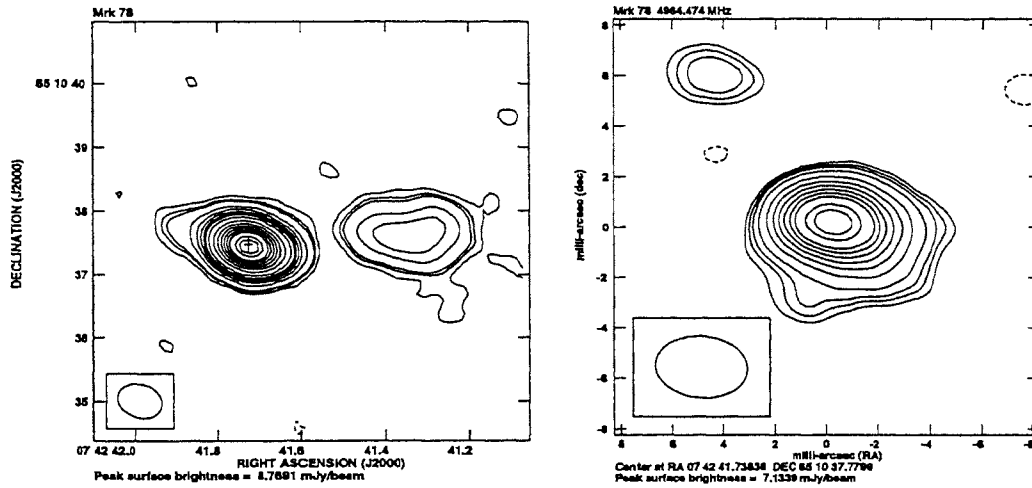


Figure 3.7: 5 GHz VLA (left) and VLBI (right) image of Mrk 78.

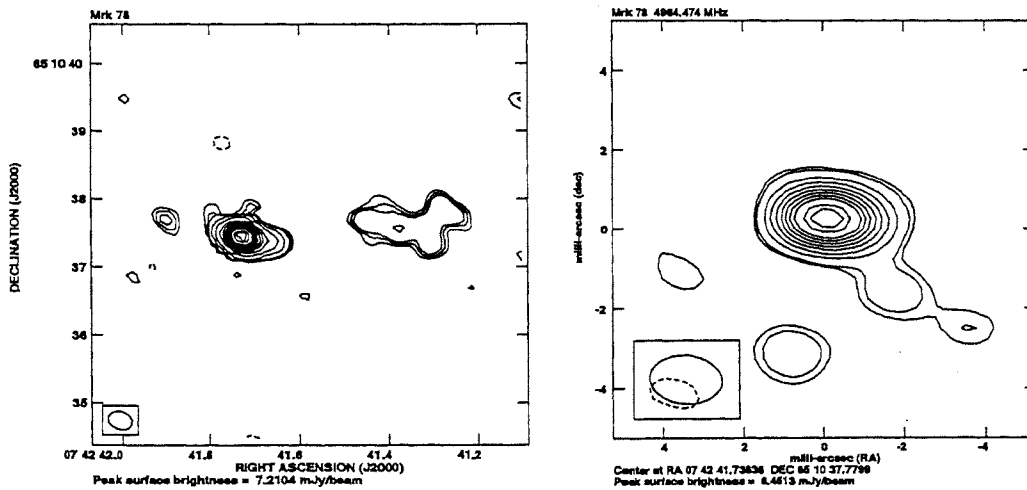


Figure 3.8: 6 cm VLA (left) image of Mrk 78, the contour levels are at -1.2, 1.2, 1.6, 2, 4, 8, 16, 24, 32, 40, 48, 56, 64, 80, 90 times $72.1 \mu\text{Jy}$ per beam. The restoring beam is 0.35×0.26 at a P.A. of $71^\circ.64$; and

6 cm VLBI (right) image of Mrk 78, the contour levels are at -6, 6, 8, 16, 24, 32, 40, 48, 56, 64, 80 and 90 times $64.5 \mu\text{Jy}$ per beam. The restoring beam is $1.81 \times 1.22 \text{ mas}^2$ at a P.A. of 85° .

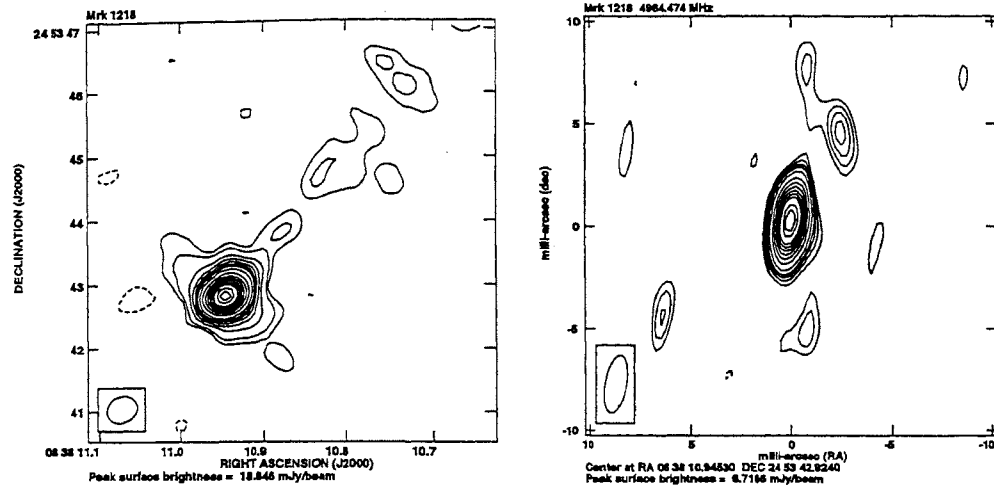


Figure 3.9: 6 cm VLA (left) and VLBI (right) image of Mrk 1218.

gives a flux density of 31.6 and 8.0 mJy for the two detected components. The flux density of the detected bright component (31.6 mJy, $0.05 \times 0.05 \text{ mas}^2$ beam size) is less than the 47 mJy (47 mJy, $2.0 \times 1.7 \text{ mas}^2$ beam size) detected by Wilson et al. (1998), but is higher than the early VLBI measurements of Hummel et al. (1982), which is 27 mJy.

NGC 4151 (1208+396)

This object was not observed by us.

VLA: This, much studied object has a total flux density of ~ 125 mJy at 6 cm (Johnston et al. 1982). The Figure 3.12 is due to the observations of Pedlar et al. (1993) using VLA at 5 GHz. The source contains multiple compact radio components. The main structure is elongated, oriented in P.A. 75° , and extending 4.0 arcsec on either side of a bright central component whose position coincides well with the position of the nucleus determined from optical studies (Pedlar et al. 1993). The A configuration VLA image of Kukula et al. (1995) shows 5 bright compact components embedded in a 4 arcsec jet. The total flux densities contained in Johnston et al.'s (1982) 20 and 6 cm maps are 330 and 120 mJy, respectively, giving an integrated spectral index, $\alpha_{20 \text{ cm}}^{6 \text{ cm}}$, of 0.8. The radio structure of this object on many resolution scales is discussed in more detail by Ulrich (2000) and references therein. The largest angular size of the source is ~ 3.3 arcsec (Kukula et al. 1995).

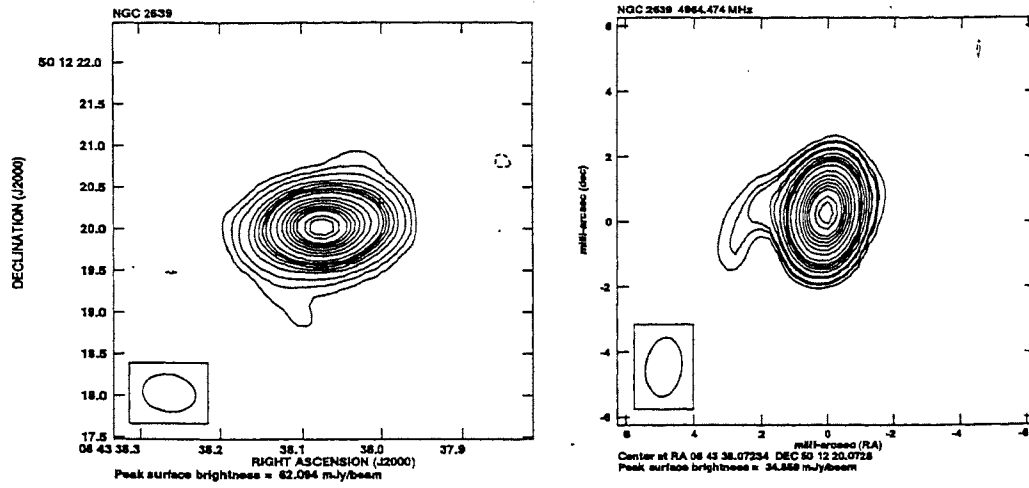


Figure 3.10: 6 cm VLA (left) and VLBI (right) image of NGC 2639.

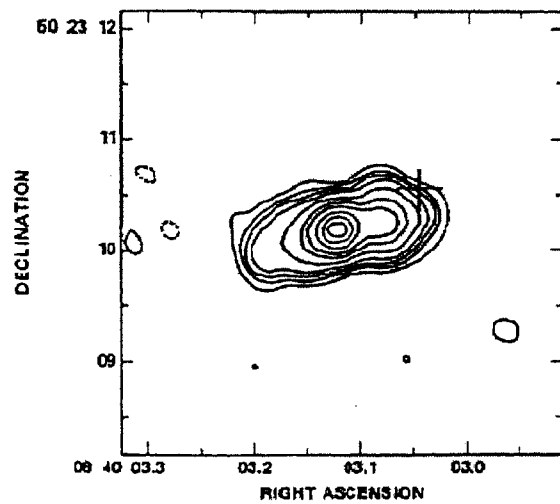


Figure 3.11: 6 cm VLA image of NGC 2639 (Ulvestad & Wilson 1989), the contour levels are at -1, 1, 2, 3, 5, 10, 20, 30, 50, 70 and 90 per cent of the peak surface brightness which is 23.4 mJy per beam. The restoring beam is $0.30 \times 0.29 \text{ arcsec}^2$ at a P.A. of 43° .

VLBI: This object was first observed using EVN by Preuss & Fosbury (1983), and recently by Ulvestad et al. (1998B) using VLBA at wavelengths of 6 and 18 cms. Ulvestad et al. (1998B) detects four radio components, spread over $\simeq 0.5$ arcsec (Figure 3.12). The easternmost pair comprises of a bright component elongated in P.A. $\simeq 20^\circ$ (component E, see 18 cm map in the same Figure (3.12)) and an extension to the north-east (component F) which curves in P.A. 75° , similar to that of the 3.5 arcsec scale radio jet and the NLR. Only component E is detected at the high resolution (mas-scales) achieved at 6 cm. This 6 cm source consists of approximately 5–6 local maxima, strung together like a linear radio source over an angular distance of 13 mas. This source has a length/width ratio of ≥ 4 , and therefore fulfills one of the classical criteria for a radio jet (Bridle & Perley 1984). Component E appears to be only part of the radio emission that contains a significant flat-spectrum component, and the central brightest unresolved sub-component of E is favoured as the optical nucleus. The peak surface brightness of 2.5 mJy/beam corresponds to a brightness temperature of 3.2×10^7 K, and all the detected components have comparable flux densities.

Mrk 766 (1215+300)

VLA: This source is essentially unresolved in our map (Figure 3.13) at 6 cm but seems to be having a weak halo-like structure. Whereas Ulvestad & Wilson (1984A) using VLA A array at 6 cm (Figure 3.14) find it to be slightly resolved showing bulk of the extended emission to lie slightly north of the bright component, and they derive a linear size of ~ 100 pc. We detect a flux density of 15 mJy which is similar to that found by Ulvestad & Wilson (1984A) at 6 cm. The peak of radio surface brightness and the optical (Clements 1981) core register well within the error-bars. The spectral indices for this source using our observations along with observations made in the past (Kukula et al. 1995 and Ulvestad & Wilson 1989) are $\alpha_{20\text{ cm}}^6 = 0.8$, and $\alpha_{6\text{ cm}}^{3.6} = 1.1$.

VLBI: The slightly resolved map (Figure 3.13) shows weak extensions towards the south (P.A. $\sim 160^\circ$).

Mrk 231 (1254+571)

This object was not observed by us.

VLA: This object has been observed often and the most recent description of this source is presented by Ulvestad et al. (1999A and 1999B). To summarise the results of

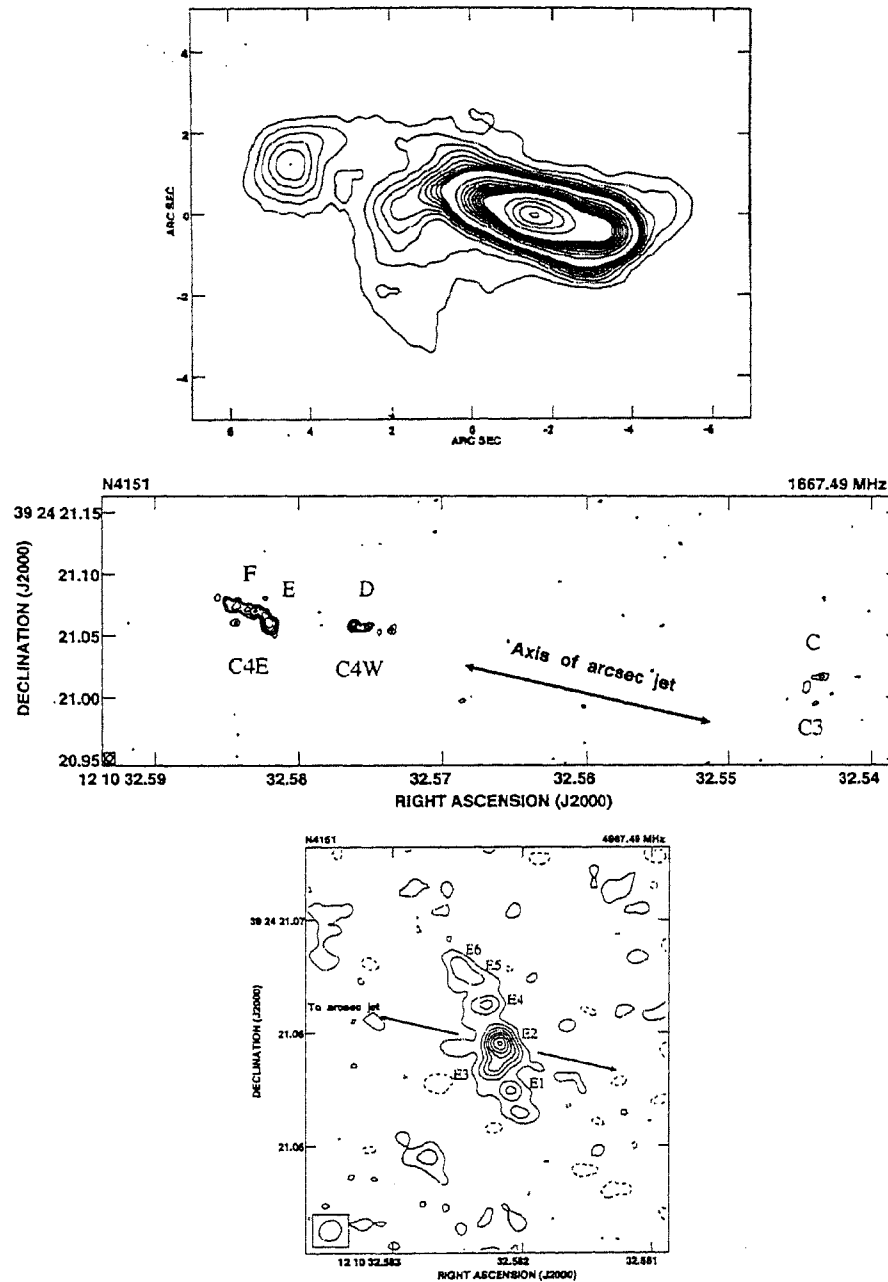


Figure 3.12: 5 GHz VLA (upper, Pedlar et al. 1993) image of NGC 4151, the resolution is $0.85 \times 0.67 \text{ arcsec}^2$ (P.A. 75°), and contour levels are 0.1, 1 and 10 mJy per beam in the ranges -0.1 to 1, 1 to 10, and 10 to 50 mJy per beam;

18 cm VLBA (middle, Ulvestad et al. 1998B) image of NGC 4151, contour levels are at logarithmic intervals of 1.7, beginning at 0.5 mJy. The peak surface brightness is 6.9 mJy per beam. The restoring beam is $5.8 \times 4.8 \text{ mas}$ in P.A. -39° ; and

6 cm VLBA (lower, Ulvestad et al. 1998B) image of NGC 4151, contour levels are linear, from 0.3 to 2.4 mJy per beam, with the dashed contour representing -0.3 mJy per beam. The restoring beam is $2.1 \times 1.8 \text{ mas}^2$ in P.A. -67° . The P.A. of the arcsec-scale jet is shown by arrows.

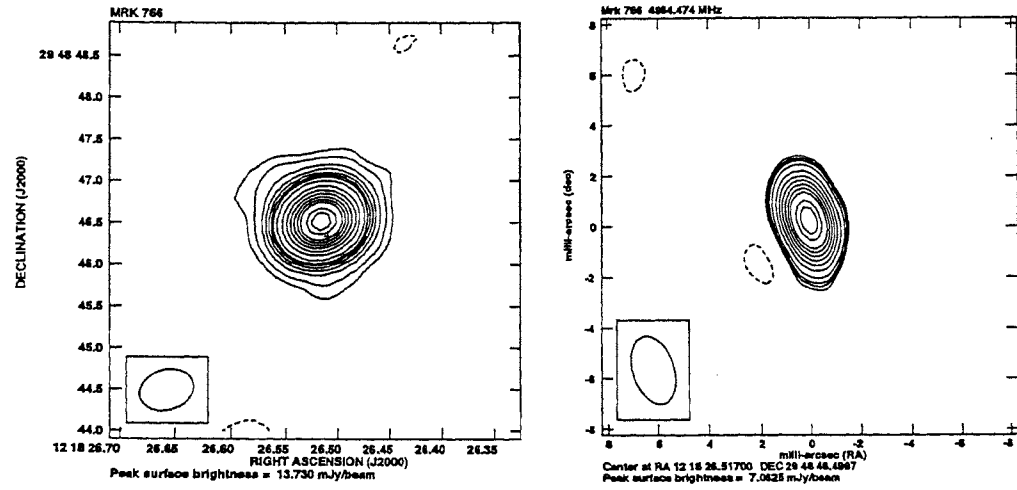


Figure 3.13: 6 cm VLA (left) and VLBI (right) image of Mrk 766.

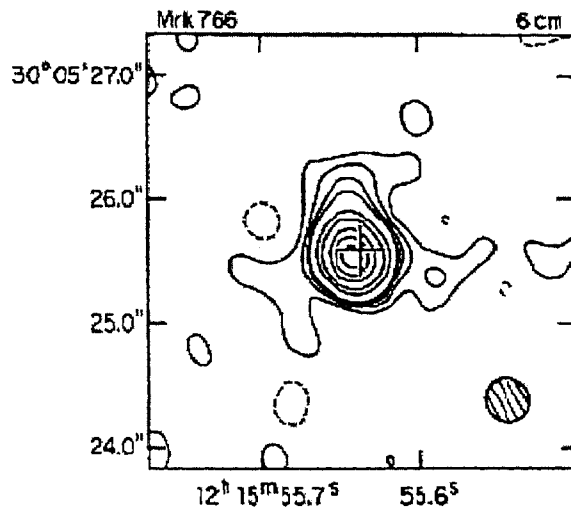


Figure 3.14: 6 cm VLA image of Mrk 766 (Ulvestad & Wilson 1984A), the contour levels are at -2.5, 2.5, 5, 7.5, 10, 20, 30, 50, 70 and 90 per cent of the peak surface brightness which is 10.4 mJy per beam. The restoring beam is $0.36 \times 0.34 \text{ arcsec}^2$ at a P.A. of 27° .

Ulvestad et al. (1999A) ($\nu = 5$ GHz, synthesised beam size of 4 arcsec (FWHM)), the core has a flux density of 343 mJy and the faint extended emission to the south is 12 mJy. Kukula et al.'s (1995) observations at 8.4 GHz (Figure 3.16) using VLA *A* array shows the object to be unresolved with no evidence for extended emission on intermediate scales. The spectral index of the extended emission is steep, both in total flux density and in a point-by-point comparison. The spectral index of the total emission is ~ 1.1 between 1.5 and 4.9 GHz. The total spectral index of the extended emission between 4.9 and 15.0 GHz is > 0.8 .

This object also shows variability. In the Table 3.4 we present the peak surface brightness, total flux densities measured by various groups in the past at various frequencies and resolutions. Neff & Ulvestad (1988) found this object to be a variable radio source with variations usually of 10% - 20% over time-scales of months. The object shows very high ($> 400\%$) radio flux density variability at 1.5 GHz, it does not show such high variations at 15 GHz. At 8.4 GHz the flux density decreased from ~ 230 mJy to a low of ~ 180 mJy and increases to ~ 200 mJy in a span of 5 years. At 5.0 GHz, the flux density almost doubles from ~ 150 mJy to ~ 280 mJy in 2 - 3 years of time and then onwards the flux remains almost constant. The flux density at 22.0 GHz drops by a factor of 2 in few years at two occasions. We present Table 3.4 giving frequency, peak surface brightness, total flux density, corresponding size of the synthesized beam, and epoch of observation along with the reference. We also show a plot (Figure 3.15) of the flux density as a function of epoch of observation at these frequencies. The object is unresolved at these scales, thus we use either total (when available) or the peak of surface brightness in the plot.

Ulvestad et al. (1999A) also presented a result from the long observation of the source at 1.4 GHz made with the phased-VLA in 1996 December. They also imaged the source in linear polarised intensity (Figure 3.17). They found that some regions of the diffuse emission to the south (~ 26 arcsec) of the VLA core are significantly polarized, reaching a peak polarized intensity of $185 \mu\text{Jy beam}^{-1}$. At this polarization peak, the percentage of polarization is $\sim 57\%$ and χ is $\sim 15^\circ$. The VLA core is less than 0.1% linearly polarized.

VLBI: The VLBA and VLA observations for this source are discussed in great detail by Taylor et al. (1999), Ulvestad et al. (1999A), Ulvestad et al. (1999B), and Lonsdale et al. (1993). Ulvestad et al.'s (1999B) VLBA, 15 GHz two epoch images (Figure 3.17) show a double source with P.A. differing by about 65° from the

Freq (GHz)	Peak FluxDensity (mJy)	Total FluxDensity (mJy)	Synthesised beam (arcsec)	Epoch of Observation	Reference
22.2	62		0.08	1996 Dec	Ulvestad et al. 1999A
22.2	136		0.30	1995 Nov	Ulvestad et al. 1999A
22.5		82	0.075	1983 Nov	Neff & Ulvestad 1988
20.0		123	94.0	1983 July	Edelson 1987
15.0	112		0.14	1996 Dec	Ulvestad et al. 1999A
15.0	135		0.40	1995 Nov	Ulvestad et al. 1999A
15.0		134	0.11	1983 Nov	Neff & Ulvestad 1988
8.4	203		0.24	1996 Dec	Ulvestad et al. 1999A
8.4	179		0.70	1995 Nov	Ulvestad et al. 1999A
8.4		225.33	2.30	1992 April	Kukula et al. 1995
8.4	211.78	234.45	0.29 x 0.25	1991 June	Kukula et al. 1995
4.9	270		0.40	1996 Dec	Ulvestad et al. 1999A
4.9	254		1.20	1995 Nov	Ulvestad et al. 1999A
4.9	4.2		7.0 x 8.3	1991 May	Baum et al. 1993
4.9		278	14.0	1983 July	Edelson 1987
5.0	155	170	2.3 x 2.3	1979/1980	Ulvestad et al. 1981
1.4	231		1.40	1996 Dec	Ulvestad et al. 1999A
1.4	241		3.90	1995 Nov	Ulvestad et al. 1999A
1.6		115	0.004	1991 Sept	Smith et al. 1998B
1.4		318.0	12.5 x 14.9	1985 Oct	Baum et al. 1993
1.6		76	0.036	1983 Oct	Neff & Ulvestad 1988
1.5		255	44.00	1983 July	Edelson 1987
1.4	210	260	25.0 x 47.0	1974 Aug - Nov	de Bruyn & Wilson 1976

Table 3.4: Radio variability of Mrk 231.

larger scale source. From the variability of the weaker component by a factor of 2.5 between epochs (1996.94 and 1998.71), authors suggest that the weaker, north-eastern component is the actual nucleus of the galaxy. The 5 GHz map (Figure 3.16) of Ulvestad et al. (1999A) obtained with VLBA shows north-south triple structure. The triple source consists of a resolved central component, together with two faint unresolved lobes. The approximate size of the triple source is 50 mas. The brightness temperature of the core is $\sim 3 \times 10^9$ K.

This object is also observed at slightly lower resolution by Kukula et al. (1999) at 18 cm using EVN. In their map the diffuse “disk” emission is resolved out, leaving only the nuclear source.

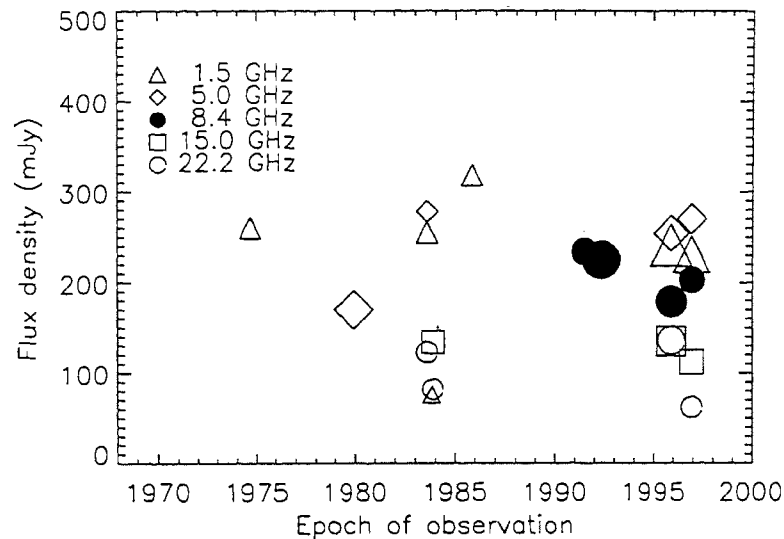


Figure 3.15: Plot showing radio variability of Mrk 231; size of the symbol (scaled as $\{0.5 \times \ln [\text{beam}/0.004] + 0.5\}$) gives the relative resolution of the instrument (larger size of the symbol indicates coarser resolution).

NGC 5135 (1322-295)

This is the only source in the sample not observed by us (due to insufficient observing time).

VLA: Ulvestad & Wilson's (1989) map shows an asymmetric structure at both 6 cm and 20 cm, with faint emission extending to the north-east of the peak of surface brightness. But, Thean et al.'s (2000) observation do not detect radio emission from the nucleus at 8.4 GHz; instead they detect a weak component with a flux density of 2.33 mJy which is not related to the active nucleus. Therefore the authors (Thean et al. 2000) agree with the suggestion made by Wynn-Williams & Becklin (1993) that most of the radio emission emanates from the structures on either side of the nucleus rather than from the nucleus itself. The 6 cm, VLA *A* array map (Figure 3.18) of Ulvestad & Wilson (1989) gives an overall linear extent ~ 9.0 arcsec (3.6 kpc). Although the optical core (Gaulouët et al. 1975) is to the north-east of the peak of radio surface brightness and is off by ~ 3 arcsec, the peak radio surface brightness is within the error-bars of optical core. The largest angular size of the source is ~ 7.1 arcsec (Ulvestad & Wilson 1989).

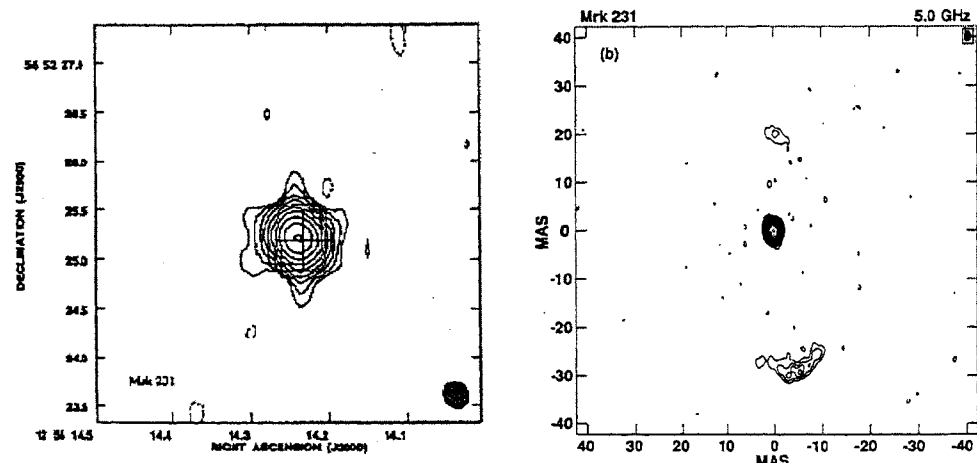


Figure 3.16: 8.4 GHz VLA image of Mrk 231 (left, Kukula et al. 1995), the contour levels are at $-0.2, 0.2, 0.4, 0.8, 1.6, 3.2, 6.4, 12.8, 25.6, 51.2$ and 102.4 times 2.0 mJy. The restoring beam is 0.294×0.246 arcsec² at a P.A. of $19^\circ.6$.

5 GHz VLBA (right, Ulvestad et al. 1999A) image of Mrk 231, the contour levels are plotted at $250 \mu\text{Jy}$ per beam times $-4, -3, -2, -1, 1, 2, 3, 4$, with higher levels spaced by factors of $2^{1/2}$. Restoring beam is 2.08×1.47 mas² in P.A. $-12^\circ.5$.

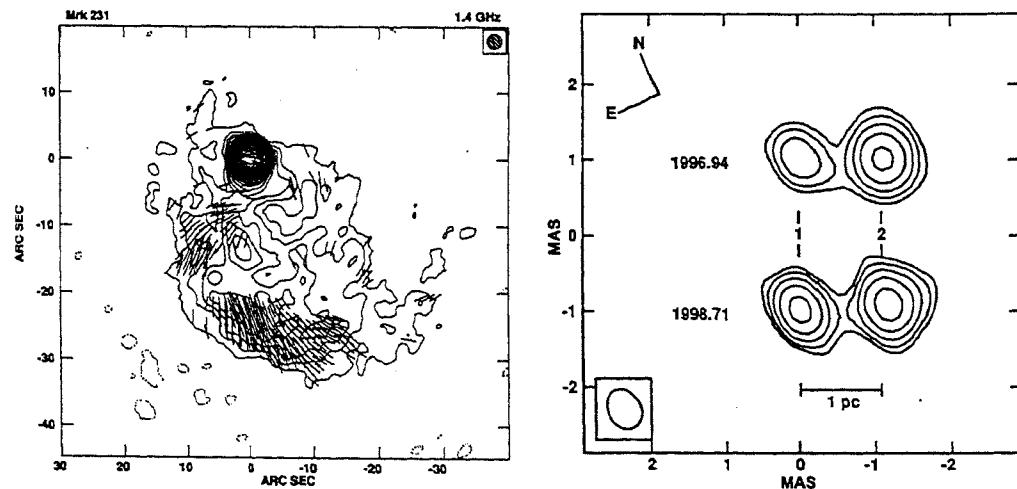


Figure 3.17: CLEANed VLA image of Mrk 231 (left, Ulvestad et al. 1999A) of Stokes I and frequency 1.4 GHz. Peak intensity is 231.4 mJy beam⁻¹, the contour levels are plotted at $80 \mu\text{Jy}$ per beam times $-4, -3, -2, -1, 1, 2, 3, 4$, with higher levels spaced by factors of $2^{1/2}$. Line lengths represent linearly polarized intensity P (1 arcsec is $36 \mu\text{Jy}$ per beam), and line orientations represent electric fields P.A. χ .

15 GHz VLBA images of Mrk 231 (right, Ulvestad et al. 1999B), the images have been rotated by 25° from the cardinal orientation, aligned at the north-eastern radio component, then offset from each other horizontally by 2 mas. Logarithmic contours start at 2 mJy per beam and increase to 32 mJy per beam by factors of 2 . The common restoring beam is 0.55×0.42 mas² at a P.A. of 0° .

VLBI: This object was observed by Roy et al. (1994) at 2.3 GHz with the 275 km long, single-baseline, the PTI. They did not detect the source and quote an upper limit of < 5.0 mJy (5σ).

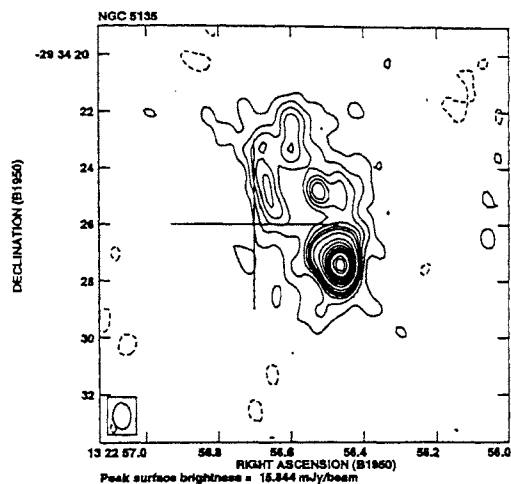


Figure 3.18: 5.0 GHz VLA image of NGC 5135 (Ulvestad & Wilson 1989) the contour levels are at -2, 2, 4, 6, 8, 10, 12, 16, 24, 32, 40, 48, 56, 64, 80 and 90 per cent of the peak surface brightness which is 16.2 mJy per beam. The restoring beam is 0.92×0.62 arcsec² at a P.A. of $2^\circ.1$.

Mrk 477 (1439+537)

VLA: The source in our map (Figure 3.19) is unresolved, whereas Ulvestad et al. (1984A) found it to be slightly resolved in their observations at the same frequency and at nearly similar resolution (Figure 3.20). The core in their map shows extensions in several different P.A. Our total flux density is consistent with theirs within the error-bars, and $\sim 90\%$ of the total flux density is in the unresolved core.

VLBI: Our radio map shows that the object is nearly unresolved with some evidence for weak halo-like emission.

NGC 5929 (1524+418)

VLA: The central component of this triple source (Su et al. 1996, Figure 3.22; VLA A array at 8.4 GHz) is not delineated in our map (Figure 3.21). It has a flat

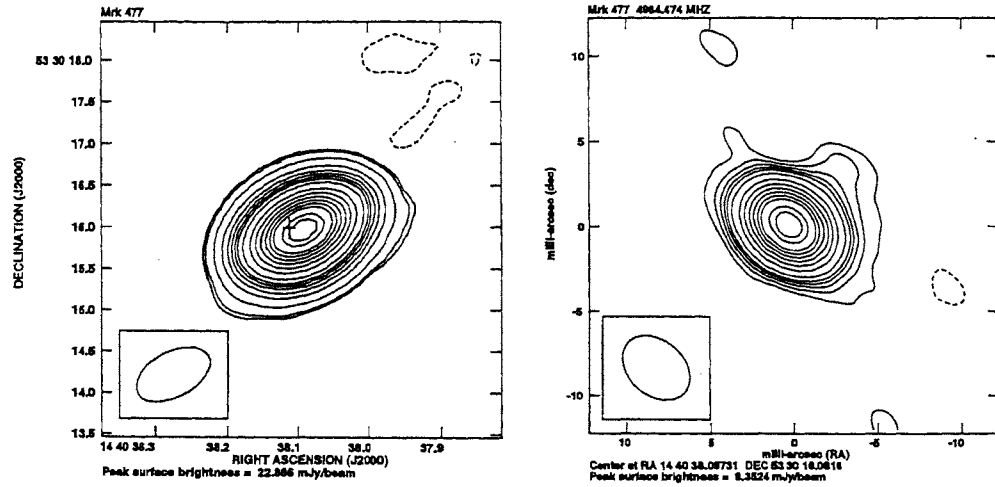


Figure 3.19: 5 GHz VLA (left) and VLBI (right) image of Mrk 477.

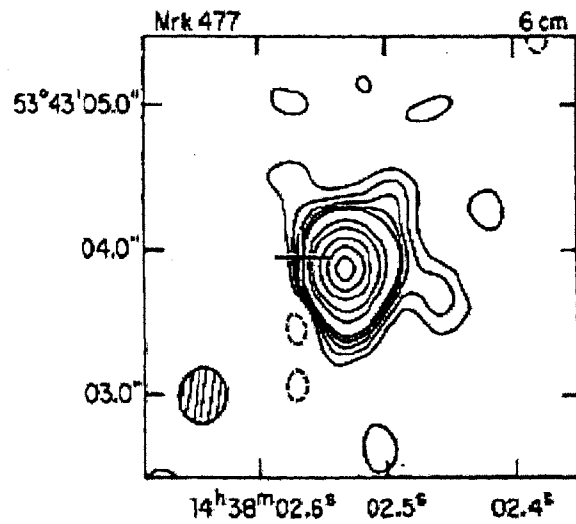


Figure 3.20: 6 cm VLA image of Mrk 477 (Ulvestad & Wilson 1984A), the contour levels are at -2, 2, 4, 6, 8, 10, 20, 30, 50, 70 and 90 per cent of the peak surface brightness which is 18.3 mJy per beam. The restoring beam is 0.39×0.33 arcsec² at a P.A. of 172°.

spectrum (Su et al. 1996 (Figure 3.22), Kukula et al. 1995, and Wilson & Keel 1989) and is close to the position of optical nucleus; hence is likely to be a core. Between 1.6 and 15 GHz measurements, the components appear to follow a simple power law. The north-east and the south-west radio components have steep spectral indices of 0.9 and 0.8 respectively, whereas the central component has a much flatter spectrum with a spectral index of 0.3 (Su et al. 1996). We also detect 8 mJy flux density from the unresolved neighboring galaxy, NGC 5930 (Figure 3.22), as reported by Kukula et al. (1995) using VLA *C* configuration data at 8.4 GHz. The largest angular size of the source is ~ 2.0 arcsec (Kukula et al. 1995).

VLBI: A compact source is detected showing slight signs of extension along P.A. $\sim 50^\circ$ (Figure 3.21). The second weak component obtained due to our model fit is point-like located to the north-east (~ 3 mas) of the bright component. Using the core spectral index, $\alpha_{2\text{ cm}}^{18} \sim 0.32$ (Su et al. 1996), the core should have flux density of 1.1 mJy at 5.0 GHz. We detect a total flux density of 6.8 mJy (sum of the two components < 4 mas across), we therefore conclude that the detected components on mas-scales correspond to one of the two steep spectrum components of the triple (Su et al. 1996) and not to the core. We have tried to map a larger field to detect the second steep-spectrum radio component, but we could not find any; however this does not rule out the possibility of the presence of a second VLBI component coincident with the far-off steep-spectrum lobe. With our data, it might be difficult to detect the effect of the second component because the spacing between the two (~ 1.3 arcsec, Su et al. 1996) will lead to extremely rapid variations in the amplitudes and phases, which may not be possible to trace with our “snapshot” (u, v) (time) coverage. Presently we feel that our data do not rule out the presence of a second component. It will be impossible to reliably image both components in a single map or to model fit the data with a double model to get parameters for both components as the expected variations in the visibilities are too rapid compared to the time coverage of our data.

NGC 7212 (204+095)

VLA: Our map of NGC 7212 (Figure 3.23) does not resolve the compact double source separated by 0.7 arcsec in the north-west direction as clearly as 8.4 GHz, VLA *A* array map of Falcke et al. (1998) (Figure 3.24). However, we see an obvious

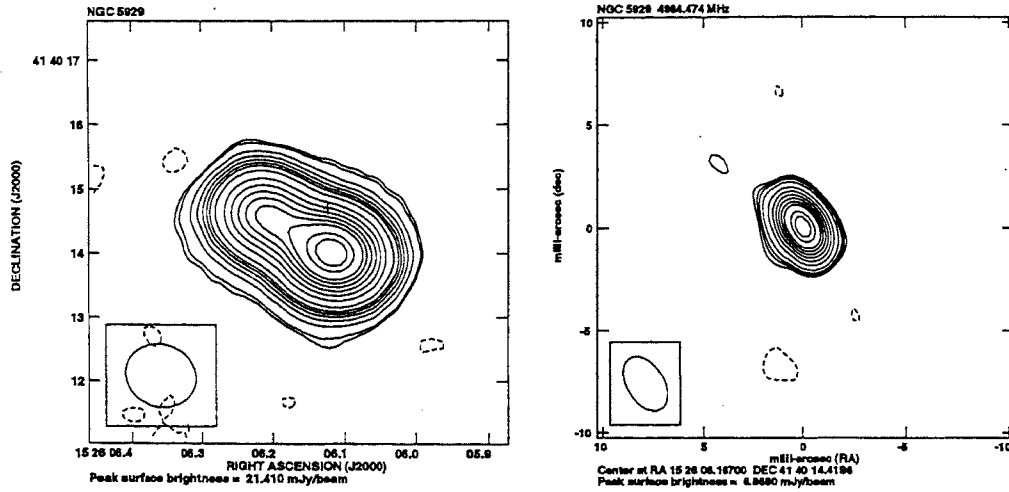


Figure 3.21: 6 cm VLA (left) and VLBI (right) image of NGC 5929.

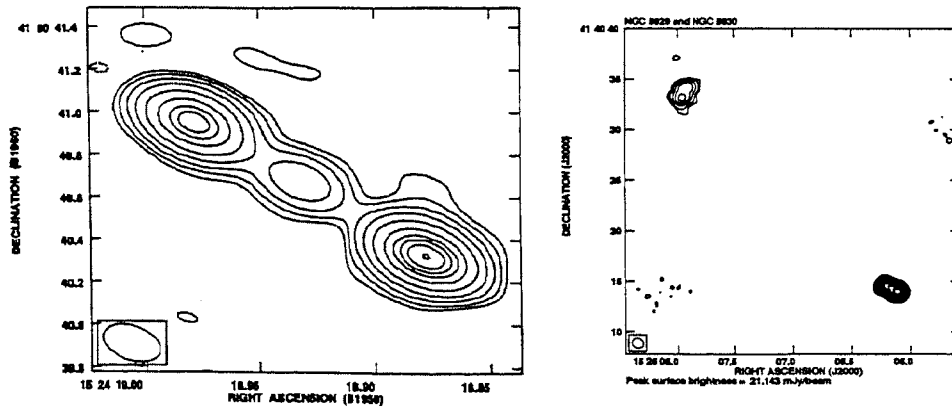


Figure 3.22: 8.4 GHz VLA image of NGC 5929 (left, Su et al. 1996). The image is restored with a 0.298×0.159 arcsec² beam (P.A. 74°). The contours levels are -2, -1, 1, 2, 4, 8, 16, 32, 50, 64, 80 and 99 per cent of the peak surface brightness, which is 6.9 mJy per beam.

Our 5 GHz map of NGC 5929 and NGC 5930 (right), the contours levels are -2.8, 2.8, 4, 6, 8, 10, 12, 16, 24, 32, 40, 48, 56, 64, 80, and 90 per cent of the peak surface brightness, which is 21.1 mJy per beam. The restoring beam is 1.16×0.98 arcsec² (P.A. $75^\circ.36$).

extension towards the north (P.A. $\sim 10^\circ$). Falcke et al. (1998, using VLA *A* array at 8.4 GHz) reported that the peak of surface brightness is offset, by almost ~ 1.0 arcsec to the east of the optical (Clements 1983) nucleus; instead, we see an offset of almost ~ 8.0 arcsec to the east of the same optical nucleus. The origin of this offset between our map and the map of Falcke et al. (1998) is not clear, though it is likely to be associated with the different phase calibrators used in the two sets of radio observations. Since the structures seen in the two maps are otherwise consistent, we believe the structure in our VLA image to be reliable, though the absolute position is likely to be offset from its true value.

We also see faint emission ~ 14 arcsec away towards the north-east of the main structure (Figure 3.24). The largest angular size of the source is ~ 3 arcsec.

VLBI: Our map (Figure 3.23) shows a weak secondary in the south-west direction (P.A. $\sim -110^\circ$). In addition, there is some extension towards north-south.

Ark 564 (2240+294)

VLA: Although our map (Figure 3.25) does not clearly resolve the triple radio source extending up to 320 pc along the P.A. = 6° seen by Schmitt et al. (2000; 8.4 GHz, VLA *A* array), it is extended in the direction of this structure. In our map the bright peak of radio surface brightness is close to the optical core (Clements 1981) within the errors. The total flux density at 6 cm is similar to what was quoted by Ulvestad et al. (1981) within the error-bars. The P.A. of the source is $\sim 0^\circ$.

VLBI: Our map (Figure 3.25) shows elongation along P.A. $\sim 110^\circ$, with 4 components each with flux density > 1 mJy. The brightest component (~ 3 mJy) is at the phase centre. Although the map shows multiple components, the visibilities are too sparse in the (u, v) plane to give us any good multiple component model fit. Our flux density is determined using a single component fit to the data.

NGC 7469 (2300+086)

VLA: The high resolution, high dynamic range map (Figure 3.27, VLA *A*, 6 cm) for this source was presented by Wilson et al. (1991). Their 6 cm radio map is dominated by a strong compact source coincident with the Seyfert nucleus. This source is extended by ~ 0.2 arcsec in P.A. = 101° on the 6 cm map and by ~ 0.1 arcsec in P.A. = 85° on the 2 cm map. They also determine the spectral index to be, $\alpha_{6\text{ cm}}^2 = 0.87$. Our map (Figure 3.26) also shows the object to have a bright core

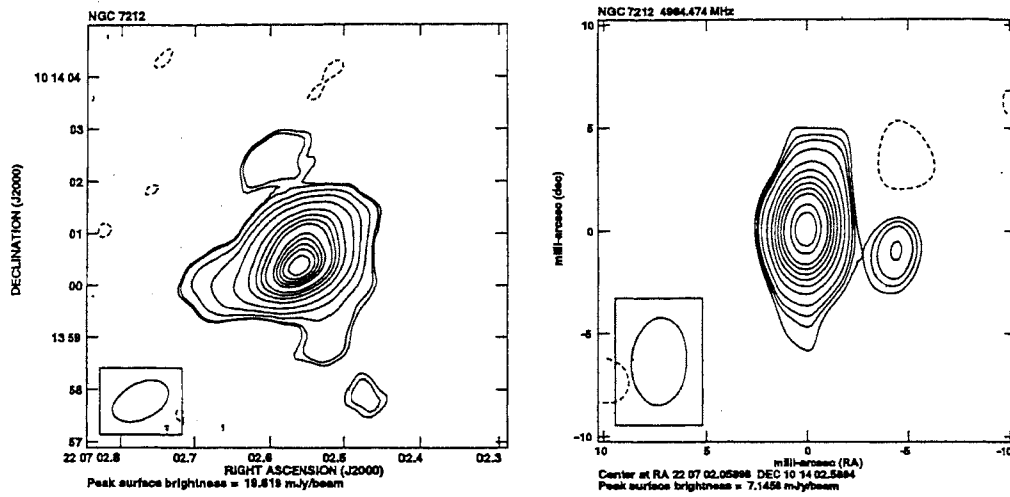


Figure 3.23: 5 GHz VLA (left) and VLBI (right) image of NGC 7212.

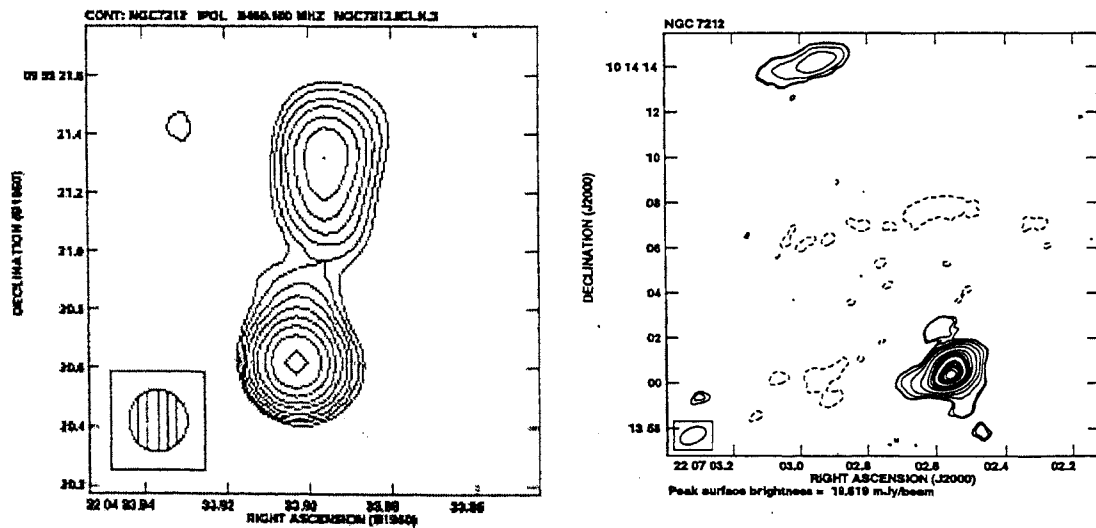


Figure 3.24: 3.5 cm VLA image of NGC 7212 (left, Falcke et al. 1998) with 0.21 arcsec beam. The peak surface brightness is 9.0 mJy per beam and contours are plotted at -1.4, -1, 1, 1.4, 2, 2.8, 4, 5.6, 8, 11, and 16 times 0.5 mJy per beam.

5 GHz VLA map of NGC 7212 (right), contours are plotted at -0.8, 0.8, 1, 2, 4, 8, 16, 24, 32, 40, 56, 64, 72, 80, and 90% peak surface brightness

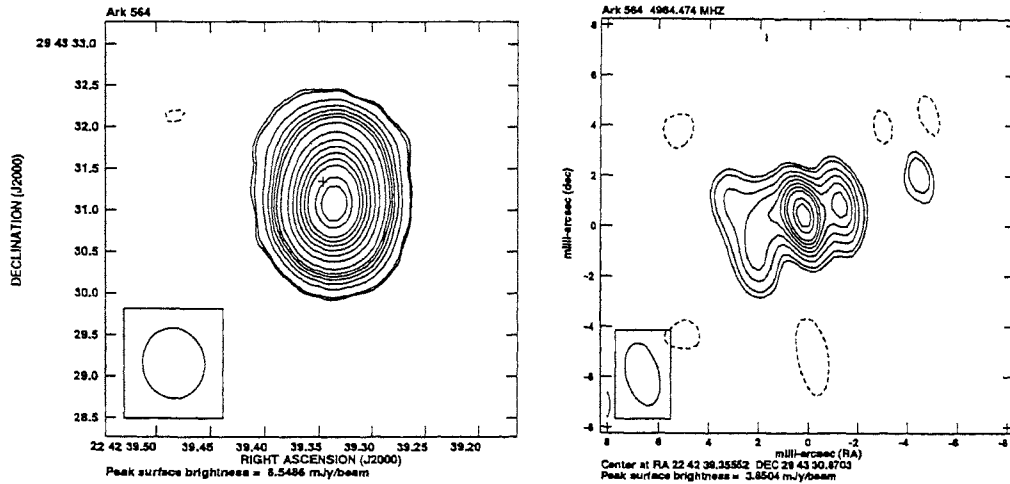


Figure 3.25: 5 GHz VLA (left) and VLBI (right) image of Ark 564.

surrounded by a halo of emission ~ 4 kpc in extent. The radio core is coincident with the optical (Clements 1981) nucleus to within the errors. The features seen in this source are also seen by Condon et al. (1982) and Ulvestad et al. (1981) in their lower resolution map. The map presented by Kukula et al. (1995) at 8.4 GHz also shows a point source surrounded by faint emission. Using our flux density and the flux density given by Kukula et al. (1995) at 8.4 GHz, we obtain the spectral indices of the integrated emission as $\alpha_{6\text{ cm}}^{3.6\text{ cm}} = 0.9$; which is similar to $\alpha_{6\text{ cm}}^2$ determined by Wilson et al. (1991). The largest angular extent of the source is ~ 2.8 arcsec.

VLBI: This source is compact, but appears to be extended toward the north-east. This is consistent with Smith et al.'s (1998B) prediction, who, based on the visibility functions suggested the presence of multiple components in it. Using our detected flux density and the correlated flux density measured by Smith et al. (1998B) at 1.4 GHz of 12 mJy, we obtain the spectral index of the source as $\alpha_{21\text{ cm}}^6\text{ cm} = 0.5$.

Mrk 926 (2302-086)

This object is not observed by us.

VLA: Most of the radio emission comes from an unresolved component in the map of Ulvestad & Wilson (1984A). But their same radio map, at 6 cm using VLA A array (Figure 3.28), also shows an east-west extension at a level of $\sim 5\%$ of the

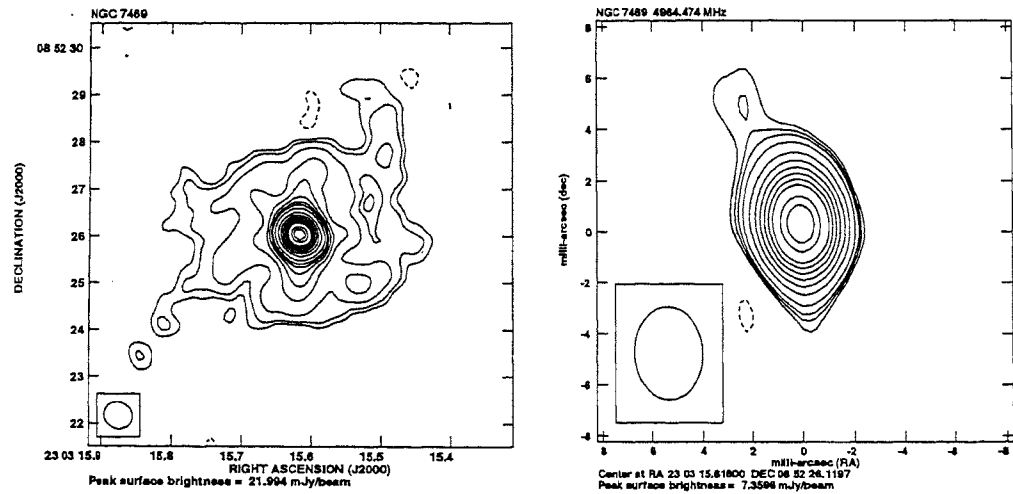


Figure 3.26: 5 GHz VLA (left) and VLBI (right) image of NGC 7469.

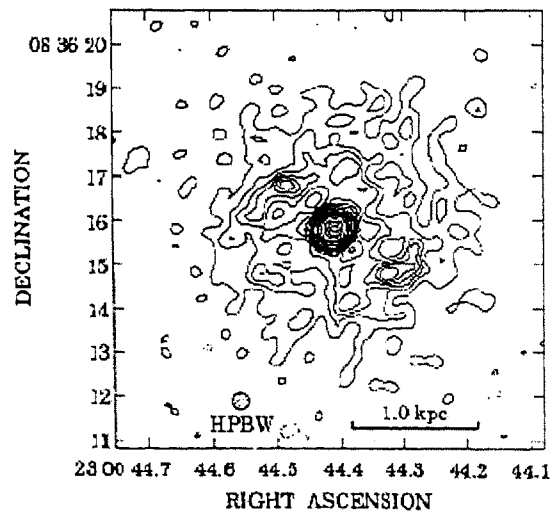


Figure 3.27: VLA image of the 6 cm brightness distribution in the central parts of NGC 7469 with beam $0.39 \times 0.37 \text{ arcsec}^2$ in P.A. 108° . Contours are plotted at -0.5, 0.5, 1, 1.5, 2, 2.5, 3, 4, 5, 7.5, 10, 15, 20, 30, 50, 70, and 90% of the peak surface brightness of 18.0 mJy per beam (Wilson et al. 1991).

peak surface brightness. The 8.4 GHz VLA image (left image of Figure 3.28, Braatz, Wilson & Dressel unpublished, quoted in Mundell et al. 2000) also shows a compact core with weak east-west extensions. The nuclear radio spectrum is relatively flat between 5 GHz and 8.4 GHz ($\alpha_{8\text{ cm}}^{3.6\text{ cm}} = 0.24$) but steepens at longer wavelengths ($\alpha_{20\text{ cm}}^6$) (Mundell et al. 2000). The peak of radio surface brightness is consistent with the optical core (Clements 1983) within the errors. The largest angular size for the source is ~ 1.3 arcsec (Ulvestad & Wilson 1984A).

VLBI: Mundell et al.'s (2000) observations at 8.4 GHz shows an unresolved source (Figure 3.28) with a peak surface brightness of 4.6 mJy beam^{-1} .

Mrk 530 (2316-000)

VLA: The source was reported to have a compact point source in Kukula et al.'s (1995) observations at 8.4 GHz, whereas our 5 GHz map (Figure 3.29) shows a compact source and a faint (3σ) extension along the north (P.A. $\sim -10^\circ$). Combining our total flux density with the 3.26 mJy found by Kukula et al. (1995) at 8.4 GHz, we derive a spectral index of $\alpha_{6\text{ cm}}^{3.6\text{ cm}} = 2$. Our total flux density is consistent with the measurements of Edelson (1987), 11.5 mJy, and of Roy et al.'s (1994) correlated flux density of 11 mJy obtained using 275 km long single baseline PTI at 2.3 GHz.

VLBI: A model with two, two-dimensional, Gaussian components gives a good fit to the visibility data. The source (Figure 3.29) seems to have an extension along the east-west direction of the peak of surface brightness at fainter levels. The total flux density of 8.6 mJy detected in mas-scale map is similar to the flux density associated with the core component (8.0 mJy) on the arcsec scale map. This implies that almost all of the radio emission detected on arcsec scale map is associated with the compact core. We also present a map for which the restoring beam is half the size of the normal beam and has the same P.A. (Figure 3.30). This map shows the orientation of the source structure to be $\sim 40^\circ$.

Mrk 533 (2325+085)

VLA: Our image (Figure 3.31) of this object is resolved and is consistent with the double radio source structure as seen by Kukula et al.'s (1995) VLA A configuration, 8.4 GHz map (Figure 3.32) and Unger et al.'s (1986) 1.6 GHz, MERLIN map. The P.A. of the source is $\sim -60^\circ$. The peak of radio surface brightness is to the

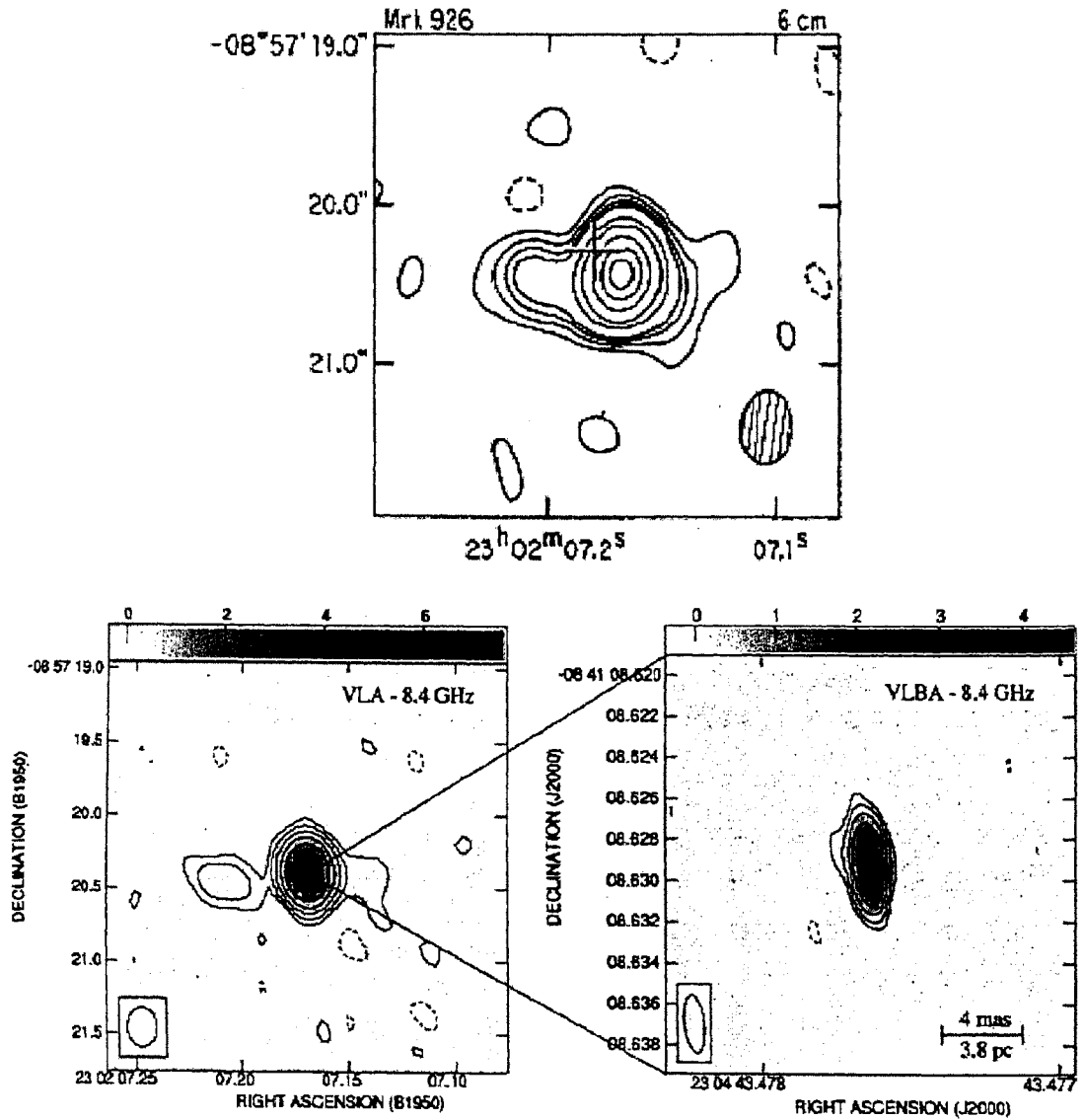


Figure 3.28: 5 GHz VLA (upper, Ulvestad & Wilson 1984A) map of Mrk 926, contour levels plotted at -2.5, 2.5, 5, 7.5, 10, 20, 30, 50, 70, and 90% of the peak surface brightness of 7.69 mJy per beam with beam $0.46 \times 0.35 \text{ arcsec}^2$ in P.A. 173° .

8.4 GHz VLA (lower left, Mundell et al. 2000) map of Mrk 926, contour levels plotted at -1, 1, 2, 4, 8, 16, 32 times 0.36 mJy per beam with beam $0.27 \times 0.21 \text{ arcsec}^2$, and 8.4 GHz VLBA (lower right, Mundell et al. 2000) map of Mrk 926, contour levels plotted at -1, 1, 2, 4, 8, 16 times 0.42 mJy per beam with beam $2.82 \times 1.02 \text{ mas}^2$.

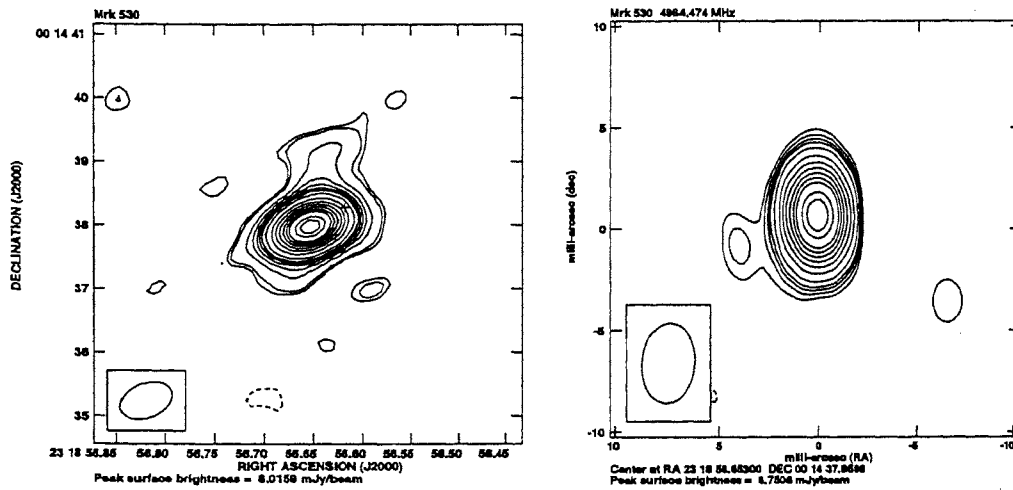


Figure 3.29: 5 GHz VLA (left) and VLBI (right) image of Mrk 530.

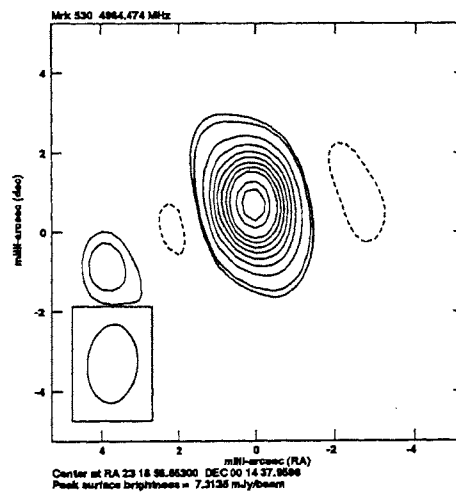


Figure 3.30: VLBI image of Mrk 530 with restoring beam $1.97 \times 1.77 \text{ mas}^2$ and P.A. $-4^\circ.8$, contours are plotted at -6, 6, 8, 16, 24, 32, 40, 48, 56, 64, 80, and 90% of the peak surface brightness which is 7.3 mJy per beam.

south of the optical core (Clements 1983) and is ~ 0.5 arcsec away. The largest angular size of the source is ~ 2 arcsec.

VLBI: A linear radio source (Figure 3.31) extending along east-west direction and the model fit shows it to have five two-dimensional Gaussian components. The CLEAN components are distributed up to ~ 15 mas on either side of the phase-centre (total extent of ~ 30 mas) along P.A. $\sim 100^\circ$ and is similar to the P.A. ($\sim -60^\circ$) of the arcsec scale radio structure. The ratio of length to the width is ~ 3 and is close to one of the criteria laid by Bridle & Perley (1984) for a radio jet.

NGC 7682 (2326+032)

VLA: Our map (Figure 3.33) of the source shows it to be an unresolved source as seen by Kukula et al. (1995). The total flux density is 22 mJy. Combining our flux density along with that given by Kukula et al. (1995) at 8.4 GHz implies the spectral index, $\alpha_{\frac{3.6}{\text{cm}}}$, of the core as 1.1. The peak of radio surface brightness registers well with the optical core (Clements 1983) and is within the errors.

VLBI: We were only able to model fit a single two-dimensional Gaussian component, though the map shows clear evidence for extensions to the south (PA $\sim 180^\circ$) and the south-east (PA $\sim 120^\circ$) (Figure 3.33).

3.5 Summary

The maps presented in this Chapter reveal for the first time the mas-scale radio structure of a large carefully selected sample of Seyfert galaxies.

We presented radio images of 15 objects that were observed by us and 4 objects that had VLBI images in the literature. Thus 19 sample objects have VLBI images, the 1 remaining has an upper limit to detection at 2.3 GHz, all 20 have VLA images, and 15 of them have simultaneous VLBI and VLA measurements. Thus, all our 19 objects that we observed with VLBI were detected. Published studies indicate that at least two (Mrk 348 and Mrk 231) of these are radio variable, underlining the advantage of the simultaneity of our VLBI and VLA data while comparing the structures on mas and arcsec-scales.

We measured the radio flux densities, sizes of the emitting regions, P.A. of the extended radio emission and their morphologies. These measurements provide the database for investigating the generic properties of compact radio cores in Seyfert nuclei.

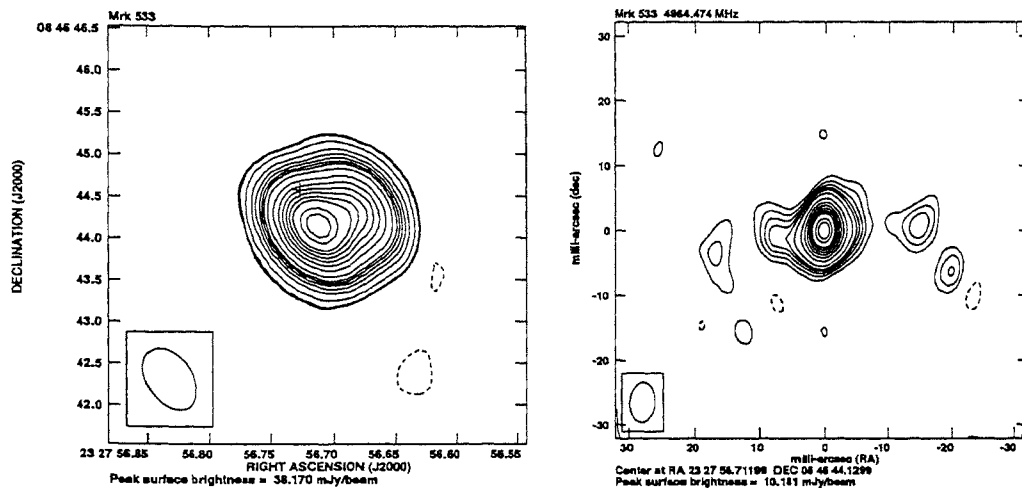


Figure 3.31: 5 GHz VLA (left) and VLBI (right) image of Mrk 533.

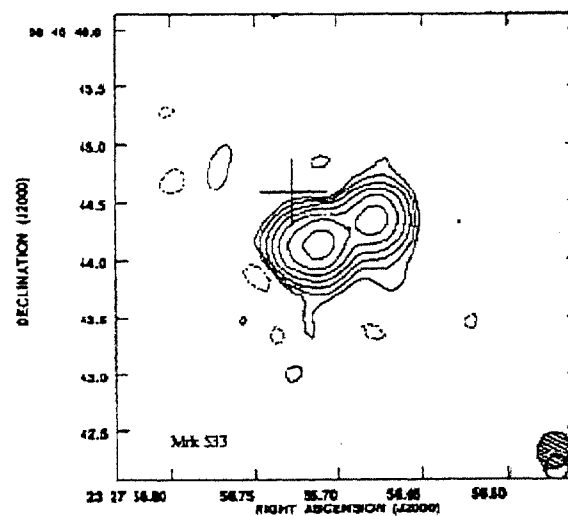


Figure 3.32: 8.4 cm VLA image of Mrk 533 (Kukula et al. 1995), the contour levels are at -0.2, 0.2, 0.4, 0.8, 1.6, 3.2, 6.4, and 12.8 times 1.0 mJy. The restoring beam is $0.325 \times 0.293 \text{ arcsec}^2$ at a P.A. of $116^\circ.8$.

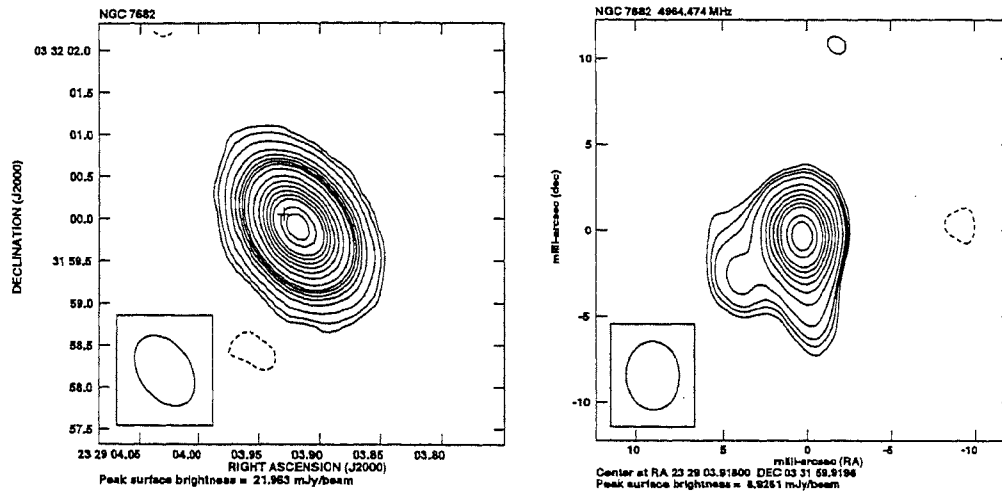


Figure 3.33: 5 GHz VLA (left) and VLBI (right) image of NGC 7682.

At pc-scales, in 40% of the cases we detect a single component and in 45% of the cases the brightest compact radio component has a flux density more than 70% of the total detected flux density. Mrk 530 has more than 50% of the total flux density associated with the brightest compact radio component, and NGC 4151 and Mrk 231 have $\sim 25\%$ of the total detected flux density associated with the brightest compact radio component.

Object	CLEAN beam (mas ²)	P.A. (deg)	Peak (mJy beam ⁻¹)	Peak (μJy beam ⁻¹)	RMS (μJy beam ⁻¹)	Contours (% of peak flux density)
Mrk 1	3.69 x 1.78	-12.2	6.73	120	-6, 8, 10, 12, 16, 24, 32, 40, 48, 56, 64, 80, 90	
MGC 8-11-11	2.08 x 1.60	-53.9	6.89	133	-8, 8, 10, 12, 16, 24, 32, 40, 48, 56, 64, 80, 90	
NGC 2273	3.02 x 2.52	28.1	7.53	124	-6, 8, 10, 12, 16, 24, 32, 40, 48, 56, 64, 80, 90	
Mrk 78	3.61 x 2.43	85.0	7.14	142	-8, 8, 10, 12, 16, 24, 32, 40, 48, 56, 64, 80, 90	
Mrk 1218	2.88 x 1.05	-10.4	6.72	114	-5, 6, 8, 10, 12, 16, 24, 32, 40, 48, 56, 64, 80, 90	
NGC 2639	1.82 x 1.08	-6.8	34.84	86	-0.8, 1, 1.6, 2, 3.2, 4, 6, 8, 10, 12, 16, 24, 32, 40, 48, 56, 64, 80, 90	
Mrk 766	2.78 x 1.65	18.3	7.07	139	-8, 8, 10, 12, 16, 24, 32, 40, 48, 56, 64, 80, 90	
Mrk 477	4.48 x 3.26	50.0	9.38	132	-4, 4, 6, 8, 10, 12, 16, 24, 32, 40, 48, 56, 64, 80, 90	
NGC 5929	2.91 x 1.80	31.5	6.87	100	-6, 8, 10, 12, 16, 24, 32, 40, 48, 56, 64, 80, 90	
NGC 7212	4.27 x 2.65	-3.5	7.15	198	-8, 8, 10, 12, 16, 24, 32, 40, 48, 56, 64, 80, 90	
Ark 564	2.54 x 1.25	13.0	3.65	163	-16, 12, 16, 24, 32, 40, 48, 56, 64, 80, 90	
NGC 7469	3.65 x 2.67	2.7	7.39	120	-8, 8, 10, 12, 16, 24, 32, 40, 48, 56, 64, 80, 90	
Mrk 530	3.93 x 2.54	-4.8	8.78	161	-6, 6, 8, 10, 12, 16, 24, 32, 40, 48, 56, 64, 80, 90	
Mrk 533	6.22 x 3.89	-4.2	10.20	112	-4, 4, 6, 8, 10, 12, 16, 24, 32, 40, 48, 56, 64, 80, 90	
NGC 7682	4.00 x 3.00	1.9	8.94	134	-6, 8, 10, 12, 16, 24, 32, 40, 48, 56, 64, 80, 90	

Table 3.5: Parameters for VLBI maps.

Object	CLEAN FWHM (arcsec ^a)	beam P.A. (deg)	Peak surface brightness (mJy beam ⁻¹)	RMS (μ Jy beam ⁻¹)	Total flux density (mJy)	Contours (% of peak flux density)
Mrk 348				76	238.00	-6, -4, -2, 2, 4, 6, 10, 50, 100, 200, 400, 800, 1200, 2400 ^a
Mrk 1	0.65 x 0.49	53.98	24.08	39	27.65	-0.3, 0.8, 1, 2, 4, 6, 8, 10, 12, 16, 24, 32, 40, 48, 56, 64, 80, 90
MCG 8-11-11	0.84 x 0.44	57.72	23.57	50	75.76	-0.6, 0.6, 1, 2, 4, 6, 8, 10, 12, 16, 24, 32, 40, 48, 56, 64, 80, 90
NGC 2273	0.70 x 0.46	60.23	12.13	83	19.92	-1.6, 1.6, 2, 4, 6, 8, 10, 12, 16, 24, 32, 40, 48, 56, 64, 80, 90
Mrk 78	0.70 x 0.52	71.64	8.87	30	9.39	-1, 1, 1.6, 2, 4, 6, 8, 10, 12, 16, 24, 32, 40, 48, 56, 64, 80, 90
Mrk 1218	0.53 x 0.41	-68.27	18.72	92	25.56	-1.2, 1.2, 2, 4, 6, 8, 10, 12, 16, 24, 32, 40, 48, 56, 64, 80, 90
NGC 2639	0.64 x 0.45	81.59	63.47	67	83.63	-0.4, 0.4, 1, 2, 4, 6, 8, 10, 12, 16, 24, 32, 40, 48, 56, 64, 80, 90
NGC 4151	0.64 x 0.53	-64.00	41.00		120.0	1, 2, 3, 4, 5, 10, 20, 30, 40, 50, 75
Mrk 766	0.65 x 0.48	-71.85	13.75	37	15.16	-0.8, 1, 2, 4, 6, 8, 10, 12, 16, 24, 32, 40, 48, 56, 64, 80, 90
Mrk 231	0.29 x 0.25	19.60	211.78	1112	234.45	-0.2, 0.2, 0.4, 0.8, 1.6, 3.2, 6.4, 12.8, 25.6, 51.2, 102.4
NGC 5135	0.92 x 0.62	2.11	16.15	13	58.80	-2, 2, 4, 6, 8, 10, 12, 16, 24, 32, 40, 48, 56, 64, 80, 90
Mrk 477	0.99 x 0.55	-63.30	22.97	36	24.39	-0.3, 0.8, 1, 2, 4, 6, 8, 10, 12, 16, 24, 32, 40, 48, 56, 64, 80, 90
NGC 5929	1.16 x 0.98	75.36	21.51	85	31.74	-0.8, 1.6, 2, 4, 6, 8, 10, 12, 16, 24, 32, 40, 48, 56, 64, 80, 90
NGC 7212	1.18 x 0.68	-65.06	19.63	86	31.21	-0.8, 0.8, 1, 2, 4, 6, 8, 10, 12, 16, 24, 32, 40, 48, 56, 64, 80, 90
Ark 564	0.85 x 0.75	8.41	8.62	39	11.30	-1.6, 1.6, 2, 4, 6, 8, 10, 12, 16, 24, 32, 40, 48, 56, 64, 80, 90
NGC 7469	0.61 x 0.55	54.87	21.97	49	43.56	-0.6, 0.6, 1, 2, 4, 6, 8, 10, 12, 16, 24, 32, 40, 48, 56, 64, 80, 90
Mrk 926	0.46 x 0.35	173.00	7.69		9.00	-2.5, 2.5, 5, 7.5, 10, 20, 30, 50, 70, 90
Mrk 530	0.82 x 0.53	35.20	8.02	41	8.21	-1.6, 1.6, 2, 4, 6, 8, 10, 12, 16, 24, 32, 40, 48, 56, 64, 80, 90
Mrk 533	0.82 x 0.53	35.20	38.19	78	60.37	-0.8, 0.8, 1, 2, 4, 6, 8, 10, 12, 16, 24, 32, 40, 48, 56, 64, 80, 90
NGC 7682	0.94 x 0.64	38.16	21.98	35	22.21	-0.4, 0.6, 1, 2, 4, 6, 8, 10, 12, 16, 24, 32, 40, 48, 56, 64, 80, 90

Notes :

Negative contours are plotted with dashed lines.

^aFor Mrk 348, the contours are in multiples of RMS.

Table 3.6: Parameters for VLA maps.

Object	Ref	A priori used for the VLBI Schedule	position VLBI Schedule RA DEC	Relative position w.r.t. phase centre α (mas) δ (mas)	Flux density (mJy)	Component size Maj x Min (mas ²)	Peak surface brightness (mJy beam ⁻¹)	Total flux density (mJy)
Mrk 348	B	00 ^h 48 ^m 47 ^s .1422	+31°57'25".044	+0.039	4.38	1.04 x 1.04	6.73	115.00
Mrk 1	A	01 ^h 16 ^m 07 ^s .2174	+33°05'21".557	-0.044	4.38	0.79 x 0.79	6.89	4.38
MGC 8-11-11	A	05 ^h 54 ^m 53 ^s .6106	+46°26'21".708	-0.013	4.89	1.17 x 1.17	7.53	4.89
NGC 2273	A	06 ^h 50 ^m 08 ^s .6403	+60°50'44".947	+0.012	6.31	0.71 x 0.71	7.14	6.31
Mrk 78	A	07 ^h 42 ^m 41 ^s .7384	+65°10'37".780	-0.002	5.55	0.27 x 0.27	7.14	7.82
				-0.920	1.39	0.38 x 0.38	6.72	9.98
Mrk 1218	A	08 ^h 38 ^m 10 ^s .9453	+24°53'42".924	-1.654	0.87	1.18 x 1.18	6.72	9.98
				+0.031	7.09	1.72 x 1.72	34.84	39.54
				-0.730	1.51	0.05 x 0.05	2.50	10.00
				-2.311	1.38	0.33 x 0.33	1.00	10.00
NGC 2639	A	08 ^h 43 ^m 38 ^s .0723	+50°12'20".073	+0.034	31.58	0.85 x 0.85	7.07	3.68
				-0.034	7.96	0.85 x 0.85	163.00	173.00
NGC 4151	C	12 ^h 10 ^m 32 ^s .5822	+39°24'21".059	+0.544	3.68	0.85 x 0.85	7.07	3.68
				+0.000	162.00	0.85 x 0.85	163.00	173.00
				-1.000	2.00	0.85 x 0.85	7.07	3.68
				+0.500	8.00	0.85 x 0.85	163.00	173.00
				+1.200	1.00	0.85 x 0.85	7.07	3.68
				+2.300	1.00	0.85 x 0.85	163.00	173.00
				+3.600	1.00	0.85 x 0.85	7.07	3.68
Mrk 766	A	12 ^h 18 ^m 26 ^s .5170	+29°48'46".500	+0.021	3.68	0.85 x 0.85	7.07	3.68
Mrk 231	D	12 ^h 56 ^m 14 ^s .2336	+56°52'25".245	+0.000	162.00	0.85 x 0.85	163.00	173.00
				-1.000	2.00	0.85 x 0.85	7.07	3.68
				+0.500	8.00	0.85 x 0.85	163.00	173.00
				+1.200	1.00	0.85 x 0.85	7.07	3.68
				+2.300	1.00	0.85 x 0.85	163.00	173.00
				+3.600	1.00	0.85 x 0.85	7.07	3.68
NGC 5135	F	14 ^h 40 ^m 38 ^s .0973	+53°30'16".062	+0.274	8.19	1.40 x 1.40	9.37	< 5.0
Mrk 477	A	15 ^h 26 ^m 06 ^s .1670	+41°40'14".420	+0.012	5.98	0.79 x 0.79	6.87	8.19
NGC 5929	A	22 ^h 07 ^m 02 ^s .0590	+10°14'02".589	+3.812	0.30	0.23 x 0.23	6.87	6.28
NGC 7212	A	22 ^h 42 ^m 39 ^s .3555	+29°43'30".870	+0.028	6.58	1.10 x 1.10	7.15	6.58
Mrk 564	A	23 ^h 03 ^m 15 ^s .6160	+08°52'26".120	+0.191	3.22	0.85 x 0.85	3.65	3.22
NGC 7469	A	23 ^h 04 ^m 43 ^s .4776	-08°41'08".629	+0.052	5.46	0.89 x 0.89	7.39	6.17
Mrk 926	E	23 ^h 27 ^m 56 ^s .7120	+08°46'44".130	+0.032	0.71	0.11 x 0.11	4.6	5.00
Mrk 530	A	23 ^h 29 ^m 03 ^s .9180	+03°31'59".920	+0.004	7.56	0.85 x 0.85	8.78	8.63
				-1.294	0.26	0.05 x 0.05	10.20	16.90
				+3.406	0.81	0.87 x 0.87	10.20	16.90
				+0.105	9.70	1.12 x 1.12	10.20	16.90
				+6.177	2.20	0.67 x 0.67	10.20	16.90
				+16.730	1.20	0.50 x 0.50	10.20	16.90
				-5.990	2.27	2.24 x 2.24	10.20	16.90
				-13.753	1.59	0.79 x 0.79	10.20	16.90
NGC 7682	A	23 ^h 29 ^m 03 ^s .9180	+03°31'59".920	+0.054	8.92	1.31 x 1.31	8.94	8.92

Notes:

A: Our measurements; B: Barvainis & Lonsdale (1998); C: Ulvestad et al. (1998B); D: Ulvestad et al. (1999A); E: Mundell et al. (2000); F: Roy et al (1995) (275 km baseline, 100 mas fringe-spacing).

Table 3.7: VLBI observational results.

	Optical position		Radio Peak position		Total flux density (mJy)	Radio type	Largest angular size (arcsec)
	RA (J2000)	DEC (J2000)	RA (J2000)	DEC (J2000)			
Mrk 348	00 ^h 48 ^m 47 ^s .16	+31°57'25".27 ^a	00 ^h 48 ^m 47 ^s .141	+31°57'25".19 ^f	346.00	L	0".20 ^p
Mrk 1	01 ^h 16 ^m 07 ^s .25	+33°05'22".40 ^a	01 ^h 16 ^m 07 ^s .209	+33°05'21".66 ^e	27.65	U	< 0".65 ^m
MCG 8-11-11	05 ^h 54 ^m 53 ^s .61	+46°26'21".61 ^a	05 ^h 54 ^m 53 ^s .620	+46°26'21".41 ^e	75.76	A	3".48 ^m
NGC 2273	06 ^h 50 ^m 08 ^s .72	+60°50'45".01 ^c	06 ^h 50 ^m 08 ^s .640	+60°50'44".95 ^e	19.93	L	2".25 ^m
Mrk 78	07 ^h 42 ^m 41 ^s .73	+65°10'37".46 ^a	07 ^h 42 ^m 41 ^s .723	+65°10'37".48 ^e	9.38	L	3".88 ^m
			07 ^h 42 ^m 41 ^s .341	+65°10'37".58 ^e	1.07		
Mrk 1218	08 ^h 38 ^m 10 ^s .95	+24°53'42".92 ^b	08 ^h 38 ^m 10 ^s .945	+24°53'42".82 ^e	24.04	L	1".28 ^m
NGC 2639	08 ^h 43 ^m 38 ^s .00	+50°12'20".32 ^c	08 ^h 43 ^m 38 ^s .072	+50°12'19".97 ^e	83.63	L	< 0".65 ^m
NGC 4151	12 ^h 10 ^m 32 ^s .58	+39°24'20".63 ^a	12 ^h 10 ^m 32 ^s .576	+39°24'20".81 ^g	120.00	L	3".30 ⁿ
Mrk 766	12 ^h 18 ^m 26 ^s .51	+29°48'46".34 ^a	12 ^h 18 ^m 26 ^s .517	+29°48'46".50 ^e	15.16	U	< 0".65 ^m
Mrk 231	12 ^h 56 ^m 14 ^s .23	+56°52'25".20 ^a	12 ^h 56 ^m 14 ^s .238	+56°52'25".21 ^h	173.00	U	< 0".29 ⁿ
NGC 5135	13 ^h 25 ^m 44 ^s .17	-29°50'01".28 ^d	13 ^h 25 ^m 43 ^s .932	-29°50'02".68 ⁱ	58.80	A	7".11 ^q
Mrk 477	14 ^h 40 ^m 38 ^s .11	+53°30'16".00 ^a	14 ^h 40 ^m 38 ^s .097	+53°30'15".96 ^e	24.39	U	< 0".99 ^m
NGC 5929	15 ^h 26 ^m 06 ^s .13	+41°40'14".72 ^b	15 ^h 26 ^m 06 ^s .113	+41°40'14".02 ^j	31.74	L	3".40 ⁿ
NGC 7212	22 ^h 07 ^m 02 ^s .01	+10°14'00".34 ^b	22 ^h 07 ^m 02 ^s .560	+10°14'00".39 ^e	31.21	L	3".09 ^m
			22 ^h 07 ^m 02 ^s .946	+10°14'14".19 ^e	2.74		
Ark 564	22 ^h 42 ^m 39 ^s .34	+29°43'31".31 ^a	22 ^h 42 ^m 39 ^s .332	+29°43'31".07 ^e	11.30	U	< 0".85 ^m
NGC 7469	23 ^h 03 ^m 15 ^s .62	+08°52'26".39 ^a	23 ^h 03 ^m 15 ^s .616	+08°52'26".02 ^e	43.56	R	2".76 ^m
Mrk 926	23 ^h 04 ^m 43 ^s .45	-08°41'08".49 ^b	23 ^h 04 ^m 43 ^s .471	-08°41'08".49 ^k	9.00	S	1".33 ^r
Mrk 530	23 ^h 18 ^m 56 ^s .62	+00°14'38".23 ^a	23 ^h 18 ^m 56 ^s .653	+00°14'37".96 ^e	9.17	U	< 0".82 ^m
Mrk 533	23 ^h 27 ^m 56 ^s .72	+08°46'44".53 ^b	23 ^h 27 ^m 56 ^s .712	+08°46'44".13 ^e	60.37	L	1".89 ^m
NGC 7682	23 ^h 29 ^m 03 ^s .93	+03°31'59".99 ^b	23 ^h 29 ^m 03 ^s .918	+03°31'59".92 ^e	22.21	U	< 0".94 ^m

References:

Optical position:

- ^aClements 1981.
^bClements 1983.
^cArgyle & Eldridge 1990.
^dGoullouët et al. 1975.

Radio peak position:

- ^eOur measurements.
^fThean et al. (2000).
^gJohnston et al. (1982).
^hUlvestad et al. (1999A).
ⁱUlvestad & Wilson (1989).
^jSu et al. (1996)
^kUlvestad & Wilson (1984A).

Largest angular size:

- ^mOur measurements.
ⁿKukula et al. (1995).
^oPedlar et al. (1993).
^pUnger et al. (1984).
^qUlvestad & Wilson (1989).
^rUlvestad & Wilson (1984A).

Table 3.8: VLA observational results.

Chapter 4

Radio continuum emission of Seyfert galaxies on kpc and pc-scales: Interpretations

4.1 Introduction

Our sample of Seyfert galaxies, matched in orientation independent parameters, which have arcsec and mas-scale observations at 6 cm, was constructed to rigorously compare (i) the detectability of compact structures on mas-scales, (ii) the radio luminosities of Seyfert 1 and Seyfert 2 types on pc-scales, (iii) the fraction of integrated $\lambda_{6\text{ cm}}$ emission that is associated with the active nucleus, as opposed to star formation or other extended emission, and (iv) the fraction of the VLA flux density on kpc-scales that is present on pc-scales.

In Chapter 3 we presented the radio images that were obtained from our observations and described the properties at these scales in the light of past observations. Here we discuss the impact of these observations on the unified scheme hypothesis. In the section below (Section 4.2) we first discuss if a starburst alone can power Seyfert galaxies. In the next Section (4.3.1) we compare the rates of detection of the Seyfert galaxy radio emission by our VLBI array. In Section (4.3.2) we further discuss the pc-scale radio morphology and its consistency with the unified scheme. We then compare the distribution of radio luminosities for Seyfert galaxies from our sample at the kpc-scales (Section 4.3.3). In Section 4.3.6 we test if relativistic beaming is likely to be present in Seyfert 1 galaxies. In the end, we also compare the distribution of radio structures of the CfA Seyfert galaxy sample at kpc-scales (Section 4.4).

4.2 Seyfert nuclei: Starburst or accretion-powered central engine ?

A key question is, can a compact starburst alone power Seyfert galaxies, thus not requiring the presence of a supermassive black hole in their nuclei? While emission from the hot stars in the torus might account for the featureless continua in Seyfert 2 galaxies (Cid Fernandes & Terlevich 1995, González-Delgado et al. 1998), starbursts cannot produce the necessary collimation to form radio jets. The existence of radio jets is, therefore, often used as an indication of the presence of a black hole and the accretion disk. Although some Seyfert galaxies are now known to possess strikingly collimated jets (*e.g.* Nagar et al. 1999B, Kukula et al. 1995, etc.), the resolution of the radio images is often insufficient to demonstrate the high degree of collimation seen in radio galaxies and radio-loud quasars.

A question that can be addressed with the help of the data presented in Chapter 3 is whether the cores of Seyfert galaxies are primarily made up of radio supernovae. For example, although Arp 220 shows a “double-structure” on kpc-scales, recent VLBI observations have revealed 13 faint sources in one of the components of the double, interpreted as radio supernovae. They occur in the inner 100 pc at 1.3 GHz with flux densities between 0.1 and 1.2 mJy, and three with flux densities between 1.0 and 1.2 mJy (Smith et al. 1998A). Smith et al. (1998A) show that these radio supernovae are of the same class as radio supernova 1986J observed in the disk of NGC 891 (Rupen et al. 1987): Type II radio supernovae with luminosities of order 10^{28} ergs $s^{-1}Hz^{-1}$ and exponential decay time of 3 yr. The number of radio supernovae observed in Arp 220 would require a massive star formation rate of $70 M_{\odot} yr^{-1}$.

To examine whether compact starbursts alone can power Seyfert galaxies, we consider the following arguments. Cid Fernandes & Terlevich (1995) and González-Delgado et al. (1998) suggest that although emission from hot stars in the torus might account for the featureless continua in Seyfert 2 galaxies, starbursts cannot produce the necessary collimation to form radio jets. We note that elongated radio structures could be attributed to star formation along the galactic plane of a Seyfert host galaxy if it is edge-on (*e.g.* M 82 a starburst galaxy, Muxlow et al. 1994). In our sample, however this cannot explain any of the elongated structures, since the sample was selected so as to avoid edge-on host galaxies (ratio of minor to major axis of the host galaxy is greater than 0.5 for all our Seyfert sources). Ulvestad et al. (1999B), on pc-scales, confirmed that Mrk 231 and also Mrk 348 are jet-producing central engine systems.

Thus, clearly all objects with elongated or “linear” radio structures, *viz.*, Mrk 348,

Object	Relative position w.r.t. phase centre $\alpha(\text{mas})$ $\delta(\text{mas})$	Component Flux density (mJy)	Component size Maj x Min (mas ²)	T_b (K)	Radio power 5 GHz (<i>pc-scales</i>) ergs s ⁻¹ Hz ⁻¹	ν_{SN} (yr ⁻¹)
Mrk 348 ^a		115.0	1.20 x 1.2 ^b	4.43 x 10 ⁹	7.043 x 10 ²⁹	72
Mrk 1	- 0.044 +0.039	4.38	1.04 x 1.04	2.24 x 10 ⁸	2.115 x 10 ²⁸	2
MGC 8-11-11	- 0.013 -0.045	4.89	0.79 x 0.79	4.35 x 10 ⁸	5.866 x 10 ²⁸	6
NGC 2273	+ 0.012 -0.104	6.31	1.17 x 1.17	2.56 x 10 ⁸	4.364 x 10 ²⁷	0.4
Mrk 78	- 0.002 +0.042	5.55	0.71 x 0.71	6.11 x 10 ⁸	2.055 x 10 ²⁹	21
	- 0.920 -0.187	1.39	0.27 x 0.27			
	- 1.654 -2.332	0.87	0.38 x 0.38			
Mrk 1218	+ 0.031 +0.107	7.09	1.18 x 1.18	2.82 x 10 ⁸	1.213 x 10 ²⁹	17
	- 0.730 -6.163	1.51	1.72 x 1.72			
	- 2.311 +4.257	1.38	1.02 x 1.02			
NGC 2639	- 0.034 +0.035	31.58	0.05 x 0.05	7.01 x 10 ¹¹	9.189 x 10 ²⁸	9
	+ 0.544 -0.067	7.96	0.33 x 0.33			
NGC 4151 ^c	+ 0.000 +0.000	2.50	2.10 x 1.80	3.67 x 10 ⁷	3.457 x 10 ²⁷	0.2
	- 1.000 -4.100	1.00				
	+ 0.500 -2.100	1.00				
	+ 1.200 +3.500	1.00				
	+ 2.300 +5.800	1.00				
	+ 3.600 +7.000	0.90				
Mrk 766	+ 0.021 +0.003	3.68	0.85 x 0.85	2.83 x 10 ⁸	1.189 x 10 ²⁸	1
Mrk 231 ^d		162.00	0.82 x 0.43	2.55 x 10 ¹⁰	2.304 x 10 ³⁰	240
		2.00				
		8.00				
Mrk 477	+ 0.274 -0.030	8.19	1.40 x 1.40	2.32 x 10 ⁸	2.271 x 10 ²⁹	24
NGC 5929	+ 0.012 -0.201	5.98	0.79 x 0.79	5.32 x 10 ⁸	9.775 x 10 ²⁷	1
	+ 3.812 +2.045	0.30	0.23 x 0.23			
NGC 7212	+ 0.028 -0.117	6.58	1.10 x 1.10	3.02 x 10 ⁸	9.209 x 10 ²⁸	10
Ark 564	+ 0.191 -0.077	3.22	0.85 x 0.85	2.47 x 10 ⁸	3.565 x 10 ²⁸	4
NGC 7469	+ 0.052 -0.046	5.46	0.89 x 0.89	3.82 x 10 ⁸	3.034 x 10 ²⁸	3
	+ 0.032 -4.511	0.71	0.11 x 0.11	3.24 x 10 ⁹		
Mrk 926 ^b	+ 0.000 +0.000	5.00	2.82 x 1.02	9.65 x 10 ⁷	2.122 x 10 ²⁹	22
Mrk 530	+ 0.004 +0.452	7.56	0.85 x 0.85	5.87 x 10 ⁸	1.491 x 10 ²⁹	15
	- 1.294 -1.404	0.26	0.05 x 0.05			
	+ 3.406 -1.120	0.81	0.87 x 0.87			
Mrk 533	+ 0.105 -0.100	9.70	1.12 x 1.12	4.29 x 10 ⁸	2.740 x 10 ²⁹	28
	+ 6.177 -1.956	2.20	0.67 x 0.67			
	+16.730 -3.990	1.20	0.50 x 0.50			
	- 5.990 +0.365	2.27	2.24 x 2.24			
	-13.753 -0.325	1.59	0.79 x 0.79			
NGC 7682	+ 0.054 -0.921	8.92	1.31 x 1.31	2.88 x 10 ⁸	4.950 x 10 ²⁸	5

References:

- a: Barvainis & Lonsdale 1998
b: Mundell et al. 2000
c: Ulvestad et al. 1998B
d: Ulvestad et al. 1999A

Table 4.1: Table showing the detected components, their positions (with respect to the phase centre), corresponding flux density, size, brightness temperature of bright component, radio power and supernova rates (ν_{SN}) necessary to reproduce radio emission.

MCG-8-11-11, NGC 2273, Mrk 78, Mrk 1218, NGC 4151, NGC 5135, NGC 5929, NGC 7212, Mrk 926, and Mrk 533 cannot be powered by a starburst alone. We now try to examine whether radio supernovae or supernova remnants in star forming regions can plausibly be retained as the explanation for those objects in the sample that do not show linear structure, *viz.* Mrk 1 and NGC 7682 which are essentially compact sources, and NGC 2639, Mrk 477, NGC 7469 and Mrk 530 which are dominated by a compact source but have low surface brightness extensions. Note that Smith et al. (1998B) have argued that Mrk 231 cannot be powered by starburst alone.

Although an individual supernova can have brightness temperature higher than the brightness temperature of a radio-quiet quasar (Rupen et al. 1987), the most luminous known radio supernova, 1986J (Rupen et al. 1987), had a peak luminosity of $\sim 10^{28}$ ergs $s^{-1}Hz^{-1}$ at 5 GHz. Given that we have obtained pc-scale flux densities for all the latter Seyfert galaxies, it turns out that 0.2 to 240 (median value of around ten) of such supernovae would be needed to power them at 5 GHz (Table 4.1). Since the typical lifetime of such a supernova event is ~ 1 year, to sustain the observed radio powers that we find, a supernova rate of $\nu_{SN} \sim 0.2$ to 240 yr^{-1} is required. Such rates are in line with those required to power the luminous radio-quiet quasars in the starburst scenario (Terlevich 1990A, 1990B). However, since our observed powers are on pc-scales, and we find evidence for one or several dominant compact components in all our 19 observed Seyfert galaxies, these supernovae must be localised within a few cubic parsec, corresponding to a density 10^7 times higher than that observed in M 82 (Muxlow et al. 1994), and higher than in the starburst model of Terlevich & Boyle (1993) by a similar factor.

Compact starbursts may coexist with AGNs in some Seyfert galaxies (Heckman et al. 1997). However the radio emission from starburst region consists of synchrotron radiation from SNRs plus thermal free-free emission from H II regions. The brightness temperature of such a region cannot exceed 10^5 K at $\nu > 1$ GHz (Condon 1992). Using the component size along with its flux density on mas-scales, we find that the brightness temperature (Table 4.1) is in the range of $\sim 0.4\text{--}7000 \times 10^8$ K for our Seyfert sample.

We therefore conclude on the basis of the high brightness temperatures ($> 10^8$), small sizes (< 1 pc) and high supernova rates to explain the detected compact components, that starbursts alone cannot explain the observed radio powers in Seyfert galaxies. We can also rule out individual or a collection of extremely bright radio supernovae as an explanation for the compact emission from the Seyfert galaxies.

4.3 Tests of the unified scheme for Seyfert galaxies

4.3.1 The contradiction with the unification scheme and its resolution

Roy et al. (1994) had observed far-infrared selected, mid-infrared selected and optically selected samples of Seyfert galaxies with a 275 km long, single-baseline, the Parkes-Tidbinbilla interferometer at 1.7 and 2.3 GHz (see Chapter 2, Section 2.4.1.1). They had reported that compact radio structures are much more common in Seyfert 2 than in Seyfert 1 galaxies in the FIR selected samples, and in the combined mid-IR and optically selected sample as well. They deduced this result based on significantly different detection rate of compact, high brightness temperature radio structure.

Their surprising result that far-infrared selected Seyfert 1 galaxies were detected less frequently by the PTI than were Seyfert 2 galaxies, is inconsistent with the standard unification scheme. The unified scheme would predict an equal fraction of detections for Seyfert 1 and Seyfert 2 galaxies. It is also in the opposite sense to what is expected from alternative models in which Seyfert 1 galaxies are expected to have more energetic cores than Seyfert 2 galaxies. Also, even if the jets were relativistically beamed, we would expect Seyfert 1 galaxies to show systematically more prominent compact radio emission than Seyfert 2 galaxies, since they are the face-on objects, and it is their jets that would be pointed towards us and therefore Doppler beamed (Section 4.3.6).

Roy et al. (1994) invoke a model which attempts to reconcile their result with the unification scheme. They consider the radio optical depth due to the free-free absorption of the NLR clouds which surround the radio emitting regions of the core and NLR, which is in line with the model first proposed by Norris et al. (1992A). There could be two distinct mechanisms (i) obscuration by the NLR and (ii) obscuration by individual NLR clouds that may contribute to the resulting radio appearance. These two mechanisms invoke free-free absorption by the NLR clouds which is highly dependent on the geometry of NLR, opening angle of the cone (anisotropic escape of photons is in the form of a cone) and the filling factor. Roy et al. (1994) propose testing of this model by repeating the experiment at a higher frequency and by testing the detection rates of cores of Seyfert 1 and Seyfert 2 galaxies.

As opposed to Roy et al.'s (1994) result, however all 19 of our 20 sample sources for which VLBI observations are available have compact features. Observations of our sample made using VLBI detects all the objects that we observed (15 of the 20) and 4 of the remaining (5) are observed by others, which are also detected. We do not

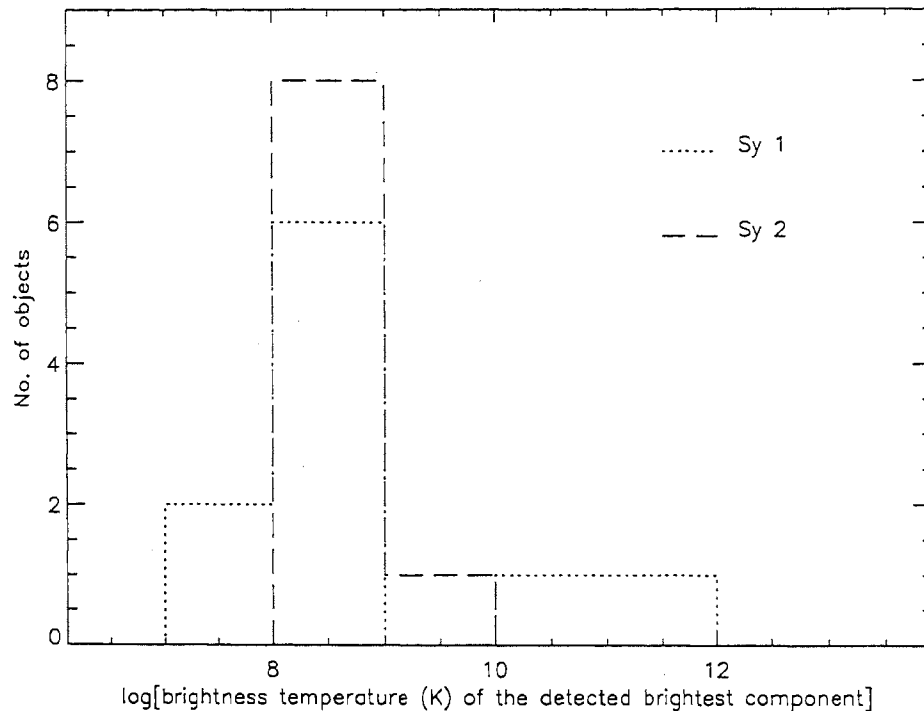


Figure 4.1: Histograms showing distribution of brightness temperature (K) of the brightest component detected on mas-scales.

find any systematically different detection rate of compact structures. We thus find that Seyfert 1 and Seyfert 2 galaxies have an equal tendency to show compact radio structures, in contrast to the results of Roy et al. (1994). Our result is thus consistent with the prediction of the simple unified scheme.

Figure 4.1 shows the distribution of brightness temperatures of the brightest component detected on mas-scales and Figure 4.2 shows the ratio of flux density detected on mas-scales to that detected on arcsec-scales (the latter is discussed further in Section 4.3.6). Mann-Whitney U test shows that the distributions (Figures 4.1 and 4.2) are marginally same at a significance level of 0.10. These distributions show that the fraction of total flux density detected on mas-scales is not different for the two groups of Seyfert galaxies. This demonstrates that the fact that our detection rate is higher than Roy et al.'s (1994) is not just due to the higher sensitivity of the interferometer we used.

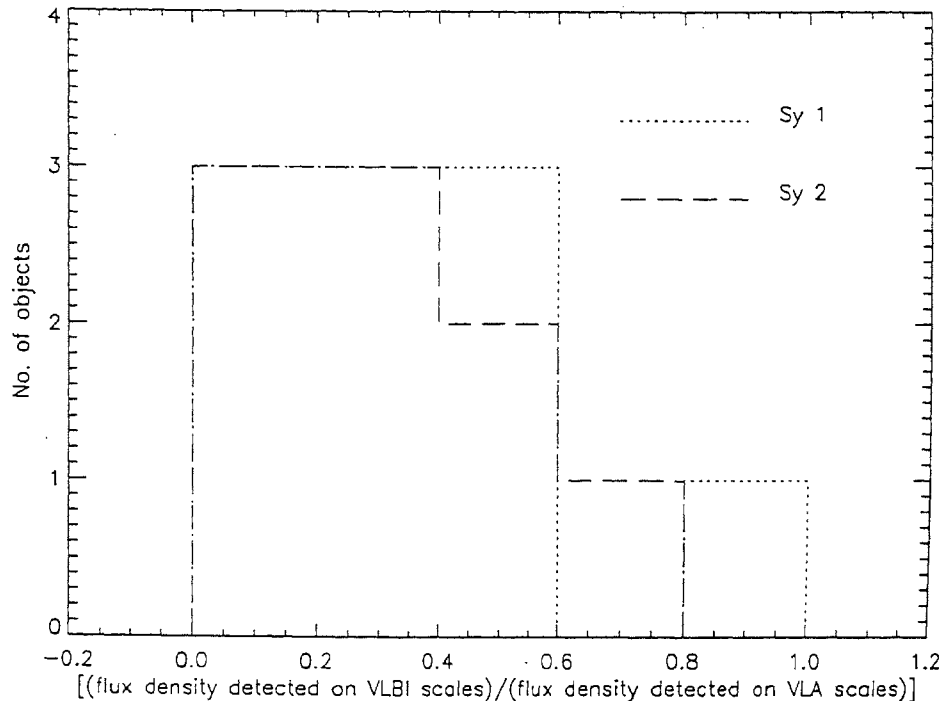


Figure 4.2: Histograms showing the ratio of flux density detected on mas-scales to the emission detected on arcsec-scales.

4.3.2 The pc-scale radio luminosities

We derive the observed radio luminosity from the observed flux density S_ν via

$$L_\nu = 4\pi S_\nu (d)^2 (1+z),$$

$$\text{where } d = \frac{cz (1 + (z/2))}{H_0 (1+z)}, \text{ and we use}$$

$$H_0 = 75 \text{ km s}^{-1} \text{ Mpc}^{-1} \text{ and } q_0 = 0.$$

We compare the distribution of radio luminosities for Seyfert 1 and Seyfert 2 galaxies. The values are given in Table 4.2.

Figure 4.3 shows the distribution of the radio power detected on pc-scales. The distribution shows that the pc-scale radio luminosities of the Seyfert 1 and the Seyfert 2 galaxies are similar. The Mann-Whitney U test shows that the distributions are statistically indistinguishable at a significance level of 0.05. Thus the distribution of pc-scale radio powers of Seyfert 1 and Seyfert 2 galaxies are consistent with the unified scheme hypothesis.

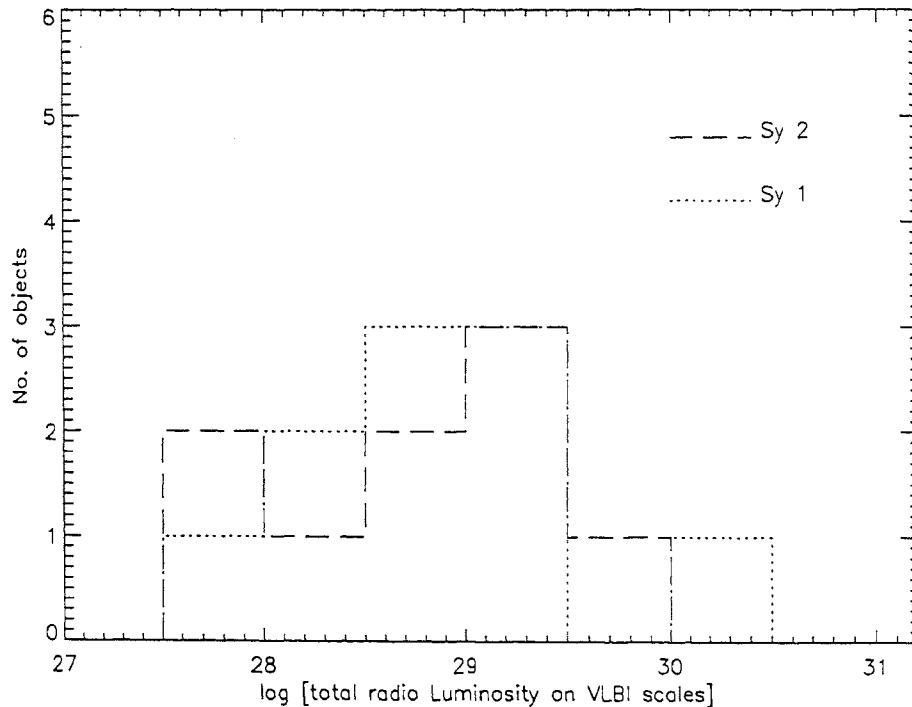


Figure 4.3: Histograms showing distribution of total radio luminosity ($\text{ergs s}^{-1}\text{Hz}^{-1}$) on mas-scales.

4.3.3 kpc-scale radio luminosities

We use the flux densities that we detect on kpc-scales (*i.e.* with our VLA observations) from Table 4.2 (Column 8) and determine the corresponding radio luminosities in 15 out of 20 cases, and from the literature for the rest (see Figure 4.4). The Mann-Whitney U test shows that there is no statistically significant difference in the distribution of radio power on arcsec-scales for Seyfert 1 and Seyfert 2 galaxies even at a significance level of 0.10. The Mann-Whitney U test also shows that there is no statistically significant difference in the distribution of core (the component of the source which is the closest to the optical nucleus within errorbars) radio power (Figure 4.5) on arcsec-scales for Seyfert 1 and Seyfert 2 galaxies even at a significance level of 0.10 (except NGC 7212, which has a positional discrepancy, see description of this object in Section 3.4.2). Our results are thus consistent with the predictions of the unification scheme hypothesis. They are also consistent with the results of Nagar et al. (1999B), who showed that the radio luminosities of Seyfert 1 and Seyfert 2 galaxies at 3.6 cm and 20 cm have

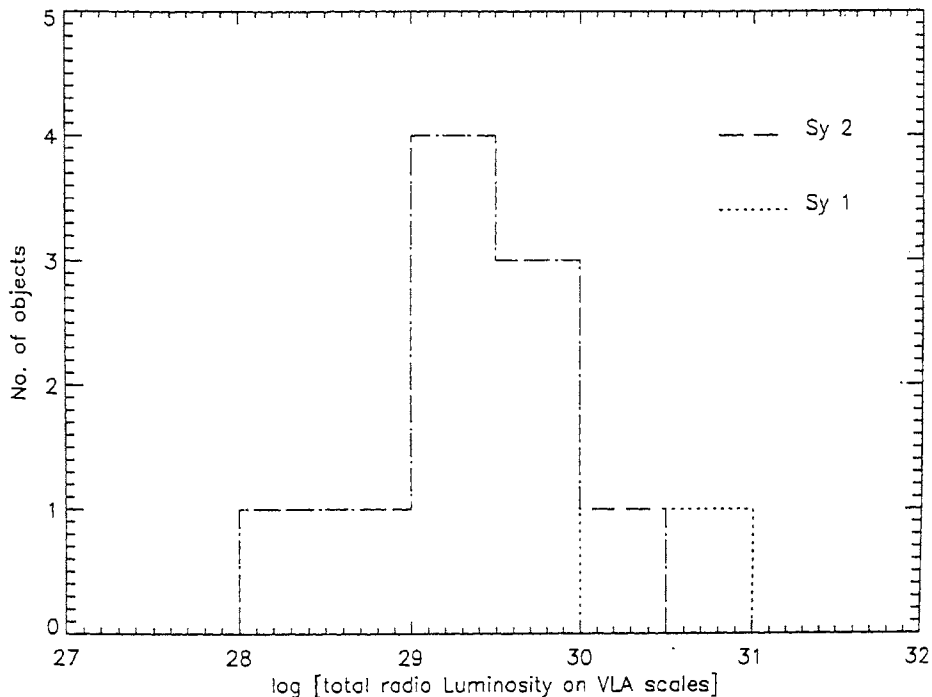


Figure 4.4: Histograms showing total radio power ($\text{ergs s}^{-1}\text{Hz}^{-1}$) on arcsec-scales.

similar distributions. Our result does not agree with Morganti et al.'s (1999), who found that Seyfert 2 galaxies tend to be more luminous than Seyfert 1 galaxies at marginal significance.

The NRAO VLA Sky Survey (NVSS, Condon et al. 1998) radio observations are made at 1.4 GHz using VLA *D* configuration. All our sample objects have measurements made using this instrument. Figure 4.6 shows that the two histograms of Seyfert 1 and Seyfert 2 galaxies are statistically similar for total 1.4 GHz radio luminosity (NVSS) as measured using VLA *D* configuration at a significance level of 0.05 using Mann-Whitney U test. This is again consistent with Nagar et al.'s (1999B) result.

4.3.4 Projected linear sizes

The linear sizes of Seyfert galaxies can be used to test the unification scheme because Seyfert 1 galaxies oriented at small angles to the line of sight should have systematically smaller linear sizes than Seyfert 2 galaxies in the plane of the sky.

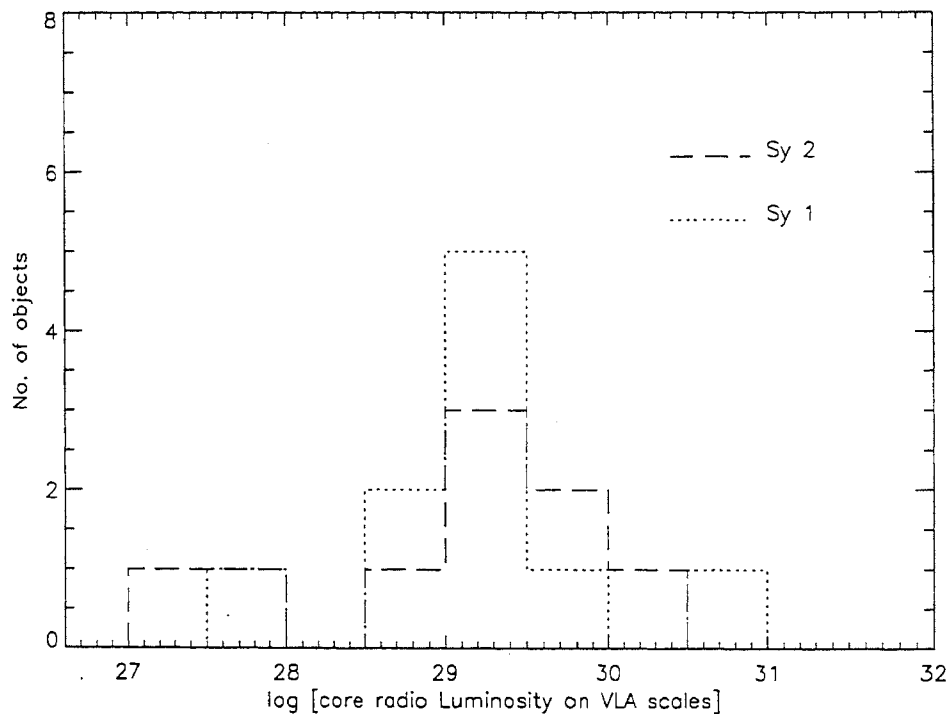


Figure 4.5: Histograms showing core radio power ($\text{ergs s}^{-1}\text{Hz}^{-1}$) on arcsec-scales.

For their distance limited sample of Seyfert galaxies, Morganti et al. (1999) found Seyfert 1 to be of systematically smaller sizes than Seyfert 2 galaxies. This is consistent with the prediction of the unified scheme. The prediction of this model is that the nuclear axes of Seyfert 1 galaxies are viewed more nearly pole-on, and so radio jets (and hence the linear sizes) for them are foreshortened by projection.

We determine the projected linear size of the source using

$$\text{Linear size of the source} = (\text{largest angular size}) \times \left(\frac{(c z) (1 + (z/2))}{H_0} \right); \quad (4.1)$$

for $q_0 = 0$. Here, c is the velocity of light, H_0 is Hubble parameter and z the redshift of the object.

We assume that the largest angular size of the source is the largest extent of the contour that is 5% of the peak surface brightness level. We have ensured that in all cases the 5% contour is well above the noise level in the map. We use this angular size to determine the linear radio size of the source. For NGC 5135, we use the 5% contour level from its 6 cm map (Ulvestad & Wilson 1989) for determining the largest

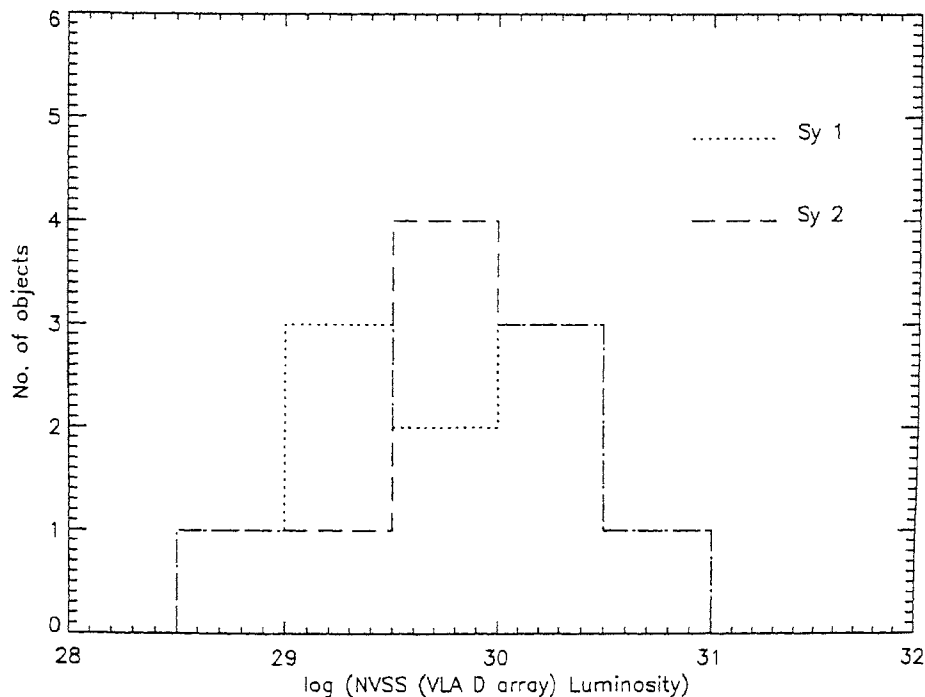


Figure 4.6: Histograms showing total (NVSS at 1.4 GHz) radio power ($\text{ergs s}^{-1}\text{Hz}^{-1}$) on arcsec-scales.

angular size. For the other objects Mrk 348 (Unger et al. 1984), NGC 4151 (Kukula et al. 1995) and Mrk 926 (Ulvestad & Wilson 1984A) we measure their corresponding largest angular sizes directly from the published maps. Mrk 231 is an unresolved object (Kukula et al. 1995). Table 4.2 gives the projected linear size of the source along with the reference.

In Figure 4.7, we plot the distribution of projected linear size for our sample of Seyfert 1 and Seyfert 2 galaxies. The Mann-Whitney U test shows that the distributions are not significantly different even at a significance level of 0.10. We also show the scatter plot of the radio luminosity on kpc-scales *versus* the projected linear size in Figure 4.8. Including the upper-limits to the linear size the correlation is significant at a level < 0.09 (Spearman's rank correlation test), for the Seyfert 1 and Seyfert 2 galaxies taken together. Thus, even though we restricted the range of the intrinsic AGN power for our sample (using $[\text{O III}] \lambda 5007$ luminosity parameter), we still find a significant correlation of these two parameters, earlier noted by Ulvestad & Wilson (1989) and Morganti et al. (1999) (Mrk 348 is one of our outliers, and is noted by

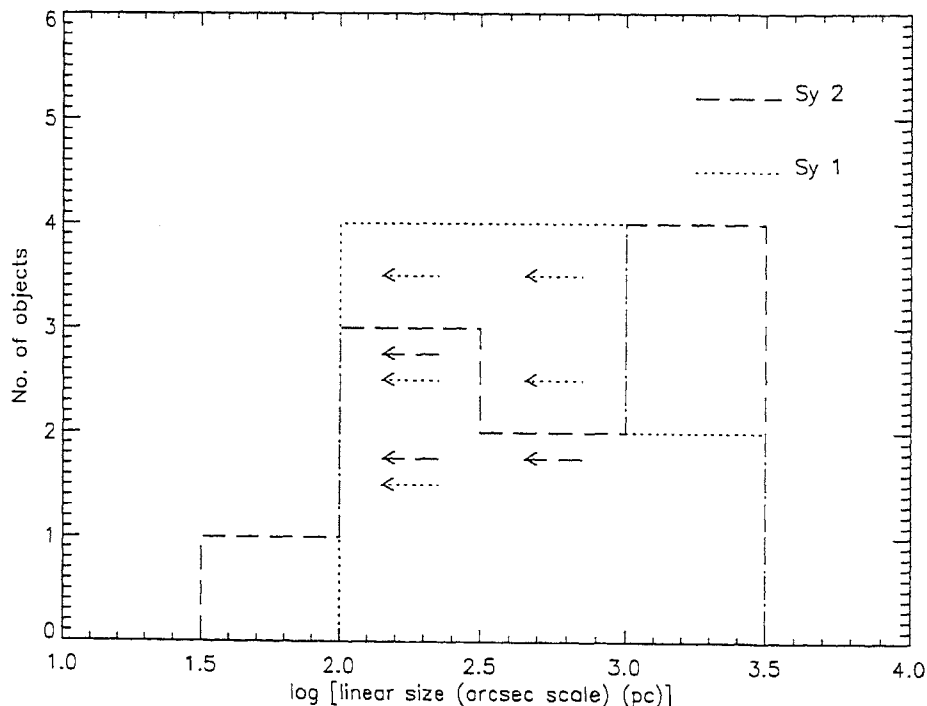


Figure 4.7: Histograms showing projected radio linear size (pc) on arcsec-scales; arrows denote objects that are unresolved.

Morganti et al. (1999); a projected linear size of 5 kpc (Baum et al. 1993) for this source puts it closer to the correlation). It thus appears that the intrinsic variation in the projected linear sizes is rather large and may swamp any systematic difference between Seyfert 1 and Seyfert 2 galaxies due to projection. Further, if the inter-stellar medium of the host galaxy affects the propagation of a Seyfert galaxy radio-jet, the fact that our sample has a paucity of Seyfert 2 galaxies with jet direction perpendicular to the host galaxy plane and Seyfert 1 galaxies with their jets propagating in the plane of the host galaxy disk, may also contribute to reduce the systematic differences in projected linear sizes between Seyfert 1 and Seyfert 2 galaxies.

4.3.5 Source spectral indices

The unified scheme predicts that Seyfert 1 and 2 galaxies arise from the same parent population of AGN and the derived orientation independent parameters should not show significantly different distributions. Morganti et al. (1999) did not find signifi-

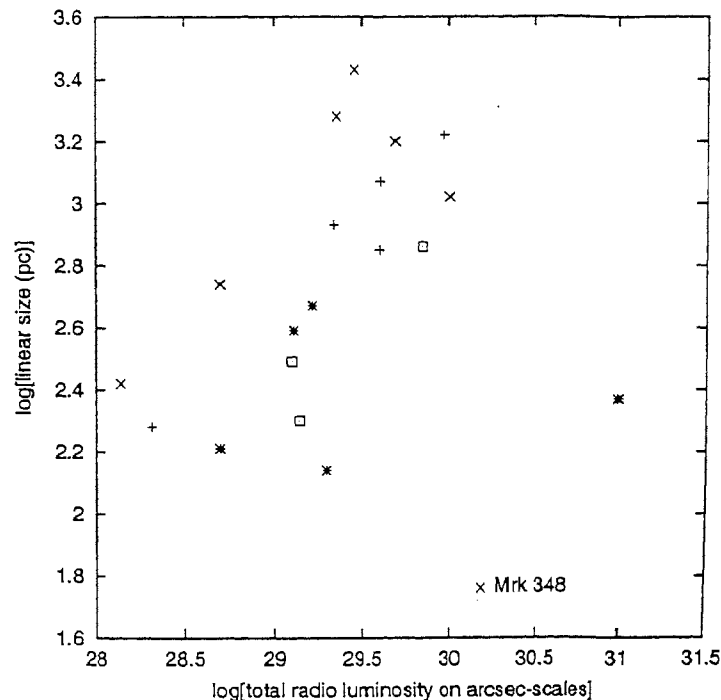


Figure 4.8: Scatter plot of projected linear size (pc) *versus* radio luminosity on kpc-scales ($\text{ergs s}^{-1}\text{Hz}^{-1}$); symbols +, x, *, and o denotes resolved Seyfert 1, resolved Seyfert 2, unresolved Seyfert 1, and unresolved Seyfert 2 galaxies respectively.

cantly different distribution of spectral index for Seyfert 1 and Seyfert 2 galaxies. We use our observations along with recent measurements at 2.0 , 3.6 , 6.0 and 20.0 cms, preferably VLA A or B configuration observations (when not available we use coarser resolution measurements) to determine the spectral indices, $\alpha_{20\text{ cm}}^6\text{ cm}$, $\alpha_{6\text{ cm}}^{3.6\text{ cm}}$, and $\alpha_{3.6\text{ cm}}^2\text{ cm}$, of the total flux density emitted (core plus the extended radio emission) of the source. The Table 4.3 gives the spectral indices for our sample. Seyfert galaxies, Mrk 348 and Mrk 231 show radio variability (see Tables 3.3 and 3.4, and Figures 3.3 and 3.15 respectively of Chapter 3). The flux density of NGC 2639 is presently rising (Wilson 1999, private communication). Mrk 231 between 1.4 and 5.0 GHz, Mrk 348 between 1.4 and 8.4 GHz, MCG 8-11-11 between 5.0 and 15 GHz, and NGC 5929 between 1.4 and 15 GHz show flat spectrum ($\alpha \leq 0.4$) radio cores. Mrk 231 between 1.4 and 5.0 GHz and Mrk 348 between 1.4 and 8.4 GHz show flat spectrum radio sources.

We plot the histograms (Figure 4.9) of the source spectral index (Column 11 of Table 4.3, $\alpha_{20\text{ cm}}^6\text{ cm}$) between 1.5 GHz (or 1.4 GHz) and 5 GHz (except for Mrk 348, where it

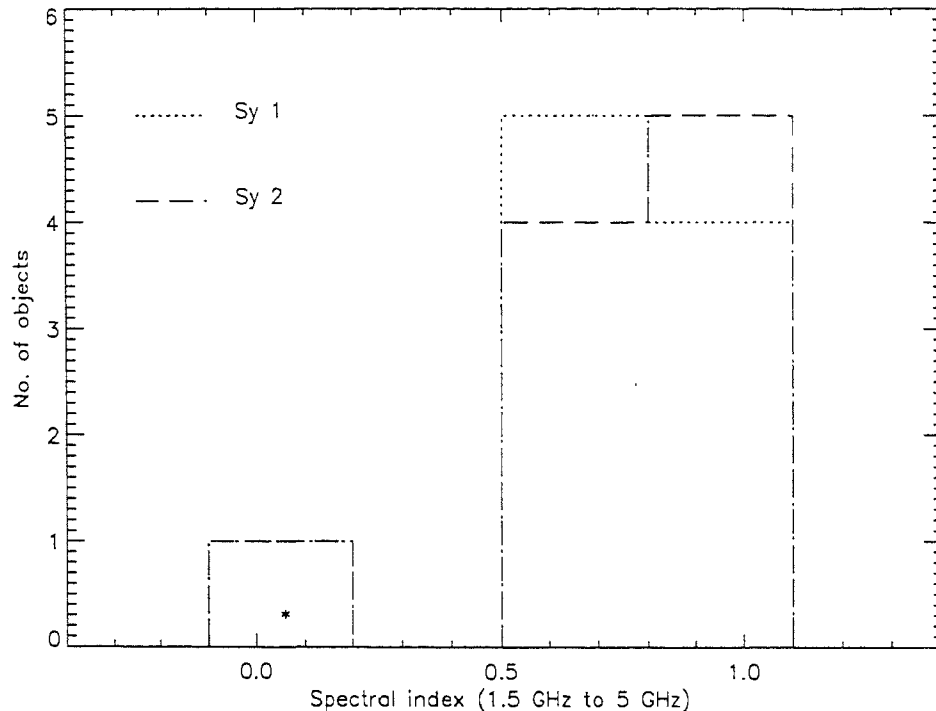


Figure 4.9: Spectral indices (between 1.5 and 5 GHz) of the sample sources; the spectral index between 1.5 and 8.4 GHz is used for Mrk 348 (denoted by asterisk '*').

is plotted between 5.0 GHz and 8.4 GHz). The Mann-Whitney U test shows that the distributions are virtually identical. Both Seyfert 1 and Seyfert 2 galaxies are equally likely to show flat/steep spectrum for the source. Our result at the stated significance level is consistent with the prediction of the unified scheme which does not have any preference for either kind of Seyfert galaxies to show flat/steep source spectrum.

4.3.6 Relativistic beaming in Seyfert galaxies?

In radio loud objects when the emitting plasma has bulk relativistic motion relative to a fixed observer, its emission is Doppler enhanced or beamed in the forward direction (in the fixed frame), a direct consequence of the transformation of angles in special relativity (a more detailed treatment is described below). An observer located in or near the path of this plasma sees much more intense emission than if the same plasma were at rest. Strong relativistic beaming is thought to explain the superluminal motion and high luminosities that characterize blazars (Blandford and Rees 1978). If present

in blazars, it may also be present in other AGNs where the radio-jet is pointed close to the line of sight of the observer.

The Doppler enhancement of flux density:

Blandford & Königl (1979) formulated the theory of bulk relativistic motion for a two-component “jet version” of the original model, and explored some of the consequences. In this model, the radio emission originates within a collimated supersonic jet that supplies the extended radio lobes with mass, momentum and energy. The required *in situ* acceleration of the emitting particles is achieved by means of mildly relativistic shocks propagating into the plasma and confined to a jet. The “fixed” component observed in the VLBI observations is identified in this model with the base of the jet.

One of the direct consequences of this bulk relativistic motion is that when the motion is in directions close to the line of sight, the observed radio flux density is apparently enhanced due to Doppler effects. The observed flux density S_{obs} of the jet at a frequency ν is related to the emitted flux density S_{em} that would be observed in the comoving frame at the same emitted frequency ν as

$$S_{obs} = S_{em} D^3.$$

D , the Doppler factor, is the ratio of observed to emitted frequency and is given by

$$D = \gamma^{-1} \left(1 - \frac{v}{c} \cos \theta\right)^{-1},$$

where θ is the angle of inclination of the direction of bulk relativistic motion to the line of sight, v is velocity of the flow, and γ is the Lorentz factor.

In this model, wherein the radio core component is constituted of relativistically moving sub-components, the observed flux density would be enhanced by Doppler effects for directions close to the line of sight.

Seyfert galaxies have low radio emission, but they do show radio emitting jet-like structures on small scales which appear to be the low-power analogues of jets seen in radio powerful AGNs (Nagar et al. 1999B and references therein). If this AGN-linked radio emission originates from plasma with sub-relativistic bulk motion, the unified scheme would predict that Seyfert 1 and Seyfert 2 galaxies should have similar radio morphologies on all scales and it would be independent of orientation of the Seyfert galaxy. But, if this radio emitting plasma has mildly relativistic bulk speeds (Bicknell, 1998, Ulvestad 1999B), the unified scheme would predict that Seyfert 1 galaxies, in

which the radio axis is oriented close to the observers line of sight, should show mild Doppler beaming of the radio cores, whereas Seyfert 2 galaxies should not exhibit such behaviour. So far all the relativistically boosted jets with superluminal motion have only been detected in radio-loud objects, except for the following result: Brunthaler et al. (2000) have recently discovered superluminal motion in the Seyfert 1 galaxy, III Zw 2. III Zw 2 is a Seyfert 1 galaxy that conforms to our definition of Seyfert galaxies. This is the first detection of superluminal motion in a Seyfert nucleus in a spiral galaxy. Recent observations of the two Seyfert galaxies, Mrk 348 and Mrk 231 by Ulvestad et al. (1999B), showed sub-relativistic expansion in them.

For our sample of Seyfert galaxies we test the beaming hypothesis, which states that if the jets of Seyfert 1 galaxies are relativistically beamed then the pc-scale radio emission would be Doppler boosted in them and not in Seyfert 2 galaxies.

In radio-loud AGN, the core flux density is Doppler enhanced due to relativistic beaming, while the extended flux density (the flux density of the lobes in radio-loud objects) is not enhanced. Therefore, the ratio of the core and extended flux densities becomes a beaming indicator (*e.g.* Kapahi & Saikia 1982). We define an analogous parameter R for Seyfert galaxies as

$$R = \frac{S_{\nu \text{ compact}}}{S_{\nu \text{ ext}}},$$

where $S_{\nu \text{ compact}}$ is the flux density that we measure on pc-scales and $S_{\nu \text{ ext}}$ is defined as the difference of the total flux density detected at kpc-scale and the flux density detected on pc-scales. If the detected pc-scale emission is coming primarily from ejected plasma close to the nucleus, then by comparing the pc-scale radio emission with the kpc-scale extended emission for the two classes of Seyfert galaxies, one could test the relativistic beaming hypothesis. This is because if there is bulk relativistic motion in Seyfert galaxies, then under the above assumptions, the Seyfert 1 galaxies would show larger R than the Seyfert 2 galaxies.

The radio flux density variability in Seyfert galaxies have not been looked for, but we know that at least two (Mrk 231 and Mrk 348) of our sample sources do show radio variability. Due to the availability of simultaneous arcsec-scale data (VLA) for our sample objects, we are able to test for the presence of beaming without worrying about possible variability in the compact radio flux densities in 15 out of 20 cases. For the rest of the sample objects (which are not observed by us) we use measurements on pc and kpc-scales which are made at epochs as closely spaced in time as possible (see Table 4.2).

In Figure 4.10, we plot the histograms of the ratio R . We also look at the the distribution of the ratio of the radio flux density detected on pc-scales to that at kpc-scales (Figure 4.2) for Seyfert 1 and Seyfert 2 galaxies. Mann-Whitney U test shows that the distributions are not significantly different even at a level of 0.10. In other words, the compact structures detected on pc-scales are not boosted in Seyfert galaxies.

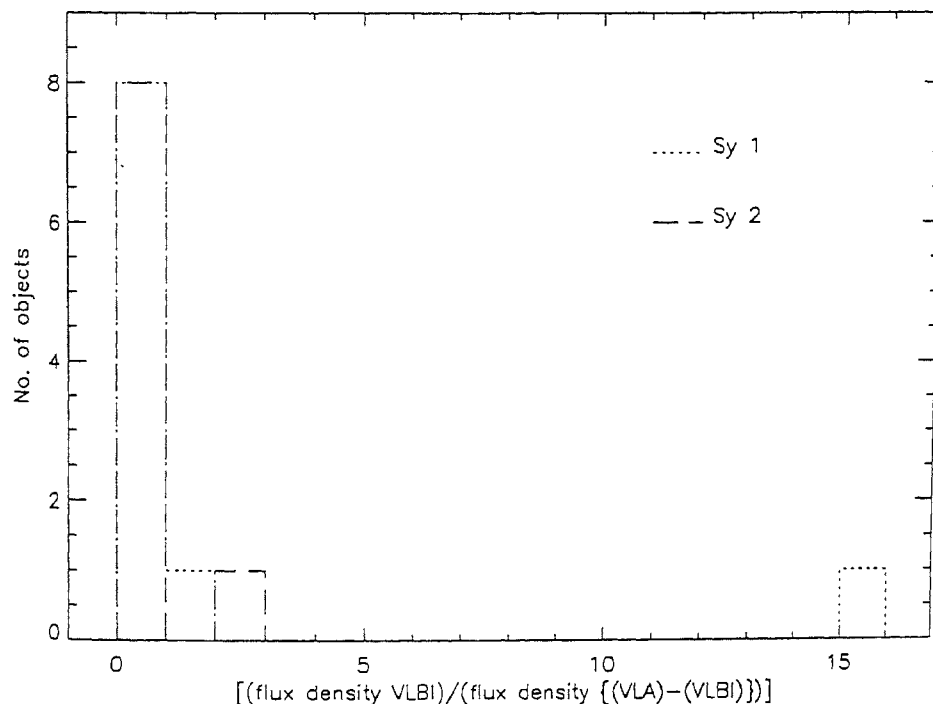


Figure 4.10: Histograms of the fraction of the total radio flux density detected on mas-scales as against the extended radio emission.

4.4 CfA Seyfert galaxy sample: kpc-scale radio morphology

The CfA Seyfert sample (Huchra & Burg 1992) is drawn from 2399 galaxies in the CfA Redshift survey (Davies et al. 1983, Huchra et al. 1983) and consists of 48 objects (24 Seyfert 1.0 & Seyfert 1.5, 4 Seyfert 1.8, 4 Seyfert 1.9, and 15 Seyfert 2.0) chosen solely on the basis of strong emission lines in their spectra. Kukula et al. (1995) made observations of the sample at 8.4 GHz with the VLA in *A* and *C* configuration in 1991 June and 1992 April respectively. The observational results of the sample along

with individual source morphology, radio maps, flux densities, etc. have been presented in their paper (Kukula et al. 1995). In the CfA Seyfert galaxy sample the unresolved optical nucleus of a Seyfert galaxy grows fainter with the square of distance, whilst the surface brightness of its host galaxy remains constant over a constant aperture. Therefore, in this sample the ratio of the two components (the host galaxy to the active nucleus surface brightness) is highly variable. In spite of this bias, it is one of the best samples available in the literature. It has a larger number of objects than in our sample. Hence, we use it to test the unified scheme hypothesis. We use Kukula et al.'s (1995) data and plot the distribution for Seyfert 1 galaxies (Seyfert 1.0, 1.5 and 1.8) and Seyfert 2 galaxies (Seyfert 1.9 and 2.0) to compare radio luminosities, projected linear sizes, and relativistic beaming. Note that, as per our definition, Seyfert 1 galaxy has Doppler widths of permitted emission lines greater than 1000 km s^{-1} , all, Seyfert 1.0, 1.5 and 1.8 show line widths which are greater than 1000 km s^{-1} ; whereas Seyfert 1.9 and 2.0 do not (Seyfert 1.9 shows faint $\text{H } \alpha$ and not $\text{H } \beta$).

4.4.1 Radio luminosity comparisons

Almost all the objects in this well defined sample were detected at radio wavelengths (40 of the 48 by VLA *A* array and 42 of the 48 by VLA *C* array), so it is valid to test for the distribution of total (VLA *A* array and VLA *C* array) radio luminosity; Figures 4.11 and 4.12 suggest that there is a strong similarity in the two distribution for Seyfert 1 and Seyfert 2 galaxies. We compare the radio powers of two classes of the Seyfert galaxies from these measurements. Arrows in the two distributions denote upper limits, which we do not include in the analysis.

We use the Mann-Whitney U test to test the hypothesis that the two distributions of total radio power detected using VLA *A* configuration and VLA *C* configuration are similar. The results of this test indicate that the distribution of Seyfert 1 and Seyfert 2 galaxies are similar (probability that the two sub-samples are different is 34% for the CfA Seyfert sample using VLA *A* array at 8.4 GHz and is 25% for the CfA Seyfert sample using VLA *C* array at 8.4 GHz). Therefore, this indicates that the VLA *A* configuration and VLA *C* configuration distributions are probably the same, although the probability that they are the same are only 66% and 74% respectively.

We also compare the distribution of the extended radio luminosity, corresponding to the difference of the flux density detected by the VLA *C* and VLA *A* array (Figure 4.13). The Mann-Whitney U test gives a probability of 40% that the distribution of Seyfert 1 and Seyfert 2 galaxies are different. In other words, the probability that the

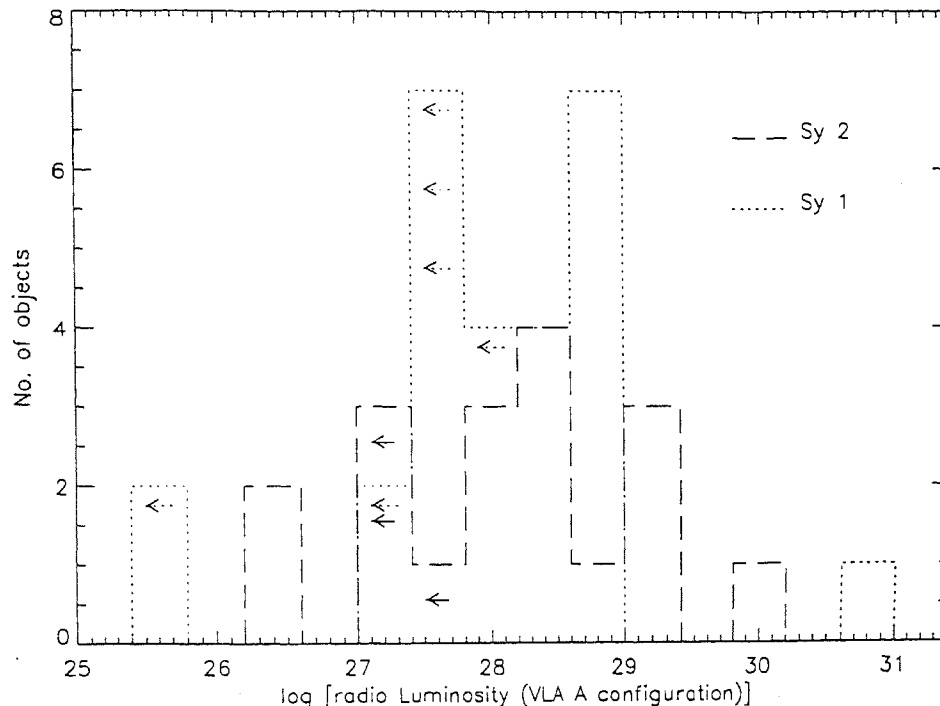


Figure 4.11: Histograms showing the total detected radio power ($\text{ergs s}^{-1}\text{Hz}^{-1}$) for the CfA Seyfert sample using VLA A array at 8.4 GHz.

distributions of the extended radio luminosities of the Seyfert 1 and Seyfert 2 galaxies are the same is 60%. This probability is not high enough to demonstrate statistically that the distributions are the same, but it does not contradict the possibility that they are the same.

We thus conclude that the distributions of the radio luminosity of Seyfert 1 and Seyfert 2 galaxies for the CfA Seyfert sample at 8.4 GHz are probably similar (core and the extended radio emission) at all scales. This is consistent with the predictions of the unified scheme, *i.e.* results obtained from the CfA Seyfert sample are also consistent with the predictions of the unified scheme.

4.4.2 Projected linear sizes

The following Table summarises the classification of the radio morphology for the CfA Seyfert sample, following the scheme of Ulvestad & Wilson (1984B). The corresponding number shows the number of sources seen of the kinds mentioned in Ulvestad & Wilson

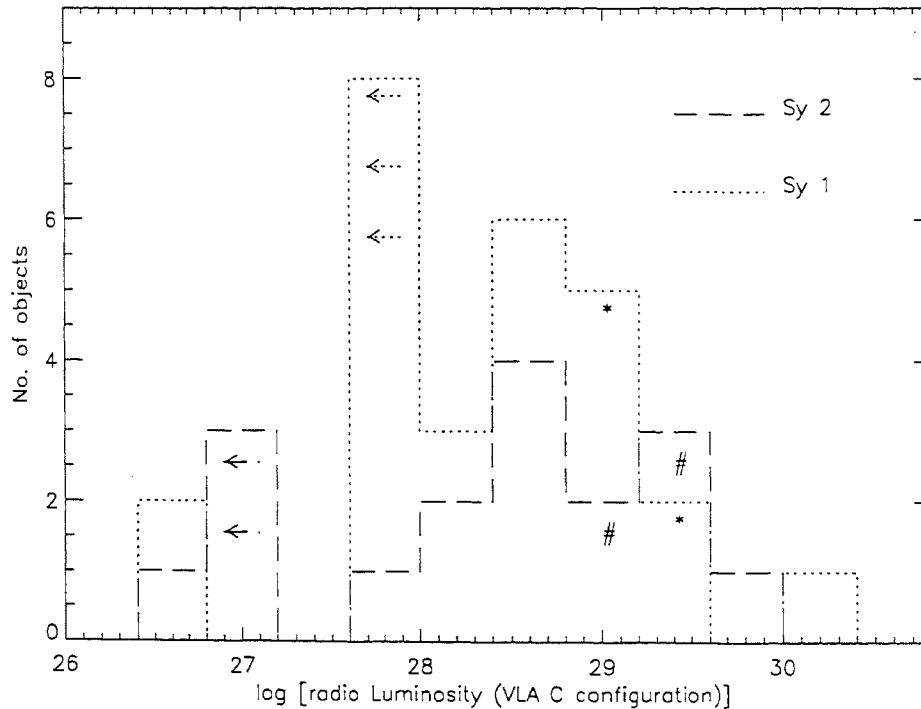


Figure 4.12: Histograms showing the radio luminosity ($\text{ergs s}^{-1}\text{Hz}^{-1}$) for the CfA Seyfert sample using VLA *C* array at 8.4 GHz; ‘*’ and ‘#’ denote an error of $\sim 20\%$ in flux density calibration for Seyfert 1 and 2 galaxies respectively, and arrows denote undetected objects.

(1984B), on each VLA configuration.

	VLA <i>A</i> array	VLA <i>C</i> array
not detected	8	6
unresolved	17	20
slightly resolved	5	9
resolved	14	8
Compact double	1	1
no data	3	4

We can compare these numbers with the results from Ulvestad & Wilson (1989 and references therein; see also the Section VI. in Wilson 1991). As compared to Wilson (1991), Kukula et al.’s (1995) measurements show a higher fraction of unresolved sources and a lower fraction of galaxies with diffuse/linear radio emission. This result

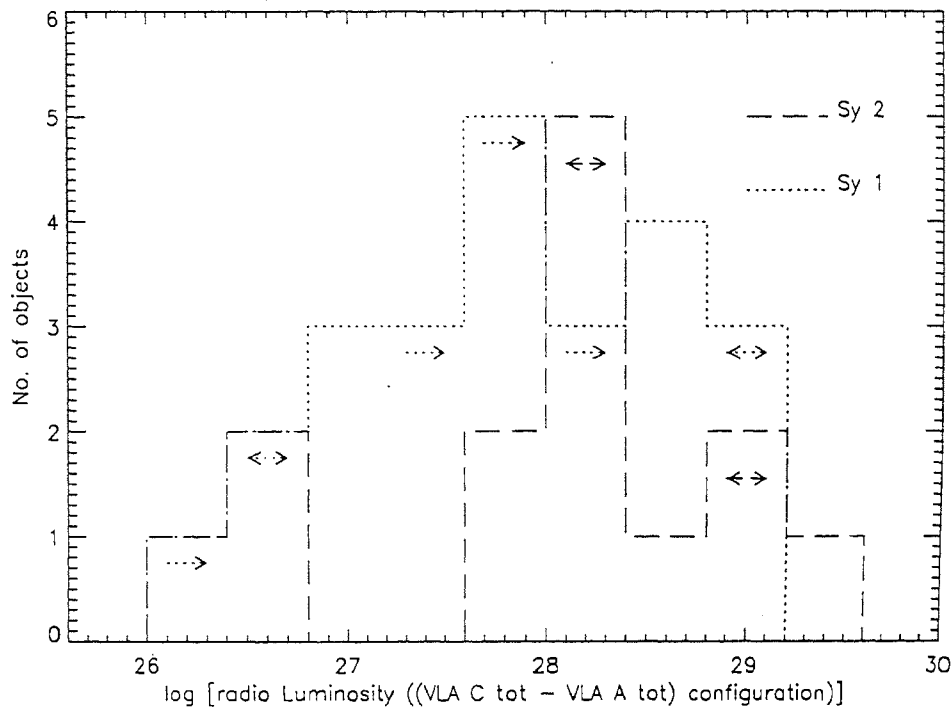


Figure 4.13: Histograms showing the total extended radio power ($\text{ergs s}^{-1}\text{Hz}^{-1}$) for the CfA Seyfert sample at 8.4 GHz; single-headed arrow indicates non-detection on VLA A configuration and double-headed arrow indicates non-detection on both the configurations.

may be due to an observational bias; these observations are not as sensitive to diffuse, extended, steep spectrum emission as are the 20 cm VLA observations of, *e.g.*, Ulvestad & Wilson (1989).

We use angular sizes tabulated in Kukula et al.'s (1995) paper along with equation 4.1 to determine the linear size and plot the distribution of linear sizes derived from VLA A array (Figure 4.14) and VLA C array (Figure 4.15) measurements for the two classes of Seyfert galaxies. Arrows denote the upper limits to the sizes and we do not take them into account while doing statistical tests.

Once again, to quantify the similarity of the two distributions we use the Mann-Whitney U test, which shows that the distribution of linear sizes are not the same. Seyfert 2 galaxies tend to show larger projected linear sizes than Seyfert 1 galaxies. The projected linear size determined on the basis of VLA C configuration measurement suggests marginal difference (the probability for Seyfert 1 and Seyfert 2 galaxies to be different is 91.6%) in the linear projected sizes of the two classes of the Seyfert galaxies.

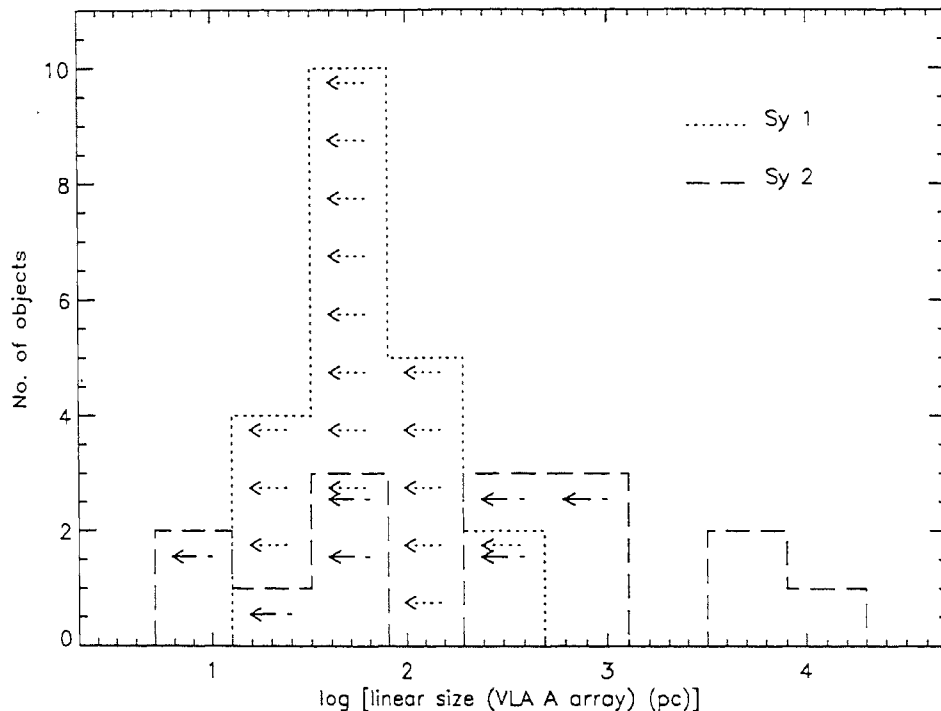


Figure 4.14: Histograms showing projected linear size (pc) of the source as measured by VLA *A* array (CfA Seyfert galaxy sample); arrows indicate unresolved objects.

Whereas the linear size corresponding to VLA *A* configuration measurement suggests that Seyfert 2 galaxies have larger projected linear sizes than Seyfert 1 galaxies, and there is statistically significant difference in the projected linear size between them ($P < 0.05$). We thus believe that there is difference in the linear sizes of the two classes of Seyfert galaxies when found using VLA *A* configuration and it is consistent with the unified scheme, whereas when found using VLA *C* configuration the difference is at the most marginal. This statistically significant difference in the projected linear radio sizes between Seyfert 1 and Seyfert 2 galaxies is consistent with the predictions of unified scheme hypothesis. This is also consistent with the result obtained by Morganti et al. (1999).

4.4.3 Relativistic beaming

To investigate relativistic beaming, we use the distribution of the ratio between the possibly beamed and extended radio flux density. We assume that the emission asso-

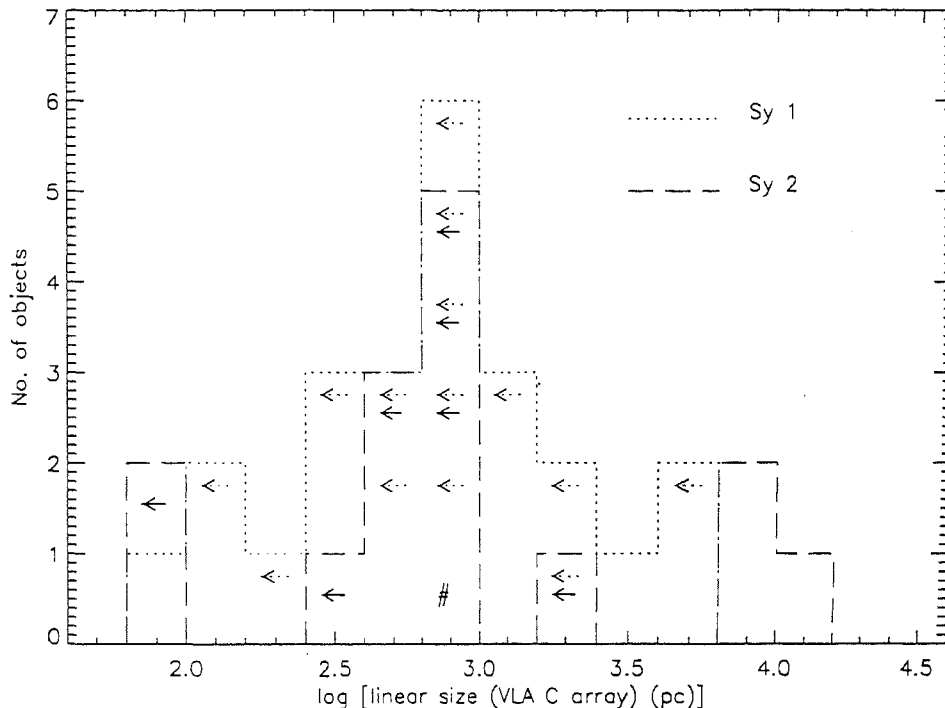


Figure 4.15: Histograms showing projected linear size (pc) of the source as measured by VLA *C* array (CfA Seyfert galaxy sample); ‘#’ for an object in a bin denotes the VLA *A* array linear size for it, and arrows indicate unresolved objects.

ciated with the difference of the emissions between VLA *C* and VLA *A* configurations would not be Doppler boosted and we call this as an extended emission. The VLA *A* configuration measurement probes structures on scales smaller than VLA *C* configuration and we use VLA *A* configuration emission as the one which would suffer from Doppler boosting if beaming is present. Using the ratio R , of the two, VLA *A* configuration emission to the extended emission, as an indicator of relativistic beaming (once again without accounting for the upper limits), we compare the distribution of R for the two classes of the Seyfert galaxies. Figure 4.16 shows the distribution. The Mann-Whitney U test is not conclusive about whether the distributions are the same or not (probability of them being different is 56%).

The distribution of R and its statistical significance does not actually compare the flux density detected on pc-scales as against the extended emission and hence is not really a measure of relativistic beaming. But nevertheless we use it as an indicator to probe the boosting of core flux density in Seyfert galaxies. Since it is equally likely

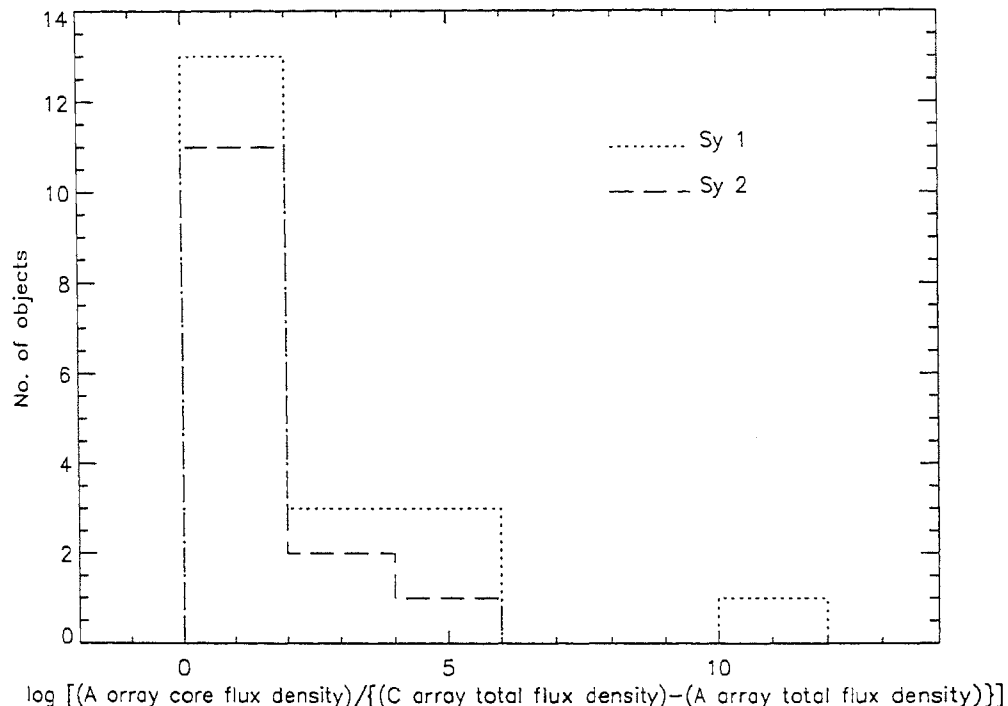


Figure 4.16: Histograms showing fraction of the radio core flux density detected by VLA *A* array as against the extended flux density at 8.4 GHz for CfA Seyfert sample.

that the distributions obtained here are either same or different, and considering also the results discussed above (based on our pc-scale result), we conclude that Seyfert galaxies do not show relativistic bulk motion in their nuclei.

4.5 Summary

Using our measured radio flux densities of the pc-scale and kpc-scale structures for Seyfert galaxies and from their detection rates, radio luminosities, spectral indices and projected linear sizes, we find that: (1) A starburst alone cannot power these radio sources because, (i) they have high brightness temperature, and (ii) the core radio luminosity at 5 GHz is $\sim 10^{28}$ ergs $s^{-1}Hz^{-1}$ and arises from a region smaller than a few cubic pc. (2) Seyfert 1 and Seyfert 2 galaxies have equal tendency to show compact radio structures, in contrast to the results of Roy et al. (1994), who concluded that compact radio structures were much more common in Seyfert 2 galaxies than in Seyfert 1 galaxies. Thus the contradiction that Roy et al. (1994) found with

the unified scheme no longer exists. (3) The distributions of pc and kpc-scale radio luminosities are similar for both Seyfert 1 and Seyfert 2 galaxies. This is consistent with the prediction of the unified scheme hypothesis. (4) We do not find any evidence for relativistic beaming in Seyfert galaxies. (5) Seyfert 1 and Seyfert 2 galaxies show similar distributions of source spectral indices. (6) The unification scheme hypothesis predicts that Seyfert 1 galaxies oriented at small angles to the line of sight should have systematically smaller projected linear size than Seyfert 2 galaxies. The kpc-scale projected linear sizes correlate with the radio luminosity. Their distributions for Seyfert 1 and Seyfert 2 galaxies of our sample are not significantly different as they would be expected in the unified scheme. This could be mainly due to a relatively large spread in the intrinsic sizes. There could also be a contribution from the selection effect, *viz.*, the paucity of Seyfert 1 galaxies with their radio axes in the plane of the host galaxy, and of Seyfert 2 galaxies with their jet axes perpendicular to the host galaxy plane.

From the observations of the CfA Seyfert galaxy sample and the kpc-scale data from them, the radio luminosities, projected linear size for the two classes of Seyfert galaxies and the ratio of flux density detected on VLA *A* configuration and the extended emission are consistent with the unification scheme hypothesis.

	S_{ν} Total (NVSS 1.4 GHz) (mJy)	S_{ν} Total (kpc-scale) (mJy)	S_{ν} Core (kpc-scale) (mJy)	S_{ν} Total (pc-scale) (mJy)	Dist (Mpc)	$L_{(NVSS\ 1.4\ GHz)}$ Total (ergs s ⁻¹ Hz ⁻¹)	$L_{(kpc-scale)}$ Total (ergs s ⁻¹ Hz ⁻¹)	$L_{(kpc-scale)}$ Core (ergs s ⁻¹ Hz ⁻¹)	$L_{(pc-scale)}$ Total (ergs s ⁻¹ Hz ⁻¹)	Linear size (log(size)) (pc)
Mrk 348	277.3	346.0 ^a	310.3 ^a	163.0 ^b	59.557	1.20 x 10 ³⁰	1.495 x 10 ³⁰	1.340 x 10 ³⁰	7.043 x 10 ²⁹	1.76 ^{Aa}
Mrk 1	70.8	27.65	24.08	4.384	63.496	3.48 x 10 ²⁹	1.359 x 10 ²⁹	1.183 x 10 ²⁹	2.115 x 10 ²⁸	< 2.30 ^{Ab}
MCG 8-11-11	228.3	75.76	23.57	4.886	98.781	2.74 x 10 ³⁰	9.095 x 10 ²⁹	2.830 x 10 ²⁹	5.866 x 10 ²⁸	3.22 ^{Ab}
NGC 2273	59.7	19.92	12.13	6.313	23.928	4.13 x 10 ²⁸	1.377 x 10 ²⁸	8.383 x 10 ²⁷	4.364 x 10 ²⁷	2.42 ^{Ab}
Mrk 78	35.0	10.46	8.87	7.815	145.36	9.20 x 10 ²⁹	2.751 x 10 ²⁹	2.333 x 10 ²⁹	2.055 x 10 ²⁹	3.43 ^{Ab}
Mrk 1218	63.6	24.04	18.72	9.984	114.365	1.03 x 10 ³⁰	3.884 x 10 ²⁹	3.024 x 10 ²⁹	1.213 x 10 ²⁹	2.85 ^{Ab}
NGC 2639	105.5	83.63	63.47	39.54	43.761	2.45 x 10 ²⁹	1.943 x 10 ²⁹	1.475 x 10 ²⁹	9.189 x 10 ²⁸	< 2.14 ^{Ab}
NGC 4151	345.8	120.0 ^c	43.0 ^c	10.0 ^d	11.982	5.98 x 10 ²⁸	2.074 x 10 ²⁸	7.432 x 10 ²⁷	3.457 x 10 ²⁷	2.57 ^{Ae}
Mrk 766	37.6	15.16	13.75	3.684	51.666	1.22 x 10 ²⁸	4.920 x 10 ²⁸	4.462 x 10 ²⁸	1.196 x 10 ²⁸	< 2.21 ^{Ab}
Mrk 231	282.9	282.0 ^e	270.0 ^e	173.0 ^e	164.614	9.59 x 10 ³⁰	5.863 x 10 ³⁰	5.524 x 10 ³⁰	2.304 x 10 ³⁰	< 2.37 ^{Ae}
NGC 5135	190.0	58.8 ^g	16.15 ^g	16.15 ^g	55.613	7.15 x 10 ²⁹	2.213 x 10 ²⁹	6.080 x 10 ²⁸	3.28 ^{Ac}	3.28 ^{Ac}
Mrk 477	60.7	24.39	22.97	8.188	149.218	1.68 x 10 ³⁰	6.766 x 10 ²⁹	6.637 x 10 ²⁹	2.271 x 10 ²⁹	< 2.86 ^{Ad}
NGC 5929	105.5	31.74	1.28 ^h	6.284	35.839	1.64 x 10 ²⁹	4.934 x 10 ²⁸	1.989 x 10 ²⁷	9.775 x 10 ²⁷	2.78 ^{Ab}
NGC 7212	108.9	33.94	11.3	6.577	106.58	1.52 x 10 ³⁰	4.753 x 10 ²⁹	1.989 x 10 ²⁷	9.209 x 10 ²⁸	3.20 ^{Ab}
Ark 564	27.7	11.3	8.62	3.222	94.875	3.06 x 10 ²⁹	1.250 x 10 ²⁹	9.540 x 10 ²⁸	3.565 x 10 ²⁸	< 2.59 ^{Ab}
NGC 7469	167.7	43.56	21.97	6.17	63.496	8.25 x 10 ²⁹	2.142 x 10 ²⁹	1.080 x 10 ²⁹	3.034 x 10 ²⁸	2.93 ^{Ab}
Mrk 926	33.0	9.0 ⁱ	7.69 ⁱ	5.0 ^j	183.78	1.40 x 10 ³⁰	3.820 x 10 ²⁹	3.264 x 10 ²⁹	2.122 x 10 ²⁹	3.07 ^{Aj}
Mrk 530	23.5	9.17	8.02	8.627	118.252	4.63 x 10 ²⁹	1.585 x 10 ²⁹	1.385 x 10 ²⁹	1.491 x 10 ²⁹	< 2.67 ^{Ab}
Mrk 533	206.4	60.37	38.2	16.962	114.365	3.33 x 10 ³⁰	9.735 x 10 ²⁹	6.169 x 10 ²⁹	2.740 x 10 ²⁹	3.02 ^{Ab}
NGC 7682	58.6	22.21	21.98	8.918	67.432	3.25 x 10 ²⁹	1.232 x 10 ²⁹	1.222 x 10 ²⁹	4.950 x 10 ²⁸	< 2.49 ^{Ab}

References:

- ^a Nov 1996, VLA 8.4 GHz measurement; Thean et al. 2000
^b Apr 1995, VLBA 8.4 GHz measurement; Barvainis & Lonsdale 1998
^c Mar 1980, VLA 5.0 GHz measurement; Johnston et al. 1982
^d May/June 1996, VLBA 5.0 GHz measurement; Ulvestad et al. 1998B
^e Dec 1996, VLA 5.0 GHz measurement; Ulvestad et al. 1999A
^f Dec 1996, VLBA 15.0 GHz measurement; Ulvestad et al. 1999B
^g Feb 1985, VLA 5.0 GHz measurement; Ulvestad & Wilson 1989
^h Mar 1989, MERLIN measurements and $\alpha_{18\ cm}^2 = 0.32$; Su et al. 1996
ⁱ May 1982, VLA 5.0 GHz measurement; Ulvestad 1984A
^j Jul 1997, VLBA 8.4 GHz measurement; Mundell et al. 2000

- ^{Aa}Unger et al. (1984)
^{Ab}Our measurements
^{Ac}Ulvestad & Wilson (1989)
^{Ad}Pedlar et al. (1993)
^{Ae}Kukula et al. (1995)
^{Aj}Ulvestad & Wilson (1984A)

Table 4.2: Table giving total, core flux densities, and the corresponding radio power on arcmin (NVSS, Condon et al. 1998), arcsec, and mas-scales, and logarithm of the linear size of source in pc; arcsec and mas-scale data are from our observations unless otherwise indicated.

Object name	Total flux density					Spectral index (total)		
	$S_{1.5}$ GHz	$S_{5.0}$ GHz	$S_{8.4}$ GHz	S_{16} GHz	S_{30} GHz	$\alpha_{5.0}^{8.4}$ cm	$\alpha_{8.4}^{16}$ cm	α_{16}^{30} cm
Mrk 348	302.2			238.0	0.14			
Mrk 1	68.0	27.65		15.4	0.86	0.75	1.13	
MCG 8-11-11	180.0	75.76		38.4	20.0	0.90	1.31	1.13
NGC 2273	52.0	19.92		10.2	0.95	0.80	1.29	
Mrk 78	31.0	10.46				0.90		
Mrk 1218	65.0	24.04				0.83		
NGC 2639	104.0	54.50				0.54		
NGC 4151	330.0	120.00		72.32	23.9	0.88	0.84	0.98
Mrk 766	39.3	15.16		8.68		0.88	0.79	1.09
Mrk 231	280.0	355.00		< 284.0		-0.20		
NGC 5135	163.2	58.80				0.85		
Mrk 477	60.7	24.39				0.76		
NGC 5929	64.7	31.74		16.75	9.0	0.78	0.59	1.23
NGC 7212	108.8	33.94	> 9.0			0.97		
Mrk 564	27.7	11.30	7.0			0.74	0.92	
NGC 7469	134.0	43.56	15.97	8.0	1.23	0.93	1.93	1.19
Mrk 926	33.0	9.00				1.07		
Mrk 530	23.5	9.17	3.26			0.78	2.00	
Mrk 533	160.0	60.37	39.77			0.81	0.81	0.80
NGC 7682	61.6	22.21	13.46			0.88	0.84	0.97

References:

- Mrk 348 1.5 & 8.4 GHz measurements are from Nagar et al. (1999B)
- Mrk 1 1.5 GHz from de Bruyn & Wilson (1976), 5.0 GHz our measurement, and 8.4 GHz from Schmitt et al. (2000)
- MCG 8-11-11 1.5 GHz from Unger et al. (1986), 5.0 GHz our measurement, 8.4 GHz from Schmitt et al. (2000), and 15 GHz from Ulvestad & Wilson (1986)
- NGC 2273 1.5 GHz from Nagar et al. (1999B), 5.0 GHz our measurement, and 8.4 GHz from Nagar et al. (1999B)
- Mrk 78 1.5 measurement from Ulvestad & Wilson (1984A) and 5.0 GHz our measurement
- Mrk 1218 1.5 & 5.0 GHz measurements are from Ulvestad & Wilson (1989)
- NGC 2639 1.5 & 5.0 GHz measurements are from Johnston et al. (1982), 8.4 GHz from Kukula et al. (1995), and 15 GHz from Wilson & Ulvestad (1982)
- NGC 4151 1.5 GHz from Nagar et al. (1999B), 5.0 GHz our measurement, and 8.4 GHz from Nagar et al. (1999B)
- Mrk 766 All measurements are from Ulvestad et al. (1999A)
- Mrk 231 1.5 & 5.0 GHz measurements are from Ulvestad & Wilson (1989)
- NGC 5135 1.5 GHz measurement is NVSS (VLA D array) and 5.0 GHz our measurement is from Ulvestad & Wilson (1984B)
- Mrk 477 All measurements are from Su et al. (1996)
- NGC 5929 1.5 GHz measurement is NVSS (VLA D array), 5.0 GHz our measurement and 8.4 GHz is from Falcke et al. (1998)
- NGC 7212 1.5 GHz measurement is NVSS (VLA D array), 5.0 GHz our measurement and 8.4 GHz is from Schmitt et al. (2000)
- Mrk 564 1.5 GHz from Unger et al. (1986), 5.0 GHz our measurement, 8.4 GHz from Kukula et al. (1995), and 15 GHz from Wilson et al. (1991)
- NGC 7469 1.5 GHz measurement is NVSS (VLA D array) and 5.0 GHz flux density measurements are from Ulvestad & Wilson (1984B)
- Mrk 926 1.5 GHz measurement is NVSS (VLA D array), 5.0 GHz our measurement and 8.4 GHz from Kukula et al. (1995)
- Mrk 530 1.5 GHz from Unger et al. (1986), 5.0 GHz our measurement and 8.4 GHz from Kukula et al. (1995)
- Mrk 533 1.5 GHz from Edelson (1987), 5.0 GHz our measurement and 8.4 GHz from Kukula et al. (1995)
- NGC 7682 1.5 GHz from Edelson (1987), 5.0 GHz our measurement and 8.4 GHz from Kukula et al. (1995)

Table 4.3: Source flux densities and spectral indices.

Chapter 5

Further tests of unification: Infrared and X-ray data

5.1 Introduction

In the previous Chapter (Chapter 4) we used our sample, matched in orientation independent parameters, to test the predictions of the unified scheme in the radio domain.

In this Chapter we use our sample to test the predictions of the unified scheme in other wavelength domains as well, the data for which have been taken from published literature. We address the following issues in this Chapter: In Section 5.2, we look at the infrared data and its consistency with the unified scheme. We also look at the radio–infrared correlation at various scales and probe the nature of emission in them. In Section 5.4 we test the consistency of hard X-ray luminosity and photon index with the unification scheme. We discuss all these parameters in the light of the unified scheme and present the implications of our results.

5.2 The infrared luminosity distribution

The unification scheme hypothesis predicts that if the infrared emission from Seyfert galaxies is an orientation independent parameter then the infrared powers should show similar distributions for Seyfert 1 and Seyfert 2 galaxies. We use the values tabulated in Lipovetsky et al.’s (1988) catalogue at 12 μm , 25 μm , 60 μm , and 100 μm data. Table 5.1 gives flux densities and corresponding luminosities for 17 out of 20 (8 Seyfert 1 and 9 Seyfert 2 galaxies) objects from our sample. The data for NGC 4151 have been taken from Rush et al. (1993). In the following Sections (5.2.1 and 5.2.2), we look at

the distribution of mid-infrared and far-infrared luminosities for our sample and test the predictions of the unification scheme hypothesis.

5.2.1 The mid-infrared luminosity

Spinoglio & Malkan (1989 and references therein) argued that the $12\ \mu\text{m}$ luminosity is the best indicator of the bolometric luminosity of AGNs. They found that at $12\ \mu\text{m}$ the absorption of the continuum is balanced by the thermal re-emission and all Seyfert galaxies (in fact all AGNs) show this behaviour. They argued that the dust preferentially absorbs continuum at the shortest wavelengths and re-emits it in the far-infrared, making the resulting energy distribution redder in the optical/ultraviolet, and in the infrared; the pivot wavelength, at which the absorption of the original continuum is balanced by the thermal re-emission is expected in the mid-infrared ($7\text{--}12\ \mu\text{m}$). If this is the case, the unified scheme would predict that the $12\ \mu\text{m}$ distribution of Seyfert 1 and Seyfert 2 galaxies be similar. If, on the other hand, the $12\ \mu\text{m}$ luminosity originates on larger scales (*e.g.* Thean et al. 2001), then the unified scheme would again predict that the $12\ \mu\text{m}$ distribution be similar, since we have matched the host galaxy stellar luminosity and also other host galaxy parameters. We show the distribution of the mid-infrared, $12\ \mu\text{m}$, power in Figure 5.1. The distributions are virtually identical. This is consistent with the unified scheme.

5.2.2 The far-infrared luminosity

As in the case of $12\ \mu\text{m}$ mid-infrared luminosity, there is no consensus on the origin of the far-infrared luminosity. Roy et al. (1998) have argued that the far-infrared luminosity is predominantly from the nuclear dust heated by the optical-ultraviolet continuum from the AGN. Wilson (1988) has argued that the far-infrared emission is associated with star-formation in the disk. In either case the far-infrared luminosity would be an orientation independent parameter. The unified scheme would then predict similar far-infrared luminosities for the two classes of Seyfert galaxies. Figures 5.2, 5.3, and 5.4 present respectively the distributions of the total $25\ \mu\text{m}$, $60\ \mu\text{m}$, and $100\ \mu\text{m}$ luminosities for the two class of Seyfert galaxies. The Mann-Whitney U test shows that the two distributions are the same at a significance level better than 0.10. Thus, our results are consistent with the predictions of the unified scheme.

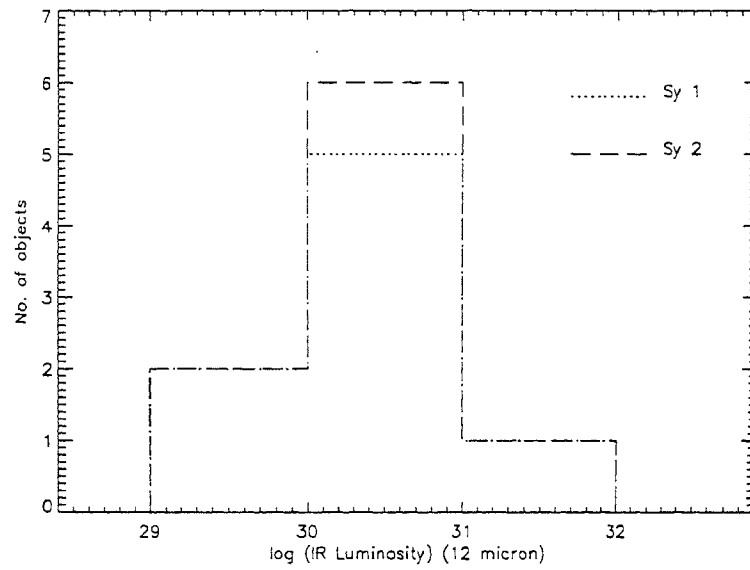


Figure 5.1: Histograms showing distribution of total 12 μm luminosity ($\text{ergs s}^{-1}\text{Hz}^{-1}$).

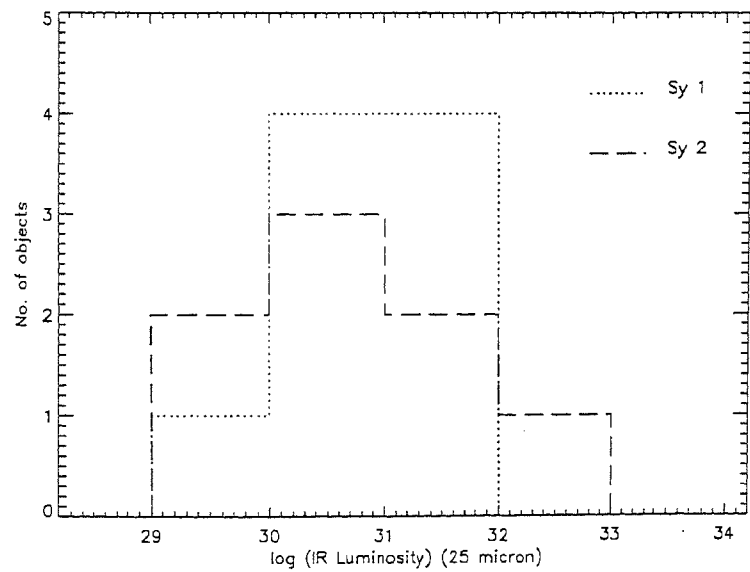


Figure 5.2: Histograms showing distribution of total 25 μm luminosity ($\text{ergs s}^{-1}\text{Hz}^{-1}$).

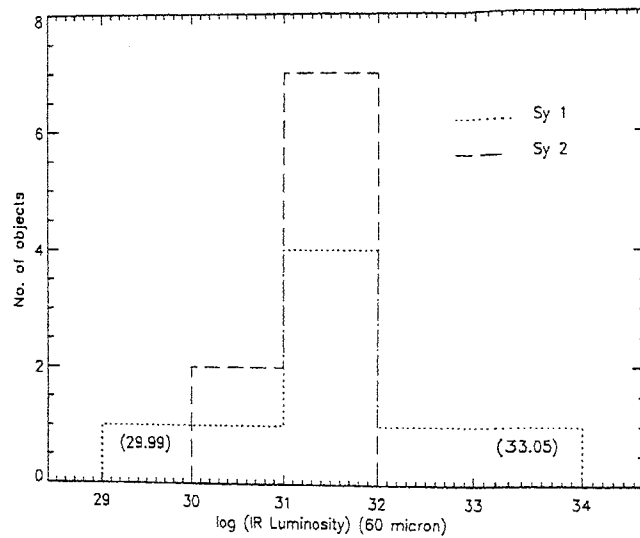


Figure 5.3: Histograms showing distribution of total 60 μm luminosity ($\text{ergs s}^{-1}\text{Hz}^{-1}$); values in the bins indicate $\log(\text{infrared luminosity})$ for the sources.

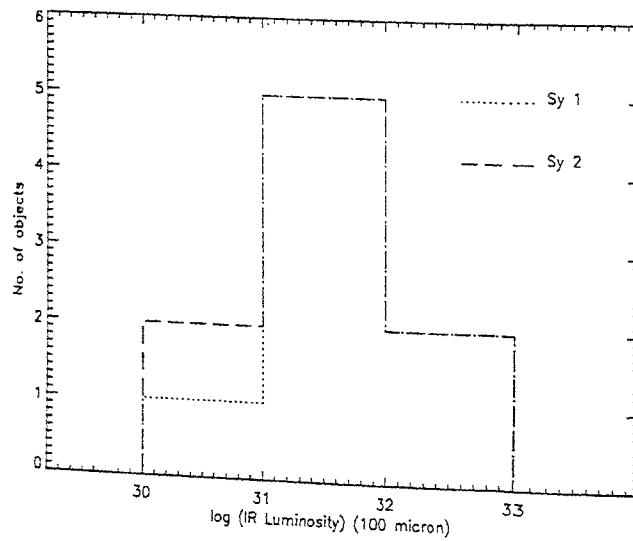


Figure 5.4: Histograms showing distribution of total 100 μm luminosity ($\text{ergs s}^{-1}\text{Hz}^{-1}$).

	100 μ		60 μ		25 μ		12 μ		1.4 GHz		Extended 5 GHz		Tot 5 GHz		Core 5 GHz		Tot 5 GHz	
	Flux density (Jy)	Lum (ergs s ⁻¹)	Flux density (Jy)	Lum (ergs s ⁻¹)	Flux density (Jy)	Lum (ergs s ⁻¹)	Flux density (Jy)	Lum (ergs s ⁻¹)	Flux density (mJy)	Lum (ergs s ⁻¹)	Flux density (mJy)	Lum (ergs s ⁻¹)	Flux density (mJy)	Lum (ergs s ⁻¹)	Flux density (mJy)	Lum (ergs s ⁻¹)	Flux density (mJy)	Lum (ergs s ⁻¹)
	(A)	(A)	(B)	(B)	(C)	(C)	(D)	(D)	(E)	(E)	(F)	(F)	(G)	(G)	(H)	(H)	(I)	(I)
Mrk 348	1.75	30.88	1.43	30.79	0.78	30.53	< 0.34	< 30.17	277.31	30.08	36.00	29.18	346.00	30.17	310.00	30.13	163.00	29.85
Mrk 1	2.73	31.13	2.28	31.05	0.80	30.60	1.80	30.95	70.78	29.54	3.57	29.32	27.65	29.13	24.08	29.07	4.38	28.33
MCG 8-11-11	4.33	31.72	2.76	31.52	2.00	31.38	0.63	30.88	228.34	30.44	52.19	30.26	75.76	29.96	23.57	29.45	4.89	28.77
NGC 2273	9.88	30.83	6.24	30.63	1.37	29.98	0.46	29.50	59.73	28.62	7.79	28.43	19.92	28.14	12.13	27.92	6.31	27.64
Mrk 78	1.18	31.49	1.12	31.47	0.54	31.15	0.25	30.82	34.96	29.96	1.59	29.81	10.46	29.44	8.87	29.37	7.82	29.31
Mrk 1218									63.63	30.01	5.32	29.81	24.04	29.59	18.72	29.48	9.98	29.21
NGC 2639	6.82	31.20	1.99	30.67	0.40	29.97	0.35	29.91	105.48	29.39	20.16	28.71	83.63	29.29	63.47	29.17	39.54	28.96
NGC 4151	8.49	30.17	5.64	29.99	5.03	29.94	1.95	29.53	345.78	28.78	77.00	28.59	120.00	28.32	43.00	27.87	20.00	27.54
Mrk 766	4.07	31.12	4.01	31.12	1.38	30.65	0.41	30.12	37.61	29.09	1.41	28.86	15.16	28.69	13.75	28.65	3.68	28.08
Mrk 231	30.03	33.00	33.26	33.05	8.56	32.46	1.82	31.79	282.89	30.98	10.00	30.57	173.00	30.77	163.00	30.74	68.00	30.36
NGC 5135	30.03	32.05	15.94	31.78	2.49	30.97	< 0.68	< 30.41	190.02	29.86	42.65	29.69	58.80	29.35	16.15	28.78		
Mrk 477	1.78	31.69	1.35	31.57	0.54	31.18	0.25	30.84	60.69	30.23	1.42	30.00	24.39	29.83	22.97	29.80		
NGC 6929	13.30	31.32	9.30	31.16	1.63	30.40	0.40	29.79	105.52	29.22	30.46	29.06	31.74	29.68	1.28	27.30	8.19	29.36
NGC 7212	4.96	31.84	2.95	31.62	0.74	31.02	0.34	30.68	108.84	30.18			33.94	29.68			6.58	28.96
Mrk 564	1.12	31.09	1.00	31.04	0.57	30.80	0.25	30.44	27.69	29.49	2.68	29.76	11.30	29.10	8.62	28.98	3.22	28.55
NGC 7469	34.43	32.23	26.67	32.12	5.52	31.43	1.30	30.81	167.72	29.92	21.59	29.79	43.56	29.33	21.97	29.03	6.17	28.48
Mrk 926									32.95	30.15	1.31	30.00	9.00	29.58	7.69	29.51	5.00	29.33
Mrk 530	2.04	31.55	0.82	31.15	0.48	30.92	< 0.25	< 30.64	23.50	29.61	1.15	29.39	9.17	29.20	8.02	29.14	8.63	29.17
Mrk 533	8.19	32.12	5.47	31.95	1.93	31.49	0.72	31.07	206.42	30.52	22.18	30.37	60.37	29.99	38.19	29.79	16.96	29.44
NGC 7682									58.56	29.51	0.23	29.30	22.21	29.09	21.98	29.09	8.92	28.69

References:

- (A), (B), (C) and (D) IRAS flux densities and luminosities; Lipovetski et al. (1988) (or de Grijp et al. 1987); NGC 4151: Rush et al. (1993).
- (E) NVSS, VLA D configuration 1.4 GHz flux density and luminosity.
- (F) Difference of VLA A configuration total and core flux densities and luminosities.
- (G) and (H) VLA A configuration total and core flux densities and luminosities.
- (I) VLBI-scale total detected flux density and luminosity.

Table 5.1: Table showing infrared and radio properties.

5.3 The radio–infrared correlation

The well known correlation between radio and far-infrared emission from normal spiral galaxies (*e.g.* Dickey & Salpeter 1984, Wunderlich et al. 1987) is displayed not only by spirals, but also by a remarkably diverse range of galaxy types. For example, Sopp & Alexander (1991) have shown that the radio and far-infrared luminosities of Seyfert galaxies and radio-quiet quasars are correlated and follow the same correlation as normal star-forming galaxies and ultra-luminous infrared galaxies, whereas, Sanders & Mirabel (1985) had shown that Seyfert galaxies display a correlation between radio and far-infrared with greater scatter than spirals. Thean et al. (2001) suggest that IRAS flux densities are dominated by large-scale emission, because correlations between 8.4 GHz VLA *A* configuration flux densities and the flux densities in all the IRAS wavebands are much weaker than the corresponding relationships between NVSS (VLA *D* configuration, 1.4 GHz measurements) flux densities and IRAS flux densities.

Radio emission from Seyfert galaxies is generated by the galaxy disk and by the AGN (*e.g.* Wilson 1988). The disk emission is distributed following optical indicators of star formation activity, and displays the normal radio–far-infrared correlation (Roy et al. 1998). The non-thermal disk emission is probably synchrotron radiation from cosmic electrons accelerated by supernovae. On the other hand, the non-thermal nuclear emission originates from a compact, high brightness temperature core. It has been argued that the radio excess that often disturbs the radio–far-infrared correlation in Seyfert galaxies originates from their nuclei (Sanders & Mirabel 1985, Baum et al. 1993). As discussed earlier (Section 5.2.2), the far-infrared emission from Seyfert galaxies is thought to be mostly thermal emission from nuclear dust that is heated by the optical-ultraviolet continuum source, rather than non-thermal synchrotron emission.

Since the Seyfert galaxies are radio-quiet objects, both the AGN and star-formation in the host galaxy disk could contribute significantly to the total radio luminosity, especially on larger spatial scales ~ 10 kpc. In Figures 5.5 to 5.16, we plot the ‘flux density–flux density’ and ‘luminosity–luminosity’ correlations between the radio and far-infrared emission in different wavebands for the two classes of the Seyfert galaxies. Note that ‘luminosity–luminosity’ correlations could be dominated by relatively large range in redshifts (Elvis et al. 1978). Table 5.2 gives the Spearman’s rank correlation coefficient for ‘flux density–flux density’ scatter diagram, γ_{ff} , and significance of correlation, α_{ff} ; and ‘luminosity–luminosity’ scatter diagram, γ_{ll} (Spearman’s rank correlation coefficient), α_{ll} (significance of correlation) for NVSS, VLA *A* configuration and VLBI measurements as compared to all the IRAS wavelengths. While the NVSS

flux density measurements which are sensitive at ~ 10 kpc and our kpc-scale flux density measurements which are sensitive at ~ 1 kpc correlate strongly with flux densities in all of the IRAS wavebands, the pc-scale flux density measurements do not correlate with the flux density in any of the IRAS wavebands. It thus seems very likely that a significant fraction of the far-infrared emission from $12 \mu\text{m}$ to $100 \mu\text{m}$ comes from the dust associated with star-formation on \sim kpc-scales.

parameters being correlated	γ_{ff}	α_{ff}	γ_{ll}	α_{ll}
	(flux densities)		(luminosities)	
NVSS (1.4 GHz) vs 12 μm	0.68	0.003	0.92	2.98×10^{-6}
NVSS (1.4 GHz) vs 25 μm	0.71	0.001	0.91	5.50×10^{-6}
NVSS (1.4 GHz) vs 60 μm	0.60	0.011	0.86	6.84×10^{-5}
NVSS (1.4 GHz) vs 100 μm	0.53	0.027	0.89	2.00×10^{-5}
VLA A (5.0 GHz) vs 12 μm	0.57	0.017	0.86	6.85×10^{-5}
VLA A (5.0 GHz) vs 25 μm	0.51	0.035	0.85	1.16×10^{-4}
VLA A (5.0 GHz) vs 60 μm	0.47	0.055	0.83	2.17×10^{-4}
VLA A (5.0 GHz) vs 100 μm	0.45	0.069	0.89	1.58×10^{-5}
VLBI (5.0 GHz) vs 12 μm	0.11	0.671	0.76	1.51×10^{-3}
VLBI (5.0 GHz) vs 25 μm	0.02	0.925	0.75	1.84×10^{-3}
VLBI (5.0 GHz) vs 60 μm	0.09	0.729	0.69	6.54×10^{-3}
VLBI (5.0 GHz) vs 100 μm	0.18	0.492	0.75	2.03×10^{-3}

Table 5.2: NVSS, VLA A array, and VLBI radio flux densities and luminosities correlated with infrared flux densities and luminosities for all IRAS wavebands. Table gives the Spearman's rank correlation coefficients (γ_{ff} and γ_{ll}) and their corresponding significances (α_{ff} and α_{ll}).

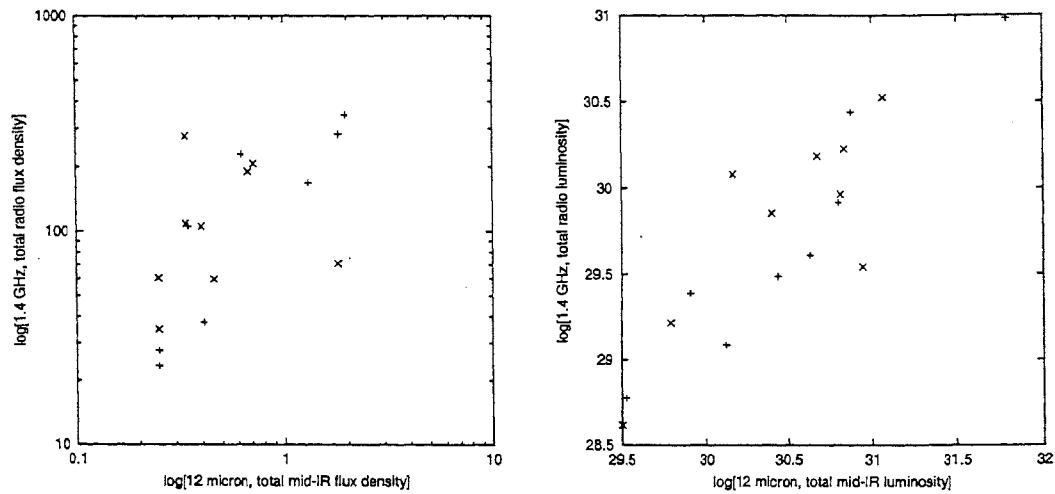


Figure 5.5: The radio (NVSS, D array) versus mid-infrared ($12\ \mu\text{m}$) scatter diagram showing Seyfert galaxies from our sample; '+' indicates Seyfert 1 galaxies and 'x' Seyfert 2 galaxies.

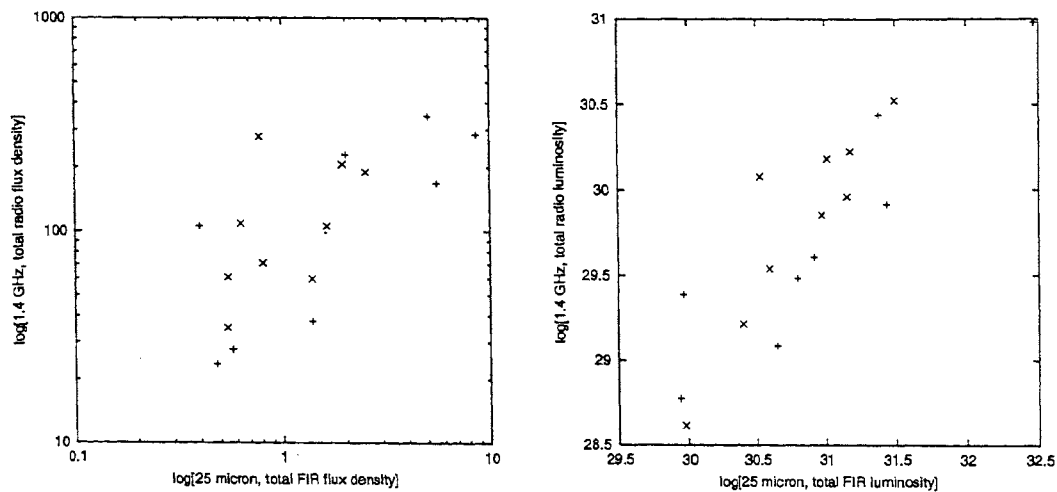


Figure 5.6: The radio (NVSS, D array) versus far-infrared ($25\ \mu\text{m}$) scatter diagram showing Seyfert galaxies from our sample; '+' indicates Seyfert 1 galaxies and 'x' Seyfert 2 galaxies.

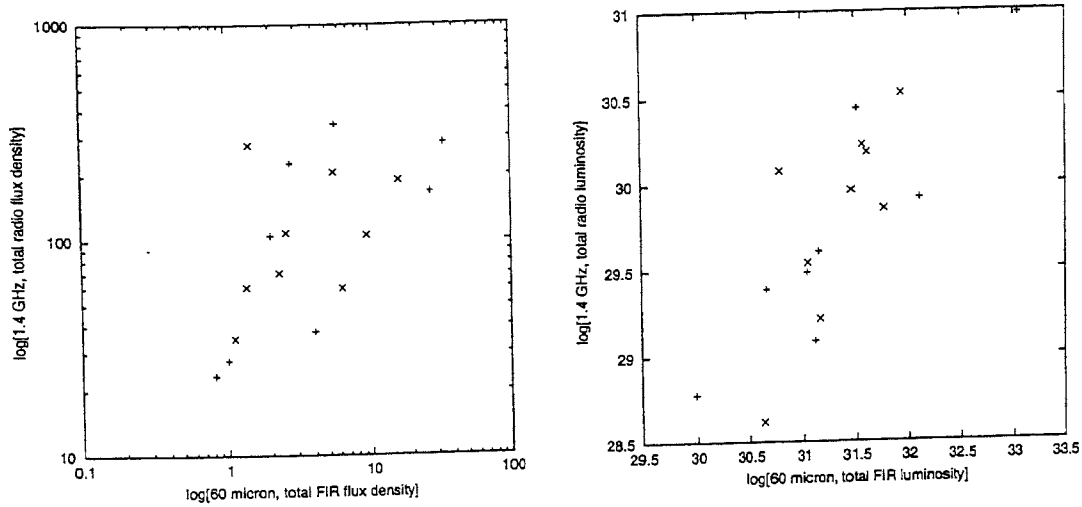


Figure 5.7: The radio (NVSS, D array) versus far-infrared ($60\ \mu\text{m}$) scatter diagram showing Seyfert galaxies from our sample; '+' indicates Seyfert 1 galaxies and 'x' Seyfert 2 galaxies.

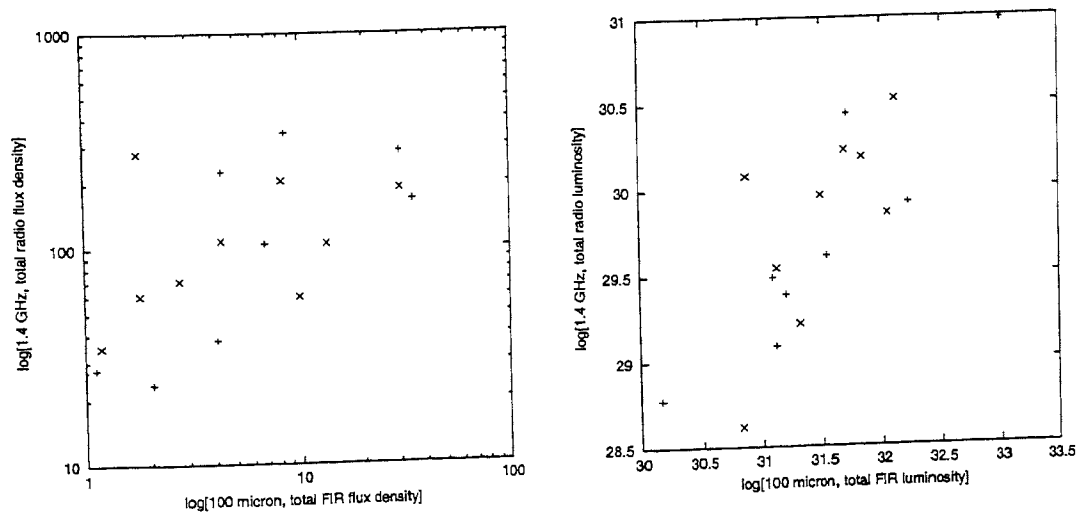


Figure 5.8: The radio (NVSS, D array) versus far-infrared ($100\ \mu\text{m}$) scatter diagram showing Seyfert galaxies from our sample; '+' indicates Seyfert 1 galaxies and 'x' Seyfert 2 galaxies.

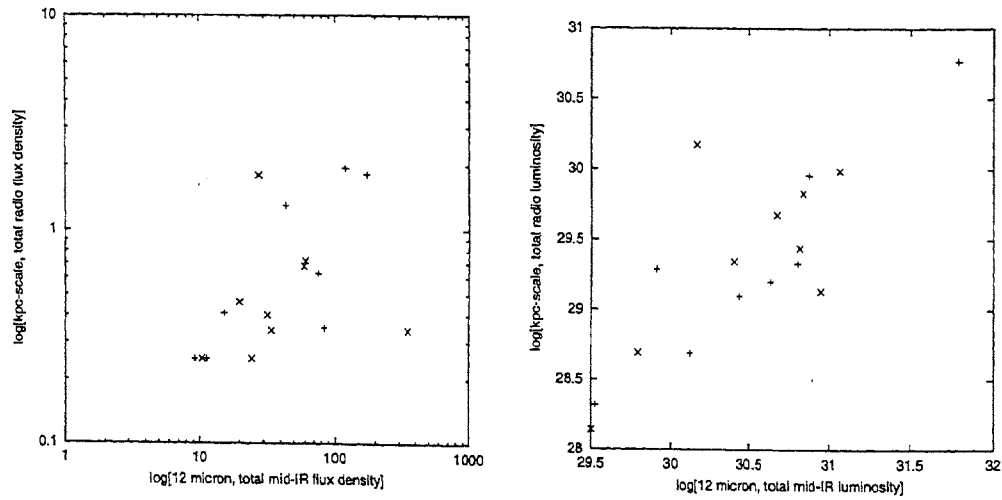


Figure 5.9: The kpc-scale radio (5 GHz) *versus* mid-infrared (12 μm) scatter diagram showing Seyfert galaxies from our sample; '+' indicates Seyfert 1 galaxies and 'x' Seyfert 2 galaxies.

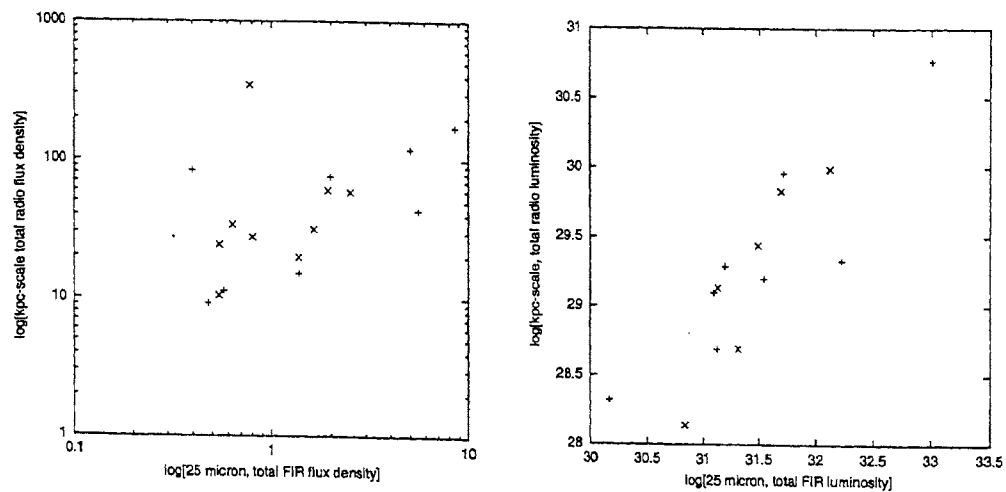


Figure 5.10: The kpc-scale radio (5 GHz) *versus* far-infrared (25 μm) scatter diagram showing Seyfert galaxies from our sample; '+' indicates Seyfert 1 galaxies and 'x' Seyfert 2 galaxies.

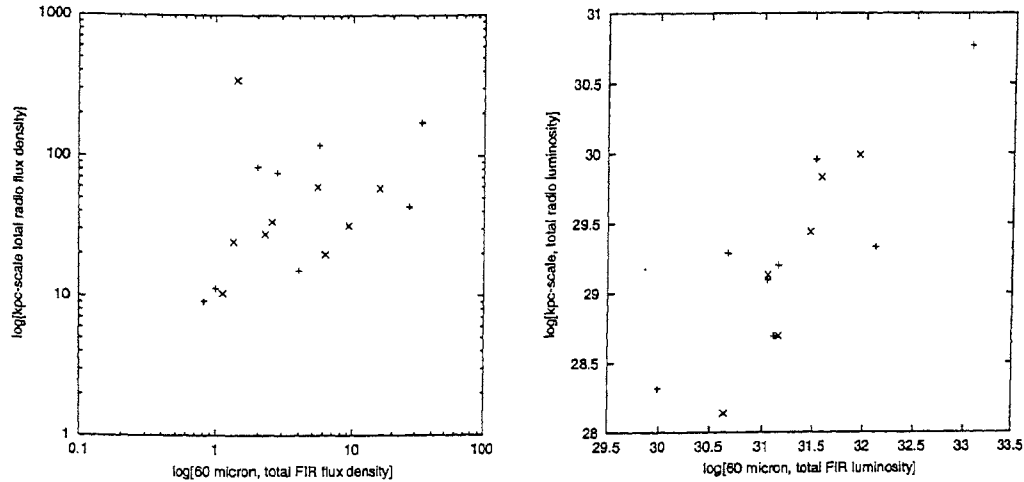


Figure 5.11: The kpc-scale radio (5 GHz) *versus* far-infrared (60 μm) scatter diagram showing Seyfert galaxies from our sample; '+' indicates Seyfert 1 galaxies and 'x' Seyfert 2 galaxies.

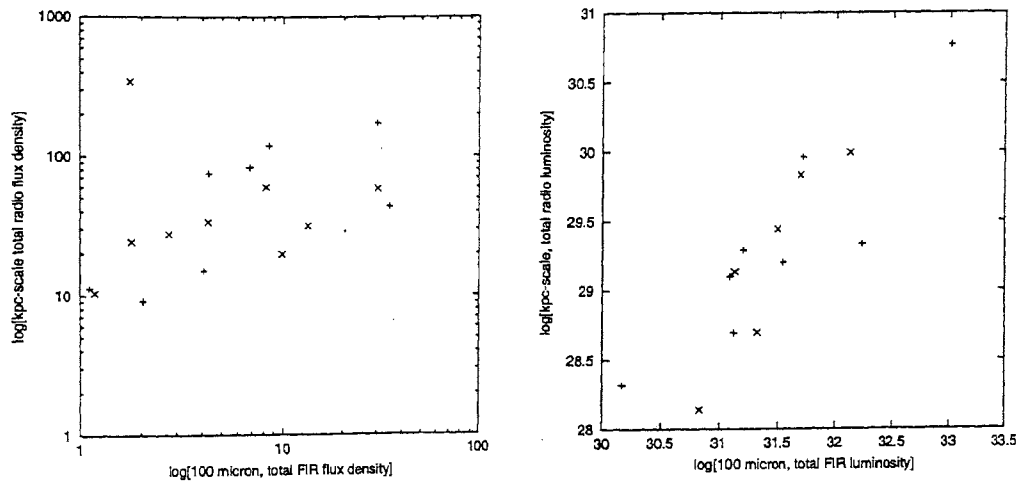


Figure 5.12: The kpc-scale radio (5 GHz) *versus* far-infrared (100 μm) scatter diagram showing Seyfert galaxies from our sample; '+' indicates Seyfert 1 galaxies and 'x' Seyfert 2 galaxies.

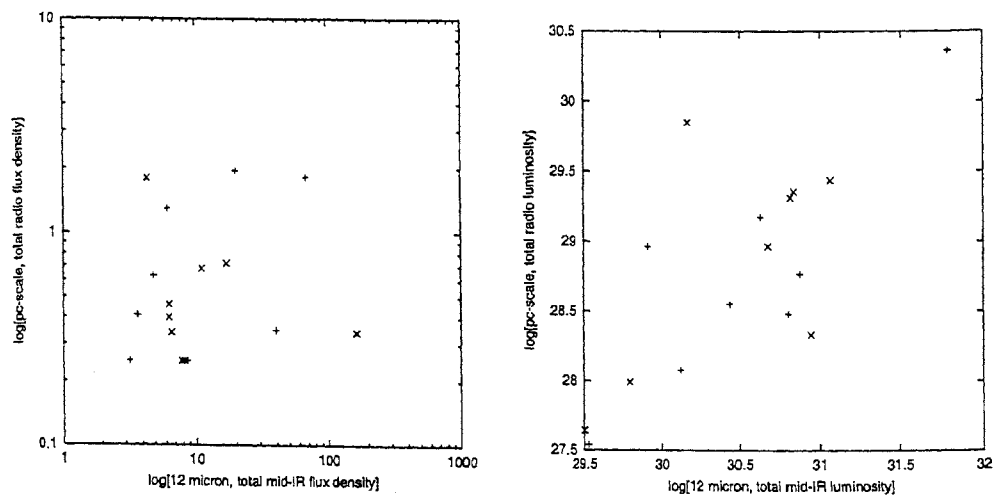


Figure 5.13: The pc-scale radio (5 GHz) *versus* mid-infrared (12 μm) scatter diagram showing Seyfert galaxies from our sample; '+' indicates Seyfert 1 galaxies and 'x' Seyfert 2 galaxies.

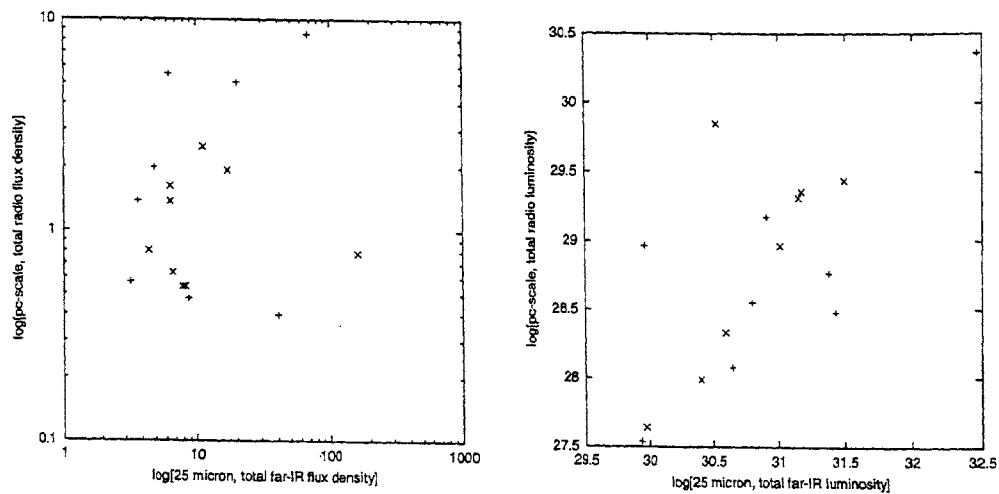


Figure 5.14: The pc-scale radio (5 GHz) *versus* far-infrared (25 μm) scatter diagram showing Seyfert galaxies from our sample; '+' indicates Seyfert 1 galaxies and 'x' Seyfert 2 galaxies.

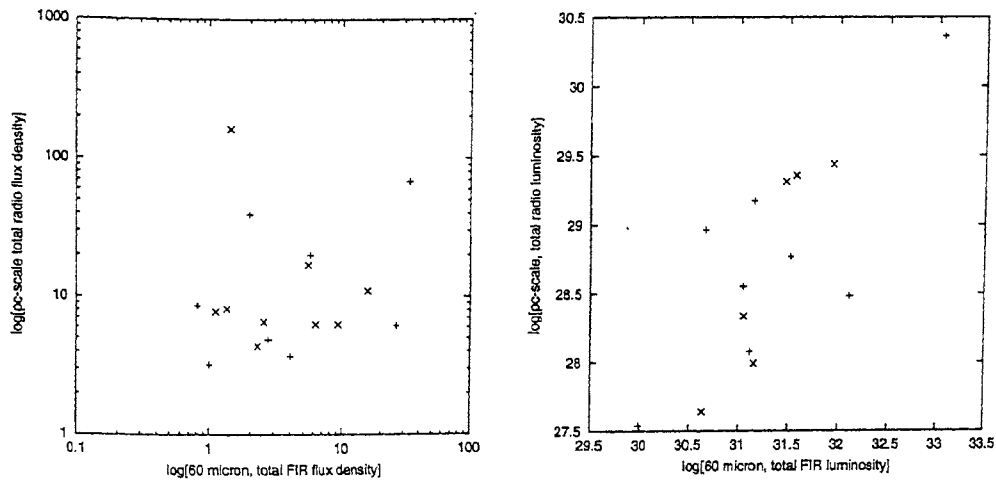


Figure 5.15: The pc-scale radio (5 GHz) *versus* far-infrared (60 μm) scatter diagram showing Seyfert galaxies from our sample; '+' indicates Seyfert 1 galaxies and 'x' Seyfert 2 galaxies.

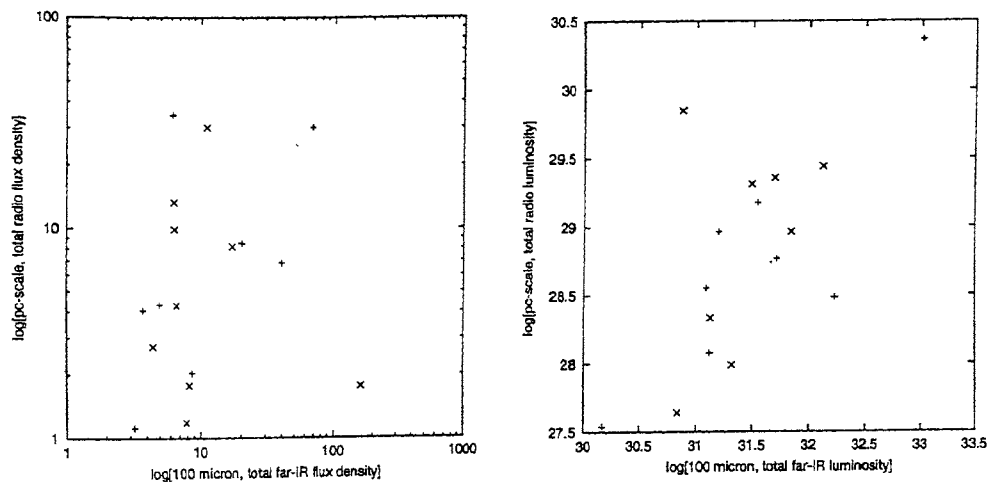


Figure 5.16: The pc-scale radio (5 GHz) *versus* far-infrared (100 μm) scatter diagram showing Seyfert galaxies from our sample; '+' indicates Seyfert 1 galaxies and 'x' Seyfert 2 galaxies.

5.4 X-ray data

The X-ray power-law component is variable. The medium energy power-law component in general varies in intensity with very little change in the spectral index. In some well-observed AGNs, the flux density variations are accompanied by a softening of the spectrum with increasing intensity (*e.g.* Perola et al. 1986, Mushotzky et al. 1993 and references therein).

We collate the X-ray luminosity measurements (data are available for 7 out of 10 Seyfert 1 galaxies and 9 out of 10 Seyfert 2 galaxies) and photon indices (data are available for 9 out of 10 Seyfert 1 galaxies and 6 out of 10 Seyfert 2 galaxies) from the literature and test the unification scheme in this waveband as well. Table 5.3 gives X-ray photon index and hard X-ray luminosity. This is only part of the sample that is being studied, because the remaining sample objects do not have measurements in the literature. In the following Section we present the results.

5.4.1 Hard X-ray luminosity

Figure 5.17 shows the distribution of the X-ray power detected by instrument onboard ASCA. The objects, Mrk 78, NGC 5929, and NGC 7682, marked with an asterisk, “*”, in the distribution, have measurements due to Ginga and HEAO1-A2 instruments. We test the hypothesis that the distribution of X-ray (2-10 keV) luminosity of Seyfert 1 galaxies and Seyfert 2 galaxies are the same. The Mann-Whitney U test shows that the distributions of X-ray (2-10 keV) luminosity for the two classes of Seyfert galaxies are significantly different ($P < 0.02$). Seyfert 1 galaxies have systematically higher X-ray luminosity than Seyfert 2 galaxies. Our result is consistent with the unified scheme hypothesis. The unified scheme predicts higher luminosity for Seyfert 1 galaxies than for Seyfert 2 galaxies because the X-ray (2-10 keV) emission in Seyfert 2 galaxies gets attenuated due to the presence of the obscuring torus in our line of sight whereas the X-rays from Seyfert 1 galaxies do not suffer from such obscuration. This is also consistent with the result of Mas-Hesse et al. (1994). They suggested that for a given far-infrared luminosity, there is a significant lack of soft X-ray emission in Seyfert 2 galaxies compared to Seyfert 1 galaxies. This lack of soft X-ray emission in Seyfert 2 galaxies could be due to partial attenuation of soft X-ray emission coming from the central source while traversing through the obscuring torus.

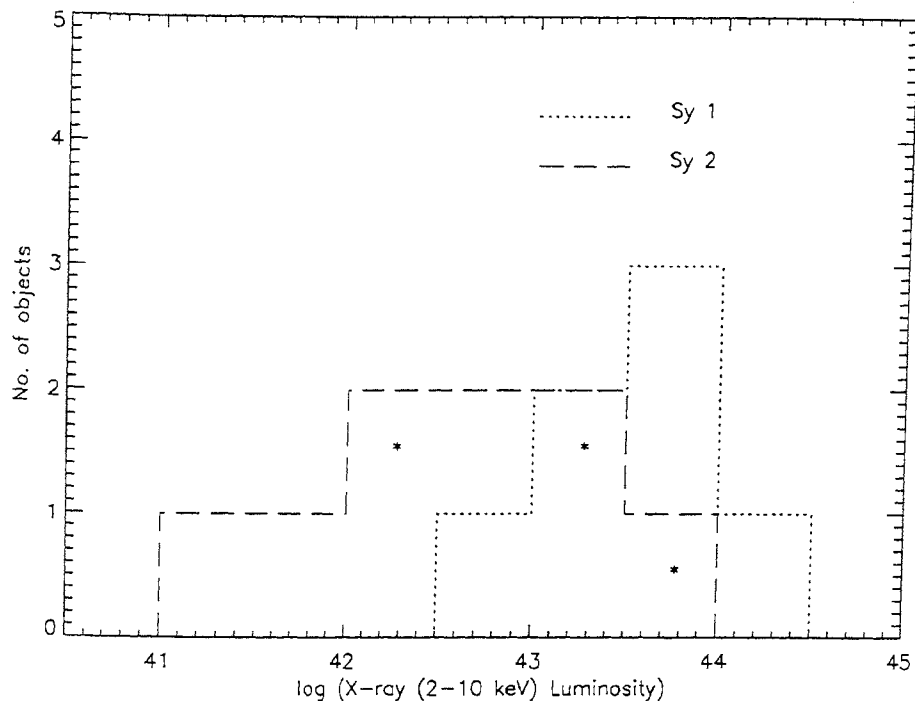


Figure 5.17: Histograms showing distribution of 2-10 keV X-ray luminosity (ergs s^{-1}); the objects with '*' have measurement not from ASCA instrument.

5.4.2 X-ray photon indices

It is now well recognised that the intrinsic high energy spectrum of Seyfert 1 galaxies consists, on an average, of a steep power-law continuum ($\Gamma \sim 1.9-2.0$, Nandra & Pounds 1994) with an exponential cut-off typically at energies larger than 150 keV (Zdziarski et al. 1996, Perola et al. 1986). Therefore one would expect that Seyfert 2 galaxies also exhibit similar high-energy properties. X-ray observations (mainly below ~ 20 keV) of Seyfert 2 galaxies, have shown a variety of spectral characteristics not always consistent with a "zeroth-order" version of the unified models (Smith & Done 1996, Cappi et al. 1996, Turner et al. 1998, Mushotzky 1984)). However, at high energies where the effects of absorption and matter reprocessing are less evident, measurements are sparse for Seyfert 2 galaxies (Johnson et al. 1997). It has been therefore difficult to assess the Seyfert 1 nature of the primary spectrum of Seyfert 2 galaxies from such X-ray observations.

Kruper et al. (1990), from the well-determined spectra of their sample showed that

the lower luminosity Seyfert 2 galaxies have significantly flatter power-law indices, $\alpha \sim 0.5$. Selection effects seem to be very important in their sample. The Seyfert 2 galaxies also tend to be relatively brighter in the radio compared to the Seyfert 1 galaxies. This is not surprising because they are optically selected. Therefore the fact that the power-law indices of Seyfert 2 galaxies appear flatter than Seyfert 1 galaxies could be either due to AGN type, or due to their low luminosity. If Kruper et al.'s (1990) result is not biased from the selection effect then it is consistent with the predictions of the unified scheme hypothesis where the attenuation of softer X-ray by the obscuring torus in Seyfert 2 galaxies (partially covered central source) would make their spectra flat as compared to Seyfert 1 galaxies.

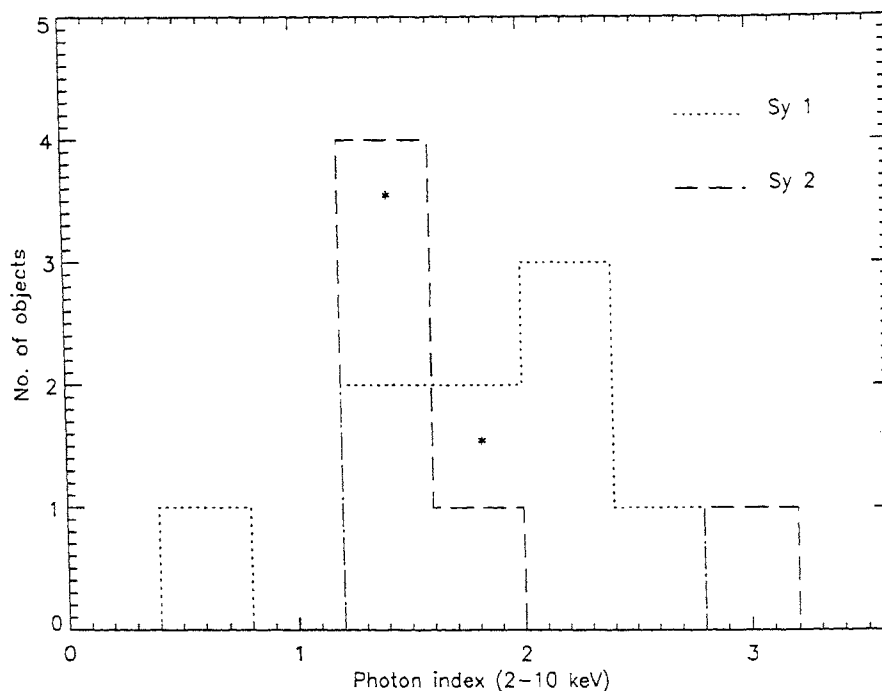


Figure 5.18: Histograms showing distribution of photon index; the objects with ‘*’ have measurement not from ASCA instrument.

In Figure 5.18 we show the distribution of 2-10 keV photon index for the two classes of Seyfert galaxies. Neither the data from a single instrument nor using many other instruments could provide us with photon index in 2-10 keV for our sample objects. The objects, Mrk 78, and Mrk 530, marked with an asterisk, ‘*’, in the distribution, have measurements due to ROSAT and HEAO2 instruments. The Mann-Whitney U test

5.5. Summary

test shows that the distributions are not statistically different even at a significance level of 0.10. Our result is consistent with the unified scheme because we do not expect flattening of the X-ray spectrum in 2-10 keV regime.

	Photon index ($\text{ph cm}^{-2}\text{sec}^{-1}\text{keV}^{-1}$)	Reference	$L_{\text{X-ray}}$ (ergs s^{-1})	Reference
Mrk 348	1.60	Awaki et al. 2000A	42.63	Awaki et al. 2000A
Mrk 1	1.55	Turner et al. 1999A	43.54	Turner et al. 1999A
MCG 8-11-11	1.45	Malaguti et al. 1994	41.93	Terashima et al. 2000
NGC 2273			43.51	Awaki & Koyama 1993
Mrk 78				
Mrk 1218	2.40	Wilson et al. 1998	43.07	Turner et al. 1999A
NGC 2639	1.58	Turner et al. 1999A	43.08	Turner et al. 1999A
NGC 4151	2.16	Turner et al. 1999A	42.90	Turner 1999A
Mrk 766	0.69	Maloney & Reynolds 2000	41.23	Turner et al. 1997
Mrk 231	2.91	Turner et al. 1997	42.81	Awaki et al. 2000A
NGC 5135	1.57	Awaki et al. 2000A	42.47	Awaki 1991
Mrk 477			42.15	Awaki et al. 2000A
NGC 5929	1.87		43.80	Turner et al. 1999B
NGC 7212	2.70	Turner et al. 1999B	43.56	Reynolds 1997
Ark 564	2.02		44.43	Turner et al. 1999A
NGC 7469	1.73	Turner et al. 1999A		
Mrk 926	1.70	Malaguti et al. 1994	43.48	Awaki et al. 2000B
Mrk 530	1.42	Awaki et al. 2000B	43.22	Della Ceca et al. 1990
Mrk 533				
NGC 7682				

Table 5.3: Table showing X-ray properties.

5.5 Summary

Using our measured flux densities of the pc-scale and kpc-scale structures along with radio types, infrared luminosities and hard X-ray luminosities and photon indices, we find that: (1) All 12 μm , 25 μm , 60 μm , and 100 μm infrared powers of Seyfert galaxies

are distributed similarly for the Seyfert 1 and Seyfert 2 galaxies from our sample. Since the infrared powers are expected to be orientation independent, these results are consistent with the unification scheme hypothesis. (2) The pc-scale radio flux density does not correlate with the mid and far-infrared flux densities, suggesting that a significant fraction of the far-infrared luminosity from $12\ \mu\text{m}$ to $100\ \mu\text{m}$ comes from the dust associated with the star-forming regions at \sim kpc-scales. (3) The distributions of hard X-ray luminosity for Seyfert 1 and Seyfert 2 galaxies are different. Since Seyfert 2 galaxies are expected to show lower luminosity than Seyfert 1 galaxies as the X-ray emission from Seyfert 2 galaxies is expected to be attenuated due to the presence of an obscuring torus, this is once again consistent with the unified scheme. (4) Finally, we do not find evidence for Seyfert 2 galaxies to show flatter X-ray photon indices than Seyfert 1 galaxies.

Chapter 6

Conclusions and future work

6.1 Summary of results

Unification of Seyfert 1 and Seyfert 2 galaxies has been attempted by various authors in the past. Their radio emission has been extensively studied at \sim arcsec-scales, but at mas-scales a systematic study has not been done before. We carefully selected and made a list of 20 Seyfert galaxies, that are matched in orientation independent parameters which are measures of intrinsic AGN power and host galaxy properties. This sample was used to test the unification scheme hypothesis rigorously by observing it at pc-scales.

We presented radio images of 15 objects that were observed by us with VLBI and 4 objects that had VLBI images in the literature. Thus 19 sample objects have VLBI images, all 20 have VLA images and 15 of them have simultaneous VLBI and VLA measurements. The maps presented in Chapter 3 reveal, for the first time, the mas-scale radio structures of a large carefully selected sample of Seyfert galaxies. All our observed objects were detected on mas-scales. We measured the radio flux densities, sizes of the emitting regions, P.A.'s of the extended radio emissions and their morphologies. These measurements provide a useful database for investigating the generic properties of compact radio cores in the nuclei of Seyfert galaxies. Earlier studies indicate that at least two (Mrk 348 and Mrk 231) of these are radio variables, thereby underlining the advantage of the simultaneity of our VLBI and VLA data for comparing the pc-scale and kpc-scale morphology.

Using our measured flux densities of the pc-scale and kpc-scale structures for Seyfert galaxies and their detection rates, radio luminosities, projected linear sizes and spectral indices, we obtained the following results: (1) The starbursts alone cannot power

these radio sources because, (i) the emission is compact on pc-scales and cannot be explained with starburst models, (ii) the brightness temperature is high, and (iii) the radio luminosity of the compact component at 5 GHz is $\sim 10^{23}$ erg s $^{-1}$ Hz $^{-1}$ and arises from a region smaller than a few cubic pc. (2) Seyfert 1 and Seyfert 2 galaxies have equal tendency to show compact radio structures. This contradicts the result of Roy et al. (1994), who had concluded that compact radio structures were much more common in Seyfert 2 galaxies than in Seyfert 1 galaxies. Thus, the inconsistency of Roy et al.'s (1994) result with the unified scheme no longer exists. (3) The distributions of the radio powers at subarcmin, arcsec and mas-scales for the two classes of Seyfert galaxies are similar. This implies that there is no statistically significant difference in radio powers of Seyfert 1 and Seyfert 2 galaxies, which is consistent with the unified scheme. (4) The projected linear sizes of Seyfert 1 galaxies are not systematically lower than Seyfert 2 galaxies, contrary to the prediction of the unified scheme. This could be mainly due to there being a relatively large spread in the intrinsic linear sizes as is suggested by the luminosity–size correlation. There could also be a contribution from the selection effect, *viz.*, the paucity of Seyfert 2 galaxies in the sample with their jets perpendicular to the plane of the host galaxy and of Seyfert 1 galaxies with their axes in the plane of the host galaxy. (5) We compared the ratio of the detected pc-scale radio flux density and the kpc-scale radio flux density using simultaneous VLBI and VLA measurements. Its distribution for the two classes of Seyfert galaxies are similar. Therefore, we believe that there is no evidence for relativistic beaming in Seyfert galaxies.

We analysed the tabulated data of the CfA Seyfert galaxy sample (Kukula et al. 1995) at kpc-scales. We found similar distributions of radio luminosities, and the ratio of radio core flux density to the extended radio flux density for the two classes of Seyfert galaxies, consistent with the predictions of the unification scheme. The distributions of the projected linear sizes appear to differ for Seyfert 1 and Seyfert 2 galaxies in a manner consistent with the unified scheme.

Using the 12 μm , 25 μm , 60 μm and 100 μm flux densities for our Seyfert sample, we find that Seyfert galaxies have similar distribution of infrared power at all IRAS wavebands. While the mid and far-infrared flux densities correlate with the kpc-scale radio flux densities, they do not correlate with the pc-scale flux densities. This suggests that the infrared emission is dominated by non-nuclear emission and a significant contribution to the infrared emission could be due to the galaxy disk. The distribution of hard X-ray luminosity for Seyfert 1 and Seyfert 2 galaxies is different. Seyfert 2

galaxies show lower luminosity than Seyfert 1 galaxies. This is consistent with the fact that the X-ray emission from Seyfert 2 galaxies is attenuated due to the presence of an obscuring torus and hence the lower luminosity for them than Seyfert 1 galaxies. Lastly, we do not find evidence for Seyfert 2 galaxies to show flatter X-ray photon indices than Seyfert 1 galaxies.

6.2 Future work

The next immediate step would be to look at the radio spectra of the cores of Seyfert galaxies at mas-scales. The radio-loud AGNs seen in any orientation have flat-spectrum radio cores on pc-scales. The radio cores of Seyfert galaxies are expected to show similar behaviour. A systematic study to look for spectra of Seyfert 1 and Seyfert 2 cores has not been done so far. We would like to supplement our data along with observations at other radio wavelengths, particularly, for those sources which are unresolved if not at all scales, at least on arcsec and mas-scales (*e.g.* Mrk 1 Mrk 766, and Mrk 477). VLBA was the key instrument in providing a range of baselines for our experiment, it has maximum sensitivity at 5 GHz. In future, along with the 14 stations we had in our observation and with the inclusion of phased-WSRT (also the Square Kilometer Array (SKA), whensoever possible) so as to maximise sensitivity, we would like to make phase-referenced measurements at other wavelengths as well, particularly at 8.4 GHz and 1.4 GHz (at these frequencies the performance of these stations are next best). This would also allow us to probe the signatures of free-free emission which are thought to be due to the torus. The inner edge of the torus, expected to be ionised by optical and ultraviolet emission from the active nucleus, will radiate direct thermal emission (*e.g.* NGC 1068: Gallimore et al. 1996A, Gallimore et al. 1997; Mrk 231: Taylor et al. 1999, Carilli et al. 1998) and will cause free-free absorption of nuclear radio components viewed through torus. Hence, our future observations would be aimed at wavelengths between 21 cm and 2 cm where the free-free turnover is expected.

The flat spectrum radio cores on arcsec-scales have also not been looked for at comparable resolutions. Studying the radio data of Seyfert galaxies at similar resolution scales and tracing flat/steep spectrum radio cores would be another study that we would like to undertake using Giant Metrewave Radio Telescope and VLA.

To increase the Seyfert sample and probe mas-structures at 5 GHz for more Seyfert galaxies, we need to add at least phased-WSRT to our existing chosen array. We would like to increase the sample size of Seyfert galaxies, matched once again in orientation independent parameters and provide a firmer footing to the unification scheme

hypothesis.

Although Seyfert galaxies show X-ray flux density variability on short time-scales (Canizares et al. 1986), systematic searches for radio variability in Seyfert galaxy cores have not been made. Two of our sample objects (Mrk 231 and Mrk 348) show radio variability. We would like to look for the flux density variability as well.

We attempted to show that the far-infrared emission from Seyfert galaxies consists mainly of thermal and weak non-thermal emission using radio–far-infrared correlation. Data currently being taken with Infrared Space Observatory (ISO) will become public in a few years. These data can be used for modelling the mid-infrared and far-infrared spectrum so that AGN and starburst components of hot and warm dust can be better determined. Analyses of the ISO data, which is of higher resolution than IRAS, would allow us to check the strength of radio–far-infrared correlation.

In spite of only a small number of Seyfert galaxies having X-ray measurements, we attempted to test the predictions of the unified scheme in X-ray wavelength using data collated from literature (mainly ASCA) obtained with different instruments. “Chandra” has superior spatial resolution than ASCA and its spectral resolution is adequate to model the observed spectrum of core and extended emission of the Seyfert galaxies. Hence, future observations with it will help us to determine the hard X-ray luminosity and photon index of Seyfert galaxies. Therefore, one can give a firm footing to the flat spectra seen in Seyfert 2 galaxies and steep spectra seen in Seyfert 1 galaxies as is alluded by Canizares et al. (1986).

Bibliography

- [1] AIPS Cookbook, 31-Dec-1999 and earlier, NRAO.
<http://www.cv.nrao.edu/aips/aipsdoc.html>
- [2] Antonucci, R.R.J., & Miller, J.S. "Spectropolarimetry and the nature of NGC 1068", 1985, *ApJ*, **297**, 621.
- [3] Antonucci, R.R.J. "Unified models for active galactic nuclei", 1993, *ARA&A*, **31**, 473.
- [4] Argyle, R.W., & Eldridge, P. "Optical positions of Seyfert galaxies - III", 1990, *MNRAS*, **243**, 504.
- [5] Awaki, H., Koyama, K., Inoue, H., & Halpern, J.P. "X-ray implications of a unified model of Seyfert galaxies", 1991, *PASP*, **43**, 195.
- [6] Awaki, H., & Koyama, K. "Ginga observations of Seyfert galaxies", 1993, *AdSR*, **13**, No. 12, p. 221.
- [7] Awaki, H., Ueno, S., & Taniguchi, Y. "X-ray emission from Seyfert 2 galaxies having polarised broad optical lines", 2000B, *AdSR*, **25**, 797.
- [8] Awaki, H., Ueno, S., Taniguchi, Y., & Weaver, K.A. "X-ray emission from Seyfert 2 galaxies with optical polarised broad lines", 2000A, *ApJ*, **542**, 185.
- [9] Barvainis, R., & Lonsdale, C.J. "Search for free-free absorption cutoff from tori in three type 2 active galactic nuclei", 1998, *ApJ*, **115**, 885.
- [10] Baldwin, J.A., Phillips, M.M., & Terlevich, R. "Classification parameters for the emission-line spectra of extragalactic objects", 1981, *PASP*, **93**, 5.
- [11] Baldwin, J.A., Wilson, A.S., & Whittle, M. "Kinematics and ionization of extended gas in active galaxies. III The extranuclear properties of NGC 1068", 1987, *ApJ*, **319**, 105.

- [12] Baum, S.A., O'Dea, C.P., Dallacassa, D., de Bruyn, A.G., & Pedlar, A. "Kiloparsec-Scale radio emission in Seyfert galaxies: Evidence for starburst-driven superwinds?", 1993, *ApJ*, **419**, 553.
- [13] Bicknell, G.V., Dopita, M.A., Tsvetanov, Z.I., & Sutherland, R.S. "Are Seyfert narrow-line regions powered by radio jets?", 1998, *ApJ*, **495**, 680.
- [14] Blandford, R.D., & Rees, M.J. "Extended and compact extragalactic radio sources - Interpretation and theory", 1978, *PhyS*, **17**, 265.
- [15] Blandford, R.D., & Königl, A. "Relativistic jets as compact radio sources", 1979, *ApJ*, **232**, 34.
- [16] Boroson, T.A., & Green, R.F. "The emission-line properties of low-redshift quasi-stellar objects", 1992, *ApJS*, **80** 109.
- [17] Bridle, A.H., & Perley, R.A. "Extragalactic radio jets", 1984, *ARA&A*, **22**, 319.
- [18] Brunthaler, A., Falcke, H., Bower, G.C., Aller, M.F., Aller, H.D., Teraesranta, H., Lobanov, A.P., Krichbaum, T.P., & Patnaik, A.R. "III Zw 2, the first superluminal jet in a Seyfert galaxy", 2000, *A&AL*, **357**, L45.
- [19] de Bruyn, A.G., & Wilson, A.S. "A 1415 MHz survey of Seyfert and related galaxies", 1976, *A&A*, **53**, 93.
- [20] de Bruyn, A.G., & Wilson, A.S. "The radio properties of Seyfert galaxies", 1978, *A&A*, **64**, 433.
- [21] Canizares, C.R., Kriss, G.A., Kruper, J., & Urry, C.M. "X-ray studies of Seyfert galaxies and quasars", in *Quasars*, eds. Swarup, G., & Kapahi, V.K. 1986, IAUS, **119**, p. 253, D. Reidel Publishing Co.
- [22] Cappi, M., Mihara, T., Matsuoka, M., Brinkmann, W., Prieto, M.A., & Palumbo, G.G.C. "Is the X-Ray spectrum of the Seyfert 2 galaxy NGC 5252 intrinsically flat?", 1996, *ApJ*, **456**, 141.
- [23] Carilli, C.L., Wrobel, J.M., & Ulvestad, J.S. "A subkiloparsec disk in Markarian 231", 1998, *AJ*, **115**, 928.
- [24] Christiansen, W.N. "A high-resolution aerial for radio astronomy", 1953, *Nature*, **171**, 831.

- [25] Cid Fernandes, & Terlevich, R. "Where are the broad lines in Seyfert 2s?", 1993, *Ap&SS*, **205**, 91.
- [26] Cid Fernandes, & Terlevich, R. "The origin of the blue continuum in type 2 Seyferts: reflection or star-forming tori?", 1995, *MNRAS*, **272**, 423.
- [27] Clements, E.D. "Optical positions of Seyfert galaxies", 1981, *MNRAS*, **197**, 829.
- [28] Clements, E.D. "Optical positions of Seyfert galaxies - II", 1983, *MNRAS*, **204**, 811.
- [29] Colina, L., Vargas, M.L.G., Rosa M. Gonzalez, Mas-Hesse, J.M., Perez, E., Alberdi, A., & Krabbe, A. "On the origin of the ultraviolet continuum in Seyfert 2 galaxies", 1997, *ApJL*, **488**, L71.
- [30] Condon, J.J., Condon, M.A., Gisler, G., & Pushell, J.J. "Strong radio sources in bright spiral galaxies. II. Rapid star formation and galaxy-galaxy interactions", 1982, *ApJ* **252**, 102.
- [31] Condon, J.J. "Radio emission from normal galaxies", 1992, *ARA&A*, **30**, 575.
- [32] Condon, J.J., Cotton, W.D., Greisen, E.W., Yin, Q.F., Perley, R.A., Taylor, G.B., & Broderick, J.J. "The NRAO VLA sky survey", 1998, *AJ*, **115**, 1693.
- [33] Cornwell, T.J., & Wilkinson, P.N. "Self-calibration" in *Proc. International Symp. on indirect imaging* (Cambridge University Press), 1984, P. 204.
- [34] Curran, S.J. "Differences in the dense gas between type 1 and type 2 Seyferts", 2000, *A&AS*, **144**, 271.
- [35] Dahari, O. "The nuclear activity of interacting galaxies", 1985, *ApJS*, **57**, 643.
- [36] Dahari, O., & De Robertis, M.M. "A statistical study of properties of Seyfert and starburst galaxies", 1988, *ApJS*, **67**, 249.
- [37] Davis, M., Huchra, J., & Latham, D. "The center for astrophysics redshift survey", in *Early evolution of universe and its present structure*, eds. Abell, G.O., & Chincarni, G., 1983, *IAUS*, **104**, p. 167, Reidel, Dordrecht.

- [38] Della Ceca, R., Palumbo, G.G.C., Persic, M., Boldt, E.A., De Zotti, G., & Marshall, E.E. "A catalog of X-ray measurements of selected samples of active galactic nuclei", 1990, *ApJS*, **72**, 471.
- [39] Dickey, J.M., & Salpeter, E.E. "1.4 GHz continuum sources in the Hercules cluster", 1984, *ApJ*, **284**, 461.
- [40] Dultzin-Hacyan, D., Krongold, Y., Fuentes-Guridi, I., & Marziani, P. "The close environment of Seyfert galaxies and its implication for unification models", 1999, *ApJL*, **513**, L111.
- [41] Edelson, R.A. "Broad-band properties of the CfA Seyfert galaxies. I . Radio properties", 1987, *ApJ*, **313**, 651.
- [42] Elvis, M., Maccacaro, T. Wilson, A.S., Ward, M.J., Penston, M.V. Fosbury, R.A.E, & Perola, G.C. "Seyfert galaxies as X-ray sources", 1978, *MNRAS*, **183**, 129.
- [43] Evans, I.N., Ford, H.C., Kinney, A.L., Antonucci, A.J., Armus, L., & Caganoff, S. "HST imaging of the inner 3 arcseconds of NGC 1068 in the light of [O III] $\lambda 5007 \text{ \AA}$ ", 1991A, *ApJL*, **369**, L27.
- [44] Evans, I.N., Ford, H.C., Kinney, A.L., Antonucci, R.R.J., Armus, L., & Caganoff, S. "HST imaging of the inner 3 arcseconds of NGC 1068 in the light of forbidden [O III] $\lambda 5007 \text{ \AA}$ ", 1991B, *ApJS*, **76** 985.
- [45] Evans, I.N., Tsvetanov, Z., Kriss, G.A., Ford, H.C., Caganoff, S., & Koratkar, A.P. "Hubble space telescope imaging of the narrow-line region of NGC 4151", 1993, *ApJ*, **417**, 82.
- [46] Evans, I.N., Ford, H.C., Kriss, G.A., & Tsvetanov, Z. "Hubble space telescope observations of active galaxies", in *First Stromlo Symposium: The physics of active galaxies*, eds Bicknell, G.V., Dopita, M.A., & Quinn, P.J., 1994, ASP Conf. Ser., **54**, p. 3.
- [47] Falcke, H., Wilson, A.S., & Simpson, C. "HST and VLA observations of Seyfert 2 galaxies: the relationship between radio ejecta and the narrow line region", 1998, *ApJ*, **502**, 199.

- [48] Falcke, H., Nagar, N.M., Wilson, A.S., & Ulvestad, J.S. "Radio sources in low-luminosity active galactic nuclei. II. Very Long Baseline Interferometry detections of compact radio cores and jets in a sample of LINERs", 2000, *ApJ*, **542**, 197.
- [49] Fath, E.A. "The spectra of some spiral nebulae and globular star clusters", 1909, *PASP*, **138** 21.
- [50] Gabuzda, D.C. "VLBI polarization measurements of BL Lacertae objects", 1988, PhD Thesis.
- [51] Gallimore, J.F., Baum, S.A., O'Dea, C.P., Brinks, E., & Pedlar, A. "H₂O and OH maser as probes of the obscuring torus in NGC 1068. 1996A", *ApJ*, **462**, 740.
- [52] Gallimore, J.F., Baum, S.A., & O'Dea, C.P. "The subarcsecond radio structure in NGC 1068. II. implication for the central engine and unifying schemes, 1996B", *ApJ*, **464**, 198.
- [53] Gallimore, J.F., Baum, S.A., & O'Dea, C.P. "A direct image of the obscuring disk surrounding an active galactic nucleus", 1997, *Nature*, **388**, 852.
- [54] Gaullouët, L., Heidmann, N., & Dempierre, F. "Optical positions of bright galaxies - IIP", 1975, *A&AS*, **19**, 1.
- [55] Giuricin, G., Mardirossian, F., Mezzetti, M., & Bertotti, G. "The radio properties of bright Seyfert galaxies", 1990, *ApJS*, **72**, 551.
- [56] Giuricin, G., Fadda, D., & Mezzetti, M. "Compact radio cores and nuclear activity in Seyfert galaxies", 1996, *ApJ*, **468**, 475.
- [57] González-Delgado, Rosa M., Heckman, T., Leitherer, C., Meurer, G., Krolik, J., Wilson, A.S., Kinney, A., Koratkar, A. "Ultraviolet-optical observations of the Seyfert 2 galaxies NGC 7130, NGC 5135, and IC 3639: Implications for the starburst-active galactic nucleus connection", 1998, *ApJ*, **505**, 174.
- [58] Goodrich, R.W. "Spectropolarimetry and variability of Seyfert 1.8 and 1.9 galaxies", 1989A, *ApJ*, **340**, 190.
- [59] Goodrich, R.W., Veilleux, S., & Hill, G.J. "Infrared spectroscopy of Seyfert 2 galaxies: a look through the obscuring torus?", 1994, *ApJ*, **422**, 521.

- [60] Greenhill, L.J., Jiang, D.R., Moran, J.M., Reid, M.J., Lo, K.Y., Claussen, M.J. "Detection of a subparsec diameter disk in the nucleus of NGC 4258", 1995, *ApJ*, **440**, 619.
- [61] de Grijp, M.H.K., Miley, G.K., Lub, J., & de Jong, T. "Infrared Seyferts - A new population of active galaxies?", 1985, *Nature*, **314**, 240.
- [62] de Grijp, M.H.K., Lub, J., & Miley, G.K. "Warm IRAS sources. I. A. Catalogue of AGN candidates from the point source catalog", 1987, *A&AS*, **70**, 95.
- [63] Heckman, T.M. "Galaxy interactions and the stimulation of nuclear activity", *Paired and Interacting Galaxies*, eds. Sulentic, J.W., Keel, W.C., & Telesco, C.M. 1990A, *IAUC*, **124**, p. 359, NASA.
- [64] Heckman, T.M. "The starburst-AGN connection", in *Massive stars in starbursts*, eds. Walborn, N., & Leitherer, C., 1990B, *Proc. of the ST ScI symposium*.
- [65] Heckman, T.M., Gonzalez-Delgado, R., Leitherer, C., Meurer, G. R., Krolik, J., Wilson, A. S., Koratkar, A., & Kinney, A. "A powerful nuclear starburst in the Seyfert galaxy Markarian 477: Implications for the starburst-active galactic nucleus connection", 1997, *ApJ*, **482**, 114.
- [66] Högbom, J. "Aperture synthesis with a non-regular distribution of interferometer baselines", 1974, *A&ASS*, **15**, 417.
- [67] Hubble, E.P. "Extragalactic nebulae", 1926, *ApJ*, **64**, 321.
- [68] Huchra, J., Davis, M., Latham, D., & Torny, J. "A survey of galaxy redshifts. IV. The data", 1983, *ApJS*, **52**, 89.
- [69] Huchra, J., Wyatt, W.L., & Davis, M. "New bright Seyfert galaxies", 1982, *AJ*, **87** 1628.
- [70] Huchra, J., & Burg, R. "The spatial distribution of active galactic nuclei. I. The density of Seyfert galaxies and LINERs", 1992, *ApJ*, **393** 90.
- [71] Hummel, E., Fanti, C., Parma, P., & Schilizzi, R.T. "VLBI observations of the core sources of a sample of spiral galaxies", 1982, *A&A*, **114**, 400.

- [72] Johnson, W.M., Zdziarski, A.A., Madejski, G.M., Pacuesas, W.S., Steinle, H. & Ying-Chi Lin. "Seyfert and radio galaxies", in *Proc. of the fourth Compton Symp.*, eds. Dremer, C.D., Strickman, M.S., & Kurfess, J.D., 1997, The Am. Inst. of Phy., p. 283.
- [73] Johnston, K.J., Elvis, M., Kjer, D., & Shen, B.S.P. "Radio jets in NGC 4151", 1982, *ApJ* **262**, 61.
- [74] Kapahi, V.K., & Saikia, D.J. "Relativistic beaming in the central components of double radio quasars", 1982, *JApA*, **3**, 465.
- [75] Keel, W.C. "An H-alpha forbidden N II survey of the nuclei of a complete sample of spiral galaxies", 1983, *ApJS*, **52**, 229.
- [76] Keel, W.C. "Star formation around active galactic nuclei", in *Star Formation in Galaxies*, 1987, NASA Conf. Publ., **2466**, 661.
- [77] Kellermann, K.I., Sramek, R., Schmidt, M., Shaffer, D.B., & Green, R. "VLA observations of objects in the Palomar bright quasar survey", 1989, *AJ*, **98**, 1195.
- [78] Khachikian, E.Y., & Weedman, D.W. "An atlas of Seyfert galaxies", 1974 *ApJ*, **192**, 581.
- [79] Kim, D.-C., Veilleux, S., & Sanders, D.B. "The IRAS 1 Jy Sample of Ultraluminous Infrared Galaxies. II. Optical Spectroscopy", 1998, *ApJ*, **508**, 627.
- [80] Kinney, A.L., Antonucci, R.R.J., Ward, M.J., Wilson, A.S., & Whittle, M. "The featureless continua and hydrogen lines of Seyfert 2 galaxies", 1991, *ApJ*, **377**, 100.
- [81] Kinney, A.L., Schmitt, H.R., Clarke, C.J., Pringle, J.E., Ulvestad, J.S., & Antonucci, R.R.J. "Jet directions in Seyfert galaxies", 2000, *ApJ*, **537**, 152.
- [82] Kriss, G.A., Tsvetanov, Z., & Davidsen, A.F. "New Insights into Seyfert Galaxies from HUT Observations of NGC 1068 and NGC 4151", in *First Stromlo Symposium: The phy of active galaxies*, eds. Bicknell, G.V., Dopita, M.A., & Quinn, P.J., 1994, ASP Conf. Ser., **54**, p. 281.
- [83] Krolik, J.H., & Begelman, M.C. "Molecular tori in Seyfert galaxies - Feeding the monster and hiding it", 1998, *ApJ*, **329**, 702.

- [84] Krolik, J.H. *Active Galactic Nuclei*, 1999, Princeton University Press.
- [85] Kruper, J.S., Canizares, C.R., & Urry, C.M. "Soft X-ray properties of Seyfert galaxies. I - Spectra", 1990, *ApJS*, **74**, 347.
- [86] Kukula, M.J., Pedlar, A., Baum, S.A., & O'Dea, C.P. "High resolution radio observations of the CfA Seyfert sample - I". The observations, 1995, *MNRAS*, **276**, 1262.
- [87] Kukula, M.J., Ghosh, T., Pedlar, A., & Schilizzi, R.T. "Parsec-scale radio structure in the nuclei of four Seyfert galaxies", 1999, *ApJ*, **518**, 117.
- [88] Lawrence, A., & Elvis, M. "Obscuration and the various kinds of Seyfert galaxies", 1982, *ApJ*, **256**, 706.
- [89] Lawrence, A. "Classification of active galaxies and the prospect of a unified phenomenology", 1987, *PASP*, **99**, 309.
- [90] Lipovetsky, V.A., Neizvestny, S.I., & Neizvestnaya, O.M. "A catalogue of Seyfert galaxies", 1988, *Soobshch. Spets. Astrofiz. Obs.*, **55**, 5.
- [91] Lonsdale, C.J., Lonsdale, C.J., & Smith, H.E. "A VLBI search for AGN radio cores in starburst galaxies", 1992, *ApJ*, **391**, 629.
- [92] Lonsdale, C.J., Smith, H.E., & Lonsdale, C.J. "The starburst-AGN connection: A sensitive VLBI survey of luminous IRAS galaxies", 1993, *ApJL*, **405**, L9.
- [93] Maiolino, R., Ruiz, M., Rieke, G.H., & Papadopoulos, P. "Molecular gas, morphology, and Seyfert galaxy activity", 1997, *ApJ*, **485**, 552.
- [94] Malaguti, G., Bassani, L., & Caroli, E. "High-energy spectra of active galactic nuclei. I. The catalog", 1994, *ApJS*, **94**, 517.
- [95] Malkan, M.A., Gorjian, V., & Tam, R. "A Hubble space telescope imaging survey of nearby active galactic nuclei", 1998, *ApJS*, **117**, 25.
- [96] Maloney, P.R., & Reynolds, C.S. "ASCA observations of an X-ray luminous active nucleus in Markarian 231", 2000, *ApJL*, **545**, L23.
- [97] Markarian, B.E. "Galaxies with an ultraviolet continuum", *Astrophysics*, 1967, **3**, 24.

- [98] Markarian, B.E., Stepanian, J.A., & Erastova, L.K. "The second Byurakan spectral sky survey V. The results of the area centered on $\alpha = 15\text{ h } 30\text{ m}$, $\delta = +59\text{ deg } 00\text{ arcmin}$ ", 1986, *Astronomy*, **25**, 345.
- [99] Mas-Hesse, J.M., Rodriguez-Pascual, P.M., de Cordoba, L.S.F., Mirabel, I. F. "Multiwavelength analysis of quasars, Seyfert galaxies, and starbursts", 1994, *ApJS*, **92**, 599.
- [100] Meurs, E.J.A., & Wilson, A.S. "Markarian Seyfert galaxies - Optical and radio luminosity functions and other statistical studies", 1984, *A&A*, **136**, 206.
- [101] Miley, G.K., Neugebauer, G., & Soifer, B.T. "IRAS observations of Seyfert galaxies", 1985, *ApJL*, **293**, L11.
- [102] Miller, J.S., & Goodrich, R.W. "Spectropolarimetry of high-polarization Seyfert 2 galaxies and unified Seyfert theories", 1990, *ApJ*, **355**, 456.
- [103] Mills, B.Y. "Observations at Sydney", 1952, *Nature*, **170**, 1063.
- [104] Mills, B.Y., & Little, A.G. "A high-resolution aerial system of a new type", 1953, *Aust. J. Phys.*, **6**, 272.
- [105] Miyoshi, M., Moran, J., Herrnstein, J., Greenhill, L., Nakai, N., Diamond, P., & Inoue, M. "Evidence for a black-hole from high rotation velocities in a sub-parsec region of NGC 4258", 1995, *Nature*, **373**, 127.
- [106] Morganti, R., Tsvetanov, Z.I., Gallimore, J., & Allen, M.G. "Radio continuum morphology of southern Seyfert galaxies", 1999, *A&AS*, **137**, 457.
- [107] Mundell, C.G., Wilson, A.S., Ulvestad, J.S., & Roy, A.L. "Parsec-scale images of flat-spectrum radio sources in Seyfert galaxies", 2000 *ApJ*, **529**, 816.
- [108] Mushotzky, R.F. "X-ray spectra and time variability of active galactic nuclei", 1984, *ASpR*, **3**, 157.
- [109] Mushotzky, R.F., Done, C., & Pound, K.A. "X-ray spectra and time variability of active galactic nuclei", 1993, *ARA&A*, **31**, 717.
- [110] Muxlow, T.W.B., Pedlar, A., Wilkinson, P.M., Axon, D.J., Sanders, E.M., & de Bruyn, A.G. "The structure of young supernova remnants in M 82", 1994 *MNRAS*, **266**, 455.

- [111] Nagar, N.M., & Wilson, A.S. "The relative orientation of nuclear accretion and galaxy stellar disks in Seyfert galaxies", 1999A, *ApJ*, **516**, 79.
- [112] Nagar, N.M., Wilson, A.S., Mulchaey, J.S., & Gallimore, J.F. "Radio structures of Seyfert galaxies. VIII. A distance and magnitude limited sample of early-type galaxies", 1999B, *ApJS*, **120**, 209.
- [113] Nagar, N.M., Falcke, H., Wilson, A.S., & Ho, L.C. "Radio sources in low-luminosity active galactic nuclei. I. VLA detections of compact, flat-spectrum cores", 2000, *ApJ*, **542**, 186.
- [114] Nandra, K., & Pounds, K.A. "GINGA observations of the X-ray spectra of Seyfert galaxies", 1994, *MNRAS*, **268**, 405.
- [115] Napier, P.J. "The VLBA design" in *VLBI and the VLBA*, eds. Zensus, J.A., Diamond, P.J., & Napier, P.J., 1995, ASP Conf Series, **82**, p. 59.
- [116] Narayan, R., & Nityananda R. "Maximum entropy image restoration in astronomy", 1986, *ARA&A*, **24**, 127.
- [117] Neff, S.G., & de Bruyn, A.G. "The compact radio core of Mkn 348: evidence for directed outflow in a type 2 Seyfert galaxy", 1983, *A&A*, **128**, 318.
- [118] Neff, S.G., & Ulvestad, J.S. "Compact radio cores in three Seyfert galaxies - High resolution studies of Mkn 3, Mkn 231, and Mkn 463", 1988, *AJ*, **96**, 841.
- [119] Nelson, C.H., & Whittle, M. "Stellar and gaseous kinematics of Seyfert galaxies. I. Spectroscopic data", 1995, *ApJS*, **99**, 67.
- [120] Nelson, C.H., & Whittle, M. "Stellar and gaseous kinematics of Seyfert galaxies. II. The role of the bulge", 1996, *ApJ*, **465**, 96.
- [121] Norris, R.P., Kesteven, M.J., Allen, D.A., & Troupe, E. "Compact radio cores in infrared galaxies", 1988A, *MNRAS*, **234**, 51.
- [122] Norris, R.P., Kesteven, M.J., Wellington, K.J., & Batti, M.J. "The Parkes-Tidbinbilla interferometer", 1988B, *ApJS*, **67**, 85.
- [123] Norris, R.P., Kesteven, M.J., Troup, E.R., Allen, D.A., & Sramek, R.A. "Compact radio cores in extremely luminous far-infrared galaxies", 1990, *ApJ*, **354**, 267.

- [124] Norris, R.P., Roy, A.L., Allen, D.A., Kesteven, M.J., Troup, E.R., & Reynolds, J.E. "Compact radio cores in Seyfert and starburst galaxies", in *Relationships between active galactic nuclei and starburst galaxies*, ed. Filippenko, A.V. 1992A, ASP Conf Series, **31**, p. 71.
- [125] Norris, R.P., Kesteven, M.J., & Calabretta, M.R. "Data reduction and image processing", 1992, JI. Elect. of Elec. and Engg., Austr., **12**, 205.
- [126] Osterbrock, D.E. "Seyfert galaxies with weak broad H alpha emission lines", 1981, ApJ, **249**, 462.
- [127] Osterbrock, D.E., & Pogge, R.W. "The spectra of narrow-line Seyfert 1 galaxies", 1985, ApJ, **297**, 166.
- [128] Pearson, T.J. *HAZI*, 1994.
<http://www.astro.caltech.edu/~tjp/citvlb/vlbhelp/hazi.html>
- [129] Pearson, T.J. *UPTIME*, 1995.
<http://www.astro.caltech.edu/~tjp/citvlb/vlbhelp/uptime.html>
- [130] Pedlar, A., Kukula, M.J., Longley, D.P.T., Muxlow, T.W.B., Axon, D.J., Baum, S.A., O'Dea, C.P., & Unger, S.W. "The radio nucleus of NGC 4151 at 5 and 8 GHz", 1993, MNRAS, **263**, 471.
- [131] Perola, G.C., Piro, L. Altamore, A., Fiore, F., Boksenberg, A., Penston, M.V., Snijders, M.A.J., Bromage, G.E., Clavel, J., Elvius, A., & Ulrich, M.H. "New results on the X-ray emission and its correlation with the ultraviolet in NGC 4151", 1986, ApJ, **306**, 508.
- [132] Peterson, B.M. *An introduction to the Active Galactic Nuclei*, 1997, Cambridge University Press.
- [133] Pogge, R.W. "Ionized gas in the nuclear regions of nearby non-Seyfert spiral galaxies", 1989, ApJS, **71**, 433.
- [134] Preuss, E., & Fosbury, R.A.E. "VLBI observations of NGC 4151, Mkn 231 and other galaxies with broad emission line nuclei", 1983, MNRAS, **204**, 783.
- [135] Pringle, J.E., Antonucci, R.R.J., Clarke, C.J., Kinney, A.L., Schmitt, H.R., & Ulvestad, J.S. "Direct measurement of the jet geometry in Seyfert galaxies", 1999, ApJL, **526**, L9.

- [136] Reynolds, C.S. "An X-ray spectral study of 24 type 1 active galactic nuclei", 1997, MNRAS, **286**, 513.
- [137] Roy, A.L. "Active galaxy unification. Radio and far-infrared studies", 1995, PhD thesis.
- [138] Roy, A.L., Norris, R.P., Kesteven, M.J., Troup, E.R., & Reynolds, J.E. "Compact radio cores in Seyfert galaxies", 1994, ApJ, **432**, 496.
- [139] Roy, A.L., Norris, R.P., Kesteven, M.J., Troup, E.R., & Reynolds, J.E. "Seyfert galaxies and the radio-far-infrared correlation", 1998, MNRAS, **301**, 1019.
- [140] Rupen, M.P., van Gorkom, J.H., Knapp, G.R., Gunn, J.E., & Schneider, D.P. "Observations of SN 1986J in NGC 891", 1987, AJ, **94**, 61.
- [141] Rush, B., Malkan, M.A., & Spinoglio, L. "The extended 12 micron galaxy sample", 1993, ApJS, **89**, 1.
- [142] Rush, B., Malkan, M.A., & Edelson, R.A. "The radio properties of Seyfert galaxies in the 12 micron and CfA samples", 1996, ApJ, **473**, 130.
- [143] Ryle, M., & Hewish, A. "The synthesis of large radio telescopes", 1960, MNRAS, **120**, 220.
- [144] Sandage, A.R. "Classification and stellar content of galaxies obtained from direct photography", in *Galaxies and the Universe*, eds. Sandage, A.R., Sandage, M., Kristian, J., *Stars and Stellar Systems*, 1975, **9**, p.1, Univ. Chicago.
- [145] Sandage, A.R. & Tammann, G.A. *A revised Shapley-Ames catalogue*, 1981 Carnegie Institution of Washington.
- [146] Sanders, D.B., & Mirabel, I.F. "CO detections and IRAS observations of bright radio spiral galaxies at cz equal or less than 9000 kilometers per second", 1985, ApJL, **298**, L31.
- [147] Schmidt, M., & Green, R.F., "Quasar evolution derived from the Palomar bright quasar survey and other complete quasar surveys", 1983, ApJ, **269**, 352.
- [148] Schmitt, H.R., Ulvestad, J.S., Antonucci, R.R.J., & Kinney, A.L. "Jet directions in Seyfert galaxies: Radio continuum imaging data", 2000, astro-ph/0012123.
- [149] Seyfert, C.K. "Nuclear emission in spiral nebulae", 1943, ApJ, **97**, 28.

- [150] Shuder, J.M. "Emission-line-continuum correlations in active galactic nuclei", 1981, *ApJ*, **244**, 12.
- [151] Smith, D.A., & Done, C. "Unified theories of active galactic nuclei: a hard X-ray sample of Seyfert 2 galaxies", 1996, *MNRAS*, **280**, 355.
- [152] Smith, H.E., Lonsdale, C.J., Lonsdale, C.J., Diamond, P.J. "A starburst revealed - Luminous radio supernovae in the nuclei of ARP 220", 1998A, *ApJL*, **493**, L17.
- [153] Smith, H.E., Lonsdale, C.J., & Lonsdale, C.J. "The starburst-agn connection. II. The nature of luminous infrared galaxies as revealed by VLBI, VLA, infrared, and optical observations", 1998B, *ApJ*, **492**, 137.
- [154] Sopp, H.M., & Alexander, P. "A composite plot of far-infrared versus radio luminosity, and the origin of far-infrared luminosity in quasars", 1991, *MNRAS*, **251**, 14P.
- [155] Spinoglio, L., & Malkan, M.A. "The 12 micron galaxy sample. I - Luminosity functions and a new complete active galaxy sample", 1989, *ApJ*, **342**, 83.
- [156] Sramek, R.A., & Tovmassian, H.M. "Markarian 348: A variable radio source", 1974, *ApJL*, **191**, L13.
- [157] Sramek, R.A., & Tovmassian, H.M. "A radio survey of Markarian galaxies at 6 centimeters", 1975, *ApJ*, **196**, 339.
- [158] Su, B.M., Muxlow, T.W.B., Pedlar, A., Holloway, A.J., Steffen, W., Kukula, M.J., & Mutel, R.L. "Compact radio structure in the Seyfert nucleus of NGC 5929", 1996, *MNRAS*, **279**, 1111.
- [159] Taylor, G.B., Silver, C.S., Ulvestad, J.S., & Carilli, C.L. "The starburst in the central kiloparsec of Markarian 231", 1999, *ApJ*, **519**, 185.
- [160] Terashima, Y., Ho, L.H., & Ptak, A.F. "Hard X-ray emission and the ionizing source in LINERs", 2000, *ApJ*, **539**, 161.
- [161] Terlevich, R., & Melnick, J. "Warmers - The missing link between starburst and Seyfert galaxies", 1985, *MNRAS*, **214** 41P.

- [162] Terlevich, R., Melnick, J., & Moles, M. "Starburst models for AGNs", in *Observational Evidence of Activity in Galaxies*, eds. Khachikian, E.E., Fricke, K.J., & Melnick, J., 1987, IAUS, **121**, p. 499, Kluwer Academic Publishers, Dordrecht.
- [163] Terlevich, R., & Melnick, J. "The relation between variability and star formation in Seyfert nuclei", in *Observational evidence for activity in activity in galaxies*, eds. Kachikian, E., Melnick, J., & Fricke, 1987, p. 393, Reidel: Dordrecht.
- [164] Terlevich, R., & Melnick, J. "A supernova in the nucleus of NGC 5548?", 1988, *Nature*, **333**, 239.
- [165] Terlevich, R. "Active galactic nuclei without black-holes", in *Evolutionary phenomenon in galaxies*, eds. Beckman, J. & Pagel, B., 1989, p. 149, (Cambridge University Press).
- [166] Terlevich, R. "Active galactic nuclei as starbursts: Modelling the multifrequency spectrum", in *Windows on galaxies*, eds. Fabbiano, G., Gallagher, J. & Renzini, A., 1990A, ASSL, p. 87, Kluwer: Dordrecht.
- [167] Terlevich, R. "Star formation in galactic nuclei", in *Structure and dynamics of the inter-stellar medium*, eds. Tenorio-Tagle, G., Moles, M., & Melnick, J., 1990B, p. 343, Springer-Verlag: Berlin.
- [168] Terlevich, R. & Boyle, B.J. "Young ellipticals at high redshift", 1993, *MNRAS*, **262**, 491.
- [169] Thean, A., Pedlar, A., Kukula, M.J., Baum, S.A., & O'Dea, C.P. "High resolution radio observations of the Seyferts in the extended 12-micron sample - I. The observations", 2000, *MNRAS*, **314**, 573.
- [170] Thean, A., Pedlar, A., Kukula, M.J., Baum, S.A., & O'Dea, C.P. "Radio observations of Seyferts from the extended 12-micron sample - II. The properties of compact radio components", 2001, astro-ph/0103266.
- [171] Tran, H.D., Miller, J.S., & Kay, L.E. "Detection of obscured broad-line regions in four Seyfert 2 galaxies", 1992, *ApJ*, **397**, 452.
- [172] Tran, H.D. "The nature of Seyfert 2 galaxies with obscured broad-line regions. I. observations", 1995, *ApJ*, **440**, 578.

- [173] Turner, T.J., George, I.M., Nandra, K., & Mushotzky, R.F. "ASCA observations of type 2 Seyfert galaxies. I. Data analysis results", 1997, *ApJSS*, **113**, 23.
- [174] Turner, T.J., George, I.M., Nandra, K., & Mushotzky, R.F. "ASCA observations of type 2 Seyfert galaxies. III. Orientation and X-ray absorption", 1998, *ApJ*, **493**, 91.
- [175] Turner, T.J. "X-ray observations of Markarian 231", 1999, *ApJ*, **511**, 142.
- [176] Turner, T.J., George, I.M., Nandra, K., & Turcan, D. "On X-ray variability in Seyfert galaxies", 1999A, *ApJ*, **524**.
- [177] Turner, T.J., George, I.M., & Netzer, H. "Arkelian 564: An unusual component in the X-ray spectra of narrow-line Seyfert 1 galaxies", 1999B, **526**, 52.
- [178] Ulrich, M.-H. "The active galaxy NGC 4151: Archetype or exception?", 2000, *A&AR*, **10**, 135.
- [179] Ulvestad, J.S., Wilson, A.S., & Sramek, R.A. "Radio structures of Seyfert galaxies II", 1981, *ApJ*, **247**, 419.
- [180] Ulvestad, J.S. "An investigation of the star-burst model for radio emission from Seyfert galaxies", 1982, *ApJ*, **259**, 96.
- [181] Ulvestad, J.S., & Wilson, A.S. "Radio structures of Seyfert galaxies V. A flux limited sample of Markarian galaxies", 1984A, *ApJ*, **278**, 544.
- [182] Ulvestad, J.S., & Wilson, A.S. "Radio structures of Seyfert galaxies V. VLA observations of nearby sample", 1984B, *ApJ*, **285**, 439.
- [183] Ulvestad, J.S. "Radio properties of type 1.8 and 1.9 Seyfert galaxies", 1986, *ApJ*, **310**, 136.
- [184] Ulvestad, J.S., & Wilson, A.S. "The radio source in the very luminous gamma-ray Seyfert galaxy MCG 8-11-11", 1986, *MNRAS*, **218**, 711.
- [185] Ulvestad, J.S., & Wilson, A.S. "Radio structures of Seyfert galaxies VII. Extension of a distance limited sample", 1989, *ApJ*, **343**, 659.
- [186] Ulvestad, J.S., & Antonucci, R.R.J., Goodrich, R.W. "Radio properties of narrow-lined Seyfert 1 galaxies", 1995, *AJ*, **109**, 81.

- [187] Ulvestad, J.S., Roy, A.L, Colbert, J.M., & Wilson, A.S. "A subparsec radio jet or disk in NGC 4151", 1998B, ApJ, **496**, 196.
- [188] Ulvestad, J.S., Wrobel, J.M., & Carilli, C.L. "Radio continuum evidence for outflow and absorption in the Seyfert 1 galaxy Markarian 231", 1999A, ApJ, **516**, 127.
- [189] Ulvestad, J.S., Wrobel, J.M., Roy, A.L, Wilson, A.S., Falcke, H., & Krichbaum, T.P. "Subrelativistic radio jets and parsec-scale absorption in two Seyfert galaxies", 1999B, ApJL, **517**, L81.
- [190] Ulvestad, J.S. "VLBA calibration transfer with external telescopes (version 1.1)", 1999, VLBA operations memo No. 34, NRAO.
<http://www.aoc.nrao.edu/vlba/html/OBSERVING>
- [191] Ulvestad, J.S. "A step-by-step recipe fo VLBA data calibration in AIPS (version 1.2)", 2000, VLBA scientific memo No. 25, NRAO.
<http://www.aoc.nrao.edu/vlba/html/MEMOS/scimemos.html>
- [192] Unger, S.W., Pedler, A., Neff, S.G., & de Bruyn, A.G. "Sub-arcsec radio structure of the core-dominated Markarian 348 (NGC 262)", 1984, MNRAS, **209**, 15P.
- [193] Unger, S.W., Pedlar, A., Booler, R.V., & Harrison, B.A. "Compact radio components in Seyfert galaxies", 1986, MNRAS, **219**, 387.
- [194] Urry, C.M., & Padovani, P. "Unified schemes for radio-loud active galactic nuclei", 1995, PASP, **107**, 803.
- [195] de Vaucouleurs, G., de Vaucouleurs, A., Corwin (Jr.) H.G., Buta, R.J., Paturel, G., & Fouque, P. *Third reference catalogue of bright galaxies (RC3), version 3.9*, 1991, Springer-Verlag, New York.
- [196] Veron, P. "Surveys of local AGNs", in *Structure and evolution of active galactic nuclei*, eds. Giuricin, G., Mardirossian, F., Mezzetti, M., & Ramella, M. 1986, ASSL, p .253, D. Reidel Publishing Co.
- [197] Veron, M.-P., & Veron, P. *A catalogue of quasars and Active Galactic Nuclei (8th edition)*, 1998, European Southern Observatory.

- [198] *VLA Calibrator manual*, 2000, NRAO.
<http://www.aoc.nrao.edu/~gtaylor/calib.html>
- [199] Walker, R.C. *The SCHED user manual*, 2001, NRAO.
<http://www.aoc.nrao.edu/~cwalker/sched/sched/sched.html>
- [200] Ward, M.J., Elvis, M., Fabbiano, G., Carleton, N.P., Willner, S.P., & Lawrence, A. "The continuum of type 1 Seyfert galaxies. I - A single form modified by the effects of dust", 1987, *ApJ*, **315**, 74.
- [201] Weedman, D.W. "Seyfert galaxies", 1977, *ARA&A*, **15**, 69.
- [202] Whittle, M., Pedlar, A., Meurs, E.J.A., Unger, S.W., Axon, D.J., Ward, M.J. "Radio lobes and forbidden O III profile substructure in Seyfert galaxies", 1988, *ApJ*, **326**, 125.
- [203] Whittle, M. "Virial and jet-induced velocities in Seyfert galaxies. I - A compilation of narrow line region and host galaxy properties", 1992A, *ApJS*, bf 79, 49.
- [204] Whittle, M., "Virial and jet-induced velocities in Seyfert galaxies. II - Galaxy rotation as virial parameter", 1992B, *ApJ*, **387**, 109.
- [205] Whittle, M., "Virial and jet-induced velocities in Seyfert galaxies. III. Galaxy luminosity as virial parameter", 1992C, *ApJ*, **387**, 121.
- [206] Wilson, A.S. "X-ray galaxies", 1979, *Proc. R. Soc. Lond. A.*, **366**, 461.
- [207] Wilson, A.S., & Willis, A.G. "Radio structures of Seyfert galaxies 1", 1980, **240**, 429.
- [208] Wilson, A.S. & Ulvestad, J.S. "Radio structures of Seyfert galaxies IV. Jets (?) in NGC 1068 and NGC 4151", 1982, *ApJ*, **263** 576.
- [209] Wilson, A.S. & Ulvestad, J.S. "Radio jets and high velocity gas in the Seyfert galaxy NGC 1068", 1983, *ApJ*, **275** 8.
- [210] Wilson, A.S., Baldwin, J.A., Sun, Sze-Dung, & Wright, A.E. "Kinematics and ionization of extended gas in active galaxies. II - A circumnuclear starburst in the type 1 Seyfert NGC 7469", 1986, *ApJ*, **310**, 121.

- [211] Wilson, A.S. "Star formation and nuclear activity in Seyfert galaxies", 1988, *A&A*, **206**, 41.
- [212] Wilson, A.S. & Keel, W.C. "High-resolution observations of the multicomponent nucleus of NGC 5929", 1989, *AJ*, **98**, 1581.
- [213] Wilson, A.S., Helfer, T.T., Haniff, C.A., & Ward, M.J. "The starburst ring around the Seyfert nucleus in NGC 7469", 1991, **381**, 79.
- [214] Wilson, A.S. "The radio emission of Seyfert galaxies", in *The interpretation of modern synthesis observations of spiral galaxies*, eds. Duric, N., & Crane, P.C., 1991, ASP, **18**, p. 227.
- [215] Wilson, A.S., Roy, A.L, Ulvestad, J.S., Colbert, J.M., Weaver, K.A., Braatz, J.A., Henkel, C., Matsuoka, M., Xue, A., Iyomoto, N. & Okada, K. "The ionization fraction in the obscuring "torus" of an active galactic nucleus", 1998, *ApJ*, **505**, 587.
- [216] Wrobel, J.M. 1995, "VLBI observing strategies", in *Very Long Baseline Interferometry and the VLBA*, eds. Zensus, J.A., Diamond, P.J., & Napier, P.J. 1995, ASP Conf Series, **82**, p. 411.
- [217] Wrobel, J.M. *VLBA observational status summary*, 2000A, NRAO.
<http://www.aoc.nrao.edu/vlba/obstatus/obssum.vlba/obssum.vlba.html>
- [218] Wrobel, J.M., Walker, R.C., Benson, J.M., & Beasley, A.J. "Strategies for phase referencing with the VLBA", 2000B, VLBA scientific memo No. 24, NRAO.
<http://www.aoc.nrao.edu/vlba/html/MEMOS/scimemos.html>
- [219] Wunderlich, E., Wielebinski, R., & Klein, U. "A further study of the relation of the radio-far-infrared in galaxies. I - Observations and data processing", 1987, *A&AS*, **69**, 487.
- [220] Wynn-Williams, C.G., & Becklin, E.E. "Luminous infrared galaxies: sizes at 10-32 microns", 1993, *ApJ*, **412**, 535.
- [221] Yee, H.K.C. "Optical continuum and emission-line luminosity of active galactic nuclei and quasars", 1980, *ApJ*, **241**, 894.

-
- [222] Zdziarski, A.A., Gierlinski, M., Gondek, D., & Magdziarz, P. “The canonical X-ray/gamma-ray spectrum of Seyfert 1s and low-state Galactic black hole candidates”, 1996, *A&AS*, **120**, 553.